LIGHT-INDUCED DYNAMICS AND SPECTROSCOPY OF CHIRAL BIOMOLECULES AND EXCITONIC NANOSTRUCTURES

DISSERTATION

zur Erlangung des akademischen Grades

Doctor rerum naturalium
(Dr. rer. nat.)

im Fach Physik

eingereicht am
Fachbereich Physik
der Freien Universität Berlin

vorgelegt von
Matthias Wohlgemuth

Berlin, 2020

Die Arbeiten für die vorliegende Dissertation wurde unter der Betreuung von Prof. Dr. Roland Mitrić an der Freien Universität Berlin und an der Julius-Maximilians Universität Würzburg durchgeführt.

Erstgutachter: Prof. Dr. Roland Mitrić

Zweitgutachter: Prof. Dr. Roland Netz

Tag der Disputation: 11. Februar 2021

SUMMARY

The interaction of biomolecules with UV light gives rise to a wide variety of fundamental processes in nature. For example, it is well known that biological molecules feature various relaxation pathways that efficiently dissipate the gained excess energy to their environment before any harmful, i.e., irreversible photoreactions can take place. The study of such processes may therefore extend the knowledge about why the biological matter is built exactly the way it is found on Earth today. In the present thesis, novel quantum-classical methods for the simulation of light-induced excited state dynamics in complex (bio)molecular systems have been developed and applied to selected examples. In addition, the methodology has been employed to simulate time-resolved spectroscopic observables.

In particular, the field-induced surface-hopping (FISH) approach has been extended to include terms beyond the electric field–electric dipole coupling as well as the interaction with circularly polarized light (CPL). The developed methodology has been applied to the smallest chiral amino acid, alanine. It has been found that asymmetric fragmentation and recombination in excited electronic states can be induced by irradiation with CPL. This leads to an enrichment of one of the stereogenic isomers up to $\pm$ 1.7%, where the sign depends on the helicity of the irradiating light.

The quantum-classical methodology has been further developed to study the photodynamics in multi-chromophoric molecular aggregates. In the newly developed multi-chromophoric FISH (McFISH) method, quantum-classical simulations in the frame of the extended Frenkel exciton model have been combined with QM/MM techniques in order to simulate the photodynamics of a double-stranded DNA decamer. In accordance with the experimental observations, a multi-exponential excited state decay involving the formation of long-lived delocalized as well as ultrafast decaying localized states resembling those of the bare nucleobases has been found.

Furthermore, a generally applicable method for the simulation of pump-probe time-resolved infrared (TRIR) spectra based on molecular dynamics simulations in the frame of the Wigner phase space representation of quantum mechanics has been developed. The obtained spectra are based on ab-initio potential energy surfaces and therefore include all anharmonicities. The developed methodology has been employed to investigate the migration dynamics of a single water molecule around the –CONH– peptide linkage in two peptide analogs serving as models for biological proteins. The simulated spectra are in excellent agreement with the experimental observations, and the simulations have allowed for an atomistic interpretation of the measured time scales, migration pathways, and their fingerprints in the experimental ps-TRIR spectra.

ZUSAMMENFASSUNG

Die Wechselwirkung von Biomolekülen mit UV-Licht führt zu einer Vielzahl von grundlegenden Prozessen. Beispielsweise ist bekannt, dass biologische Moleküle über verschiedene Relaxationswege verfügen, wodurch die überschüssige Lichtenergie effizient an die Umgebung abgegeben werden kann, bevor schädliche, d. h. irreversible Photoreaktionen stattfinden können. Die Untersuchung solcher Prozesse kann daher das Wissen darüber erweitern, warum biologische Materie genau so aufgebaut ist, wie sie heute auf der Erde zu finden ist. In der vorliegenden Arbeit wurden neuartige quantenklassische Methoden zur Simulation der lichtinduzierten Dynamik in komplexen (bio)molekularen Systemen entwickelt und auf ausgewählte Beispiele angewendet.

Zur Simulation der lichtinduzierten Dynamik in chiralen Biomolekülen wurde die feldinduzierte Surface-Hopping (FISH) Methode um höhere Kopplungsterme sowie um die Einbeziehung von zirkular polarisiertem Licht erweitert. Die entwickelte Methode wurde auf die kleinste chirale Aminosäure, Alanin, angewendet. Es konnte gezeigt werden, dass eine asymmetrische Fragmentierung und Rekombination in angeregten elektronischen Zuständen induziert werden kann. Abhängig von der Drehrichtung des eingestrahlten Lichts kann so eine Anreicherung eines der stereogenen Isomere von bis zu $\pm$ 1,7% erreicht werden.

Die lichtinduzierte Dynamik in molekularen Aggregaten konnte durch die neu entwickelte multi-chromophoren FISH (McFISH)-Methode, basierend auf dem erweiterten Frenkel-Exzitonenmodell kombiniert mit QM/MM-Techniken, simuliert werden. Die Methode wurde an der Photodynamik eines doppelsträngigen DNA-Dekamers demonstriert. In Übereinstimmung mit den experimentellen Beobachtungen wurde ein multiexponentieller Zerfall angeregter Zustände gefunden, der sowohl die Bildung langlebiger delokalisierter als auch den ultraschnellen Zerfall lokalisierter Zustände, die denen der reinen Nukleobasen ähneln, beinhaltet.

Darüber hinaus wurde eine allgemein anwendbare Methode für die Simulation von zeitaufgelösten Infrarotspektren (TRIR) auf Grundlage von Molekulardynamik-Simulationen im Rahmen der Wigner-Phasenraumdarstellung der Quantenmechanik entwickelt. Die erhaltenen Spektren basieren auf ab-initio-Potentialenergieflächen und beinhalten daher alle Anharmonizitäten. Die entwickelte Methodologie wurde verwendet um die Migrationsdynamik eines Wassermoleküls um eine Peptidbindung in zwei Peptid-Analoga zu simulieren, die Modelle für biologische Proteine darstellen. Die simulierten Spektren sind in exzellenter Übereinstimmung mit den experimentellen Befunden. Durch die Simulationen wurde eine atomistische Interpretation der gemessenen Zeitskalen, Migrationspfade und ihrer Fingerabdrücke in den experimentellen ps-TRIR-Spektren ermöglicht.

PUBLICATIONS

THE FOLLOWING PUBLICATIONS CONSITUTE THE MAIN PART OF THE THESIS:

[1]M. Wohlgemuth, M. Miyazaki, K. Tsukada, M. Weiler, O. Dopfer, et al., "Deciphering environment effects in peptide bond solvation dynamics by experiment and theory," Phys. Chem. Chem. Phys. **19**, 22564–22572 (2017).

[2]M. Wohlgemuth and R. Mitrić, "Photochemical chiral symmetry breaking in alanine," J. Chem. Phys. A **120**, 8976–8982 (2016).

[3]M. Wohlgemuth, M. Miyazaki, M. Weiler, M. Sakai, O. Dopfer, et al., "Solvation dynamics of a single water molecule probed by infrared spectra–theory meets experiment," Angew. Chem. Int. Ed. **53**, 14601–14604 (2014).

[4]M. Wohlgemuth and R. Mitrić, "Excitation energy transport in DNA modelled by multi-chromophoric field-induced surface hopping," Phys. Chem. Chem. Phys. **22**, 16536–16551 (2020).

THE FOLLOWING PUBLICATIONS ARE INCLUDED AS APPENDIX DUE TO FORMAL REASONS:

[5]M. Miyazaki, T. Nakamura, M. Wohlgemuth, R. Mitrić, O. Dopfer, et al., "Single water solvation dynamics in the 4-aminobenzonitrile–water cluster cation revealed by picosecond time-resolved infrared spectroscopy," Phys. Chem. Chem. Phys. **17**, 29969–29977 (2015).

[6]G. Tomasello, M. Wohlgemuth, J. Petersen, and R. Mitrić, "Photodynamics of free and solvated tyrosine," J. Phys. Chem. B **116**, 8762–8770 (2012).

CONTENTS

INTRODUCTION

For understanding the molecular evolution on earth, the exploration of biomolecules as the building blocks of life is essential. In the course of geological history, the smallest building blocks, namely amino acids, sugars, and nucleobases, formed increasingly complex molecular structures fulfilling numerous functionalities in living cells. While the variety of macromolecular structures found in living organisms is large and the functionality of each individual macromolecule is very specific, the building blocks form only a small subset of conceivable molecules. For example, only a combination of four nucleobases (adenine A, guanine G, cytosine C, and thymine T) together with the sugar ribose form the desoxyribonucleic acid (DNA), which carries the whole genetic information of a living organism and serves as the construction template for the biosynthesis of proteins and cellular self-replication. Similarly, proteins are essentially built from only 21 amino acids and are responsible for many metabolic processes, like molecular transport through cell membranes, signal conduction or as catalysts of chemical reactions. The enormous diversity of functionality of the macromolecular structures on the one side and the striking simplicity of the underlying building blocks on the other motivated numerous experimental and theoretical investigations in the past decades and has driven the development of new technologies.[1]

Amongst others, one major topic which is explored by this research, is dealing basically with the origin of life, trying to answer questions about how and why evolution has essentially chosen a handful of building blocks to organize life on earth. Here, the influence of UV radiation on those biomolecules has attracted particular attention, since the energy introduced by the absorption of UV light can lead to highly reactive electronic excited states or may even detach an electron completely, creating a cationic state (photoionization).[2] Moreover, vital processes such as energy conversion, as done by light harvesting complexes in the course of photosynthesis, rely fundamentally on photoinduced processes.[3,4] In general, the photoinduced excited state dynamics of molecules is characterized by nonadiabatic processes in which the coupling between the nuclear and electronic motion leads to nonradiative transitions between electronic states. Numerous fundamental photochemical processes, such as internal conversion, electron and proton transfer, photoisomerization, etc., rely fundamentally on the nonadiabatic effects.[5,6] However, the biological molecules found in nature are characterized by the presence of various relaxation pathways that efficiently dissipate the gained excess energy to the surrounding environment before any harmful, i.e., irreversible photoreactions can take place.[7,8] This ensures, amongst other mechanisms, the viability of biological organisms and protects, e.g., DNA against cancerogenic

mutations.[9] For example, the canonical nucleobases exhibit remarkably short (< 1 ps)[10] excited-state lifetimes and therefore a resultant low fluorescence quantum yield (< 1%)[8,10,11] – indicators for a high photostability – whereas this is often not observed in even highly similar compounds generated by minor chemical modifications.[8,10,11] The hypothesis grounded on this observation is that during the evolutionary process, nature selected building blocks that are resistant to UV radiation.[2,12]

The recent advances in modern laser spectroscopy made it possible to explore ultrafast processes happening on the timescale of a few picoseconds down to the attosecond regime.[13,14] Employing techniques such as time-resolved absorption and fluorescence spectroscopy as well as time-resolved photoelectron or infrared spectroscopy provided new insights not only to structural information but also a highly resolved dynamical picture.[15,16] The combination with sophisticated theoretical methods allows for the investigation of such ultrafast processes on the molecular level and thus provides an atomistic picture and interpretation of the experimental observations. Therefore, an accurate and efficient theoretical description of light-induced processes is highly desirable. Here, especially the combination of mixed quantum-classical molecular dynamics and the semiclassical representation of light-matter interaction can then be used to simulate either light-induced excitation processes or to calculate time-resolved spectroscopic observables.

In the following, three major scientific problems related to the evolution of biomolecules on Earth, which are touched in this thesis, are introduced and the respective methodological developments are sketched.

1.1 HOMOCHIRALITY AND THE ORIGIN OF LIFE

In the context of chemistry, the term chirality describes a spatial arrangement of atoms in a molecule in which simple symmetry operations do not lead to self-imaging. Here, a single or multiple atoms (most commonly asymmetric carbon atoms) in a molecule can have one or more stereogenic centers, or the entire molecular shape can make up the chirality (e.g., the helical structure of DNA). Two molecules having the same constitution (composition and topology) and are mirror images of each other, but are non-superposable (cf. Fig. 1), are called enantiomers and are classified into right-handed (D/R) and left-handed (L/S) form, respectively.

The existence of chiral molecules, being the same molecule's mirror-images, raised some fundamental questions in quantum mechanics. Specifically, if only electrostatic interactions exist between nuclei and electrons, then the electronic Schrödinger equation must be invariant with respect to spatial reflection. Hence, it is not conceivable that solutions of such a parity-even equation may be chiral. However, for chiral molecules, the enantiomeric solution must be equally admissible, and therefore a chiral molecular wave function cannot describe a stationary state. This is known as Hund's paradox.[17] Due to the high and broad energy barrier connecting the potential minima of the

enantiomers, the inversion frequency is very low (e.g., more than 1000 years for the simplest chiral amino acid alanine), and therefore quasi-stability is implied.[18] Although Hund's paradox is not of great practical importance, it is however not always trivial why a specific chiral molecule occurs in nature and not its counterpart.

THEORY OF EXTRATERRESTRIAL ENANTIOMERIC ENRICHMENT. Chiral molecules are widely spread in nature and are of great importance in chemistry and pharmacy.[19,20] In particular, the crucial building blocks associated with life, such as amino acids or sugars, are chiral. Interestingly, the monomers associated with life's principal biopolymers have unique and characteristic chiralities associated with them. With rare exceptions (e.g phospholipid membranes of single-celled archaea[21]), they possess either all-D or all-L configurations. For example, in biological organisms, proteins are solely built from L-amino acids or DNA/RNA contains D-sugars exclusively (cf. Fig. 2).

This homochirality is essential for life since the residues in biopolymers must have the same chirality so that, e.g., DNA/RNA can serve as a template in replication or proteins can fold into appropriate structures. Moreover, due to those building blocks' biased nature, the derived biologically active components (e.g., neurotransmitters) are chiral and their functionality is strongly dependent on the stereogenic configuration. Therefore, identifying chiral molecules and separation of racemic mixtures (that is, with equal quantities of the two enantiomers) is of great importance for synthesizing effective pharmaceuticals. However, in a prebiotic chemical world, the small molecules from which these macromolecules could be synthesized tend to have existed as racemic mixtures.[22] This brings up a significant sub-problem, i.e., the origin of this symmetry-breaking enantioselectivity of nature in the course of the geological evolution.[23–25]

In this context, several hypotheses about the origin of homochirality on Earth have been brought up and discussed in the past decades (cf. Refs. [22, 26–29] and references therein). The discovery of the Murchison and Murray meteorites revealed the presence

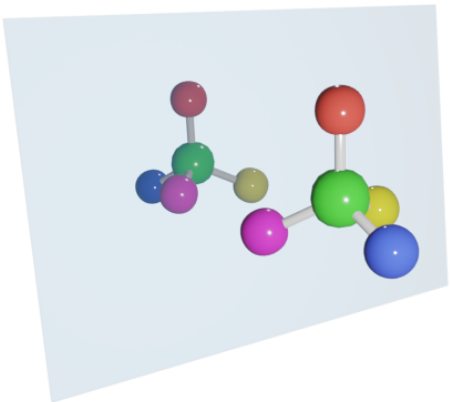

Figure 1: Schematic representation of two enantiomers of a chiral molecule, which are mirror images of each other, but are non-superposable.

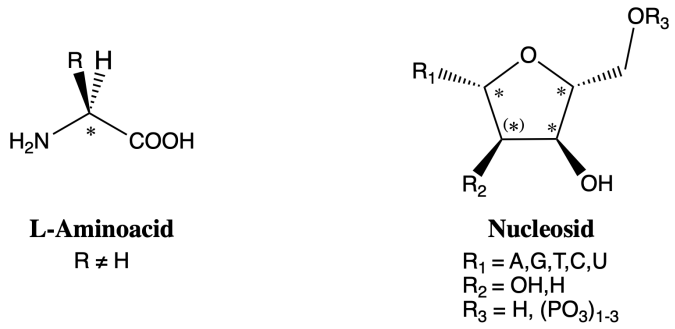

Figure 2: General structural formulas of L-aminoacids (left) and D-ribose as found in DNA/RNA nucleosides (right). The inset asterisks annotate the stereogenic carbon centers. The labels $R_{(n)}$ denote variable residues determining the biological building block.

of a series of aromatic and aliphatic compounds, including both saturated and unsaturated hydrocarbons, amino acids, small amounts of aldehydes and ketones as well as a wide spectrum of carboxylic acids and hydroxycarboxylic acids,[30,31] several nucleobases, and sugar acids.[32] Surprisingly, all amino acids showed a predominance of the L-form configuration at their asymmetric carbon atom.[33] In particular, the α-substituted amino acids, which are known to be especially resistant to racemization, exhibited an extremely high asymmetric enrichment ranging up to 60% for D-alloisoleucine[34] and 18% for L-isovaline[35] in the investigated meteorites. Contrary, meteoritic aliphatic amines and carboxylic acids that might share a common chemical origin with amino acids were found to be racemic with the exception of lactic acid.[36]

The observation of enantiomerically enriched left-handed meteoric amino acids[33] led to the proposal that some cosmic factors are responsible for the chiral imbalance on Earth. In that case, the enantiomerically enriched biomolecules were brought to Earth on meteorites and comets and have been subsequently amplified to the present homochiral state. A rather popular idea is the deracemization of preformed racemic compounds by, i.e., chiral irradiation or chiral magnetic[37,38] or gravitational[39] fields. It was shown that circularly polarized light (CPL) might cause slightly enantioselective destruction (deracemization) of chiral compounds. Numerous extensive papers and reviews analyze astronomical sources of circularly polarized light[40–42] and results of model experiments on deracemization of amino acids[28,32,43,44] in terms of possible origins of biological homochirality on the Earth.[32,45] In particular, early photolysis experiments on alanine[46] and leucine[47] in aqueous solution have shown that the L-form of these amino acids can be enantioselectively enriched by up to 2.5% using CPL via a $n\pi^*$ excited state.[47] Recently, Meierheinrich and co-workers showed by irradiation of thin alanine films by circularly polarized Synchrotron radiation enantiomeric enrichment of L-alanine up to 4.5% for left and -4.2% for right CPL, depending on the excitation energy, irradiation time, and the environmental conditions.[48,49] Further, recent works suggested that the

magnetic field of a nascent neutron star from core-collapsed supernovae may induce deracemization of the amino acids by the neutrinos that would be emitted.[37,38]

Conversely, the asymmetric synthesis of chiral biomolecules from achiral precursors by CPL on stellar objects is discussed and was modeled in laboratory.[50,51] The experiments, in which models of extraterrestrial ice were irradiated by CPL, revealed that in total, 16 amino acids were formed, where five of them (α-alanine, 2,3-diaminopropionic acid, 2-aminobutyric acid, valine and norvaline) were analyzed by enantioselective mass spectrometry techniques. The results showed that induced enantiomeric enrichment rises with irradiation time from 0.2% to 2.54%, where the sign depends on the helicity of the CPL.[50,51]

In the past decades, interest also focused on whether and to what extent the influence of parity-violating weak nuclear forces effect spectroscopy and dynamics of chiral molecules.[52,53] This might have played a role in preferentially stabilizing one enantiomer as opposed to the other in the evolutionary process.[18] However, the direct observation of chirality in space is not possible through remote detection. Recently, a fascinating space mission has been started to explore the chemical composition of comets. Launched 11 years ago, the Philae lander of the ESA Rosetta spacecraft has landed in 2014 on the 67P/Churyumov-Gerasimonko (67P/C-G) comet. Among other instruments, the lander is equipped with a Cometary Sampling and Composition (COSAC) instrument, which can identify, separate, and quantify organic molecules, including enantiomers expected to be found in the cometary ices.[54] The COSAC module has successfully identified several chiral organic molecules, such as amino acids, carboxylic acids, and hydrocarbons.[55,56] Unfortunately, because of its disadvantageous final position, the Philae lander lost its power, such that no enantiomeric on-site analysis has been performed.

In conclusion, many possible mechanisms have been proposed for the homochiral nature on Earth, where most of them suggest the involvement of circularly polarized light, either by asymmetric formation or destruction of chiral molecules. However, no final conclusion can be made, and the question is still the subject of current research. Since this topic is highly relevant for understanding the origin of life, a thorough understanding of the underlying mechanisms and theoretical investigation of the light-matter interaction is crucial.

CIRCULAR DICHROISM. An inherent property of chiral molecules is that they are optically active. Since CPL itself is chiral, the optical activity results from the molecular conformations interacting differently with left (l-) and right (r-) CPL. For linearly CPL, which can be understood as a superposition of two parallel left- and right-handed circularly polarized waves, the polarized light's plane is rotated. In particular, the optical rotatory dispersion (ORD) is the consequence of the fact that in an optically active medium, the index of refraction is different for l- and r-CPL or, in other words, an optically active substance transmits r-CPL with a different velocity than l-CPL.

Accompanied by this anomalous rotatory dispersion is that, for wavelengths that are absorbed by the optically active sample, the two circularly polarized components will be absorbed to differing extents, giving rise to the circular dichroism (CD) being the difference of the two absorption coefficients ε:

$$\Delta\varepsilon(\lambda) = \varepsilon_l(\lambda) - \varepsilon_r(\lambda). \tag{1.1}$$

It was shown that ORD and CD are connected by the Kronig-Kramer relation and if the entire ORD spectrum is known, the CD spectrum can be calculated, and vice versa. Although ORD and CD spectroscopy is normally used to investigate chiral molecules, even substances that lack chirality can be studied using a static magnetic field known as magnetic optical rotatory dispersion (MORD) regions of absorption, magnetic circular dichroism (MCD) is observable.

From the point of theory, when light passes through an absorbing optically active medium, the electric field causes a linear displacement of charge (electric dipole). In contrast, its magnetic field causes a circulation of charge (magnetic dipole). It was shown by Rosenfeld in 1928 that, similarly as the ordinary absorbance ε is proportional to the oscillator strength $f \propto \left|\langle \psi_g \,|\, \hat{\boldsymbol{\mu}} \,|\, \psi_e \rangle\right|^2$, the optical activity for an electronic transition from state g to e is directly connected and proportional to the rotatory strength R:[57]

$$\Delta\varepsilon \propto R = \operatorname{Im} \langle \psi_g \,|\, \hat{\boldsymbol{\mu}} \,|\, \psi_e \rangle \cdot \langle \psi_g \,|\, \hat{\boldsymbol{m}} \,|\, \psi_e \rangle , \tag{1.2}$$

where $\hat{\boldsymbol{\mu}}$ represents the electric transition dipole moment and $\hat{\boldsymbol{m}}$ the magnetic transition dipole moment operators, respectively. Note that the expectation value of $\hat{\boldsymbol{\mu}}$ is real and it is imaginary for $\hat{\boldsymbol{m}}$, such that the oscillator strength f and rotatory strength R are both real quantities. To obtain non-zero R or $\Delta\epsilon$, respectively, it is required that electric *and* magnetic dipole operators transform as the same irreducible representation. This is only the case for the point groups C_n and D_n, and therefore only chiral molecules are CD active.

Due to the intrinsic link of optical activity with the molecular structure, CD spectroscopy has been an important tool for gathering structural information about chemical and biological compounds,[58] and advances in modern laser spectroscopy made it possible to extend the toolbox for studying CD effects. Thus several experimental methods, such as laser ionization mass spectrometry,[59–61] fluorescence[62] or photoelectron spectroscopy[63] have been developed. Further, CD effects in two- and multiphoton excitations have been studied experimentally[64] and theoretically.[65,66] Employing ultrashort laser pulses opens new perspectives to time-resolved spectroscopy and optimal control by pulse shaping for chiral molecules. Here, time-dependent CD (TDCD) spectroscopy lead to mechanistic insights into fundamental photochemical processes and were also successfully applied to mass spectrometric measurements for the separation of enantiomers.[59,60,67,68]

From a theoretical point of view, dynamical CD effects have only been studied using electron wave packet dynamics so far. Here, enantiomeric enrichment in the

sense of asymmetric population transfer due to the application of CPL at a two-level chiral model system[69,70] and 3-Methylcyclopentanone[71] has been shown. However, those studies neglect nuclear motion's influence, which leads to nonadiabatic coupling between electronic states. Since these nonadiabatic effects ultimately determining the course of various fundamental photochemical processes, the theoretical treatment of coupled electron-nuclear dynamics driven by complex-shaped laser pulses is required.

FIELD-INDUCED SURFACE-HOPPING. To study the photodynamics of molecules, a particularly attractive approach is the semiclassical molecular dynamics "on the fly" combined with the field-induced surface hopping (FISH) method[72] since it allows for the explicit inclusion of the exciting laser pulse. In the original formulation of the FISH approach by Petersen et al., the irradiating laser field was introduced to the electron dynamics using a linear dipolar coupling term. It was successfully applied to simulate the photodynamics of several biomolecules, such as tyrosine[73] and adenine,[74] optimal control,[75] as well as for the simulation of spectroscopic observables such as time-resolved photoelectron spectra (TRPES).[76,77] The FISH approach has been subsequently extended, e.g., to include non-linear coupling terms to study non-linear absorption phenomena.[78]

The electric dipole–electric field coupling gives the leading contribution in most applications. However, as can be shown by the symmetry properties of the laser field and the molecular properties, a chiroptical response capable to discriminate between two enantiomers is only obtainable if terms beyond the electric dipole–electric field interaction are considered. Particularly, the inclusion of magnetic dipole–magnetic field and electric quadrupole–electric field interaction terms are essential for capturing the properties inherent to chiral molecules.

Therefore, a focus of this thesis was to extend the FISH method to include also higher-order terms than the electric dipole–electric field coupling. The implemented method has been subsequently applied to study alanine's photodynamics, which is the smallest chiral amino acid. It thus serves as a prototype system for the investigation of enantiomeric enrichment under interstellar conditions. Therefore, it has been subject to numerous experimental studies[48,49,51,79–83] and of significant interest in theoretical works.[84–88] While the results are detailed in chapter 3, the performed simulations revealed that, in accordance with experimental findings, circularly polarized light can distinguish dynamically on the molecular level between left- and right-handed enantiomers. The photolysis induced by excitation with circularly polarized light leads to non-vanishing enantiomeric enrichment up to $\pm 1.7\%$ of either of the enantiomers, depending on the helicity of the included laser field.[89] Further, it has been shown that the inversion of the chiral center in the excited state induced by circularly polarized light is, in principle, possible. These results support the hypothesis that homochirality can be induced by circularly polarized light, which may be responsible for the enantiomeric

enrichment of chiral molecules on extraterrestrial objects prior to their arrival on Earth.[89]

1.2 EXCITATION ENERGY TRANSPORT IN MULTI-CHROMOPHORIC COMPLEXES

Although the bare building blocks of life also occur in their pristine or chemically modified form in nature (e.g., as neurotransmitters) and are therefore interesting research subjects in their own right, their full capability reveals if they are building up supramolecular structures and molecular aggregates. For example, the genetic information of all living organisms (except certain viruses) is encoded in the specific sequence of the nucleobases: adenine (A), thymine (T), guanine (G), and cytosine (C). Since DNA serves as the construction template for the biosynthesis of proteins and is responsible for cellular self-replication, its stability against harmful environmental impacts is essential for life. However, the DNA is also a strong UV light absorber, leaving it highly susceptible to photomutagenic damage. It is well established that UV radiation can trigger carcinogenic mutations directly or indirectly in DNA.[90–92] Particularly, the irradiation with UV-B light may cause the formation of pyrimidine dimers,[93] that is an abnormal bond between adjacent pyrimidine bases (T and C). Therefore, the geological evolution has established effective mechanisms,[94] such as enzymatic repair actions (e.g., photolyase or using the complementary strand as a template) or apoptosis due to checkpoint inhibition, to reduce the risk of malignant degeneracy. However, since most biological organisms are constantly exposed to sunlight, the energetically expensive repair would be futile. Therefore efficient mechanisms have to be present to ensure that the induced photon energy does not lead to photodamages in DNA.

In contrast to the bare nucleobases, which exhibit various nonradiative decay channels allowing the relaxation to the ground state in several hundred femtoseconds,[8,10,95] long-living delocalized excited states are observed in the aggregated form of DNA.[96,97] Those delocalized states, known as excimers or exciplexes, allow the radiationless transport of excitation energy and therefore provide an efficient pathway to transfer and distribute the excess energy introduced by the irradiating light.[96]

Those energy transfer (ET) processes are also found in photosynthetic complexes such as the photosystem II. Here, nature developed sophisticated and highly efficient molecular aggregates that efficiently absorb sunlight and convert it into chemical energy. This energy is finally used by photosynthetic organisms, such as bacteria, algae, or plants, to live and grow. The understanding of this light-harvesting (LH) processes occurring in photosynthetic complexes has been an important goal since the first high-resolution structure of the Fenna–Matthews–Olson (FMO) complex appeared.[98] Furthermore, designing and controlling ET in synthetic LH materials that mimic the natural ones can provide a route to organic photovoltaics,[99] light-emitting diods[100] and sensors.[101]

EXCITATION ENERGY TRANSPORT. The transport of energy from one location to another is an important research problem in all fields of physics (e.g., the conduction of heat or electric current). The observation of ET over distances larger than the sum of the radii of the interacting molecules or atoms was the first indication of dipole-dipole resonance transfer. Subsequently, it has been experimentally observed that energy could be transferred from an excited molecule to a nearby molecule over distances far exceeding the molecular dimensions.[102] The observation of this resonant energy transfer was first explained by Jean-Baptiste and Francis Perrin in the frame of the intermolecular near-field dipole-dipole mechanism,[103,104] which, however, overestimated the distance dependency of ET rates. The correct R^{-6} distance dependency was later found by Theodor Förster[1] and the mechanism is therefore known as Förster Resonance Energy Transfer (FRET).[107] The FRET mechanism relies on the assumption that the excitation is completely localized on either the donor or acceptor side and that the two interacting molecules are very far apart, such that the interaction of the charge densities can be approximated by point dipole-dipole interactions. Therefore, it applies to situations where the coupling between the donor and acceptor molecule is very weak and the molecules are capable of optical transitions between the respective energy levels.

As it became known that photosynthetic complexes are constituted from highly organized close-lying molecules, so that the simple point dipole-dipole approximation may no longer be valid, Förster's theory has been further developed by modeling the extended charge distribution beyond the point dipole approximation. In this context, Dexter and co-workers proposed an electron exchange mechanism when there is an overlap of atomic orbitals and the ET is also possible between two molecules with forbidden optical transitions.[108,109]

FRENKEL EXCITON MODEL. Experimentally, excitation energy transfer (EET) dynamics is commonly studied by a variety of time-resolved spectroscopy techniques, such as pump-probe and transient absorption measurements or 2D electron spectroscopy, which have been used to investigate the energy migration in and electronic relaxation in LH complexes,[110] chromophore rings[111] or dendrimers.[112] Those measurements can provide detailed and highly resolved information on EET, which have to be met by the corresponding theoretical model.

Ideally, one would like to model non-adiabatic processes for complex molecular aggregates such as DNA or LH complexes. Unfortunately, the complexity of those systems has precluded the direct application of the approaches presented so far. A typical multi-chromophoric (MC) system that consists of coupled π-conjugated chromophores may be described in the frame of the Frenkel exciton model, in which the individual chromophores are treated as independent subunits. Those subunits are

1 It is generally not well recognized that William Arnold and Robert Oppenheimer derived the correct mechanism and theory earlier.[105,106]

subject to the regular quantum chemical methods and the coupling of those subunits is then approximated as a purely electrostatic interaction.

Martinez and co-workers have recently combined Tully's fewest switching algorithm (cf. Sec. 2.2) with the exciton model to study the excitation energy transport and non-adiabatic dynamics in the LHII complex.[113,114] Here, the chromophores are coupled by coulombic dipole-dipole interaction and the electronic wave function is represented in the basis of excitonic eigenstates obtained from the product basis of ground- and singly-excited adiabatic wave functions of the individual chromophores. The approach has been subsequently extended by Gonzalez and co-workers by introducing a mixed quantum mechanical–molecular mechanics (QM/MM) model, which allows for the simulation of chemically bonded chromophores as well. However, both methods lack the explicit inclusion of the irradiating laser pulse and the excited state dynamics are usually initiated by setting one of the monomers into the excited state close to the absorption band.[115]

In the frame of this thesis, the field-induced surface-hopping approach has been combined with the Frenkel exciton model. This allowed for investigating the excitation energy transport as well as nonradiative relaxation including all degrees of freedom. The method has been applied to simulate the excitation energy transport in DNA. The methodology is outlined in section 2.5 and the results of this study are detailed in chapter 4. In summary, it has been shown that, in accordance with previous experimental results,[96] after the initial excitation of exciton states, the total excited-state population of the excited states is multi-exponentially decaying. While the fast component relies here on the ultrafast nonradiative relaxation known from the bare nucleobases, the slow component has its origin in forming long-living exciton states. These lead to an increased photostability of DNA and ensure that the introduced energy is dissipated efficiently along the whole DNA strand.

1.3 THE ROLE OF SOLVENT AND ITS SPECTROSCOPY

In the previous sections, two important problems in the field of the photochemistry of biomolecules have been introduced. Specifically, in section 1.1 the influence of the molecular constitution in the sense of molecular chirality on the photodynamics has been outlined, which plays an important role in the origin of the homochirality of the building blocks of life. Furthermore, the preceding section has drawn the focus on the photodynamics of molecular aggregates such as light-harvesting complexes or DNA, where the interaction of neighboring chromophores leads to distinct properties in the dynamics of excited molecules that allow for the transport of energy over large distances.

An important aspect of the biological environment in which those biomolecules exist has not been considered so far: the influence of solvent. In particular, as long as biomolecules exist in their natural environment, they are surrounded by water

molecules and ions. The interaction of water with biomolecules and the formation of complex hydrogen-bonded (H-bonded) networks are important driving forces in biochemical reactions and structural rearrangements.[116–122] In particular, the structure and function of proteins are intimately connected with the dynamics of the water network. Furthermore, although water does not absorb light in the region emitted by the sun, it plays an important role in the non-adiabatic relaxation of biomolecules, and the involved mechanisms are of great diversity.[6,123,124] An example for those light-induced water-mediated relaxation processes is presented in appendix A. Here, the FISH approach combined with the hybrid quantum mechanical–molecular mechanical (QM/MM) technique has been employed to investigate the photodynamics of tyrosine in the gas-phase as well as solvated in water. For the gas phase, the relaxation evolves from the initially excited bright $\pi\pi^*$ state to the lowest dark $n\pi^*$ state via internal conversion. Subsequently, efficient nonradiative relaxation to the ground state occurs either through a repulsive $\pi\sigma^*$ state leading to breakage of the O-H bond or the transfer of a proton from the side chain to the phenyl ring. In the later two-step deactivation mechanism, the carboxyl group of the side chain first passes its proton to the amino group, from which it further migrates to the phenyl ring. This is accompanied by efficient fluorescence quenching, where the degeneracy is induced by an out-of-plane bending of the aromatic carbon atom, which is being protonated. In comparison to the simulations in the gas phase, an analogous relaxation mechanism has been found for the simulations including water, since it also involves the transfer of a proton from the side chain to the phenyl ring. However, in this case, a proton is donated from the protonated amino group to a nearby water molecule in the first step, which acts as a mediator and subsequently passes the proton to the phenyl ring. This emphasizes the decisive role of water in the photodynamics of tyrosine.[73]

Another example of the important role of water is the influence on protein folding and enzyme activity involving hydrogen-bond dynamics. With their –CONH– linkages along the peptide chain, proteins offer attractive hydrogen bonding sites, where water can bind either as a proton donor at the CO site or as proton acceptor at the NH site, respectively.[125] Various experimental methods have probed the solvation dynamics around proteins. One of the typical methods to observe the solvation dynamics has been the dynamic Stokes shift, i.e., the time-dependent spectral shift of fluorescence.[126,127] Here, the photoexcitation of a solute molecule causes a sudden change in the solute—solvent interaction, which is the driving force for the rearrangement. The triggered gradual reorientation of the solvent induces a spectral shift in the fluorescence of the solute molecule. This method has been applied in time-resolved studies to a wide variety of systems, ranging from dyes[128] to biological molecules, such as aromatic amino acid residues and proteins.[129–131] Since proteins are often embedded in multiple solvation layers and the individual methods may measure water molecules in different layers, the results are often inconsistent and contradictory.[132–138] Hence, experimentally, averaged results over various water molecules in different local environments are

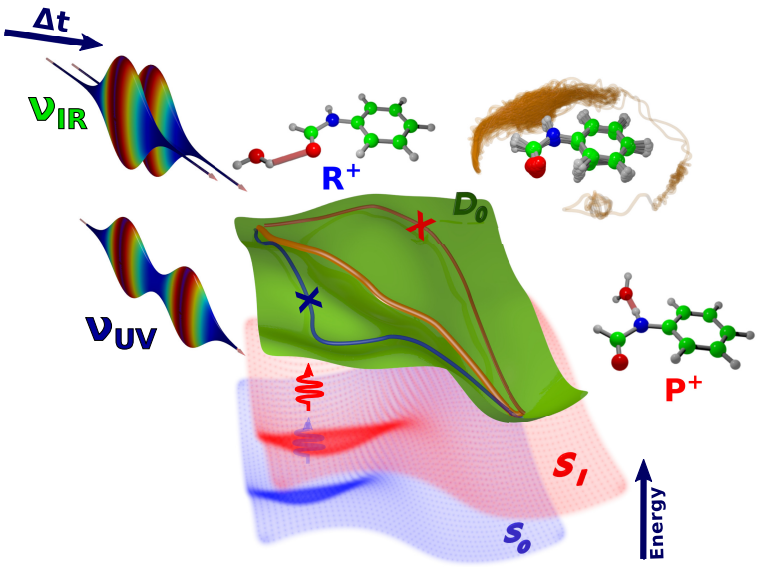

Figure 3: Scheme illustrating the experimental pump-probe procedure and dynamical time evolution after the ionization of the trans-formanilide–water (FA − W) cluster (reproduced with permission from Ref. [152]).

obtained, giving rise to only a limited picture of the dynamics of individual water molecules.[135] One possibility to overcome these limitations is the generation of size- and isomer-selected (micro-)hydrated peptides in the gas phase and study the dynamics of a single or several selected solvent molecules with time-resolved pump-probe techniques, such as time-resolved photoelectron spectroscopy[139–142] or the recently developed picosecond time-resolved infrared (ps-TRIR) spectroscopy.[143,144]

The latter one has successfully been applied to monitor in real-time the ionization-induced $\pi \rightarrow$H site-switching dynamics of rare gas ligands attached to the phenol molecule[143,145–148] as well as the water migration dynamics in the 4-aminobenzonitrile-water (cf. appendix B[149]), trans-acetanilide–water (cf. chapter 5[150,151]) and formanilide–water (cf. chapter 6[152]) cluster cations, which are part of this thesis. Combined with theoretical simulations, such experiments provide a detailed atomistic picture of the dynamics of individual solvent molecules.

The concept and the experimental procedure of pump-probe TRIR spectroscopy are illustrated in figure 3 on the example of the water migration dynamics of the formanilide–water (FA-W) cluster. Water in the neutral FA-W cluster being in the ground electronic state (S_0 in Fig. 3) is initially hydrogen-bonded to the CO site of the peptide linkage (R^+). At $t = 0$ the pump pulse resonantly ionizes the cluster via the first excited state (S_1) into the cation ground state (D_0) using size- and isomer-selective two-photon ionization. This ionization triggers a response of the solvent to the sudden change of the charge distribution since the interaction potential energy surface in the ionized D_0 state changes drastically. Consequently, water is released from its

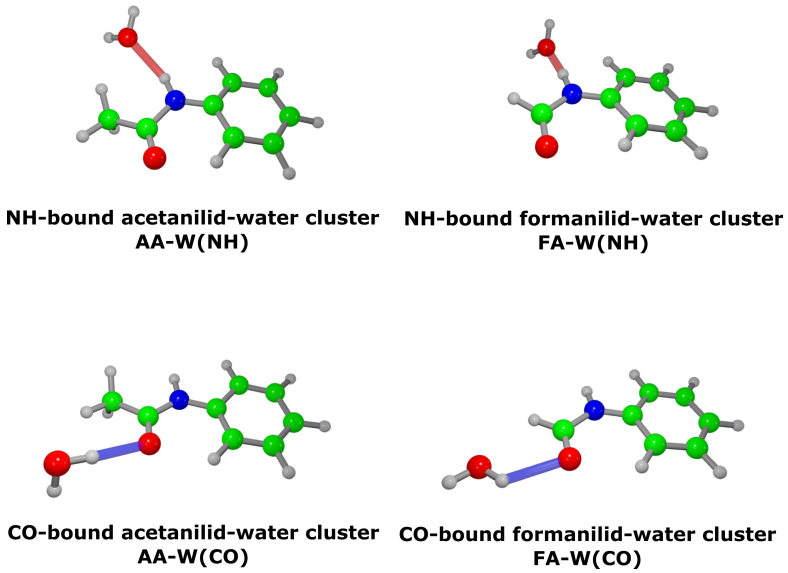

Figure 4: Structure of the NH- and CO-bound isomers of acetanilid–water and formanilid–water clusters.

initial CO-site in the neutral cluster and undergoes an exothermic large-amplitude migration reaction toward the now more attractive NH binding site (P^+) in the cationic cluster. This motion evolves in the picosecond timescale, which can be measured by a tunable IR probe-laser (ν_{IR}) introduced at a variable delay Δt after the ionization event. Because resonant vibrational excitation induces the dissociation of the cluster, it probes the isomerization dynamics, and the transient time-dependent IR spectrum can be measured. This allows for obtaining the vibrational fingerprints of the corresponding transient structures.[152]

Although the experimental ps-TRIR spectra yield new valuable insight into general reaction parameters (overall time constants, existence of an intermediate), important details of the reaction path (geometry, energetics, barriers, pathways) cannot be extracted. High-level theoretical molecular dynamics simulations are required to extract full information from the observed TRIR spectra. Moreover, to obtain a direct comparison to the experiment, the development of a sophisticated methodology to simulate pump-probe TRIR spectra was needed, which was not available so far. This is particularly challenging because the water migration processes under investigation are far from the equilibrium structures so that a harmonic approximation is no longer valid.

Therefore, in the frame of this thesis, a generally applicable methodology for the simulation of pump-probe TRIR spectroscopy based on molecular dynamics "on-the-fly" has been developed, which is presented in section 2.6. The developed methodology has been applied to investigate the water migration dynamics around the –CONH– peptide linkage in the two small model peptides trans-acetanilide and formanilide (cf. Fig. 4), respectively, and the results are presented in detail in the chapters 5 and 6. For both isomers, water is bound to the CO site in the neutral ground state. After

photoionization, water is migrating to the NH site within 10 ps in the case of the formanilid–water (FA-W) cluster and within 5 ps in the case of the acetanilid–water (AA-W) cluster. The simulated spectra are in excellent agreement with the experimental observations. The simulations have allowed for an atomistic interpretation of the measured timescales, migration pathways and their fingerprints in the experimental ps-TRIR spectra. In particular, the simulation of the AA-W cluster revealed that two pathways are participating in the migration dynamics, where one of them is responsible for the observation of an intermediate band in the ps-TRIR spectra. In contrast, although formanilid lacks only a single methyl group compared to acetanilid, both pathways are completely absent in the FA-W simulations and still an intermediate band is observed. Moreover, interestingly water approaches the NH site already within 500 fs, while the overall dynamics are much slower, which is also reflected by the ps-TRIR spectra. A profound analysis of the trajectories revealed that in the case of AA-W the methyl-group serves as a bath for vibrational kinetic energy, which efficiently withdraws the translational kinetic energy from the water migration channel leading to faster cooling.

BIBLIOGRAPHY

[1] A. H. Zewail, "Femtochemistry. past, present, and future," Pure Appl. Chem. **72**, 2219–2231 (2000).

[2] O. Leslie E, "Prebiotic chemistry and the origin of the RNA world," Crit. Rev. Biochem. Mol. Biol. **39**, 99–123 (2004).

[3] K. K. Rohatgi-Mukherjee, *Fundamentals of photochemistry* (New Age International, 1978).

[4] W. Wohlleben, T. Buckup, J. L. Herek, H. Hashimato, R. J. Cogdell, et al., "Energy flow in photosynthetic light harvesting: spectroscopy and control," in *Femtochemistry and femtobiology: ultrafast events in molecular science*, edited by M. M. Martin and J. T. Hynes (Elsevier, 2004), pp. 91–94.

[5] N. J. Turro, *Modern molecular photochemistry* (University science books, 1991).

[6] M. Wohlgemuth, R. Mitrić, and V. Bonačić-Koutecký, "Time-dependent density functional theory excited state nonadiabatic dynamics combined with quantum mechanical/molecular mechanical approach: photodynamics of indole in water," J. Chem. Phys. **135**, 054105 (2011).

[7] A. H. Zewail, "Femtochemistry: atomic-scale dynamics of the chemical bond," J. Phys. Chem. A **104**, 5660–5694 (2000).

[8] A. A. Beckstead, Y. Zhang, M. S. de Vries, and B. Kohler, "Life in the light: nucleic acid photoproperties as a legacy of chemical evolution," Phys. Chem. Chem. Phys. **18**, 24228–24238 (2016).

[9] S. Tommasi, M. F. Denissenko, and G. P. Pfeifer, "Sunlight induces pyrimidine dimers preferentially at 5-methylcytosine bases," Cancer Res. **57**, 4727–4730 (1997).

[10] C. E. Crespo-Hernández, B. Cohen, P. M. Hare, and B. Kohler, "Ultrafast excited-state dynamics in nucleic acids," Chem. Rev. **104**, 1977–2020 (2004).

[11] M. Daniels and W. Hauswirth, "Fluorescence of the purine and pyrimidine bases of the nucleic acids in neutral aqueous solution at 300 k," Science **171**, 675–677 (1971).

[12] W. J. Schreier, P. Gilch, and W. Zinth, "Early events of DNA photodamage," Annu. Rev. Phys. Chem. **66**, 497–519 (2015).

[13] A. L. Cavalieri, N. Müller, T. Uphues, V. S. Yakovlev, A. Baltuška, et al., "Attosecond spectroscopy in condensed matter," Nature **449**, 1029–1032 (2007).

[14] J. Mauritsson, T. Remetter, M. Swoboda, K. Klünder, A. L'Huillier, et al., "Attosecond electron spectroscopy using a novel interferometric pump-probe technique," Phys. Rev. Lett. **105**, 053001 (2010).

[15] M. H. Vos, F. Rappaport, J.-C. Lambry, J. Breton, and J.-L. Martin, "Visualization of coherent nuclear motion in a membrane protein by femtosecond spectroscopy," Nature **363**, 320–325 (1993).

[16] P. Hannaford, *Femtosecond laser spectroscopy* (Springer Science & Business Media, 2004).

[17] F. Hund, "Zur deutung der molekelspektren. III.," Z. Phys. **43**, 805–826 (1927).

[18]N. Berova, P. L. Polavarapu, K. Nakanishi, and R. W. Woody, *Comprehensive chiroptical spectroscopy: applications in stereochemical analysis of synthetic compounds, natural products, and biomolecules*, Vol. 2 (John Wiley & Sons, 2012).

[19]G. D. Fasman, *Circular dichroism and the conformational analysis of biomolecules* (Springer Science & Business Media, 2013).

[20]E. Francotte and W. Lindner, *Chirality in drug research*, Vol. 33 (Wiley-VCH Weinheim, 2006).

[21]J. S. S. Damsté, S. Schouten, E. C. Hopmans, A. C. T. van Duin, and J. A. J. Geenevasen, "Crenarchaeol the characteristic core glycerol dibiphytanyl glycerol tetraether membrane lipid of cosmopolitan pelagic crenarchaeota," J. Lipid Res. **43**, 1641–1651 (2002).

[22]R. Breslow, "The origin of homochirality in amino acids and sugars on prebiotic earth," Tetrahedron Lett. **52**, 4228–4232 (2011).

[23]S. F. Mason, "Origins of biomolecular handedness," Nature **311**, 19–23 (1984).

[24]W. A. Bonner, "Chirality and life," Orig. Life Evol. Biosph. **25**, 175–190 (1995).

[25]D. G. Blackmond, "The origin of biological homochirality," Philos. Trans. R. Soc. Lond. B Biol. Sci. **366**, 2878–2884 (2011).

[26]W. A. Bonner, "The origin and amplification of biomolecular chirality," Orig. Life Evol. Biosph. **21**, 59–111 (1991).

[27]I. Budin and J. W. Szostak, "Expanding roles for diverse physical phenomena during the origin of life," Annu. Rev. Biophys. **39**, 245–263 (2010).

[28]C. Meinert, P. de Marcellus, L. L. S. d'Hendecourt, L. Nahon, N. C. Jones, et al., "Photochirogenesis: photochemical models on the absolute asymmetric formation of amino acids in interstellar space," Phys. Life Rev. **8**, 307–330 (2011).

[29]V. A. Davankov, "Biological homochirality on the earth, or in the universe? a selective review," Symmetry **10**, 749 (2018).

[30]E. T. Peltzer and J. L. Bada, "α-hydroxycarboxylic acids in the murchison meteorite," Nature **272**, 443–444 (1978).

[31]J. R. Cronin, S. Pizzarello, S. Epstein, and R. V. Krishnamurthy, "Molecular and isotopic analyses of the hydroxy acids, dicarboxylic acids, and hydroxydicarboxylic acids of the murchison meteorite," Geochim. Cosmochim. Acta **57**, 4745–4752 (1993).

[32]I. Myrgorodska, C. Meinert, Z. Martins, L. L. S. d'Hendecourt, and U. J. Meierhenrich, "Molecular chirality in meteorites and interstellar ices, and the chirality experiment on board the esa cometary rosetta mission," Angew. Chem. Int. Ed. **54**, 1402–1412 (2015).

[33]M. H. Engel, "Distribution and enantiomeric composition of amino acids in the murchison meteorite," Nature **296**, 837–840 (1982).

[34]S. Pizzarello, D. L. Schrader, A. A. Monroe, and D. S. Lauretta, "Large enantiomeric excesses in primitive meteorites and the diverse effects of water in cosmochemical evolution," Proc. Natl. Acad. Sci. **109**, 11949–11954 (2012).

[35]D. P. Glavin and J. P. Dworkin, "Enrichment of the amino acid l-isovaline by aqueous alteration on ci and cm meteorite parent bodies," Proc. Natl. Acad. Sci. **106**, 5487–5492 (2009).

[36]S. Pizzarello, Y. Wang, and G. M. Chaban, "A comparative study of the hydroxy acids from the murchison, gra 95229 and lap 02342 meteorites," Geochim. Cosmochim. Acta **74**, 6206–6217 (2010).

[37]R. N. Boyd, T. Kajino, and T. Onaka, "Supernovae and the chirality of the amino acids," Astrobiology **10**, 561–568 (2010).

[38]R. N. Boyd, T. Kajino, and T. Onaka, "Supernovae, neutrinos and the chirality of amino acids," Int. J. Mol. Sci. **12**, 3432–3444 (2011).

[39]N. Micali, H. Engelkamp, P. G. van Rhee, P. C. M. Christianen, L. M. Scolaro, et al., "Selection of supramolecular chirality by application of rotational and magnetic forces," Nat. Chem. **4**, 201–207 (2012).

[40]J. Bailey, A. Chrysostomou, J. H. Hough, T. M. Glehill, A. McCall, et al., "Circular polarization in star-formation regions: implications for biomolecular homochirality," Science **281**, 672–674 (1998).

[41]J. Bailey, "Astronomical sources of circularly polarized light and the origin of homochirality," Orig. Life Evol. Biosph. **31**, 167–183 (2001).

[42]T. Fukue, M. Tamura, R. Kandori, N. Kusakabe, J. H. Hough, et al., "Extended high circular polarization in the orion massive star forming region: implications for the origin of homochirality in the solar system," Orig. Life Evol. Biosph. **40**, 335–346 (2010).

[43]C. Meinert, J.-J. Filippi, L. Nahon, S. V. Hoffmann, L. d'Hendecourt, et al., "Photochirogenesis: photochemical models on the origin of biomolecular homochirality," Symmetry **2**, 1055–1080 (2010).

[44]A. C. Evans, C. Meinert, J. H. Bredehoeft, C. Giri, N. C. Jones, et al., "Anisotropy spectra for enantiomeric differentiation of biomolecular building blocks," in *Differentiation of enantiomers ii*, Vol. 341, edited by V. Schurig, Topics in Current Chemistry (2013), pp. 271–299.

[45]J. E. Bartmess and R. M. Pagni, "A photochemical mechanism for homochirogenesis. Part 2," Chirality **25**, 16–21 (2013).

[46]B. Norden, "Was photoresolution of amino acids the origin of optical activity in life?" Nature **266**, 567–568 (1977).

[47]J. J. Flores, W. A. Bonner, and G. A. Massey, "Asymmetric Photolysis of (LS)-Leucine with Circularly Polarized Ultraviolet Light," J. Am. Chem. Soc. **99**, 3623–3625 (1977).

[48]C. Meinert, P. Cassam-Chenai, N. C. Jones, L. Nahon, S. V. Hoffmann, et al., "Anisotropy-guided enantiomeric enhancement in alanine using far-uv circularly polarized light," Orig. Life Evol. Biosph. **45**, 149–161 (2015).

[49]C. Meinert, S. V. Hoffmann, P. Cassam-Chenai, A. C. Evans, C. Giri, et al., "Photonenergy-controlled symmetry breaking with circularly polarized light," Angew. Chem. Int. Ed. **53**, 210–214 (2014).

[50]P. De Marcellus, C. Meinert, M. Nuevo, J.-J. Filippi, G. Danger, et al., "Non-racemic amino acid production by ultraviolet irradiation of achiral interstellar ice analogs with circularly polarized light," Astrophys. J. Lett. **727**, L27 (2011).

[51]P. Modica, C. Meinert, P. de Marcellus, L. Nahon, U. J. Meierhenrich, et al., "Enantiomeric excesses induced in amino acids by ultraviolet circularly polarized light irradiation of extraterrestrial ice analogs: a possible source of asymmetry for prebiotic chemistry," Astrophys. J. **788**, 79 (2014).

[52]S. F. Mason and G. E. Tranter, "The parity-violating energy difference between enantiomeric molecules," Chem. Phys. Lett. **94**, 34–37 (1983).

[53]M. Quack, "Structure and dynamics of chiral molecules," Angew. Chem. Int. Ed. **28**, 571–586 (1989).

[54]E. Gibney, "Comet craft ready to wake," Nature **205**, 269–270 (2014).

[55]F. Goesmann, H. Rosenbauer, J. H. Bredehöft, M. Cabane, P. Ehrenfreund, et al., "Organic compounds on comet 67p/Churyumov-Gerasimenko revealed by COSAC mass spectrometry," Science **349** (2015).

[56]N. Fray, A. Bardyn, H. Cottin, K. Altwegg, D. Baklouti, et al., "High-molecular-weight organic matter in the particles of comet 67P/Churyumov–Gerasimenko," Nature **538**, 72–74 (2016).

[57]L. Rosenfeld, "Quantenmechanische theorie der natürlichen optischen aktivität von flüssigkeiten und gasen," Z. Phys. **52**, 161–174 (1929).

[58]L. D. Barron, *Molecular light scattering and optical activity*, 2nd ed. (Cambridge University Press, Cambridge, 2004).

[59]U. Boesl and A. Bornschlegl, "Circular dichroism laser mass spectrometry: differentiation of 3-methylcyclopentanone enantiomers," Chem. Phys. Chem. **7**, 2085–2087 (2006).

[60]A. Bornschlegl, C. Logé, and U. Boesl, "Investigation of CD effects in the multi photon ionisation of R-(+)-3Methylcyclopentanone," Chem. Phys. Lett. **447**, 187 (2007).

[61]P. Horsch, G. Urbasch, K.-M. Weitzel, and D. Kröner, "Circular dichroism in ion yields employing femtosecond laser ionization - the role of laser pulse duration," Phys. Chem. Chem. Phys. **13**, 2378 (2011).

[62]K. E. Gund and F. S. Richardso, "Fluorescence - detected two-photon circular dichroism of gd^3+ in trigonal $na_3[gd(c_4h_405)_3]$ $2nac_104$ 6 h_20," Chem. Phys. **194**, 195 (1995).

[63]T. Lischke, N. Böwering, B. Schmidtke, N. Müller, T. Khalil, et al., "Circular dichroism in valence photoelectron spectroscopy of free unoriented chiral molecules: camphor and bromocamphor," Phys. Rev. A **70**, 022507 (2004).

[64]P. Fischer and F. Hache, "Nonlinear optical spectroscopy of chiral molecules," Chirality **17**, 421 (2005).

[65]A. Rizzo, N. Lin, and K. Ruud, "Ab initio study of one- and two-photon circular dichroism of R-(+)-3-methyl-cyclopentanone," J. Chem. Phys. **128**, 164312 (2008).

[66]D. H. Friese and K. Ruud, "Three-Photon circular dichroism: towards a generalization of chiroptical non-linear light absorption," Phys. Chem. Chem. Phys., 4174–4184 (2015).

[67]R. Li, R. Sullivan, W. Al-Basheer, R. M. Pagoni, and R. N. Compton, "Linear and nonlinear circular dichrosim of r-(+)-3-methylcyclopentanone," J. Chem. Phys. **125**, 144304 (2006).

[68]H. G. Breunig, G. Urbasch, P. Horsch, J. Cordes, U. Koert, et al., "Circular dichroism in ion yields of femtosecond-laser mass spectrometry," Chem. Phys. Chem. **10**, 1199 (2009).

[69]Y. Ma and A. Salam, "On chiral selectivity of enantiomers using a circular polarized pulsed laser under resonant and off-resonant conditions," Chem. Phys. **324**, 367 (2006).

[70]Y. Ma and A. Salam, "Controlling state population of enantiomers of real chiral molecules by using a circular polarized pulsed laser," Chem. Phys. Lett. **431**, 247 (2006).

[71]D. Kröner, "Chiral distinction by ultrashort laser pulses: electron wavepacket dynamics incorporating magnetic interactions," J. Phys. Chem. A **115**, 14510–14518 (2011).

[72]R. Mitrić, J. Petersen, and V. Bonačić-Koutecký, "Laser-field-induced surface-hopping method for the simulation and control of ultrafast photodynamics," Phys. Rev. A **79**, 053416 (2009).

[73]G. Tomasello, M. Wohlgemuth, J. Petersen, and R. Mitrić, "Photodynamics of free and solvated tyrosine," J. Phys. Chem. B **116**, 8762–8770 (2012).

[74]J. Petersen, M. Wohlgemuth, B. Sellner, V. Bonačić-Koutecký, H. Lischka, et al., "Laser pulse trains for controlling excited state dynamics of adenine in water," Phys. Chem. Chem. Phys. **14**, 4687–4694 (2012).

[75]J. Petersen, R. Mitrić, V. Bonačić-Koutecký, J.-P. Wolf, J. Roslund, et al., "How shaped light discriminates nearly identical biochromophores," Phys. Rev. Lett. **105**, 073003 (2010).

[76]R. Mitrić, J. Petersen, M. Wohlgemuth, U. Werner, V. Bonačić-Koutecký, et al., "Time-resolved femtosecond photoelectron spectroscopy by field-induced surface hopping," J. Phys. Chem. A **115**, 3755–3765 (2011).

[77]R. Mitrić, J. Petersen, M. Wohlgemuth, U. Werner, and V. Bonačić-Koutecký, "Field-induced surface hopping method for probing transition state nonadiabatic dynamics of ag(3)," Phys. Chem. Chem. Phys. **13**, 8690–8696 (2011).

[78]M. I. S. Röhr, J. Petersen, M. Wohlgemuth, V. Bonačić-Koutecký, and R. Mitrić, "Nonlinear absorption dynamics using field-induced surface hopping: zinc porphyrin in water," ChemPhysChem **14**, 1377–1386 (2013).

[79]U. J. Meierhenrich, J.-J. Filippi, C. Meinert, J. H. Bredehoeft, J. Takahashi, et al., "Circular dichroism of amino acids in the vacuum-ultraviolet region," Angew. Chem. Int. Ed. **49**, 7799–7802 (2010).

[80]I. Powis, E. E. Rennie, U. Hergenhahn, O. Kugeler, and R. Bussy-Socrate, "Investigation of the gas-phase amino acid alanine by synchrotron radiation photoelectron spectroscopy," J. Phys. Chem. A **107**, 25–34 (2003).

[81]M. Tia, B. C. de Miranda, S. Daly, F. Gaie-Levrel, G. A. Garcia, et al., "Chiral asymmetry in the photoionization of gas-phase amino-acid alanine at lyman-α radiation wavelength," Phys. Chem. Lett. **4**, 2698–2704 (2013).

[82]M. Tia, B. C. de Miranda, S. Daly, F. Gaie-Levrel, G. A. Garcia, et al., "VUV photodynamics and chiral asymmetry in the photoionization of gas phase alanine enantiomers," J. Phys. Chem. A **118**, 2765–2779 (2014).

[83]C. Meinert, J. H. Bredehoeft, J.-J. Filippi, Y. Baraud, L. Nahon, et al., "Anisotropy spectra of amino acids," Angew. Chem. Int. Ed. **51**, 4484–4487 (2012).

[84]I. Powis, "Photoelectron circular dichroism of the randomly oriented chiral molecules glyceraldehyde and lactic acid," J. Chem. Phys. **112**, 301 (2000).

[85]T. Fukuyama, K. Matsuo, and K. Gekko, "Vacuum-Ultraviolet electronic circular dichroism of l-Alanine in aqueous solution investigated by time-dependent density functional theory," J. Phys. Chem. A **109**, 6928–6933 (2005).

[86]A. Osted, J. Kongsted, K. V. Mikkelsen, and O. Christiansen, "The electronic spectrum of the micro-solvated alanine zwitterion calculated using the combined coupled cluster/molecular mechanics method," Chem. Phys. Lett. **429**, 430–435 (2006).

[87]H. M. Jaeger, I. I. I. Henry F. Schaefer, J. Demaison, A. G. Csaszar, and W. D. Allen, "Lowest-lying conformers of alanine: pushing theory to ascertain precise energetics and semiexperimental re structures," J. Chem. Theory Comput. **6**, 3066–3078 (2010).

[88]H. Farrokhpour, F. Fathi, and A. Naves De Brito, "Theoretical and experimental study of valence photoelectron spectrum of d,l-alanine amino acid," J. Phys. Chem. A **116**, 7004–7015 (2012).

[89]M. Wohlgemuth and R. Mitrić, "Photochemical chiral symmetry breaking in alanine," J. Chem. Phys. A **120**, 8976–8982 (2016).

[90]G. P. Pfeifer, Y.-H. You, and A. Besaratinia, "Mutations induced by ultraviolet light," Mutat. Res. **571**, 19–31 (2005).

[91]J. S. Taylor, "Unraveling the molecular pathway from sunlight to skin cancer," Acc. Chem. Res. **27**, 76–82 (1994).

[92]A. A. Lamola and J. Eisinger, "On the mechanism of thymine photodimerization," Proc. Natl. Acad. Sci. **59**, 46 (1968).

[93]D. S. Goodsell, "The molecular perspective: ultraviolet light and pyrimidine dimers," Oncologist **6**, 298–299 (2001).

[94]C. F. Errol, C. W. Graham, S. Wolfram, D. W. Richard, A. S. Roger, et al., *DNA repair and mutagenesis, second edition* (American Society of Microbiology, 2006).

[95]R. Improta, F. Santoro, and L. Blancafort, "Quantum mechanical studies on the photophysics and the photochemistry of nucleic acids and nucleobases," Chem. Rev. **116**, 3540–3593 (2016).

[96]C. E. Crespo-Hernández, B. Cohen, and B. Kohler, "Base stacking controls excited-state dynamics in A·T DNA," Nature **436**, 1141 (2005).

[97]C. T. Middleton, K. de La Harpe, C. Su, Y. K. Law, C. E. Crespo-Hernández, et al., "DNA excited-state dynamics: from single bases to the double helix," Annu. Rev. Phys. Chem. **60**, 217–239 (2009).

[98]R. E. Fenna and B. W. Matthews, "Chlorophyll arrangement in a bacteriochlorophyll protein from chlorobium limicola," Nature **258**, 573–577 (1975).

[99]B. Kippelen and J.-L. Brédas, "Organic photovoltaics," Energy Environ . Sci. **2**, 251–261 (2009).

[100]J. H. Burroughes, D. D. C. Bradley, A. R. Brown, R. N. Marks, K. Mackay, et al., "Light-emitting diodes based on conjugated polymers," Nature **347**, 539–541 (1990).

[101]V. Schroeder, S. Savagatrup, M. He, S. Lin, and T. M. Swager, "Carbon nanotube chemical sensors," Chem. Rev. **119**, 599–663 (2018).

[102]R. M. Clegg, "The history of fret," in *Reviews in fluorescence 2006* (Springer, 2006), pp. 1–45.

[103]J. Perrin, "Fluorescence et induction moléculaire par résonance," CR Hebd. Seances Acad. Sci **184**, 1097–1100 (1927).

[104]F. Perrin, "Théorie quantique des transferts d'activation entre molécules de même espèce. cas des solutions fluorescentes," in Annales de physique, Vol. 10, 17 (EDP Sciences, 1932), pp. 283–314.

[105]J. R. Oppenheimer, "Internal conversion in photosynthesis," Phys. Rev. **60**, 158 (1941).

[106]W. Arnold and J. R. Oppenheimer, "Internal conversion in the photosynthetic mechanism of blue-green algae," J. Gen. Physiol. **33**, 423–435 (1950).

[107]T. Förter, "Energiewanderung und fluoreszene," Nat. Sci. **6**, 166–175 (1946).

[108]D. L. Dexter, "A theory of sensitized luminescence in solids," J. Chem. Phys. **21**, 836–850 (1953).

[109]D. L. Dexter and J. H. Schulman, "Theory of concentration quenching in inorganic phosphors," J. Chem. Phys. **22**, 1063–1070 (1954).

[110]S. E. Bradforth, R. Jimenez, F. van Mourik, R. van Grondelle, and G. R. Fleming, "Excitation transfer in the core light-harvesting complex (LH-1) of rhodobacter sphaeroides: an ultrafast fluorescence depolarization and annihilation study," J. Phys. Chem. **99**, 16179–16191 (1995).

[111]C.-K. Yong, P. Parkinson, D. V. Kondratuk, W.-H. Chen, A. Stannard, et al., "Ultrafast delocalization of excitation in synthetic light-harvesting nanorings," Chem. Sci. **6**, 181–189 (2015).

[112]O. Varnavski, I. D. W. Samuel, L.-O. Pålsson, R. Beavington, P. L. Burn, et al., "Investigations of excitation energy transfer and intramolecular interactions in a nitrogen corded distrylbenzene dendrimer system," J. Chem. Phys. **116**, 8893–8903 (2002).

[113]A. Sisto, D. R. Glowacki, and T. J. Martinez, "Ab initio nonadiabatic dynamics of multichromophore complexes: a scalable graphical-processing-unit-accelerated exciton framework," Acc. Chem. Res. **47**, 2857–2866 (2014).

[114]A. Sisto, C. Stross, M. W. van der Kamp, M. O'Connor, S. McIntosh-Smith, et al., "Atomistic non-adiabatic dynamics of the LH2 complex with a GPU-accelerated ab initio exciton model," Phys. Chem. Chem. Phys. **19**, 14924–14936 (2017).

[115]M. Wohlgemuth and R. Mitrić, "Excitation energy transport in DNA modelled by multichromophoric field-induced surface hopping," Phys. Chem. Chem. Phys. **22**, 16536–16551 (2020).

[116]G. A. Jeffrey and W. Saenger, *Hydrogen bonding in biological structures* (Sprinter-Verlag, New York, 1991).

[117]T. S. Zwier, "The spectroscopy of solvation in hydrogen-bonded aromatic clusters," Annu. Rev. Phys. Chem. **47**, 205–241 (1996).

[118]K. Müller-Dethlefs and P. Hobza, "Noncovalent interactions: a challenge for experiment and theory," Chem. Rev. **100**, 143–168 (2000).

[119]C. E. H. Dessent and K. Müller-Dethlefs, "Hydrogen-bonding and van der waals complexes studied by zeke and rempi spectroscopy," Chem. Rev. **100**, 3999–4022 (2000).

[120]J. P. Schermann, *Spectroscopy and modelling of biomolecular building blocks* (Elsevier, 2008).

[121]P. Hobza and K. Müller-Dethlefs, *Non-covalent interactions, Theory and experiment*, RSC Theoretical and Computational Chemistry Series (The Royal Society of Chemistry, 2009), pp. 1–226.

[122]K. Mizuse and A. Fujii, "Infrared spectroscopic studies on hydrogen-bonded water networks in gas phase clusters," Int. Rev. Phys. Chem. **32**, 266–307 (2013).

[123]Y. Chen, F. Gai, and J. W. Petrich, "Solvation of 7-azaindole in alcohols and water: evidence for concerted, excited-state, double-proton transfer in alcohols," J. Am. Chem. Soc. **115**, 10158–10166 (1993).

[124]D. E. Folmer, E. S. Wisniewski, J. R. Stairs, and A. W. Castleman, "Water-assisted proton transfer in the monomer of 7-azaindole," J. Phys. Chem. A **104**, 10545–10549 (2000).

[125]S. G. Kalko, E. Guardia, and J. A. Padro, "Molecular dynamics simulation of the hydration of the alanine dipeptide," J. Phys. Chem. B **103**, 3935–3941 (1999).

[126]G. R. Fleming and M. Cho, "Chromophore-solvent dynamics," Annu. Rev. Phys. Chem. **47**, 109–134 (1996).

[127]N. Nandi, K. Bhattacharyya, and B. Bagchi, "Dielectric relaxation and solvation dynamics of water in complex chemical and biological systems," Chem. Rev. **100**, 2013–2046 (2000).

[128]R. Jimenez, G. R. Fleming, P. V. Kumar, and M. Maroncelli, "Femtosecond solvation dynamics of water," Nature **369**, 471–473 (1994).

[129]B. Bagchi, "Dynamics of solvation and charge transfer reactions in dipolar liquids," Annu. Rev. Phys. Chem. **40**, 115–141 (1989).

[130]S. M. Bhattacharyya, Z.-G. Wang, and A. H. Zewail, "Dynamics of water near a protein surface," J. Phys. Chem. B **107**, 13218–13228 (2003).

[131]L. Nilsson and B. Halle, "Molecular origin of time-dependent fluorescence shifts in proteins," Proc. Natl. Acad. Sci. **102**, 13867–13872 (2005).

[132]V. P. Denisov, B.-H. Jonsson, and B. Halle, "Hydration of denatured and molten globule proteins.," Nat. Struct. Mol. Biol. **6**, 253–260 (1999).

[133]N. V. Nucci, M. S. Pometun, and A. J. Wand, "Site-resolved measurement of water-protein interactions by solution nmr," Nat. Struct. Mol. Biol. **18**, 245–249 (2011).

[134]B. Halle, "Protein hydration dynamics in solution: a critical survey," Philos. Trans. R. Soc. London Ser. B **359**, 1207–1224 (2004).

[135]B. Bagchi, "Water dynamics in the hydration layer around proteins and micelles," Chem. Rev. **105**, 3197–3219 (2005).

[136]D. Zhong, "Hydration dynamics and coupled water-protein fluctuations probed by intrinsic tryptophan," Adv. Chem. Phys. **143**, 83–149 (2009).

[137]M. Grossman, B. Born, M. Heyden, D. Tworowski, G. Fields, et al., "Correlated structural kinetics and retarded solvent dynamics at the metalloprotease active site.," Nat. Struct. Mol. Biol. **18**, 1102–1108 (2011).

[138]A. C. Fogarty, E. Duboue-Dijon, F. Sterpone, J. T. Hynes, and D. Laage, "Biomolecular hydration dynamics: a jump model perspective," Chem. Soc. Rev. **42**, 5672–5683 (2013).

[139]D. M. Neumark, "Time-resolved photoelectron spectroscopy of molecules and clusters," Annu. Rev. Phys. Chem. **52**, 255–277 (2001).

[140]A. Stolow, A. E. Bragg, and D. M. Neumark, "Femtosecond time-resolved photoelectron spectroscopy," Chem. Rev. **104**, 1719–1758 (2004).

[141]T. Suzuki, "Femtosecond time-resolved photoelectron imaging," Annu. Rev. Phys. Chem. **57**, 555–592 (2006).

[142]A. Stolow and J. G. Underwood, "Time-resolved photoelectron spectroscopy of nonadiabatic dynamics in polyatomic molecules," in *Advances in chemical physics*, edited by S. A. Rice (John Wiley & Sons, Inc., 2008), pp. 497–584.

[143]M. Fujii and O. Dopfer, "Ionisation-induced site switching dynamics in solvated aromatic clusters: phenol-(rare gas)$_n$ clusters as prototypical example," Int. Rev. Phys. Chem. **31**, 131–173 (2012).

[144]O. Dopfer and M. Fujii, "Probing solvation dynamics around aromatic and biological molecules at the single-molecular level," Chem. Rev. **116**, 5432–5463 (2016).

[145]S. Ishiuchi, M. Sakai, Y. Tsuchida, A. Takeda, Y. Kawashima, et al., "Real-Time Observation of Ionization-Induced Hydrophobic $\rightarrow$ Hydrophilic Switching," Angew. Chem. Int. Ed. **44**, 6149–6151 (2005).

[146]M. Miyazaki, A. Takeda, S. Ishiuchi, M. Sakai, O. Dopfer, et al., "Photoionization-induced large-amplitude pendular motion in phenol$^+$-Kr," Phys. Chem. Chem. Phys. **13**, 2744–2747 (2011).

[147]S. Ishiuchi, M. Miyazaki, M. Sakai, M. Fujii, M. Schmies, et al., "Ionization-induced $\pi \rightarrow$H site switching dynamics in phenol-Ar_3," Phys. Chem. Chem. Phys. **13**, 2409–2416 (2011).

[148]M. Miyazaki, Y. Sakata, M. Schütz, O. Dopfer, and M. Fujii, "Photoionization-induced $\pi \leftrightarrow$ H site switching dynamics in phenol$^+$-Rg (Rg = Ar, Kr) dimers probed by picosecond time-resolved infrared spectroscopy," Phys. Chem. Chem. Phys. **18**, 24746–24754 (2016).

[149]M. Miyazaki, T. Nakamura, M. Wohlgemuth, R. Mitrić, O. Dopfer, et al., "Single water solvation dynamics in the 4-aminobenzonitrile-water cluster cation revealed by picosecond time-resolved infrared spectroscopy," Phys. Chem. Chem. Phys. **17**, 29969–29977 (2015).

[150]K. Tanabe, M. Miyazaki, M. Schmies, A. Patzer, M. Schütz, et al., "Watching water migration around a peptide bond," Angew. Chem. Int. Ed. **124**, 6708–6711 (2012).

[151]M. Wohlgemuth, M. Miyazaki, M. Weiler, M. Sakai, O. Dopfer, et al., "Solvation dynamics of a single water molecule probed by infrared spectra—theory meets experiment," Angew. Chem. Int. Ed. **53**, 14601–14604 (2014).

[152]M. Wohlgemuth, M. Miyazaki, K. Tsukada, M. Weiler, O. Dopfer, et al., "Deciphering environment effects in peptide bond solvation dynamics by experiment and theory," Phys. Chem. Chem. Phys. **19**, 22564–22572 (2017).

The results presented in this thesis are based on a mixed quantum-classical treatment of light-induced molecular dynamics. In the following section 2.1 the theoretical derivation of the trajectory-based molecular dynamics approach founded on the Born-Oppenheimer approximation is therefore presented. For the description of the dynamics in electronically excited states, which is determined by non-radiative processes, the surface hopping approach is presented section 2.2, followed by a short introduction to the theoretical foundations of light-matter interaction given in section 2.3.

The combination of semiclassical molecular dynamics and the semiclassical representation of light-matter interaction can then be used to simulate either light-induced excitation processes or to calculate time-resolved spectroscopic observables. Specifically, the multipolar extension of the field-induced surface-hopping (FISH) approach to simulate the enantiomeric discrimination of chiral molecules is introduced in section 2.4, followed by the multi-chromophoric field-induced surface-hopping (McFISH) method to simulate energy transport processes in molecular aggregates (Sec. 2.5). The simulation of time-resolved pump-probe infrared spectra is finally presented in section 2.6.

2.1 MIXED QUANTUM-CLASSICAL MOLECULAR DYNAMICS

The dynamics in molecules is characterized by the motion of the electrons and nuclei. In the frame of quantum mechanics this motion is described by the time-dependent Schödinger equation for the wave function Ψ:[1,2]

$$i\hbar\frac{\partial\Psi(\boldsymbol{r},\boldsymbol{R},t)}{\partial t} = \hat{H}_{mol}\,\Psi(\boldsymbol{r},\boldsymbol{R},t), \tag{1.1a}$$

$$\begin{aligned}\hat{H}_{mol}\,(\boldsymbol{r},\boldsymbol{R}) &= -\frac{\hbar^2}{2}\nabla_{\boldsymbol{R}}\boldsymbol{M}^{-1}\nabla_{\boldsymbol{R}} - \frac{\hbar^2}{2m_e}\nabla^2_{\boldsymbol{r}} + \hat{U}\,(\boldsymbol{r},\boldsymbol{R}) \\ &= \hat{T}_N\,(\boldsymbol{R}) + \hat{H}_{el}\,(\boldsymbol{r},\boldsymbol{R}).\end{aligned} \tag{1.1b}$$

Here, $\boldsymbol{r}$ and $\boldsymbol{R}$ are the collective positions of all electrons and nuclei with their respective masses m_e and $\boldsymbol{M}$, where $\boldsymbol{M}$ is a square diagonal matrix. The terms of the molecular Hamilton operator $\hat{H}_{mol}$ (Eqn. (1.1b)) in the coordinate representation correspond to the nuclear kinetic energy operator $\hat{T}_N = \frac{\hbar^2}{2}\nabla_{\boldsymbol{R}}\boldsymbol{M}^{-1}\nabla_{\boldsymbol{R}}$ and the electronic Hamiltonian $\hat{H}_{el}$, where the latter collects the kinetic energy operator for the electrons ($-\frac{\hbar^2}{2m_e}\nabla^2_{\boldsymbol{r}}$) and the potential $\hat{U}$ for electron-electron, nuclear-nuclear and electron-nuclear interactions.

The total wave function Ψ can be exactly represented in terms of coupled electronic and nuclear wave functions using the Born-Oppenheimer expansion:[3]

$$\Psi(\boldsymbol{r}, \boldsymbol{R}, t) = \sum_i \psi_i(\boldsymbol{r}; \boldsymbol{R}) \chi_i(\boldsymbol{R}, t), \tag{1.2}$$

where the adiabatic electronic wave functions ψ_i form a complete orthogonal basis ($\langle \psi_i \,|\, \psi_j \rangle = \delta_{ij}$) and are eigenfunctions of the electronic Hamiltonian $\hat{H}_{el}$. The adiabatic electronic wave functions are therefore solutions of the time-independent electronic Schrödinger equation

$$\hat{H}_{el}\, \psi_i(\boldsymbol{r}; \boldsymbol{R}) = E_i(\boldsymbol{R}) \psi_i(\boldsymbol{r}; \boldsymbol{R}), \tag{1.3}$$

where both ψ_i and the eigenvalues E_i depend parametrically on the nuclear coordinates. Inserting this adiabatic basis into the time-dependent Schrödinger equation (1.1a) followed by projection on the electronic eigenfunctions yields a set of coupled equations for the nuclear wave functions χ_k:

$$i\hbar \dot{\chi}_k(\boldsymbol{R}) = \left[\hat{T}_N + E_k(\boldsymbol{R})\right] \chi_k(\boldsymbol{R}) - \frac{\hbar^2}{2} \sum_l \left[2\boldsymbol{d}_{kl}^{(1)} \cdot \boldsymbol{M}^{-1} \nabla_{\boldsymbol{R}} + d_{kl}^{(2)}\right] \chi_l(\boldsymbol{R}). \tag{1.4}$$

Since the adiabatic electronic wave function is parametrically dependent on the nuclear coordinates, the rotation of the nuclear kinetic energy operator in the adiabatic basis leads to off-diagonal matrix elements known as non-adiabatic coupling vectors ($\boldsymbol{d}_{kl}^{(1)} = \langle \psi_k \,|\, \nabla_{\boldsymbol{R}} \,|\, \psi_l \rangle_{\boldsymbol{r}}$) and second-order non-adiabatic coupling ($d_{kl}^{(2)} = \langle \psi_k \,|\, \nabla_{\boldsymbol{R}} \boldsymbol{M}^{-1} \nabla_{\boldsymbol{R}} \,|\, \psi_l \rangle_{\boldsymbol{r}}$). The first-order non-adiabatic coupling vectors can be determined according to the Hellman–Feynman theorem as:

$$\boldsymbol{d}_{kl}^{(1)} = \frac{\langle \psi_k \,|\, \nabla_{\boldsymbol{R}} \hat{H}_{el} \,|\, \psi_l \rangle_{\boldsymbol{r}}}{E_l - E_k}, \tag{1.5}$$

and since $\boldsymbol{d}_{kl}$ is anti-Hermitian $\boldsymbol{d}_{kk} = 0$ can be imposed for real electronic wave functions, which can always be applied for non-degenerate electronic states. The diagonal terms of the second-order non-adiabatic coupling $d_{kk}^{(2)}$ constitute a small correction to the adiabatic potential energy which can often be neglected as well as the off-diagonal terms $d_{kl}^{(2)}$.

In the limiting case of slowly moving nuclei (compared to the motion of the electrons) and non-degenerate electronic states, the total wave function can be represented by a single product of nuclear and electronic wave function $\Psi = \psi(\boldsymbol{r}; \boldsymbol{R}) \chi(\boldsymbol{R})$, which implies that the off-diagonal terms vanish.[4] Therefore, the equations of motion for the nuclear wave functions (1.4) are decoupled, yielding the Born-Oppenheimer (BO) approximation:[3]

$$i\hbar \dot{\chi}_k(\boldsymbol{R}) \approx \left[\hat{T}_N + E_k(\boldsymbol{R})\right] \chi_k(\boldsymbol{R}). \tag{1.6}$$

In other words, if the changes of the nuclear geometry are sufficiently small, the nuclear motion proceeds without changes of the electronic state of the electrons belonging

to the instantaneous electronic Hamiltonian and the functions $E_k(\boldsymbol{R})$ form (3N-6)-dimensional (where N is the number of nuclei) adiabatic potential energy surfaces (PES) on which the nuclear wave packet is evolving.

Although the BO approximation is valid under most circumstances, it breaks down in the case of degenerate electronic states. Those points are referred to as to intersection seam at which the dimensionality of the PES is reduced to 3N-8. The sub-space spanned by the difference of the energy gradient vectors (g-vector) and the non-adiabatic coupling vector of the two intersecting electronic states is referred to as branching space. The PES within this sub-space have the form of two cones whose tips touch each other at the point of degeneracy. Therefore, this point is known as conical intersection, which is responsible for many photochemical phenomena, such as charge/proton transfer processes or photoisomerisation reactions. The inclusion of nonadiabatic effects will be the subject of section 2.2. For now, we assume the BO approximation is valid and the nuclear wave function is propagated on a single potential energy surface $E_i(\boldsymbol{R})$.

CLASSICAL NUCLEAR DYNAMICS. In order to simulate the nuclear motion on that surface one needs to solve the equations of motion (1.6). Although a direct numerical integration of equation (1.6) is possible within the framework of nuclear quantum wave packet dynamics, its application is often limited to small molecular systems. This limitation arises from the fact that the global multidimensional electronic potential energy surface (at least for the vicinity of the studied process) has to be known in advance, which is a serious problem for complex molecules including all nuclear degrees of freedom.

For larger systems only an entirely classical treatment of the nuclei, where the nuclear motion is governed by the Hamiltonian (or Newtonian) equations of motion, is possible. Replacing the wave packet of a finite width by a point particle is however a quite rough approximation. A better starting point for a classical description of wave packet motion is obtainable by considering the density operator formulation of quantum mechanics. For this purpose it is pursuing to introduce the density operator $\hat{\rho} = |\Psi\rangle\langle\Psi|$, whose time evolution is given by the Liouville–von Neumann equation:[5]

$$\frac{\partial \hat{\rho}(\boldsymbol{r},\boldsymbol{R})}{\partial t} = -\frac{i}{\hbar}\left[\hat{H}_{mol}(\boldsymbol{r},\boldsymbol{R}),\hat{\rho}(\boldsymbol{r},\boldsymbol{R})\right] \tag{1.7}$$

which replaces the Schrödinger equation (1.1a).

For a single-component system it is well known that the classical Liouville equation can be derived as the $\hbar \to 0$ limit by means of the Wigner transformation,[6,7] which transforms quantum mechanical operators to functions of positions and momenta. In close analogy, a partial Wigner transform can be defined, which acts only on the nuclear degrees of freedom while leaving the electron dynamics unchanged. For this purpose $\hat{H}_{mol}$ and $\hat{\rho}$ are expanded in the adiabatic basis and by projecting from the

right with $|\psi_l\rangle$ and from the left with $\langle\psi_k|$ followed by integration a set of differential equations is obtained:

$$\frac{\mathrm{d}\,\hat{\rho}_{kl}\,(\boldsymbol{R})}{\mathrm{d}t} = -\frac{i}{\hbar}\sum_i \left(\hat{H}_{ki}\,(\boldsymbol{R})\,\hat{\rho}_{il}\,(\boldsymbol{R}) - \hat{\rho}_{ki}\,(\boldsymbol{R})\,\hat{H}_{il}\,(\boldsymbol{R})\right) \tag{1.8}$$

where the diagonal elements of ρ_{kl} represent the quantum mechanical state populations and the off-diagonal elements describe the coherence. In the case of pure electronic states (BO approximation) we are interested in the diagonal elements $\hat{\rho}_{kk}$ such that the Liouville–von Neumann equation in the adiabatic basis reads:

$$\frac{\partial\,\hat{\rho}_{kk}\,(\boldsymbol{r},\boldsymbol{R})}{\partial t} = -\frac{i}{\hbar}\left[\hat{H}_{kk}\,,\hat{\rho}_{kk}\right]. \tag{1.9}$$

Applying the Wigner transformation to Eqn. (1.9) yields the classical Liouville equation:

$$\begin{aligned}\frac{\partial\rho_W}{\partial t} &= -\frac{i}{\hbar}\left((\hat{H}_{kk}\,\hat{\rho}_{kk})_W - (\hat{\rho}_{kk}\,\hat{H}_{kk})_W\right)\\ &= \{\rho_W(\boldsymbol{R},\boldsymbol{P}), H_W(\boldsymbol{R},\boldsymbol{P})\} + \mathcal{O}(\hbar)\end{aligned} \tag{1.10}$$

where the subscript W denotes the Wigner transform of the respective operators, the curly braces are the classical Poisson brackets and $\mathcal{O}(\hbar)$ terms of higher order in $\hbar$. In that sense, the motion of the quantum mechanical wave packet can be approximated by a collection of classical point particles, represented by the phase space probability function $\rho(\boldsymbol{R},\boldsymbol{P},t)$ and the quantum Hamiltonian operator $\hat{H}_{mol}$ is replaced by the classical Hamiltonian function $H(\boldsymbol{R},\boldsymbol{P})$, where the PES is originating from the fast moving electrons serving as an effective potential depending on the instantaneous nuclear geometry.

In trajectory-based approaches the phase space probability distribution function is represented by an ensemble of classical trajectories that mimics a localized quantum mechanical wave packet:

$$\rho(\boldsymbol{R},\boldsymbol{P},t) = \sum_{i=1}^{N_{traj}} \delta(\boldsymbol{R}-\boldsymbol{R}_i(t;\boldsymbol{R}_{i,0},\boldsymbol{P}_{i,0}))\delta(\boldsymbol{P}-\boldsymbol{P}_i(t;\boldsymbol{R}_{i,0},\boldsymbol{P}_{i,0})), \tag{1.11}$$

with the initial conditions ($\boldsymbol{R}_{i,0}$, $\boldsymbol{P}_{i,0}$) chosen such as to best represent a quantum mechanical wave packet. The trajectories evolve independently in phase space under Hamiltonian dynamics, which are propagated by solving the Hamiltonian equations of motion:

$$\dot{\boldsymbol{R}}_i = \nabla_{\boldsymbol{P}_i} H = \boldsymbol{M}^{-1}\boldsymbol{P}_i \tag{1.12a}$$

$$\dot{\boldsymbol{P}}_i = -\nabla_{\boldsymbol{R}_i} H = -\nabla_{\boldsymbol{R}_i} E_k(\boldsymbol{R}_i). \tag{1.12b}$$

Equivalently, instead of solving the system of first-order differential equations (1.12a) and (1.12b) for the phase-space variables $\boldsymbol{R}$ and $\boldsymbol{P}$, Newtons equation of motion:

$$\boldsymbol{M}\ddot{\boldsymbol{R}}_i = \boldsymbol{F}_i = -\nabla_{\boldsymbol{R}_i} E_k(\boldsymbol{R}_i), \tag{1.13}$$

can be solved by substituting $\boldsymbol{P}_i = \boldsymbol{M}\dot{\boldsymbol{R}}_i$ in Eqn. (1.12b). In both cases the classical equations of motion can be solved numerically by discretizing the time into finite steps Δt and using symplectic integration schemes, that provide both numerical efficiency as well as have to satisfy formal demands such as time invariance and conservation of linear or angular momentum.

In order to avoid the precalculation of a multi-dimensional potential energy surface $E_k(\boldsymbol{R}_i)$ it is more convenient to calculate the energy and gradients "on the fly" for a given nuclear configuration present at a given time. In order to obtain the electronic state energies, in principle any quantum chemical method can be used, most of them providing also analytical gradients to the electronic energy. The continuing advances in the field of electronic structure methods such as density functional theory, ab initio methods providing more electron correlation as well as improved semiempirical methods make it possible to run simulations for a large variety of applications with increasing complexity.

This classical approach often yields remarkably good results corresponding to quantum dynamics and reproducing the results of detailed experiments. However, intrinsically quantum molecular processes involving multiple electronic states or dominated by quantum tunneling cannot be correctly modeled by purely classical methods. It is nonetheless often useful, for both conceptual and computational reasons, to retain a trajectory-based description of manifestly quantum phenomena. One such quantum trajectory approach is based on the hydrodynamic formulation of quantum mechanics. Originally proposed by Bohm[8] as a way of constructing a quantum theory without giving up realism, the approach formulates quantum dynamics in terms of classical-like trajectories evolving under the influence of both the classical potential and a non-classical wave function-dependent quantum potential.

2.2 NON-ADIABATIC DYNAMICS AND SURFACE-HOPPING

In the vicinity of conical intersections, that is in regions where the energy gap between the adiabatic states becomes small, the non-adiabatic coupling terms in Eqn. (1.4) are not negligible anymore and therefore invalidating the aforementioned Born-Oppenheimer approximation (cf. Sec. 2.1). Consequently, the total wave function is not a single product wave function anymore but a linear combination of the adiabatic electronic states. In these cases the wave packet is partially propagated in two adiabatic surfaces. If the spin multiplicity of both surfaces are the same (singlet-singlet or triplet-triplet), this process is known as internal conversion in which the electronic relaxation occurs without the emission of light (non-radiative relaxation).

A full quantum mechanical description of such processes is possible, but solving the quantum mechanical equations is usually too demanding to simulate the dynamics of realistic complex molecules. Therefore, for the field-free non-adiabatic dynamics a variety of approaches have been devised (cf. Ref. [9]). Here, in the context of semiclassi-

cal trajectory-based approaches, the Ehrenfest[10] and surface-hopping[11,12] methods are worth mentioning. The assumption of the former is, that the trajectories are propagated on a single effective mean potential, whose composition of adiabatic states is determined from independent propagation of the electronic wave function including terms for the non-adiabatic coupling. Therefore, after passing a region of strong coupling between two states, the effective potential is composed of negligible contributions from both states. This, however, represents the main drawback of the Ehrenfest approach, since this composition of the effective potential does not change anymore, even if the coupling vanishes. The physical expected behavior would be that, after passage through the crossing region, the trajectory would continue on a single adiabatic surface.[13] Another more technical implication of this fact is that, in the case of a mixed effective potential, several energy gradients have to be calculated to obtain the mean-field force.

An attempt to tackle the problem of the loss of electron-nuclear correlation in the Ehrenfest approach is the trajectory surface-hopping (TSH) approach developed by Tully.[11,12] While the TSH method cannot be derived from first principles (e.g. time-dependent variational principle), its successful application to a wide range of photochemical or photophysical problems has been proven.[9] Rather than "feeling" an effective potential, the nuclei are propagated on the pure BO potential energy surfaces $E_i(\boldsymbol{R}(t))$, as in conventional adiabatic dynamics. Now, the idea of TSH is to assign a finite probability to switch ("hop") the electronic state reproducing the quantum population from propagation of the electronic wave function. For this purpose the total wave function is expanded in the basis of the adiabatic electronic states $|\psi_i\rangle$:

$$|\Psi(\boldsymbol{r}, \boldsymbol{R}(t))\rangle = \sum_i c_i(t) \, |\psi_i(\boldsymbol{r}; \boldsymbol{R}(t))\rangle \tag{2.1}$$

where $|\psi_i\rangle$ is parametrically dependent on the instantaneous nuclear geometry $\boldsymbol{R}$(t) and $c_i(t)$ are the time-dependent expansion coefficients. The equations of motion of these coefficients are obtained by inserting Eqn. (2.1) in the time-dependent Schrödinger equation (1.1a) and projecting on the eigenstate $|\psi_j\rangle$:

$$i\hbar \dot{c}_i(t) = E_i(\boldsymbol{R}(t)) c_i(t) - i\hbar \sum_j \left\langle \psi_j(\boldsymbol{r}; \boldsymbol{R}(t)) \,\middle|\, \frac{\mathrm{d}}{\mathrm{d}t} \psi_i(\boldsymbol{r}; \boldsymbol{R}(t)) \right\rangle c_j(t) \tag{2.2a}$$

$$= E_i(\boldsymbol{R}(t)) c_i(t) - i\hbar \sum_j \boldsymbol{d}_{ji} \cdot \dot{\boldsymbol{R}}(t) c_j(t), \tag{2.2b}$$

where the parametric dependency of the eigenfunctions on the trajectory $\boldsymbol{R}(t)$ have been used to obtain the non-adiabatic coupling vectors $\boldsymbol{d}_{ji} = \langle \psi_j \,|\, \nabla_{\boldsymbol{R}} \,|\, \psi_i \rangle$ in the last equation.

Although $\boldsymbol{d}_{ji}$ is already available from many quantum chemistry methods, its calculation is, however, not essentially required for propagating Eqn. (2.2b). Instead, the scalar non-adiabatic coupling $D_{ji} = \langle \psi_j | \frac{\mathrm{d}}{\mathrm{d}t} \psi_i \rangle$, occurring in the former equation (2.2a), may

be approximated by the finite difference of the overlap between the wave functions at two subsequent nuclear time steps:

$$\left\langle \psi_j(\boldsymbol{r};\boldsymbol{R}(t)) \,\middle|\, \frac{\mathrm{d}}{\mathrm{d}t}\psi_i(\boldsymbol{r};\boldsymbol{R}(t)) \right\rangle \approx \frac{1}{2\Delta t}\left[\left\langle \psi_j(\boldsymbol{r};\boldsymbol{R}(t)) \,\middle|\, \psi_i(\boldsymbol{r};\boldsymbol{R}(t+\Delta t)) \right\rangle - \left\langle \psi_j(\boldsymbol{r};\boldsymbol{R}(t+\Delta t)) \,\middle|\, \psi_i(\boldsymbol{r};\boldsymbol{R}(t)) \right\rangle\right]. \tag{2.3}$$

At the beginning of the simulation the coefficients are set to $c_i(t) = \delta_{ij}$, where i is the state where the trajectory initially starts, and are further propagated alongside the classical equations of motion for the nuclei. Since the time-evolution of the coefficients can be highly peaked and strongly oscillating, the integration of Eqn. (2.2) requires a much smaller time step ($\approx 10^{-5}$ fs) compared to the integration of the nuclear equations of motion, which is usually between 0.1 fs to 2.0 fs.

The hopping probability is designed to reproduce the quantum population obtained from Eqn. (2.2).[11] This, however, introduces an excessive and nonphysical number of hopping events, effectively becoming mean-field dynamics, which is inadequate for processes exhibiting branching along different pathways. Therefore, Tully later introduced the fewest-switching surface-hopping (FSSH) approach, in which the number of hops is minimized.[12] For this purpose, in each nuclear time step the electronic density matrix $\rho_{ij} = c_i^* c_j$ is calculated, where the diagonal and off-diagonal elements are denoted as quantum populations and coherences, respectively. The hopping probability for switching from the current state i to the state f is then obtained as:

$$P_{i\to f}(t) = \max\left[0, -\frac{2}{\hbar}\frac{\mathrm{Re}(\rho_{if}(t)\boldsymbol{d}_{fi}(\boldsymbol{R}(t))\cdot\dot{\boldsymbol{R}}(t)}{\rho_{ii}(t)}\Delta t\right]. \tag{2.4}$$

The probability is compared to a random number to determine if a hop occurs and to switch the state. In that case, the conservation of energy has to be ensured, since due to the stochastic nature of the surface-hopping approach hops may already occur where both states are not exactly degenerate. This is usually achieved by rescaling the nuclear momenta in the direction of the coupling vector:[14–17]

$$\boldsymbol{p} \to \boldsymbol{p} - \alpha_{fi}\boldsymbol{d}_{fi} \tag{2.5a}$$

$$\alpha_{fi} = \frac{\dot{\boldsymbol{R}}\cdot\boldsymbol{d}_{fi} + \mathrm{sgn}\left(\dot{\boldsymbol{R}}\cdot\boldsymbol{d}_{fi}\right)\sqrt{(\dot{\boldsymbol{R}}\cdot\boldsymbol{d}_{fi})^2 + 2\boldsymbol{d}_{fi}\boldsymbol{M}^{-1}\boldsymbol{d}_{fi}(E_i - E_f)}}{\boldsymbol{d}_{fi}\boldsymbol{M}^{-1}\boldsymbol{d}_{fi}}, \tag{2.5b}$$

where the sign depends on the angle between the nuclear velocities and the coupling vector. Alternatively, if only the scalar non-adiabatic coupling $D_{ji} = \boldsymbol{d}_{ji}\cdot\dot{\boldsymbol{R}}$ is available, a uniform rescaling procedure can be applied according to:

$$\boldsymbol{p} \to \boldsymbol{p}\sqrt{1 + 2\frac{E_i - E_f}{\dot{\boldsymbol{R}}\boldsymbol{M}\dot{\boldsymbol{R}}}}. \tag{2.6}$$

While the case going energetically downwards ($E_f < E_i$) is unproblematic, there is also a chance for the increase of the potential energy ($E_f > E_i$). In that case and if

there is insufficient kinetic energy in direction of the coupling (or globally if uniform rescaling is applied) available[1] the state switch is rejected. For those cases, several alternative schemes have been proposed, including reversal of momenta in direction of the coupling vector,[16] introduction of time uncertainty to allow flexibility in energy conservation,[18] or completely retain the nuclear momenta.[19] Recently it was also suggested that only for the ensemble of trajectories as a whole the conservation of energy should be enforced.[20,21]

Due to its complete foundation on classical nuclear dynamics, Tully's FSSH approach has become the most widely spread method for studying nonradiative relaxation in complex systems. The comparison with experimental results for a variety of systems has validated the reliability of surface-hopping simulations.[22–26] The advances of quantum chemical methods and their combination with surface-hopping (e.g. time-dependent density functional theory[26–28] and its tight-binding counterpart (TDDFTB),[29] semiempirical methods[24,30] or CAS-MRCI[31]) made it possible to study nonradiative relaxation processes in increasingly complex molecules. Further, the combination with mixed quantum mechanical–molecular mechanical (QM/MM) approaches, based on e.g. semiempirical[32–35] or time-dependent density function theory (TDDFT),[36,37] allowed for the investigation of systems embedded in proteins, DNA as well as in the condensed phase. Moreover, recently surface-hopping in the frame long-range corrected tight-binding time-dependent density functional theory (LC-TDDFTB) has been implemented. This enables the study of excitation energy transport and exciton dynamics in molecular aggregates.[38,39] For a comprehensive overview of recent advances in this field, cf. Refs. [9, 40, 41].

In this context, closely related to Tully's surface-hopping approach, the field-induced surface-hopping (FISH) method has been developed.[42] In contrast to the field-free simulation methods of the nonadiabatic processes presented here, the FISH method represents an efficient approach to incorporate the field-induced couplings explicitly into the surface-hopping procedure. Therefore, it provides a more complete picture of the photoexcitation and nonadiabatic relaxation processes. Furthermore, since time- and frequency dependent parameters, such as polarization and shape of the laser field, can be directly accounted for in the simulations, the FISH approach allows a more general applicability.

The further development of the FISH method for the treatment of photodynamics in chiral molecules and molecular aggregates are the focus of the chapters 3 and 4. Therefore, in the following section a brief introduction to the quantum and mixed quantum-classical treatment of light-matter interaction is given (Sec. 2.3), in which at the end a multipolar interaction Hamiltonian is derived that enters to the surface-hopping procedure as described in section 2.4.

1 The square root in Eqns. (2.5b) or (2.6), respectively, become imaginary.

2.3 LIGHT-MATTER INTERACTION

In general, in the frame of time-dependent perturbation theory the Hamiltonian for a system interacting with a laser field can be expressed by the sum of three Hermitian terms:

$$\hat{H} = \hat{H}_0 + \hat{H}_{int} = \left(\hat{H}_{mol} + \hat{H}_{rad}\right) + \hat{H}_{int}\,, \tag{3.1}$$

where $\hat{H}_{mol}$ and $\hat{H}_{rad}$ both are the unperturbed operators for the molecular system and the irradiating laser field, respectively, and $\hat{H}_{int}$ represents the interaction of both quantum systems. In section 2.1 it was shown that within the Born-Oppenheimer approximation the motion of the electrons and nuclei can be separated and it suffices to consider only the electronic Hamiltonian for the further discussion and to replace $\hat{H}_{mol}$ by $\hat{H}_{el}$ (cf. Sec. 2.1), obeying the time-independent Schrödinger equation $\hat{H}_{el}\,|\psi_i\rangle = E_i\,|\psi_i\rangle$. In the following the form of the $\hat{H}_{rad}$ and the interaction term $\hat{H}_{int}$ are derived.

QUANTIZED ELECTROMAGNETIC FIELD. In the spirit of classical particle mechanics, it is expedient to start from the classical formulation of electrodynamics to obtain the quantum Hamiltonian operator of radiation. In classical electrodynamics the electromagnetic (EM) field consists of the electric $\boldsymbol{E}$ and magnetic $\boldsymbol{B}$ fields. However, it is often more convenient to express these both fields by a scalar electric potential ϕ (further denoted as scalar potential) and a magnetic vector potential $\boldsymbol{A}$ (further denoted as vector potential), which are related to $\boldsymbol{E}$ and $\boldsymbol{B}$ by:

$$\boldsymbol{E}(\boldsymbol{r},t) = -\nabla\phi(\boldsymbol{r},t) - \frac{\partial \boldsymbol{A}(\boldsymbol{r},t)}{\partial t} \tag{3.2a}$$

$$\boldsymbol{B}(\boldsymbol{r},t) = \nabla \times \boldsymbol{A}(\boldsymbol{r},t). \tag{3.2b}$$

By confining to an arbitrary cubic volume $V = L^3$, the vector potential may be expressed by the Fourier expansion:

$$\boldsymbol{A}(\boldsymbol{r},t) = \sum_{\eta=\pm1,\boldsymbol{k}} \left[\boldsymbol{\varepsilon}_{\eta,\boldsymbol{k}} a_{\eta,\boldsymbol{k}}(t)\exp(i\boldsymbol{k}\boldsymbol{r}) + \bar{\boldsymbol{\varepsilon}}_{\eta,\boldsymbol{k}}\bar{a}_{\eta,\boldsymbol{k}}(t)\exp(-i\boldsymbol{k}\boldsymbol{r})\right], \tag{3.3}$$

where $a_{\eta,\boldsymbol{k}} = a_0\exp\left(i\omega_{\boldsymbol{k}}t\right)$ and $\bar{a}_{\eta,\boldsymbol{k}} = \bar{a}_0\exp\left(-i\omega_{\boldsymbol{k}}t\right)$ are the coefficients of the expansion, and the roofing bar denotes complex conjugation. Here, η denotes the state of polarization and $\boldsymbol{k}$ is the wave vector of the incident photons. As the consequence of the boundary condition that $\boldsymbol{A}$ has the same value on opposite walls of the confining volume, the spatial components of the wave vector $\boldsymbol{k}$ have discrete values $\{k_i = 2\pi n_i/L\}_{n=\pm1,\pm2,\ldots}$. An individual photon, which is classically represented by a mode $(\eta,\boldsymbol{k})$ in the Fourier expansion, can be described as having either right or left circular polarization, or a superposition of them. The electric polarization vector $\boldsymbol{\varepsilon}_{\eta,\boldsymbol{k}}$ for left $(+1)$ or right (-1) circular polarization on a Cartesian basis with unit vectors $(\hat{\boldsymbol{\imath}},\hat{\boldsymbol{\jmath}},\hat{\boldsymbol{k}})$ can be represented as:

$$\boldsymbol{\varepsilon}_{\pm1,\boldsymbol{k}} = \frac{1}{\sqrt{2}}\left(\hat{\boldsymbol{\imath}} \pm i\hat{\boldsymbol{\jmath}}\right) \tag{3.4}$$

and accordingly the magnetic polarization vector as:

$$\hat{\boldsymbol{k}} \times \boldsymbol{\varepsilon}_{\pm 1,\boldsymbol{k}} = \mp i \boldsymbol{\varepsilon}_{\pm 1,\boldsymbol{k}}. \tag{3.5}$$

Clearly, since the modes $(\eta, \boldsymbol{k})$ in Eqn. (3.3) form a finite discrete set, the Fourier coefficients $a_{\eta,\boldsymbol{k}}$ and $\bar{a}_{\eta,\boldsymbol{k}}$ define the vector potential and therefore the state of the electromagnetic field. Similar to the familiar quantization rules for particles (i.e. replacing the momentum $\boldsymbol{p}$ by the operator $\hat{\boldsymbol{p}} = -i\hbar\nabla_{\boldsymbol{r}}$) the EM field can be quantized by:

$$a_{\eta,\boldsymbol{k}}(t) \to \sqrt{\frac{\hbar}{2\epsilon_0 V \omega_{\boldsymbol{k}}}}\, \hat{a}_{\eta,\boldsymbol{k}} \tag{3.6a}$$

$$\bar{a}_{\eta,\boldsymbol{k}}(t) \to \sqrt{\frac{\hbar}{2\epsilon_0 V \omega_{\boldsymbol{k}}}}\, \hat{a}^\dagger_{\eta,\boldsymbol{k}}\,, \tag{3.6b}$$

which promotes the expansion coefficients $a_{\eta,\boldsymbol{k}}$ and $\bar{a}_{\eta,\boldsymbol{k}}$ to the operators $\hat{a}_{\eta,\boldsymbol{k}}$ and $\hat{a}^\dagger_{\eta,\boldsymbol{k}}$, respectively. Inserting those into the expansion (3.3) yields the corresponding quantized vector potential:

$$\boldsymbol{A}(\boldsymbol{r}, t) = \sum_{\eta,\boldsymbol{k}} \sqrt{\frac{\hbar}{2\varepsilon_0 V \omega_{\boldsymbol{k}}}} \left[\boldsymbol{\varepsilon}_{\eta,\boldsymbol{k}}\, \hat{a}_{\eta,\boldsymbol{k}} \exp(i\boldsymbol{k}\boldsymbol{r}) + \bar{\boldsymbol{\varepsilon}}_{\eta,\boldsymbol{k}}\, \hat{a}^\dagger_{\eta,\boldsymbol{k}} \exp(-i\boldsymbol{k}\boldsymbol{r})\right], \tag{3.7}$$

from which the electric and magnetic fields can be derived using the field equations (3.2). The quantum Hamilton operator for the radiation can be derived by inserting the quantized electric and magnetic field in the classical Hamiltonian function [2]:

$$\hat{H}_{rad} = \sum_{\eta,\boldsymbol{k}} \hbar\omega_{\boldsymbol{k}} \left(\hat{a}^\dagger_{\eta,\boldsymbol{k}}\, \hat{a}_{\eta,\boldsymbol{k}} + \frac{1}{2}\right). \tag{3.8}$$

Note the similarity to the Hamiltonian of the second quantized quantum harmonic oscillator. Here, when applied to a state $|n\rangle$, the operator $\hat{a}^\dagger$ excites to a state $\sqrt{n+1}\,|n+1\rangle$ and conversely $\hat{a}$ dexcites to a state $\sqrt{n}\,|n-1\rangle$. Those operators are therefore called creation and annihilation operators, respectively. Similarly, the creation operator $\hat{a}^\dagger_{\eta,\boldsymbol{k}}$ creates a photon of polarization η and with the direction $\boldsymbol{k}$ and the annihilation operator $\hat{a}_{\eta,\boldsymbol{k}}$ destroys that photon. Therefore, $\hat{H}_{rad}$ may be considered as a Hamiltonian of independent oscillators of energy $\omega_{\boldsymbol{k}} = c\,|\boldsymbol{k}|$, which oscillate along the direction $\boldsymbol{k}$.

The expression of the vector potential in terms of the Fourier expansion (3.7) yields an orthogonal basis $|\eta, \boldsymbol{k}\rangle$, which therefore obeys the time-independent Schrödinger equation $\hat{H}_{rad}\,|\eta, \boldsymbol{k}\rangle = \hbar\omega_{\boldsymbol{k}}\,|\eta, \boldsymbol{k}\rangle$, where $\hbar\omega_{\boldsymbol{k}}$ is the energy of the incident photon. Since the adiabatic electronic wave functions $|\psi_i\rangle$ and states $|\eta, \boldsymbol{k}\rangle$ each form an orthogonal set for the respective system alone, the product eigenstates of these operators form a basis for the coupled system. Therefore, the unperturbed Hamiltonian $\hat{H}_0 = \hat{H}_{el} + \hat{H}_{rad}$ obeys

$$\left(\hat{H}_{el} + \hat{H}_{rad}\right)|\psi_i, \eta, \boldsymbol{k}\rangle = (E_i + \hbar\omega_{\boldsymbol{k}})\,|\psi_i, \eta, \boldsymbol{k}\rangle\,. \tag{3.9}$$

In the regime of perturbation theory, those system eigenstates $|\psi_i, \eta, \boldsymbol{k}\rangle$ are coupled by interaction Hamiltonian $\hat{H}_{int}$, which is derived in the following.

2 Given by $H(\boldsymbol{r}, t) = \frac{\epsilon_0}{2}\int_V \left(|\boldsymbol{E}|^2 + c^2|\boldsymbol{B}|^2\right)$, where c is the speed of light.

MINIMAL COUPLING AND MULTIPOLAR EXPANSION. In order to couple the electromagnetic field to the electrons, the light-matter interaction $\hat{H}_{int}$ is obtained by adding the scalar potential $-e\phi(\boldsymbol{r},t)$ and replacing the canonical momentum operator for the electrons $\hat{\boldsymbol{p}} = -i\hbar\nabla_{\boldsymbol{r}}$ by the kinetic momentum $\hat{\boldsymbol{\pi}} = \hat{\boldsymbol{p}} + e\boldsymbol{A}(\boldsymbol{r},t)$ in the electronic Hamiltonian $\hat{H}_{el}$ (cf. Eqn. (1.1b)):

$$\begin{aligned}\hat{H}_{int} = \hat{H}_{el} - \frac{\hat{\boldsymbol{p}}^2}{2m_e} - \hat{U}(\boldsymbol{r},\boldsymbol{R}) &= \frac{e}{2m_e}\left[\hat{\boldsymbol{p}}\cdot\boldsymbol{A}(\boldsymbol{r},t) + \boldsymbol{A}(\boldsymbol{r},t)\cdot\hat{\boldsymbol{p}}\right] + \frac{e^2}{2m_e}\boldsymbol{A}^2(\boldsymbol{r},t) - e\phi \\ &= \frac{e}{2m_e}\boldsymbol{A}(\boldsymbol{r},t)\cdot\hat{\boldsymbol{p}} + \frac{e^2}{2m_e}\boldsymbol{A}^2(\boldsymbol{r},t) - e\phi(\boldsymbol{r},t), \qquad (3.10)\end{aligned}$$

where e denotes the charge of the electron. Note that in quantum mechanics the momentum operator and the vector potential do not commute, therefore the Coulomb gauge ($\nabla_{\boldsymbol{r}}\boldsymbol{A} = 0$) has been employed to obtain the last equation. The first term, which is proportional to $\boldsymbol{A}\cdot\hat{\boldsymbol{p}}$, represents the interaction of the external field with the orbital motion of the electron and is known as the orbital paramagnetic operator. As shown later, it invokes the electric En and magnetic Mn multipoles. In contrast, the quadratic term $\boldsymbol{A}^2$ in Eqn. (3.10), which is called diamagnetic operator, leads to the pondermotive potential in intense fields and diamagnetism.[43] It may be viewed as a small positive correction to the interaction of the electrons with the scalar potential ϕ, counteracting the external magnetic field according to Lenz's law. From a classical point of view it describes the deceleration of the electron orbits around the nucleus as a consequence of the external magnetic field (retardation).[44] In comparison with the aforementioned paramagnetism the effect of diamagnetism is very small and does not play a significant role if weak magnetic fields are imposed. However, the influence increases quadratically with the distance of the electron to the nucleus, such that the diamagnetic term is not negligible for Rydberg atoms in even moderately strong magnetic fields.[44]

The interaction Hamiltonian (Eqn. (3.10)) is the so called minimal coupling Hamiltonian and contains the same interaction terms as would have been present in the classical Hamiltonian function. However, note that it fails in the presence of an external magnetic field, since the spin of the electrons is not considered here. In that case, the canonical momentum is $\boldsymbol{\sigma}\,\hat{\boldsymbol{\pi}}_i$, where $\boldsymbol{\sigma}$ are Pauli spin matrices, yielding an additional spin paramagnetic operator $\frac{e}{m_e}(\nabla_{\boldsymbol{r}}\times\boldsymbol{A})\cdot\hat{\boldsymbol{s}}$ (Zeeman interaction) in Eqn. (3.10), in which $\hat{\boldsymbol{s}}$ is the spin angular momentum operator. The inclusion of the Zeeman interaction removes the degeneracy of the angular momentum spectrum, which is not considered further in the following discussions.

The expression of the interaction Hamiltonian (3.10) in terms of the complex vector potential $\boldsymbol{A}$ and the scalar potential ϕ is convenient, because it only depends on four rather than six components as the real electric $\boldsymbol{E}$ and magnetic $\boldsymbol{B}$ field. However, it is not unique due to the freedom of gauge, as can be straightforwardly shown by inserting $\boldsymbol{A} \to \boldsymbol{A} + \nabla\chi$ and $\phi \to \phi + \partial\chi/\partial t$ in Eqn. (3.10), where χ is an arbitrary gauge function. In order to remove the ambiguity caused by the freedom of gauge, it is required to express $\hat{H}_{int}$ in terms of the electric $\boldsymbol{E}$ and magnetic $\boldsymbol{B}$ fields, which

are related to $\boldsymbol{A}$ and ϕ by Maxwell's equations. This can be accomplished in several ways. One is to switch from the particle approach as defined by Eqn. (3.10) to a field description of the electrons and applying a unitary transformation to remove the gauge dependency, yielding the Power-Zienau-Woolley formulation of electrodynamics.[45] Alternatively, one may expand $\boldsymbol{E}$ and $\boldsymbol{B}$ in a Taylor series with the origin set to zero and find expansions of $\boldsymbol{A}$ and ϕ in terms of $\boldsymbol{E}$ and $\boldsymbol{B}$ equaling the former expansions.[46] In the end however, a multipolar interaction Hamiltonian yielding the familiar electric and magnetic multipoles (E1, M1, E2 etc.) is derived:

$$\hat{H}_{int} = -\hat{\boldsymbol{\mu}} \cdot \boldsymbol{E}(t) - \hat{\boldsymbol{m}} \cdot \boldsymbol{B}(t) - \hat{\boldsymbol{Q}} : \nabla \boldsymbol{E}(t) - \ldots, \tag{3.11}$$

in which : denotes the dyadic double dot product ($\hat{\boldsymbol{Q}} : \nabla \boldsymbol{E} = \sum_{i,j} Q_{ij} \nabla_j E_i$) and the following definitions for the electric dipole moment $\hat{\boldsymbol{\mu}}$, magnetic dipole moment $\hat{\boldsymbol{m}}$ and electric quadrupole moment $\hat{\boldsymbol{Q}}$ operators are used:

$$\hat{\boldsymbol{\mu}} = -e \sum_{i}^{elec.} \boldsymbol{r}_i \tag{3.12a}$$

$$\hat{\boldsymbol{m}} = -\frac{e}{2m_e} \sum_{i}^{elec.} \boldsymbol{r}_i \times \boldsymbol{p_i} = -\frac{e}{2m_e} \hat{\boldsymbol{L}} \tag{3.12b}$$

$$\hat{\boldsymbol{Q}} = -\frac{e}{2} \sum_{i}^{elec.} \boldsymbol{r}_i \boldsymbol{r}_i. \tag{3.12c}$$

Note that the magnetic dipole moment operator (Eqn. (3.12b)) is proportional to the orbit angular momentum operator $\hat{\boldsymbol{L}} = -i\hbar(\boldsymbol{r} \times \nabla_{\boldsymbol{r}})$. Further note that in Eqn. (3.10) the field quantities $\boldsymbol{E}(t)$ and $\boldsymbol{B}(t)$ no longer depend on spatial variables and acquire the spatially fixed origin of the multipole expansion.

In the following no higher order interaction terms than given in Eqn. (3.11) are considered, which suffice to represent all currently known molecular chiroptical properties. In order to estimate the relative magnitude of each term in Eqn. (3.11), it is expedient to assume each electron having a radial distribution of the order of the Bohr radius a_0. Subsequently, its electric dipole is ea_0, its quadrupole moment is ea_0^2, and its magnetic dipole moment is proportional to an angular momentum $\hbar$. As can be easily shown, the magnitudes of M1 to and E2 are both smaller than E1 by a factor of the fine structure constant $\alpha \approx 1/137$[47] and it is therefore often adequate to truncate the expansion after the first term:

$$\hat{H}_{int}^{ED} \approx -\hat{\boldsymbol{\mu}} \cdot \boldsymbol{E}(t), \tag{3.13}$$

which is known as dipole approximation. However, although the effects of magnetic and quadrupolic coupling present in the full multipolar expansion (Eqn. (3.11)) are small, the inclusion of those terms is essential to fully capture the photophysics of e.g. chiral molecules (see below).

A NOTE ON CHIRAL MOLECULES. As already mentioned previously, the dipolar coupling gives the leading contribution in any application where its matrix elements are non-zero. However, it follows from the character of the fundamental space- and time symmetry rules that a chiroptical response may be caused by either the chiral nature of the incident light or the matter, respectively. As can be shown by the symmetry of the laser field and the molecular properties, which both enter the multipolar interaction hamiltonian, such a response is only obtainable if terms beyond the electric dipole–electric field interaction are considered. Particularly, the inclusion of magnetic dipole–magnetic field and electric quadrupole–electric field interaction terms are essential for capturing the properties inherent to chiral molecules.

The parities upon charge ($\mathcal{C}$), space ($\mathcal{P}$) and time ($\mathcal{T}$) inversion operations are of fundamental significance to optical and electromagnetic phenomena[3]. Each of them has eigenvalues of ± 1 denoting even or odd parity and double operation is an identity operation. In the context of chiral molecules, the symmetry operation for the spatial inversion $\mathcal{P}$ is of particular interest.

The consequence of applying $\mathcal{P}$ to an enantiomer is that it is transferred to the other enantiomer. Therefore the wave function for either individual enantiomer is not an eigenstate of $\mathcal{P}$. Hence it lacks the full symmetry of the corresponding molecular Hamiltonian, which is parity even in $\mathcal{P}$ and $\mathcal{T}$ since it delivers an energy.[48]

A profound analysis of the symmetry properties of the interaction terms in Eqn. (3.11) and their chiroptical implications are comprehensively discussed in Ref. [47]. At this point, it may suffice to summarize that the character of the fundamental space- and time symmetry rules precludes any spontaneous generation of chirality and the parity of the light-matter interactions included in Eqn. (3.11) is therefore essential for the optical response of chiral molecules. Specifically, an intrinsically achiral system cannot become chiral without some form of chiral stimulus. For example, light without any helicity irradiating a racemic mixture cannot produce any effect that leads to an enantiomeric excess or any response differentiating between the individual forms. Consequently, a chiroptical response may be caused by either the chiral nature of the incident light or the matter, respectively.[47]

The role of higher order terms in Eqn. (3.11) may be elucidated by considering a general interaction that takes a system from an initial state $|I\rangle = |\psi_I, \eta_I, \boldsymbol{k}_I\rangle$ to a final state $|F\rangle = |\psi_F, \eta_F, \boldsymbol{k}_F\rangle$, both being eigenstates of the unperturbed Hamiltonian $\hat{H}_0$ with eigenvalues $\mathcal{E}_I$ and $\mathcal{E}_F$, respectively. In the frame of perturbation theory, hence assuming weak fields, Fermi's golden rule gives the transition probability Γ_{IF} per unit time (transition rate):

$$\Gamma_{IF} = \frac{2\pi}{\hbar} \left| \langle F \left| \hat{M} \right| I \rangle \right|^2 \rho(E_F) = \frac{2\pi}{\hbar} |M_{IF}|^2 \, \delta(\mathcal{E}_F - \mathcal{E}_I), \tag{3.14}$$

3 Because of the invariant nature of matter (electrons have negative and nuclei have a positive charge) charge conjugation simply does not arise in our normal world and it suffices to consider only $\mathcal{PT}$ symmetry.

where the delta function ensures the conservation of energy by the molecule-light system as a whole. The matrix elements M_{IF} that indicate the electrodynamic coupling may be written as an infinite series using the propagator $\hat{T}_0 \approx (E_I - \hat{H}_0)^{-1}$:[49]

$$\begin{aligned} M_{IF} &= \sum_{p=0}^{\infty} \langle F \,|\, \hat{H}_{int}\, (\hat{T}_0\, \hat{H}_{int})^p \,|\, I \rangle \\ &= \langle F \,|\, \hat{H}_{int} \,|\, I \rangle + \sum_R \frac{\langle F \,|\, \hat{H}_{int} \,|\, R \rangle \langle R \,|\, \hat{H}_{int} \,|\, I \rangle}{E_I - E_R} + \\ &\quad + \sum_{R,S} \frac{\langle F \,|\, \hat{H}_{int} \,|\, S \rangle \langle S \,|\, \hat{H}_{int} \,|\, R \rangle \langle R \,|\, \hat{H}_{int} \,|\, I \rangle}{(E_I - E_R)(E_I - E_S)} + \ldots, \end{aligned} \tag{3.15}$$

where the virtual states $|R\rangle$, $|S\rangle$, ... are introduced by inserting the completeness relation. Here it may suffice to focus on the first term in Eqn. (3.15) that is responsible for single-photon processes, and inserting the multipolar Hamiltonian (3.11) yields according to Fermi's golden rule a transition rate of:

$$\begin{aligned} \Gamma_{IF} = \frac{2\pi}{\hbar} [&\langle F \,|\, \hat{\boldsymbol{\mu}} \cdot \boldsymbol{E} \,|\, I \rangle \langle I \,|\, \hat{\boldsymbol{\mu}} \cdot \bar{\boldsymbol{E}} \,|\, F \rangle \\ &+ \langle F \,|\, \hat{\boldsymbol{\mu}} \cdot \boldsymbol{E} \,|\, I \rangle \langle I \,|\, \hat{\boldsymbol{m}} \cdot \bar{\boldsymbol{B}} \,|\, F \rangle + \langle F \,|\, \hat{\boldsymbol{m}} \cdot \boldsymbol{B} \,|\, I \rangle \langle I \,|\, \hat{\boldsymbol{\mu}} \cdot \bar{\boldsymbol{E}} \,|\, F \rangle \\ &+ \langle F \,|\, \hat{\boldsymbol{\mu}} \cdot \boldsymbol{E} \,|\, I \rangle \langle F \,|\, \hat{\boldsymbol{Q}} : \nabla \bar{\boldsymbol{E}} \,|\, I \rangle + \langle F \,|\, \hat{\boldsymbol{Q}} : \nabla \boldsymbol{E} \,|\, I \rangle \langle I \,|\, \hat{\boldsymbol{\mu}} \cdot \bar{\boldsymbol{E}} \,|\, F \rangle \\ &+ \ldots] \, \delta(\mathcal{E}_F - \mathcal{E}_I). \end{aligned} \tag{3.16}$$

Now note that the electric multipoles En are all of parity $(-1)^n$ under spatial inversion $\mathcal{P}$, while the magnetic multipoles Mn are all of parity $(-1)^{n+1}$. Specifically, the electric dipole moment operator $\hat{\boldsymbol{\mu}}$ is $\mathcal{P}$-odd, the magnetic dipole moment operator $\hat{\boldsymbol{m}}$ is $\mathcal{P}$-even, and so is the electric quadrupole moment operator $\hat{\boldsymbol{Q}}$. The electric field $\boldsymbol{E}$ is $\mathcal{P}$-odd and the magnetic field $\boldsymbol{B}$ is $\mathcal{P}$-even.[47] The first term in Eqn. (3.16), which gives the leading contribution, retains its sign irrespective of the circular handedness of the field or the enantiomeric form. However, the following interference terms do change their sign either by substituting the opposite enantiomer or inverting the helicity of the incident light. It follows that a chiroptical response may be caused by either the chiral nature of the incident light or the matter, respectively, and moreover that the inclusion of higher-order terms in the multipole expansion of the interaction Hamiltonian is essential for discriminating enantiomers.

2.4 FIELD-INDUCED SURFACE-HOPPING BEYOND DIPOLE APPROXIMATION

For the full quantum dynamical description of light-matter interaction the time-dependent Schrödinger equation (Eqn. (1.1a)) for the Hamiltonian (3.1) needs to be solved, which invokes the application of quantum electrodynamics (QED). However, this is computationally very demanding even for simple systems. Therefore, a semiclassical description of light-matter interaction is adopted in the following, which often obeys much simpler equations. Particularly, in semiclassical calculations, the light

is treated as a classical electromagnetic field described by Maxwell's equations and the matter is described by quantum mechanics. By treating the light classically, the quantum operators for electric and magnetic fields are replaced by their expectation value and therefore commute with other operators in $\hat{H}$. This allows to separate the field variables from the equations of motion for the molecular system and the problem reduces to solving the Schrödinger equation for the semiclassical Hamiltonian $\hat{H} = \hat{H}_{mol} + \hat{H}_{int}$, in which the interaction with the laser field acts as a perturbation to the quantum dynamics (or quantum-classical dynamics) of the system. Therefore, only the equations of motion for the matter need to be solved, leaving the state of the light unaffected by the interaction.

As with any approximation, the semiclassical description of light-matter interaction has advantages and limitations. As already mentioned, the semiclassical equations of motion are easier to solve than the full quantum problem. Moreover, the classical description of light is naturally connected to the conventional methods for characterizing light signals (e.g., intensity, frequency, polarization, etc.) and allows for a physically intuitive picture of how the incident light affects the quantum dynamics of the molecular system. However, due to the missing linkage between light and matter, the concept of energy conservation does not naturally arise from the semiclassical equations. Particularly, in the full quantum picture, the interaction of light with matter would lead to the annihilation/creation of photons as a consequence of rising/lowering the quantum state of the molecular system. Consequently, processes relying on the creation of photons, such as spontaneous emission, cannot be derived by semiclassical calculations. Further, the classical description is valid only for light of weak or moderate intensity. For extremely low light intensities (e.g., single-photon spectroscopy), quantum effects, such as photon entanglement or quantum noise become important. On the other hand, for extremely strong laser fields, the treatment of the light-matter interaction is no longer perturbative and needs to be considered in the quantum-classical treatment of nuclear motion (see below). Finally, due to the finite speed of light, separating the light from the system leaves out some retardation effects arising in extended chromophore systems (e.g., crystals or molecular aggregates).

We may further assume that the wavelength of the radiational field (e.g., UV ranges from 100 to 380 nm) is much longer than the dimension of the system under investigation (e.g., even large light-harvesting complexes have a diameter of $<$30 nm[50]). It follows that the interaction with the field adds a spatially constant potential to the full molecular Hamiltonian, which leaves the equation of motion for the nuclei unaffected. Therefore, in the spirit of quantum-classical molecular dynamics, the classical Hamiltonian (Eqn. (1.12)) or Newtonian (Eqn. (1.13)) equations of motion can be solved even in the presence of an interacting laser field, in which the forces on the nuclei are determined as the gradients of the electronic potential energy.

Finally, in this semiclassical picture of nuclear motion and light-matter interaction, the quantum problem is reduced to solving the time-dependent Schrödinger equation for the electronic Hamiltonian $\hat{H}_{el}$ that interacts with the laser field according to:

$$\hat{H} = \hat{H}_{el} + \hat{H}_{int}\,. \tag{4.1}$$

Assuming a weak laser field that acts as a perturbation, the total wave function may be expanded in the basis of the adiabatic electronic states $|\psi_i\rangle$ that depend parametrically on the instantaneous nuclear geometry and are the eigenfunctions of the electronic Hamiltonian:

$$|\Psi\rangle = \sum_i c_i(t)\,|\psi_i(\boldsymbol{R}(t)\rangle\,, \tag{4.2}$$

where c_i are time-dependent expansion coefficients. Since $|\psi_i\rangle$ are eigenstates of the electronic Hamiltonian, they obey the time-independent Schrödinger equation and give rise to the adiabatic potential energy surface $E_i(\boldsymbol{R}(t))$. The equations of motion of coefficients c_i are obtained by inserting Eqn. (4.2) together with Eqn. (4.1) in the time-dependent Schrödinger equation:

$$\begin{aligned}
i\hbar\dot{c}_i(t) =& E_i(\boldsymbol{R}(t))c_i(t) - i\hbar\sum_j \left\langle \psi_i(\boldsymbol{r};\boldsymbol{R}(t)) \,\middle|\, \frac{\mathrm{d}}{\mathrm{d}t}\psi_j(\boldsymbol{r};\boldsymbol{R}(t)) \right\rangle c_j(t) \\
&+ \sum_j \left\langle \psi_i(\boldsymbol{r};\boldsymbol{R}(t)) \,\middle|\, \hat{H}_{int} \,\middle|\, \psi_j(\boldsymbol{r};\boldsymbol{R}(t)) \right\rangle c_j(t) \\
=& E_i(\boldsymbol{R}(t))c_i(t) - i\hbar\sum_j \boldsymbol{d}_{ij}(\boldsymbol{R})\dot{\boldsymbol{R}}(t)c_j(t) \\
&- \sum_j \left[\boldsymbol{\mu}_{ij}(\boldsymbol{R})\cdot\boldsymbol{E}(t) + \boldsymbol{m}_{ij}(\boldsymbol{R})\cdot\boldsymbol{B}(t) + \boldsymbol{Q}_{ij}(\boldsymbol{R}) : \nabla\boldsymbol{E}(t)\right] c_j(t),
\end{aligned} \tag{4.3}$$

where the multipolar expansion Eqn. (3.11) of the interaction Hamiltonian $\hat{H}_{int}$ has been used in the last equation. The quantities $\boldsymbol{\mu}_{ij} = \langle \psi_i \,|\, \hat{\boldsymbol{\mu}} \,|\, \psi_j \rangle$, $\boldsymbol{m}_{ij} = \langle \psi_i \,|\, \hat{\boldsymbol{m}} \,|\, \psi_j \rangle$ and $\boldsymbol{Q}_{ij} = \langle \psi_i \,|\, \hat{\boldsymbol{Q}} \,|\, \psi_j \rangle$ denote the electric dipole, magnetic dipole and electric quadrupole transition moments, respectively, and $\boldsymbol{d}_{ij} = \langle \psi_i \,|\, \nabla \,|\, \psi_j \rangle$ are the non-adiabatic coupling vectors.

Solving Eqn. (4.3) for the for the coefficients c_i along the nuclear trajectory yields the quantum populations $\rho_{ii} = c_i^* c_i$ of the adiabatic states, from which – in the spirit of Tully's surface-hopping approach – a probability $P_{i\to j}$ for switching from the current state i to the state j at a nuclear time step Δt can be calculated as:[51]

$$P_{i\to j} = \left[\Theta(-\dot{\rho}_{ii})\frac{-\dot{\rho}_{ii}}{\rho_{ii}}\Delta t\right] \cdot \left[\Theta(\dot{\rho}_{jj})\frac{\dot{\rho}_{jj}}{\sum_k \Theta(\dot{\rho}_{kk})\dot{\rho}_{kk}}\right]. \tag{4.4}$$

The first factor represents the depopulation probability of the current state i, which is nonzero only if the population of this state decreases. Consequently, the population probability of the state j, which is represented by the second factor, is nonzero if its population is increasing. These boundary conditions are ensured by the Heaviside

function $\Theta(x)$, which is unity for $x \geq 0$ and zero otherwise. The rate of population change $\dot{\rho}_{ii}$ can be calculated from the population at subsequent two nuclear time steps as $\dot{\rho}_{ii}(t) = (\rho_{ii}(t) - \rho_{ii}(t - \Delta t))\Delta t^{-1}$. Note that this definition of hopping probability is an improvement to the original formulation by Tully.[12] Since Eqn. (4.4) incorporates only the smoothly changing populations ρ_{ii}, but excluding the rapidly changing coherences ρ_{ij} and field coupling terms the hopping procedure is numerically more stable.

Due to the close relation to Tully's surface-hopping approach introduced in section 2.2, but at the same time incorporating the light-matter interaction, the method is known as field-induced surface-hopping (FISH).[42] Since the electric dipole–electric field coupling gives the leading contribution, in most applications, it usually suffices to include the $-\boldsymbol{\mu} \cdot \boldsymbol{E}$ term of Eqn. (4.3) only. In this form, the FISH approach has been employed numerous studies on laser-induced and -controlled processes and enables the simulation of a diversity of spectroscopic observables.

As indicated in section 2.3 the electric dipolar coupling is, however, incapable to fully capture the photodynamics of chiral molecules. The inclusion of the magnetic dipole–magnetic field $-\boldsymbol{m} \cdot \boldsymbol{B}$ and electric quadrupole–electric field $-\boldsymbol{Q} : \nabla \boldsymbol{E}$ coupling terms is therefore essential to obtain discrimination of enantiomers by the FISH approach. Hence, to explore the homochiral nature of the biological matter in geological evolution, the implementation of those higher-order terms in Eqn. (4.3) has been the subject of this thesis. The derived methodology has been tested on the smallest chiral amino acid alanine and the results are detailed in chapter 3.

2.5 MULTI-CHROMOPHORIC FIELD-INDUCED SURFACE-HOPPING

Excited-state dynamics of multi-chromophoric complexes (MC), such as light-harvesting complexes (LHC) or DNA, are governed by efficient energy transport mechanisms that allow the non-radiative transfer of excitation energy between the individual chromophores. Although the development of efficient quantum chemical methods and advances in computing power made it possible to treat systems of increasing size, the complexity of those large MC precludes the direct application of the approaches presented so far. Those systems usually consist of π-conjugated individual chromophoric subunits (e.g., that absorb light in the UV range). The general procedures for simulating light-induced non-adiabatic dynamics in the frame of quantum-classical molecular dynamics combined with field-induced surface-hopping (FISH) have been explicated in the previous sections.

In the following, a hybrid quantum mechanical – molecular mechanical (QM/MM) model combining the field-induced surface-hopping (FISH) method (cf. Sec. 2.4) with the Frenkel exciton model is presented. The multi-chromophoric field-induced surface-hopping (McFISH) approach allows the simulation of the energy transport in extended molecular systems irradiated by an external laser field and includes environmental effects as well.

QM/MM EXCITON MODEL. Most biological multi-chromophoric systems, such as DNA or light-harvesting complexes, are supramolecular structures that consist of many close-lying chromophores and are surrounded by an environment of solvent molecules (usually water), ions and other compounds. Despite the availability of very efficient electronic structure methods applicable to quite complex molecules, the complete quantum chemical description of multi-chromophoric systems still cannot be performed without further approximations.

However, usually, not all parts of the system directly participate in the non-radiative relaxation after electronic excitation due to the irradiation by UV light. Specifically, only the π-conjugated chromophoric subunits of the MC (e.g., the nucleobases in DNA) usually absorb light at wavelengths that are important for biological processes. Moreover, within the frame of Förster's theory, the non-radiative excitation energy transfer (EET) will dominantly occur between similar chromophores that have energy levels being resonant to each other. The hybrid quantum mechanical–molecular mechanics (QM/MM) approach, in which the system partitioned into one part (the MC) that is described fully quantum mechanically (QM part), and another one (the environment), for which molecular mechanics treatment is sufficient (MM part),[52–54] provides a possible strategy to overcome the limitations of quantum mechanical treatment of large systems such as DNA. In this QM/MM approach, the total energy of the combined system can then be written as:

$$E = \left\langle \Psi_{MC} \middle| \hat{H}_{MC} \middle| \Psi_{MC} \right\rangle + E_{MM}(\boldsymbol{R}_{MM}) + E_{QM/MM}(\boldsymbol{R}_1, \ldots, \boldsymbol{R}_N, \boldsymbol{R}_{MM}), \tag{5.1}$$

where $\boldsymbol{R}_{\{1\ldots N\}}$ denote the coordinates of each chromophoric subunit in the MC and $\boldsymbol{R}_{MM}$ the coordinates of the MM part. The first term in Eqn. (5.1) is the energy of the MC, the second term is the classical force field energy of the MM region and the third term is the interaction between the chromophoric complex and the MM system, respectively. Within this approach, the electronic structure for the MM part is completely neglected, and the energy is represented by bonding and nonbonding interactions that are analytic functions depending on geometrical parameters such as bond lengths, angles and interatomic distances. The concrete functional form of the used potentials depends on the employed empirical force field. However, due to the computational efficiency, usually harmonic approximations for bonded interactions and classical Coulomb as well as van-der-Waals potentials for the nonbonding interactions are used. The necessary parameters such as force constants, equilibrium values of bond lengths and angles, as well as the partial atomic charges and van-der-Waals parameters are usually determined by fitting to experimental values or from quantum chemical calculations.

The second term in Eqn. (5.1), that describes the interaction of the MC and the MM system, includes terms for the nonbonding interaction of both systems as well as the bonded interactions if the boundary of both systems cuts a chemical bond. For the latter interaction usually the same force field is used as for the MM system

and the dangling bond at the QM part is capped by a link atom (e.g., hydrogen) to conserve its spin multiplicity.[53] For the nonbonding interaction of QM and MM region, several levels of approximations have been devised.[53] In the simplest case, the electrostatic interaction is treated on the MM level by classical Coulomb and Van-der-Waals potentials (mechanical embedding). However, certain issues may occur by, e.g., the difficulty of assigning appropriate MM properties such as atom-centered point charges to the QM region. Another problem is that in the mechanical embedding scheme, the interaction of both systems does affect neither the atomic charges of the MM part due to polarization by the QM system nor the electronic structure of the QM system[55]. The electrostatic embedding scheme accounts for the latter problem by including the MM point charges as one-electron terms in the QM Hamiltonian operator and by employing polarizable force field fields that allow the flexible assignment of MM charges according to QM calculations, also the polarization of the MM system can be accounted for (polarized embedding). However, since the polarized embedding scheme is computationally challenging, it has been scarcely applied to bio-molecular simulations that are limited to explicit solvation models[55]. Therefore, in the following, the electrostatic embedding scheme is employed, which leaves only the bonding (if existent) as well as the nonbonding Van-der-Waals potentials in $E_{QM/MM}$.

Finally, the energy of the MC, represented by the first term in Eqn. (5.1), is subject to quantum chemical calculations. In close analogy to the Frenkel exciton model,[56] the electronic structure of a multi-chromophoric complex being built from N individual chromophores can be written as:

$$\hat{H}_{MC} = \sum_I \hat{H}_I + \frac{1}{2} \sum_I \sum_{J \neq I} \hat{V}_{IJ} + \hat{H}_{int} \,, \tag{5.2}$$

where $\hat{H}_I$ denote the monomeric Hamiltonian operators of each subsystem, $\hat{H}_{int}$ the interaction with the laser field (cf. Sec. 2.3) and $\hat{V}_{IJ}$ pairwise interaction of the subunits at the sites I and J, respecivily. In the frame of Förster theory the interaction term $\hat{V}_{IJ}$ is of purely electrostatic nature and is given by:

$$\hat{V}_{IJ} = \hat{V}_{IJ}^{(nn)} + \hat{V}_{IJ}^{(en)} + \hat{V}_{IJ}^{(ee)} \,, \tag{5.3}$$

including the nuclear-nuclear ($\hat{V}_{IJ}^{(nn)}$), the electron-nuclear ($\hat{V}_{IJ}^{(en)}$) and the electron-electron ($\hat{V}_{IJ}^{(ee)}$) contributions. At this point, we may follow the idea of the electrostatic embedding scheme introduced for the conventional QM/MM procedure and shift the nuclear contributions $\hat{V}_{IJ}^{(nn)}$ and $\hat{V}_{IJ}^{(en)}$ into the monomeric Hamiltonians $\hat{H}_I$ in order to allow the polarization of each monomers due to the presence of the others. Therefore, $\hat{V}_{IJ}$ reduces to purely electron-electron and Van-der-Waals interactions and the monomeric Hamiltonians read:

$$\hat{H}_I = \hat{H}_{mol}\left(\boldsymbol{R}_I\right) + \hat{V}_{MM} + \frac{1}{2} \sum_{J \neq I} \left(\hat{V}_{IJ}^{(nn)} + \hat{V}_{IJ}^{(en)} \right) , \tag{5.4}$$

where $\hat{H}_{mol}$ represents the unembedded molecular Hamiltonian and $\hat{V}_{MM}$ the one-electron contributions of the MM region. Solving the Schrödinger equation for $\hat{H}_I$ in the frame of the Born-Oppenheimer approximation yields a set of orthogonal eigenstates $|\psi_i\rangle$ with the eigenvalues $E_i(\boldsymbol{R}_I)$ and represents the energy of the Ith monomer in the presence of the other monomers as well as the MM environment.

The first two terms in Eqn. (5.2) are time-independent and are completely determined by the structure of the individual monomers. Therefore the natural basis for solving the time-dependent Schrödinger equation with the Hamiltonian $\hat{H}_{MC}$ is the basis spanned by the eigenstates of the time-independent part of Eqn. (5.2). However, since $\hat{V}_{IJ}^{(ee)}$ depends on the electron coordinates of two subsystems, this cannot be obtained easily in a self-consistent way. Therefore, in order to make such an exciton model practical for calculations in large systems, the following approximations are introduced:

1. the wave functions of the individual chromophores are approximated by the wave functions of the isolated ones embedded in the field of charges of the other monomers,
2. no exchange of electrons is allowed between the subunits[4], and
3. the wave functions of different subunits are considered to be orthogonal, which is strictly not exact, since the orbitals are determined independently.

Those approximations allow to represent the basis states $|\phi_{ab\ldots z}\rangle$ of $\hat{H}_{MC}$ as direct products of the electronic wave function of each chromophore:

$$|\phi_{ab\ldots z}\rangle = \left|\psi_a^{(1)}\right\rangle \otimes \left|\psi_b^{(2)}\right\rangle \otimes \ldots \otimes \left|\psi_z^{(N)}\right\rangle = \left|\prod_I \psi_{k_I}^{(I)}\right\rangle, \tag{5.5}$$

where each eigenstate $\left|\psi_i^{(I)}\right\rangle$ fulfills the general orthogonality relation $\left\langle\psi_i^{(I)}\middle|\psi_j^{(J)}\right\rangle = \delta_{ij}\delta_{IJ}$. Here, the superscripts 1, 2, …, N denote the index number of each chromophore within the MC, the indices a, b, … z are running over all included electronic states for each monomer and k_I is the index of the electronic state of the I-th monomer in the set $ab\ldots z$. The multi-chromophoric Hamiltonian operator $\hat{H}_{MC}$ in this basis can therefore be written as a super-matrix $\boldsymbol{H}_{MC}$ with the matrix elements:

$$\begin{aligned}\left(\hat{H}_{MC}\right)_{ab\ldots z,a'b'\ldots z'} = &\sum_I \left\langle\phi_{ab\ldots z}\middle|\hat{H}_I\middle|\phi_{a'b'\ldots z'}\right\rangle + \frac{1}{2}\sum_I\sum_{J\neq I}\left\langle\phi_{ab\ldots z}\middle|\hat{V}_{IJ}^{(ee)}\middle|\phi_{a'b'\ldots z'}\right\rangle \\ &+ \left\langle\phi_{ab\ldots z}\middle|\hat{H}_{int}\middle|\phi_{a'b'\ldots z'}\right\rangle\end{aligned} \tag{5.6}$$

4 Note that a subunit may consist of multiple individual chromophores. Hence, an exchange of electrons can occur between the individual chromophores within a subunit.

Due to the orthogonality relation of the monomeric wave functions, the first sum represents the diagonal elements of the matrix $\boldsymbol{H}_{MC}$ and reduces to the sum of adiabatic electronic energies of the individual monomers:

$$\begin{aligned}\sum_I \left\langle \phi_{ab\ldots z} \,\middle|\, \hat{H}_I \,\middle|\, \phi_{a'b'\ldots z'} \right\rangle &= \sum_I \left\langle \psi_{k_I}^{(I)} \,\middle|\, \hat{H}_I \,\middle|\, \psi_{k_I}^{(I)} \right\rangle \\ &= E_a^{(1)} + E_b^{(2)} + \ldots + E_z^{(N)} = E_{ab\ldots z}, \end{aligned} \tag{5.7}$$

which will be further denoted as adiabatic excitonic energy. The second and third terms represent the off-diagonal elements of the Hamiltonian matrix. Particularly, we may assume that each chromophore is interacting individually with the external laser field, such that the last term in Eqn. (5.6) can be written as:

$$\left\langle \phi_{ab\ldots z} \,\middle|\, \hat{H}_{int} \,\middle|\, \phi_{a'b'\ldots z'} \right\rangle = \sum_I \left\langle \psi_k^{(I)} \,\middle|\, \hat{\boldsymbol{\mu}}^{(I)} \cdot \boldsymbol{E}(t) \,\middle|\, \psi_{k'}^{(I)} \right\rangle = \sum_I \boldsymbol{\mu}_{kk'}^{(I)} \cdot \boldsymbol{E}(t), \tag{5.8}$$

where the electric dipole approximation Eqn. (3.13) (cf. Sec. 2.3) has been employed and $\boldsymbol{\mu}_{kk'}^{(I)}$ is the transition dipole moment for the excitation from electronic state k to k' within the monomer I. Furthermore, the matrix elements of the $\hat{V}_{IJ}^{(ee)}$ operator, which represent the coupling of the monomers I and J, respectively, reduce to purely electronic Coulomb interactions between 4 electronic states:

$$\left\langle \phi_{ab\ldots z} \,\middle|\, \hat{V}_{IJ}^{(ee)} \,\middle|\, \phi_{a'b'\ldots z'} \right\rangle = \left\langle \psi_k^{(I)} \psi_l^{(J)} \,\middle|\, \sum_{\eta,\nu} \frac{1}{\left| \boldsymbol{r}_\eta^{(I)} - \boldsymbol{r}_\nu^{(J)} \right|} \,\middle|\, \psi_{k'}^{(I)} \psi_{l'}^{(J)} \right\rangle \tag{5.9}$$

$$= \int \mathrm{d}\boldsymbol{r}_1^{(I)} \int \mathrm{d}\boldsymbol{r}_1^{(J)} \frac{\rho_{kk'}^{(I)}\left(\boldsymbol{r}_1^{(I)}\right) \rho_{ll'}^{(J)}\left(\boldsymbol{r}_1^{(I)}\right)}{\left| \boldsymbol{r}_1^{(I)} - \boldsymbol{r}_1^{(J)} \right|} = J_{kl,k'l'}^{IJ}, \tag{5.10}$$

where the indices η and ν run over electron coordinates within the monomers I and J, respectively, and the one-electron transition density, defined as:

$$\rho_{kk'}(\boldsymbol{r}_1) = N_{el} \int \mathrm{d}\boldsymbol{r}_2 \cdots \int \mathrm{d}\boldsymbol{r}_{N_{el}} \psi_k(\boldsymbol{r}) \psi_{k'}(\boldsymbol{r}), \tag{5.11}$$

has been introduced in order to derive the last equation. The total multi-chromophoric Hamiltonian in matrix form can therefore be written as:

$$\boldsymbol{H}_{MC} = \sum_I \left(\boldsymbol{H}_I - \sum_{kk'} \boldsymbol{\mu}_{kk'}^{(I)} \cdot \boldsymbol{E}(t) \delta_{kk'} \right) \otimes \mathbf{1}_I + \frac{1}{2} \sum_I \sum_{J \neq I} \boldsymbol{J}_{IJ} \otimes \mathbf{1}_{IJ}, \tag{5.12}$$

where $\mathbf{1}_I$ and $\mathbf{1}_{IJ}$ are identity matrices acting on the electrons of all monomers, except the Ith or the Ith and Jth, respectively. For example, the Hamiltonian for a complex consisting of two monomers each having a ground (g) and an excited state (e) may be written in the following way:

$$\boldsymbol{H}_{MC} = \begin{bmatrix} E_g^{(1)} + E_g^{(2)} & -\boldsymbol{\mu}_{eg}^{(1)} \boldsymbol{E}(t) & -\boldsymbol{\mu}_{eg}^{(2)} \boldsymbol{E}(t) & 0 \\ -\boldsymbol{\mu}_{eg}^{(1)} \boldsymbol{E}(t) & E_e^{(1)} + E_g^{(2)} & J_{eg,ge} & -\boldsymbol{\mu}_{eg}^{(2)} \boldsymbol{E}(t) \\ -\boldsymbol{\mu}_{eg}^{(2)} \boldsymbol{E}(t) & J_{eg,ge} & E_g^{(1)} + E_e^{(2)} & -\boldsymbol{\mu}_{eg}^{(1)} \boldsymbol{E}(t) \\ 0 & -\boldsymbol{\mu}_{eg}^{(2)} \boldsymbol{E}(t) & -\boldsymbol{\mu}_{eg}^{(1)} \boldsymbol{E}(t) & E_e^{(1)} + E_e^{(2)} \end{bmatrix}. \tag{5.13}$$

NUCLEAR DYNAMICS IN EXCITONIC STATES. In order to propagate the light-induced dynamics we may employ the same assumption as has been used for the FISH approach (cf. Sec. 2.4). Specifically, we assume the incident light to be of weak or moderate intensity and that the wavelength of the light is much longer than the system under investigation. Note that the latter approximation may still be valid for large multi-chromophoric systems such as light-harvesting complexes that have a diameter less then 30 nm[50]) or short DNA strands. Hence, to propagate the nuclear trajectories in the basis of excitonic states as defined by Eqn. (5.5) the Newtonian or Hamiltonian equations of motions have to be solved. In the spirit of the previously introduced surface-hopping approach, the trajectories can be propagated on the adiabatic excitonic surfaces $E_{ab\ldots z}$ represented by the diagonal elements of the MC Hamiltonian (Eqn. (5.7)). For this purpose it is expedient to define the ground-state energy E_0 as well as the excitation energy $\omega_{ab\ldots z}$ to the state $ab\ldots z$ as:

$$E_0 = \sum_I E_0^{(I)} + E_{MM} + E_{QM/MM} \tag{5.14a}$$

$$\omega_{ab\ldots z} = E_{ab\ldots z} - \sum_I E_0^{(I)}, \tag{5.14b}$$

where $E_0^{(I)}$ denotes the ground-state energy of the Ith monomer. The forces acting on the nuclei are therefore obtained as:

$$\boldsymbol{F} = -\nabla_{\boldsymbol{R}} E_0 - \nabla_{\boldsymbol{R}} \omega_{ab\ldots z}. \tag{5.15}$$

Note that in the frame of this formulation the gradients ∇J_{IJ} are neglected, which is in contrast to the previously published approaches of Martinez[57,58] and Gonzalez.[59] Those approaches are based on the diagonalization of the multi-chromophoric Hamiltonian and nuclear as well as electronic propagation on the resultant adiabatic electronic surfaces. While being quantum mechanically fully equivalent to the presented approach, their semiclassical limits is different since the nuclear gradients of the adiabatic electronic surfaces include contributions from the gradient of the excitonic coupling. However, due to the slow variation of the excitonic coupling in the course of the dynamics, those gradients are small and can be neglected, as has been done in the presented method.[60,61] Additionally, the inclusion of these effects is associated with the cost of calculating a large number of forces that increases exponentially with the number of monomers and excited states. More precisely, in the extreme case, gradients of potential energy and excitonic coupling in all electronic states of all monomers are required. The approach presented here has the advantage that due to the uncoupled calculation only a single gradient evaluation is required and therefore it scales linear with the number of monomers.

EXCITATION ENERGY TRANSPORT. In order to simulate the excitation energy transport between the chromophoric subunits the FISH approach as presented in Sec.

2.4 is employed. For this purpose the total (time-dependent) multi-chromophoric wave function is expanded in the excitonic basis as defined in Eqn. (5.5):

$$|\Psi_{MC}(t)\rangle = \sum_{ab\ldots z} c_{ab\ldots z}(t)\,|\phi_{ab\ldots z}(t;\boldsymbol{R}(t))\rangle\,, \tag{5.16}$$

with $c_{ab\ldots z}(t)$ being the time-dependent expansion coefficients and the excitonic states being parametrically dependent on the nuclear trajectory $\boldsymbol{R}(t)$. Inserting Eqns. (5.16) and (5.2) into the time-dependent Schrödinger equation (1.1a) yields a set of differential equations for the expansion coefficients $\mathbf{C}=[c_{ab\ldots z}, c_{a'b\ldots z}, \ldots, c_{a'b'\ldots z'}]$:

$$i\hbar\dot{\mathbf{C}}(t) = \boldsymbol{H}_{MC}\boldsymbol{C}(t) - i\hbar\boldsymbol{D}\boldsymbol{C}(t), \tag{5.17}$$

where $\boldsymbol{D}$ is the non-adiabatic coupling matrix, whose elements have the general form:

$$(\boldsymbol{D})_{ab\ldots z,a'b'\ldots z'} = \left\langle \phi_{ab\ldots z} \middle| \frac{\mathrm{d}}{\mathrm{d}t}\phi_{a'b'\ldots z'} \right\rangle. \tag{5.18}$$

In the case that the vibrational modes of the individual monomers are uncoupled the non-adiabatic coupling matrix reduces to:

$$\boldsymbol{D} = \sum_I \boldsymbol{D}_I \otimes \mathbf{1}_I = \sum_I \mathbf{1}_I \otimes \sum_{kk'} \boldsymbol{d}^I_{kk'}(\boldsymbol{R}_I(t)) \cdot \dot{\boldsymbol{R}}_I(t) \tag{5.19}$$

where $\boldsymbol{d}^I_{kk'}$ are the non-adiabatic coupling vectors and $\dot{\boldsymbol{R}}_I$ are the velocities of the nuclei of the Ith monomer. Inserting the MC Hamiltonian (5.12) in Eqn. (5.17) yields the matrix differential equations:

$$\begin{aligned} i\hbar\dot{\mathbf{C}}(t) = &\left[\sum_I \left(\boldsymbol{H}_I - \sum_{kk'}\boldsymbol{\mu}_{kk'}\cdot\boldsymbol{E}(t) - i\hbar\sum_{kk'}\boldsymbol{d}^{(I)}_{kk'}\cdot\dot{\boldsymbol{R}}_I(t)\right)\otimes\mathbf{1}_I\right]\boldsymbol{C}(t) \\ &+ \frac{1}{2}\sum_I\sum_{J\neq I}(\boldsymbol{J}_{IJ}\otimes\mathbf{1}_{IJ})\,\boldsymbol{C}(t), \end{aligned} \tag{5.20}$$

which can be propagated alongside the nuclear trajectory to obtain hopping probabilities allowing the trajectories either to switch between the adiabatic excitonic states due to the coupling to the laser field or due the the inter-chromophoric coupling introduced by the new coupling term $\boldsymbol{J}_{IJ}$.

ENERGY CONSERVATION STRATEGY. In the spirit of FISH (cf. Sec. 2.4) the hopping probability can be defined as given by Eqn. (4.4). However, there are several possibilities for state switches:

1. changing from the ground state to an excited state (e.g. $|\phi_{00\ldots0}\rangle \rightarrow |\phi_{ab\ldots z}\rangle$), most likely due to excitation by the electric field,
2. changing from an excited state to the ground state (e.g. $|\phi_{ab\ldots z}\rangle \rightarrow |\phi_{00\ldots0}\rangle$), due to non-adiabatic relaxation processes, or
3. a switch of the excitation site (e.g. $|\phi_{a'b\ldots z}\rangle \rightarrow |\phi_{ab'\ldots z}\rangle$).

The first two cases are diabatic events within a single monomer (diabatic hop) and describe the excitation and the non-radiative relaxation. The latter case involves state switches in multiple monomers (excitonic hop) and is responsible for energy transport. Depending on the type of state switch, different energy rescaling mechanisms have to be employed.

It is assumed that all energy originating from the laser pulse is absorbed by the molecule. Therefore, no velocity rescaling is performed on the occasion of a state switch while the pulse is active. After the pulse has ceased, only diabatic hops due to non-adiabatic relaxation or excitonic hops due to interchromophoric coupling can occur. In the case of non-adiabatic relaxation processes, the conventional rescaling procedures as presented in Sec. 2.2 can be used. However, the velocity rescaling for excitonic hops that involve two chromophores (or more) can not be straightforwardly done.

In the simplest case, when the respective energy levels of the involved subsystems are exactly in resonance, the energy gained from the deexcitation can be used for the excitation. However, due to the stochastic nature of the surface-hopping approach, hops may occur where the systems are not exactly in resonance. If a combined deexcitation in monomer I and excitation in monomer J occur the energy is redistributed according to the following procedure:

1. The whole deexcitation energy of monomer I is transferred to the monomer J, where it is used for the excitation.

2. Residual deexcitation energy from I is distributed on the both participating monomers.

3. If more energy is required to excite monomer J than available from the deexcitation of monomer I, the required energy is withdrawn from the vibrational kinetic energy of both monomers.

4. The state switch is rejected if the available energy is insufficient.

The rescaling factors are obtained such that the total energy is conserved and that the change of kinetic energy is minimized in both monomers.

2.6 SIMULATION OF TIME-RESOLVED INFRARED SPECTROSCOPY

In the preceding sections the semiclassical representation of light-matter interaction and nuclear motion has been used to simulate excitation processes during the irradiation with light. However, this approach can also be used to obtain spectroscopic observables. In the following a generally applicable approach is presented allowing for the simulation of accurate pump-probe time-resolved infrared (TRIR) spectroscopy from semiclassical molecular dynamics simulations.

The general experimental procedure has been outlined in Sec. 1.3 of the introductory part. Hence, in order to simulate time-resolved pump-probe IR spectra, two interactions with the laser field, separated by the time delay Δt, have to be considered:

1. the interaction with the UV pump laser pulse centered at $t = 0$ which excites or ionizes the system, and
2. the interaction with the probe IR laser pulse centered at the time delay Δt, which gives the resultant spectrum.

In the spirit of the semiclassical treatment of light-matter interaction (cf. Sec. 2.3), the Hamiltonian for a system driven by a laser field $\boldsymbol{E}(t, \Delta t)$ centered at delay time Δt and oscillating with a frequency ω reads:

$$\hat{H} = \hat{H}_0 - \hat{\boldsymbol{\mu}} \cdot \boldsymbol{E}(t; \omega, \Delta t) \tag{6.1}$$

where H_0 is the field-free Hamiltonian operator of the molecular system and $\hat{\boldsymbol{\mu}}$ is the dipole moment operator.

In section 2.1 the partial Wigner representation of quantum mechanics has been introduced in order to obtain the classical equations of motion for nuclei. Here, the Liouville–von-Neumann equation, which replaces the time-dependent Schrödinger equation, has been brought into the adiabatic basis and for the diagonal elements the classical Liouville equation:

$$\dot{\rho}(\boldsymbol{q}, \boldsymbol{p}, t) = \{H(\boldsymbol{q}, \boldsymbol{p}, t), \rho(\boldsymbol{q}, \boldsymbol{p}, t)\} \tag{6.2}$$

has been derived after Wigner transformation of the nuclear degrees of freedom (cf. Sec. 2.1). Hence, the quantum mechanical operators are transformed to classical functions of the canonical variables $\boldsymbol{q}$ and $\boldsymbol{p}$. In trajectory-based approaches the classical phase-space density ρ can be represented by an ensemble of classical trajectories as introduced by Eqn. (1.11) and equivalently to solve Liouville's equation one may solve Hamilton's equations of motion:

$$\dot{\boldsymbol{q}} = \nabla_{\boldsymbol{p}} H = \boldsymbol{M}^{-1} \boldsymbol{p} \tag{6.3a}$$

$$\dot{\boldsymbol{p}} = -\nabla_{\boldsymbol{q}} H = -\nabla_{\boldsymbol{q}} E_k + \nabla_{\boldsymbol{q}} \boldsymbol{\mu} \cdot \boldsymbol{E}(t, \Delta t). \tag{6.3b}$$

The forces acting on the nuclei are $-\nabla_{\boldsymbol{q}} E_k = \boldsymbol{F}_i$ and are obtained as gradients of the electronic potential energy surface E_k, which are solutions of the unperturbed time-independent Schrödinger equation. In the 0th order of perturbation, which can be employed for weak laser fields, the last term of Eqn. (6.3b) can be neglected, and therefore the nuclei can be propagated freely using quantum chemical MD "on the fly" as described previously in section 2.1.

The rate of the energy absorption induced by the interaction with the probe field can be calculated in the phase space representation as

$$\begin{aligned}\frac{\mathrm{d}\langle E\rangle}{\mathrm{d}t} &= \frac{\mathrm{d}}{\mathrm{d}t}\int \mathrm{d}\boldsymbol{p}\int \mathrm{d}\boldsymbol{q}\, H_0(\boldsymbol{q},\boldsymbol{p})\rho(\boldsymbol{q},\boldsymbol{p},t) = \int \mathrm{d}\boldsymbol{p}\int \mathrm{d}\boldsymbol{q}\, H_0(\boldsymbol{q},\boldsymbol{p})\frac{\mathrm{d}\rho}{\mathrm{d}t}(\boldsymbol{q},\boldsymbol{p},t)\\ &= \int \mathrm{d}\boldsymbol{p}\int \mathrm{d}\boldsymbol{q}\, H_0(\boldsymbol{q},\boldsymbol{p})\left\{H(\boldsymbol{q},\boldsymbol{p},t),\rho(\boldsymbol{q},\boldsymbol{p},t)\right\},\end{aligned} \tag{6.4}$$

where in the last step Eqn. (6.2) has been employed. By expanding the Poisson bracket and using partial integration, Eqn. (6.4) can be reduced to

$$\frac{\mathrm{d}\langle E\rangle}{\mathrm{d}t} = \int \mathrm{d}\boldsymbol{p}\int \mathrm{d}\boldsymbol{q}\,\rho(\boldsymbol{q},\boldsymbol{p},t)\frac{\mathrm{d}\boldsymbol{\mu}(\boldsymbol{q})}{\mathrm{d}t}\cdot\boldsymbol{E}(t;\omega,\Delta t), \tag{6.5}$$

The total absorption of energy for a given frequency ω and time delay Δt introduced by the probe laser, which corresponds to the experimental measured transient ps-TRIR spectrum, can be calculated by integrating the rate of energy absorption Eqn. (6.5) over time:

$$\langle\sigma_{probe}(\omega,\Delta t)\rangle = \int_{-\infty}^{\infty}\mathrm{d}t\,\frac{\mathrm{d}\langle E\rangle}{\mathrm{d}t} = \int_{-\infty}^{\infty}\mathrm{d}t\int \mathrm{d}\boldsymbol{p}\mathrm{d}\int \boldsymbol{q}\,\rho(\boldsymbol{q},\boldsymbol{p},t)\frac{\partial\boldsymbol{\mu}(\boldsymbol{q})}{\partial t}\cdot\boldsymbol{E}(t;\omega,\Delta t), \tag{6.6}$$

The phase-space integral can be simplified by introducing the representation of the the phase-space density by nuclear trajectories given by Eqn. (1.11), yielding final expression for the probe signal that can be obtained from the unperturbed molecular dynamics simulations:

$$\langle\sigma_{probe}(\omega,\Delta t)\rangle = \sum_{i}^{N_{traj}}\int_{-\infty}^{\infty}\mathrm{d}t\,\frac{\mathrm{d}\boldsymbol{\mu}(\boldsymbol{q}_i(\boldsymbol{q}_0,\boldsymbol{p}_0,t))}{\mathrm{d}t}\cdot\boldsymbol{E}(t;\omega,\Delta t) \tag{6.7}$$

Note that, if an enveloped (shaped) sinusoidal plane wave is employed for the laser field, this expression can be interpreted as a trajectory average of the windowed Fourier transform of the dipole derivative function of each trajectory, where the probe pulse envelope serves as a window.

Finally, the pump pulse has to be considered too. Although a generally applicable strategy for the simulation of excitation (or ionization) processes has already been presented in the previous sections, which could also have been applied here, the focus of the present work has been on the simulation of the IR signal. Hence, the trajectories have been propagated both in the initial as well as in the target state and an envelope function $P(t)$ has been used that mimics the transient population of the target state. The final pump-probe signal is therefore obtained by convoluting the probe signal σ_{probe} with the rate of population change $\mathrm{d}P/\mathrm{d}t$:

$$\langle\sigma(\omega,\Delta t)\rangle = \int_{-\infty}^{\infty}\mathrm{d}t\,\frac{\mathrm{d}P}{\mathrm{d}t}\langle\sigma(\omega,t-\Delta t)\rangle. \tag{6.8}$$

In the case that a Gaussian pump-pulse envelope is employed $\frac{\mathrm{d}P}{\mathrm{d}t}$ is an error function.

2.7 DISCUSSION

In this thesis, a selection of still not fully disclosed phenomena arising from the interaction of biomolecules with UV light has been investigated. In this context, novel quantum-classical methods for the simulation of light-induced excited state dynamics in complex molecular systems have been developed. The methodological development and the obtained results from molecular dynamics simulations can extend the knowledge about why the biological matter is built exactly the way as it is found on Earth today.

Motivated by the homochiral nature of the building blocks of life and the observation of enantiomerically enriched left-handed amino acids on meteorites and comets, in this work, the field-induced surface-hopping (FISH) approach has been extended. Specifically, the inclusion of higher-order terms in the multipole expansion of the Hamiltonian for the light-matter interaction and the interaction with circularly polarized light allows for the accurate description of chiroptical properties. The developed methodology has been applied to the smallest chiral amino acid, alanine. It has been shown that asymmetric fragmentation in excited electronic states can be induced by circularly polarized light. Although the effects are minor, this finding supports the hypothesis that originally racemic mixtures of chiral biomolecules can be enantiomerically enriched by circularly polarized radiation before their arrival on Earth and then autocatalytically amplified to their present homochiral state. Additionally, the simulations revealed that irradiation with circularly polarized light could cause an asymmetric formation of chiral products from achiral fragments in small amounts. Since enantiomerically pure or at least enriched chiral substances are of great importance for drug development in the pharmaceutical industry, this observation may be utilized to employ circularly polarized shaped laser pulses to achieve controlled and enantioselective synthesis of chiral molecules.

Although the bare building blocks of life also occur in their pristine or chemically modified form in nature (e.g., as neurotransmitters) and are, therefore, interesting subjects of research in their own right, their full capability is revealed if they are building up supramolecular structures and molecular aggregates. The light-induced processes occurring specifically in molecular aggregates were subject to the further development of the quantum-classical methodology. The theoretical treatment of photodynamics in those extended systems is particularly challenging since a direct application of semiclassical molecular dynamics approaches is not possible anymore due to the size of the system. In this context, the multi-chromophoric FISH (McFISH) method has been developed. Here, the system is subdivided into computationally feasible fragments coupled in the frame of an extended Frenkel exciton model. The combination with hybrid quantum mechanical–molecular mechanical (QM/MM) techniques accounts for effects caused by the environment. The approach has been demonstrated by simulating the photodynamics of a model of a double-stranded DNA decamer. The photodynamics in DNA is of particular importance since, in contrast to the bare nucleobases, long-

living excited states are observed. After the initial excitation of delocalized excitonic states, a branching into localized and delocalized excited states is found, which results in a multi-exponential decay of the excited state population. The fast component of the decay can be attributed to the localized states in which conical intersections with the electronic ground-state, resembling those of the bare nucleobases, are reached. The long-living component originates from the formation of delocalized states and charge resonance states counteracting the localization of the excitation on a single base and preventing the deactivation to the ground state. The chosen idealized DNA model, including 12 nucleobases in the quantum-mechanical region, served well for the demonstration of the developed methodology and studying the mechanisms of excitation energy transport and non-radiative relaxation. However, due to the high efficiency of the developed method, larger quantum-mechanical regions could be used, and the dependency of photodynamics on the size of the quantum region could be studied. Moreover, in future works, more realistic DNA models, including natural DNA and unusual DNA structures as found in, e.g., i-motif DNA, could be investigated. The presented method is generally and widely applicable and can serve, e.g., to investigate excitation energy transfer processes occurring in light-harvesting complexes, biological imaging applications in fluorescent proteins, or the study and design of photoactivatable drugs as used in photodynamic therapy.

While the studies mentioned above focused on the light-induced dynamics of the chromophores, the influence on the environment has been considered as well. The interaction of water with biomolecules and the formation of complex hydrogen-bonded networks are important driving forces in biochemical reactions and structural rearrangements. In particular, the structure and function of proteins are intimately connected with the water network dynamics, and the photoexcitation of a solute molecule may trigger a rearrangement of the solvent molecules. A valuable means to probe this type of dynamics is the picosecond time-resolved pump-probe infrared (ps-TRIR) spectroscopy. However, based on experimental data alone, it is difficult to gain an atomistic understanding of the underlying processes. Therefore, a generally applicable method for the simulation of pump-probe TRIR spectra based on molecular dynamics simulations and the Wigner phase-space representation of quantum mechanics has been devised. The developed methodology has been employed to investigate the migration dynamics of a single water molecule around the –CONH– peptide linkage in two peptide analogs serving as models for biological proteins. It has been shown that for both peptide analogs, a water molecule bound initially at the CO site of the peptide linkage is migrating to the NH site after photoionization. The simulated spectra are in excellent agreement with the experimental observations. The simulations have allowed for an atomistic interpretation of the measured time scales, migration pathways, and their fingerprints in the experimental ps-TRIR spectra. In particular, it has been shown that in two studied peptides differing only by a methyl substitution at the peptide linkage, completely different migration dynamics are observed in the

simulations. While for acetanilide, two migration pathways are found, which take a course above the molecular plane, only a single in-plane migration pathway is observed in formanilide. In future work, the presented method could be generalized to obtain other time-resolved spectroscopic observables, such as transient absorption spectra, or to simulate time-resolved Raman spectroscopy. Additionally, in close analogy to the FISH method, this approach could be used to simulate quantum dynamics in the space of selected vibrational modes under the influence of an infrared pulse.

In general, in this work, particular emphasis was put on developing and implementing the above summarized methods. The software that has been written in this context has interfaces to various quantum chemical programs and can make use of numerous high-level quantum chemical methods, such as, e.g., time-dependent linear response density functional theory (TDDFT) and the approximate coupled-cluster singles and doubles (CC2) or algebraic diagrammatic construction (ADC(2)) models. Moreover, it includes an own implementation of molecular mechanical force fields, which allows for the simulation of the photodynamics in extended mixed QM/MM models. The program can be easily extended and is highly configurable. Therefore, the developed methods can be straightforwardly applied to simulate a broad range of light-induced phenomena, thus enabling the comprehensive investigation of photodynamics in complex systems.

BIBLIOGRAPHY

[1]E. Schrödinger, "Quantisierung als Eigenwertproblem," Ann. Phys. **384**, 361–376 (1926).

[2]P. A. M. Dirac, *The principles of quantum mechanics*, International Series of Monographs on Physics (Clarendon Press, 1930).

[3]M. Born and R. Oppenheimer, "Zur Quantentheorie der Moleküle," Ann. Phys. **389**, 457–484 (1927).

[4]M. Born and V. Fock, "Beweis des Adiabatensatzes," Z. Phys. **51**, 165–180 (1928).

[5]J. v. Neumann, *Mathematische Grundlagen der Quantenmechanik*, Vol. 38 (Springer-Verlag, 2013).

[6]E. Wigner, "On the quantum correction for thermodynamic equilibrium," Phys. Rev. **40**, 749–759 (1932).

[7]M. O. S. M. Hillery, R. F. O'Connell, M. O. Scully, and E. P. Wigner, "Distribution functions in physics: fundamentals," Physics reports **106**, 121–167 (1984).

[8]D. Bohm, "A suggested interpretation of the quantum theory in terms of"hidden"variables. I," Phys. Rev. **85**, 166 (1952).

[9]T. R. Nelson, A. J. White, J. A. Bjorgaard, A. E. Sifain, Y. Zhang, et al., "Non-adiabatic excited-state molecular dynamics: theory and applications for modeling photophysics in extended molecular materials," Chem. Rev. **120**, 2215–2287 (2020).

[10]P. Ehrenfest, "Bemerkung über die angenäherte Gültigkeit der klassischen Mechanik innerhalb der Quantenmechanik," Z. Phys. **45**, 455–457 (1927).

[11]J. C. Tully and R. K. Preston, "Trajectory surface hopping approach to nonadiabatic molecular collisions: the reaction of H+ with D_2," J. Chem. Phys. **55**, 562–572 (1971).

[12]J. C. Tully, "Molecular dynamics with electronic transitions," J. Chem. Phys. **93**, 1061–1071 (1990).

[13]N. L. Doltsinis and D. Marx, "First principles molecular dynamics involving excited states and nonadiabatic transitions," J. Theor. Comput. Chem. **1**, 319–349 (2002).

[14]M. F. Herman, "Nonadiabatic semiclassical scattering. I. analysis of generalized surface hopping procedures," J. Chem. Phys. **81**, 754–763 (1984).

[15]M. F. Herman, "Nonadiabatic semiclassical scattering. II. Solution of two-dimensional models and comparison with quantum results," J. Chem. Phys. **81**, 764–774 (1984).

[16]S. Hammes-Schiffer and J. C. Tully, "Proton transfer in solution: molecular dynamics with quantum transitions," J. Chem. Phys. **101**, 4657 (1994).

[17]E. Fabiano, T. W. Keal, and W. Thiel, "Implementation of surface hopping molecular dynamics using semiempirical methods," Chem. Phys. **349**, 334 (2008).

[18]A. W. Jasper, S. N. Stechmann, and D. G. Truhlar, "Fewest-switches with time uncertainty: a modified trajectory surface-hopping algorithm with better accuracy for classically forbidden electronic transitions," J. Chem. Phys. **116**, 5424–5431 (2002).

[19]U. Müller and G. Stock, "Surface-hopping modeling of photoinduced relaxation dynamics on coupled potential-energy surfaces," J. Chem. Phys. **107**, 6230–6245 (1997).

[20]A. V. Akimov and O. V. Prezhdo, "Second-quantized surface hopping," Phys. Rev. Lett. **113**, 153003 (2014).

[21]C. C. Martens, "Nonadiabatic dynamics in the semiclassical liouville representation: locality, transformation theory, and the energy budget," Chem. Phys. **481**, 60–68 (2016).

[22]M. Barbatti, M. Ruckenbauer, and H. Lischka, "The photodynamics of ethylene: a surface-hopping study on structural aspects," J. Chem. Phys. **122**, 174307 (2005).

[23]R. Mitrić, V. Bonačić-Koutecký, J. Pittner, and H. Lischka, "Ab initio nonadiabatic dynamics study of ultrafast radiationless decay over conical intersections illustrated on the na 3 f cluster," J. Chem. Phys. **125**, 024303 (2006).

[24]E. Fabiano and W. Thiel, "Nonradiative deexcitation dynamics of 9h-adenine: an om2 surface hopping study," J. Phys. Chem. A **112**, 6859–6863 (2008).

[25]M. Barbatti and H. Lischka, "Nonadiabatic deactivation of 9H-Adenine: a comprehensive picture based on mixed quantum-Classical dynamics," J. Am. Chem. Soc. **130**, 6831 (2008).

[26]U. Werner, R. Mitrić, T. Suzuki, and V. Bonačić-Koutecký, "Nonadiabatic dynamics within the time dependent density functional theory: ultrafast photodynamics in pyrazine," Chem. Phys. **349**, 319 (2008).

[27]E. Tapavicza, I. Tavernelli, and U. Rothlisberger, "Trajectory surface hopping within linear response time-dependent density-functional theory," Phys. Rev. Lett. **98**, 023001 (2007).

[28]R. Mitrić, U. Werner, and V. Bonačić-Koutecký, "Nonadiabatic dynamics and simulation of time resolved photoelectron spectra within time-dependent density functional theory: ultrafast photoswitching in benzylideneaniline," J. Chem. Phys. **129**, 164118 (2008).

[29]R. Mitrić, U. Werner, M. Wohlgemuth, G. Seifert, and V. Bonačić-Koutecký, "Nonadiabatic dynamics within time-dependent density functional tight binding method," J. Phys. Chem. A **113**, 12700 (2009).

[30]G. Granucci, M. Persico, and A. Toniolo, "Direct semiclassical simulation of photochemical processes with semiempirical wave functions," J. Chem. Phys. **114**, 10608 (2001).

[31]M. Barbatti, G. Granucci, M. Persico, M. Ruckenbauer, M. Vazdar, et al., "The on-the-fly surface-hopping program system newton-x: application to ab initio simulation of the nonadiabatic photodynamics of benchmark systems," J. Photochem. Photobiol. A **190**, 228–240 (2007).

[32]C. Ciminelli, G. Granucci, and M. Persico, "The photoisomerization of a peptidic derivative of azobenzene: a nonadiabatic dynamics simulation of a supramolecular system," Chem. Phys. **349**, 325 (2008).

[33]Z. Lan, Y. Lu, E. Fabiano, and W. Thiel, "QM/MM nonadiabatic decay dynamics of 9h-adenine in aqueous solution," ChemPhysChem **12**, 1989–1998 (2011).

[34]Y. Lu, Z. Lan, and W. Thiel, "Monomeric adenine decay dynamics influenced by the DNA environment," J. Comput. Chem. **33**, 1225–1235 (2012).

[35]B. Heggen, Z. Lan, and W. Thiel, "Nonadiabatic decay dynamics of 9H-guanine in aqueous solution," Phys. Chem. Chem. Phys. **14**, 8137–8146 (2012).

[36]M. Wohlgemuth, R. Mitrić, and V. Bonačić-Koutecký, "Time-dependent density functional theory excited state nonadiabatic dynamics combined with quantum mechanical/molecular mechanical approach: photodynamics of indole in water," J. Chem. Phys. **135**, 054105 (2011).

[37]I. Tavernelli, B. F. E. Curchod, and U. Rothlisberger, "Nonadiabatic molecular dynamics with solvent effects: a LR-TDDFT QM/MM study of ruthenium (II) tris (bipyridine) in water," Chem. Phys. **391**, 101–109 (2011).

[38]C. Lambert, F. Koch, S. F. Völker, A. Schmiedel, M. Holzapfel, et al., "Energy transfer between squaraine polymer sections: from helix to zigzag and all the way back," J. Am. Chem. Soc. **137**, 7851–7861 (2015).

[39]E. Titov, A. Humeniuk, and R. Mitrić, "Exciton localization in excited-state dynamics of a tetracene trimer: a surface hopping LC-TDDFTB study," Phys. Chem. Chem. Phys. **20**, 25995–26007 (2018).

[40]M. Persico and G. Granucci, "An overview of nonadiabatic dynamics simulations methods, with focus on the direct approach versus the fitting of potential energy surfaces," Theor Chem Acc **133**, 1526 (2014).

[41]B. F. E. Curchod and T. J. Martıìnez, "Ab initio nonadiabatic quantum molecular dynamics," Chem. Rev. **118**, 3305–3336 (2018).

[42]R. Mitrić, J. Petersen, and V. Bonačić-Koutecký, "Laser-field-induced surface-hopping method for the simulation and control of ultrafast photodynamics," Phys. Rev. A **79**, 053416 (2009).

[43]C. J. Joachain, N. J. Kylstra, and R. M. Potvliege, *Atoms in intense laser fields* (Cambridge University Press, 2012).

[44]I. V. Hertel and C. P. Schulz, *Atoms, molecules and optical physics 1: atoms and spectroscopy*, Graduate Texts in Physics (Springer Berlin Heidelberg, 2014).

[45]M. Babiker, E. A. Power, and T. Thirunamachandran, "On a generalization of the power–zienau–woolley transformation in quantum electrodynamics and atomic field equations," Proc. Math. Phys. Eng. Sci. **338**, 235–249 (1974).

[46]L. D. Barron and C. G. Gray, "The multipole interaction hamiltonian for time dependent fields," J. Phys. A: Math. Nucl. Gen. **6**, 59 (1973).

[47]D. L. Andrews, "Quantum formulation for nanoscale optical and material chirality: symmetry issues, space and time parity, and observables," J. Opt. **20**, 033003 (2018).

[48]"Reply to "fundamental symmetry aspects of optical activity"," Chem. Phys. Lett. **79**, 395–398 (1981).

[49]C. Cohen-Tannoudji, J. Dupont-Roc, G. Grynberg, and P. Thickstun, *Atom-photon interactions: basic processes and applications*, Physics Textbook (Wiley, 1992).

[50]B. Loll, J. Kern, W. Saenger, A. Zouni, and J. Biesiadka, "Towards complete cofactor arrangement in the 3.0 å resolution structure of photosystem II," Nature **438**, 1040–1044 (2005).

[51]P. G. Lisinetskaya and R. Mitrić, "Simulation of laser-induced coupled electron-nuclear dynamics and time-resolved harmonic spectra in complex systems," Phys. Rev. A **83**, 033408 (2011).

[52]A. Warshel and M. Levitt, "Theoretical studies of enzymic reactions: dielectric, electrostatic and steric stabilization of the carbonium ion in the reaction of lysozyme," J. Mol. Biol. **103**, 227–249 (1976).

[53]H. M. Senn and W. Thiel, "QM/MM methods for biomolecular systems," Angew. Chem. Int. Ed. **48**, 1198–1229 (2009).

[54]E. Brunk and U. Rothlisberger, "Mixed quantum mechanical/molecular mechanical molecular dynamics simulations of biological systems in ground and electronically excited states," Chem. Rev. **115**, 6217–6263 (2015).

[55]H. Lin and D. G. Truhlar, "QM/MM: what have we learned, where are we, and where do we go from here?" Theor Chem Acc **117**, 185 (2007).

[56]T. Förster, "Delocalized excitation and excitation transfer.," in *Modern quantum chemistry, part III. Action of light and organic crystals*, edited by O. Sinanoglu (Academic Press, New York, 1965).

[57]A. Sisto, D. R. Glowacki, and T. J. Martinez, "Ab initio nonadiabatic dynamics of multichromophore complexes: a scalable graphical-processing-unit-accelerated exciton framework," Acc. Chem. Res. **47**, 2857–2866 (2014).

[58]A. Sisto, C. Stross, M. W. van der Kamp, M. O'Connor, S. McIntosh-Smith, et al., "Atomistic non-adiabatic dynamics of the LH2 complex with a GPU-accelerated ab initio exciton model," Phys. Chem. Chem. Phys. **19**, 14924–14936 (2017).

[59]M. F. S. J. Menger, F. Plasser, B. Mennucci, and L. González, "Surface hopping within an exciton picture. an electrostatic embedding scheme," J. Chem. Theory Comput. **14**, 6139–6148 (2018).

[60]B. Bouvier, T. Gustavsson, D. Markovitsi, and P. Millié, "Dipolar coupling between electronic transitions of the DNA bases and its relevance to exciton states in double helices," Chem. Phys. **275**, 75–92 (2002).

[61]B. Bouvier, J.-P. Dognon, R. Lavery, D. Markovitsi, P. Millié, et al., "Influence of conformational dynamics on the exciton states of DNA oligomers," J. Phys. Chem. B **107**, 13512–13522 (2003).

Chapter 3

PHOTOCHEMICAL CHIRAL SYMMETRY BREAKING IN ALANINE

M. Wohlgemuth and R. Mitrić:
"Photochemical chiral symmetry breaking in alanine,"
J. Chem. Phys. A, **120**, 8976–8982 (2016).

http://dx.doi.org/10.1021/acs.jpca.6b07611

THE JOURNAL OF PHYSICAL CHEMISTRY A

Article

pubs.acs.org/JPCA

Photochemical Chiral Symmetry Breaking in Alanine

Matthias Wohlgemuth and Roland Mitrić*

Institute for Physical and Theoretical Chemistry, Julius Maximilians University Würzburg, Emil-Fischer-Str. 42, 97074 Würzburg, Germany

Supporting Information

ABSTRACT: We introduce a general theoretical approach for the simulation of photochemical dynamics under the influence of circularly polarized light to explore the possibility of generating enantiomeric enrichment through polarized-light-selective photochemistry. The method is applied to the simulation of the photolysis of alanine, a prototype chiral amino acid. We show that a systematic enantiomeric enrichment can be obtained depending on the helicity of the circularly polarized light that induces the excited-state photochemistry of alanine. By analyzing the patterns of the photoinduced fragmentation of alanine we find an inducible enantiomeric enrichment up to 1.7%, which is also in good correspondence to the experimental findings. Our method is generally applicable to complex systems and might serve to systematically explore the photochemical origin of homochirality.

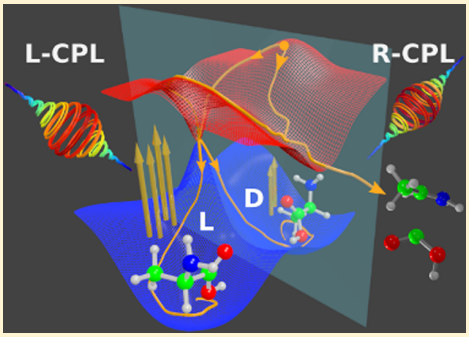

INTRODUCTION

The building blocks of life on Earth, like enzymes and nucleic acids, are composed of homochiral monomers, namely, L-amino acids and D-sugars, and the origin of this symmetry-breaking enantioselectivity of Nature still remains unknown. Since the first investigations of chiral molecules by Pasteur[1] many hypotheses and speculations on the source of symmetry breaking have been proposed. The observation of enantiomeric enrichment (ee) of left-handed meteoric amino acids[2] lead to the proposal that extraterrestrially formed enantiomerically enriched biomolecules were brought to Earth on meteorites and comets and have been subsequently amplified to the present homochiral state. The direct observation of chirality in space is not possible through remote detection. Recently, fascinating space missions have been started to explore the chemical composition of comets. Launched 11 years ago, the Philae lander of the ESA Rosetta space craft has landed in 2014 on the 67P/Churyumov-Gerasimonko (67P/C-G) comet. Among other instruments the lander is equipped with a Cometary Sampling and Composition (COSAC) instrument, which is able to identify, separate, and quantify organic molecules, including enantiomers expected to be found in cometary ices.[3] After its complicated landing on the comet's surface on November 12, 2014 most of the experiments were finished 2 days later. The COSAC module has successfully identified several organic molecules.[4] Unfortunately, because of its disadvantageous final position the Philae lander lost its power, such that not all measured data were transferred to Earth. However, the lander awakened on June 13, 2015 for several days and sent a subset of the 8000 measured data sets, which are partly still under investigation.[5]

The optical activity of chiral molecules is their inherent property that arises as a consequence of the specific interaction of the electric and magnetic dipoles with the electric/magnetic components of the polarized light. Thus, several photochemical mechanisms for generating ee[6−8] were proposed based on the interaction with polarized light that is present in the interstellar space.[9,10] In circularly polarized light (CPL) the electric and the magnetic fields, which are perpendicular to each other, rotate about the axis of the direction of field propagation. The helicity of the rotation determines the handedness of the CPL. The different absorption cross section of left (L-)CPL and right (R-)CPL by chiral molecules is known as circular dichroism (CD) and can lead to the preferential photochemical fragmentation of one of the enantiomers, and thus the remaining substance becomes enriched in the other form.[7,11,12] This makes the exposition of extraterrestrial organic material to CPL on cosmic objects a promising mechanism for ee.

Although ultrashort laser pulses are not particularly relevant in the astrochemical context, employing such pulses in the laboratory for the detection of CD opens new perspectives for the application of time-resolved spectroscopy and optimal control by pulse shaping to chiral molecules. Time-dependent CD (TDCD) spectroscopy has led to mechanistic insights into fundamental photochemical processes.[13,14] Because of the weak CD effect, measuring TDCD is an experimentally challenging task. Rhee et al. presented a vibrational TDCD spectroscopy study employing femtosecond laser pulses.[15] Ultrashort laser pulses were also successfully applied to mass spectrometric measurements for the separation of enantiomers.[16−19]

From the theoretical point of view dynamical CD effects have only been studied in the frame of electron dynamics simulations with fixed nuclei.[20−24] For a two-level chiral model system it has been shown that a state population difference induced upon

Received: July 28, 2016
Revised: October 25, 2016
Published: October 25, 2016

DOI: 10.1021/acs.jpca.6b07611
J. Phys. Chem. A 2016, 120, 8976−8982

excitation by left and right CPL can occur. The origin of CD are the magnetic transition dipole moments, which have the same magnitude but an opposite sign for the two enantiomers. However, the magnetic transition dipole moments are 2 orders of magnitude smaller than their electric counterparts, and the selectivity of excitation depends strongly on the orientation of the electric and magnetic dipole moments to the external laser field.[20,21] Extensive studies on TDCD effects of 3-methylcyclopentanone, employing laser-driven electron dynamics, demonstrated the influence of polarized laser pulses on electronic state populations and ion yields due to multiphoton excitations.[22−24] As yet, all theoretical investigations, however, neglect the influence of the nuclear motion leading to nonadiabatic coupling between the electronic states. The explicit treatment of the nuclear dynamics is essential for the understanding of the photochemical processes in chiral molecules under the influence of CPL. In this context, a particularly attractive approach, which is generally applicable also to complex systems, is based on the semiclassical molecular dynamics "on the fly", in which the nuclear motion is described by classical trajectories, and the electronic structure is calculated using various quantum chemical methods. For the field-free nonadiabatic dynamics a variety of approaches have been devised, the most widely used being Tully's surface-hopping procedure.[25,26] The inclusion of laser pulses into molecular dynamics simulations has been achieved in the framework of our field-induced surface-hopping method (FISH)[27] and successfully applied, for example, for the simulation of light-induced photodynamics, time-resolved photoelectron spectroscopy (TRPES),[28−30] or coherent control,[27,31,32] respectively.

Here we focus on the photodynamics of the amino acid alanine (Ala), which has been subject to numerous experimental studies[11,12,33−38] and of significant interest in theoretical works.[39−43] Our aim is to explore the photochemistry of Ala induced by the interaction with circularly polarized UV light. Ala is the smallest chiral amino acid and thus serves as a prototype system for the investigation of ee under interstellar conditions. To study the photodynamics using polarized laser pulses, we extended our FISH approach[27,28] by the explicit inclusion of the magnetic field, coupled to the molecule via the magnetic transition dipole moments. This methodology is generally applicable to the investigation of the photochemistry of chiral compounds and it includes both electronic and nuclear dynamics at the mixed quantum-classical level.

METHODS SECTION

The simulations are performed by the following steps: First, 3000 initial conditions for an ensemble of trajectories were generated from a 1 ns long trajectory in the electronic ground-state at constant temperature (T = 50 K). The temperature was chosen to mimic the temperature of objects in the Kuiper belt, which is presumed to be the region of origin for many comets.[44] To average over the molecular orientations we rotated each starting geometry $\mathbf{R}_{i,\mathrm{D}}(t = 0) = \mathbf{M}_z(\alpha_i)\mathbf{M}_y(\beta_i)\mathbf{M}_z(\gamma_i)\tilde{\mathbf{R}}_{i,\mathrm{D}}$ as well as the velocities by the uniformly randomized Euler angles $\{0 < \alpha_i < 2\pi\}$, $\{0 < \beta_i < \pi\}$, and $\{0 < \gamma_i < 2\pi\}$, respectively. The L-enantiomer of Ala was obtained by inversion of the atomic coordinates of D-Ala through the center of coordinates, which was chosen to be the chiral carbon atom.

From these initial conditions, we have launched our semiclassical FISH molecular dynamics running for 1.5 ps in the manifold of the lowest 4 excited states and the ground-state. The Newtonian equations of motion for the nuclei are integrated using the velocity Verlet algorithm[45] with a time step of Δt = 0.1 fs, where the gradients on the nuclei are obtained from the multireference configuration interaction OM2 method.[46] Along each trajectory $\mathbf{R}(t)$ the electronic degrees of freedom are propagated by solving the time-dependent Schrödinger equation in the manifold of adiabatic electronic states coupled by the electric field $\mathbf{E}(t)$, by the magnetic field $\mathbf{B}(t)$, and by the nonadiabatic coupling terms $\mathbf{d}_{ij}$:

$$i\hbar\dot{c}_i(t) = E_i(\mathbf{R}(t))c_i(t) - i\hbar\sum_j [\mathbf{d}_{ij}(\mathbf{R}(t))\cdot\dot{\mathbf{R}}(t)]c_j(t) - \sum_j [\boldsymbol{\mu}_{ij}(\mathbf{R}(t))\cdot\mathbf{E}(t) - \mathbf{m}_{ij}(\mathbf{R}(t))\cdot\mathbf{B}(t)]c_j(t) \quad (1)$$

Here, $E_i(\mathbf{R}(t))$ represents the adiabatic energy of the ith electronic state, $\boldsymbol{\mu}_{ij}$ and $\mathbf{m}_{ij}$ are the electric and magnetic transition dipole moments, respectively, and $c_i(t)$ are the expansion coefficients of the electronic wave function. The equation was numerically integrated using the 4th order Runge−Kutta method with a step size of 1×10^{-5} fs.

The electronic state in which the trajectory resides is determined by a stochastic surface-hopping algorithm, using the hopping probabilities calculated from the change of the quantum electronic state populations $\rho_{ii} = c_i^* c_i$ according to

$$P_{i\to j} = \Theta(-\dot{\rho}_{ii})\Theta(\dot{\rho}_{jj})\frac{-\dot{\rho}_{ii}}{\rho_{ii}}\frac{\rho_{jj}}{\sum_k \Theta(\dot{\rho}_{kk})\dot{\rho}_{kk}}\Delta\tau \quad (2)$$

where the Θ functions are defined to be one for positive arguments and zero otherwise. Notice that in eq 1 the shape as well as the polarization of the laser field are not restricted to specific cases. This leads to a variety of possible pulse envelopes and polarizations, including left and right circular or elliptical polarization, allowing us to apply our formalism for many purposes like control of laser-induced processes or the simulation of spectroscopic observables. Also notice that the transition dipole matrix elements $\boldsymbol{\mu}_{ij}$ and $\mathbf{m}_{ij}$ as well as the nonadiabatic coupling term $\mathbf{d}_{ij}$ in eq 1 are parametrically dependent on the nuclear trajectory $\mathbf{R}(t)$ and thus are calculated in each nuclear time step.

Throughout this work, we used CPL where the laser field is propagated in z-direction and has a Gaussian shaped envelope:

$$\mathbf{E}(t) = \mathcal{E}_0\cdot\exp\left(-\frac{(t-t_c)^2}{2\sigma}\right)\mathrm{Re}[(\hat{\mathbf{e}}_x + \hat{\mathbf{e}}_y\exp(i\delta))\exp\times(-i\omega t)] \quad (3)$$

where $\delta = \frac{\pi}{2}$ for L-CPL, $\delta = -\frac{\pi}{2}$ for R-CPL, respectively. The magnetic field is defined perpendicular to the electric field (eq 3):

$$\mathbf{B}(t) = \frac{1}{c}(\hat{\mathbf{e}}_z \times \mathbf{E}(t)) \quad (4)$$

The pulse was chosen to have a full width at half-maximum (FWHM) of 500 fs ($\sigma \approx 212$ fs) and is centered at $t_c \approx 554$ fs, such that the molecule is allowed to relax in the excited state for ~0.5 ps after the pulse has ended. During the pulse ($0 \le t \le$ FWTM ≈ 911 fs, FWTM: full width at tenth of maximum) the energy conservation due to electronic state change is switched off, under the presumption that all energy originating from the

DOI: 10.1021/acs.jpca.6b07611
J. Phys. Chem. A 2016, 120, 8976−8982

laser pulse is absorbed by the molecule. After 911 fs we switch on energy conservation, employing uniform rescaling of the velocities of the nuclei when a state switch occurs according to the energy difference of the electronic states. The field amplitude was chosen $\mathcal{E}_0 = 2\sqrt{2}$ GV/m, to yield a reasonable excitation efficiency to the excited state.

Notice that the inclusion of the coupling of the field to the electric quadruple moment $\mathbf{Q}$, which is in the same order of magnitude as the magnetic dipole coupling, is straightforward by including a third term of the form $\frac{i\omega}{2c}\mathbf{Q}\cdot\hat{\mathbf{e}}_z\cdot\mathbf{E}(t)$ into eq 1. However, analytically the contribution of electric quadrupole coupling vanishes upon rotational averaging,[47] which was employed in this study.

The chirality on the asymmetric carbon atoms is determined with the following algorithm: (1) we assigned the priority of each ligand according to the nuclear charges, (2) the ligand with the lowest priority (hydrogen) is aligned to the z-axis and the molecule is projected on the x−y-plane, and (3) the ligand with the second priority (methyl group) is aligned to the y-axis and the molecule is projected on to the x-axis. Now, if the ligand with the highest priority is on the left of the chiral carbon atom on the x-axis we assigned it to S-type and, otherwise, to the R-type.

RESULTS AND DISCUSSION

We explore the photochemistry of Ala under the influence of circularly polarized light employing the extended version of the FISH method.

Ala has five energetically close-lying conformers[49] in the ground electronic state, which are connected by low energy barriers. To sample the most abundant conformers, we ran a 1 ns long molecular dynamics (MD) simulation of D-Ala in the electronic ground state using the multireference configuration interaction (MR-CI) OM2 method.[46] To obtain statistically reliable ee values in the excited-state dynamics simulations, one must run a large number of trajectories. Thus, we sampled 3000 structures and velocities in regular time intervals from the constant-temperature MD. These structures served as starting points for the simulation of the photochemistry of Ala under the influence of the CPL.

Circular Dichroism Spectroscopy. In Figure 1 we present the UV/vis, electronic CD (ECD), and anisotropy spectra of Ala calculated from the sampled geometries. The oscillator strength $f_i \propto |\boldsymbol{\mu}_{0i}|^2$ in the UV/vis spectrum (Figure 1a) is directly linked to the extinction coefficient $\epsilon = \epsilon_{\mathrm{L-CPL}} + \epsilon_{\mathrm{R-CPL}}$, while the rotatory strength $R_i \propto |\boldsymbol{\mu}_{0i}||\mathbf{m}_{0i}|$ in the ECD spectrum (Figure 1b) is related to the differential extinction coefficient $\Delta\epsilon = \epsilon_{\mathrm{L-CPL}} - \epsilon_{\mathrm{R-CPL}}$. These two quantities can be used to define the anisotropy $g = \Delta\epsilon/\epsilon$ (Figure 1c), which measures the ratio between $\Delta\epsilon$ and ϵ. It has been experimentally shown that the anisotropy allows, together with the extent of the photolysis reaction, ξ, for an estimation of the lower limit for the photochemically inducible ee values: $\mathrm{ee} \geq (1 - (1 - \xi)^{g/2})$.[11,37] The anisotropy factor may be approximated by $g_i \approx 4\frac{R_{0i}}{f_{0i}}$, presuming the shape of the CD and absorption signal are the same and the permittivity is set to 1.[50] As can be seen from Figure 1b,c the ECD and anisotropy spectra differ in their sign for both enantiomers, where the red curves indicate the envelope of the L-Ala spectra, and the blue curve indicates the envelope of the D-Ala spectra.

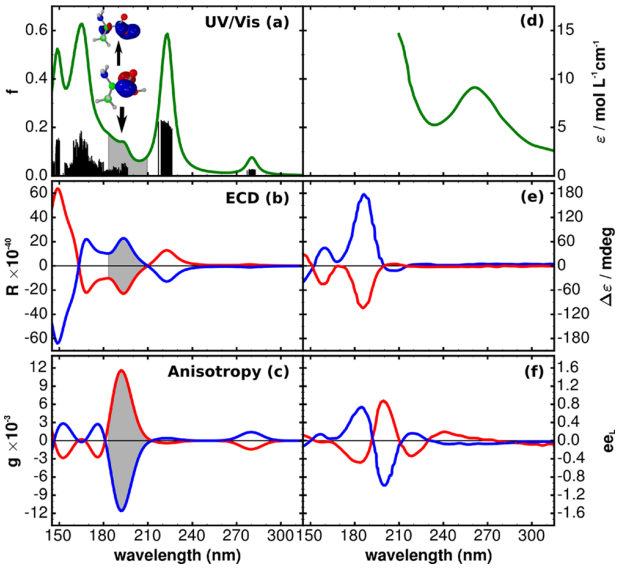

Figure 1. (a) UV/vis, (b) ECD (in cgs units), and (c) anisotropy spectra derived from the 3000 initial structures for the MD simulations. The sticks (shown in (a)) represent the electronic excitation energies and oscillator strength for each geometry in the ensemble of initial conditions. Each stick is convoluted by a Lorentzian with a width of 12 nm. (inset) The dominant contribution to the S_3 electronic excited state, which is of $\pi \rightarrow \pi^*$character. For the ECD (b) and anisotropy (c) spectra the red line indicates the envelope of the spectra L-Ala, and the blue line indicates the envelope for the D-Ala spectra; each is given in cgs units. The shaded area indicates the region of highest anisotropy. The spectra were shifted by 15 nm. Experimental (d) UV/vis spectrum recorded in methanol solution,[48] (e) ECD,[33] and (f) anisotropy spectra obtained from thin films[37] of L- (red line) and D-Ala (blue line). The right scale of the anisotropy spectra gives an estimate for the inducible $\mathrm{ee_L}$ according $\mathrm{ee} \geq (1 - (1 - \xi)^{g/2})$ using an extent of reaction of ξ = 93%.[11,37]

The UV/vis spectrum (Figure 1a) shows two well-separated absorption peaks at ∼270 nm (S_1) and 220 nm (S_2), respectively. While the S_1 state shows only a weak absorption in the UV/vis and ECD spectrum (Figure 1b), the S_2 state has high oscillator and rotatory strengths. In this spirit the S_2 state would be a good choice as a target state for the laser-driven molecular dynamics. However, it bears only a very small intensity in the anisotropy spectrum (Figure 1c). To obtain high population transfer to the excited state as well as high ee values, we therefore chose the S_3 state, located at 190 nm, as the target state, which has a high anisotropy factor compared to the S_2 state. The S_4 state is close to the S_3 state, but it has lower oscillator and rotatory strength. For comparison experimental spectra are given in Figure 1d−f. Note that the calculated spectra in Figure 1 were red-shifted by 15 nm. The UV/vis spectrum (Figure 1d), obtained from Ala in methanol solution,[48] indicates a weak band at ∼250 nm and an intense band below 210 nm. Thus, the energies are red-shifted by ∼20 nm, which can be attributed to the influence of the polar solvent. The experimental ECD spectra of cold Ala films (Figure 1e[33]) have a weak band at 200 nm and two stronger bands at 180 and 158 nm, both with opposite sign compared to the first one. The calculated (Figure 1c) and the experimentally obtained anisotropy spectra (Figure 1f[37]) both exhibit a weak band at ∼200 nm, an intense band at ∼190 nm and a weaker band at 180 nm, each with opposite signs. Note, however, that

DOI: 10.1021/acs.jpca.6b07611
J. Phys. Chem. A 2016, 120, 8976−8982

the experimental values for the ECD and anisotropy spectra were obtained from Ala films, where the zwitterionic form is the predominant isomer,[33] while we investigated the neutral Ala that is the dominant form in the gas phase. The same holds true for the UV/vis spectrum obtained in methanol, however, to our knowledge no absorption spectra of Ala films have been published so far. Although the comparison of the measured and predicted spectra is not straightforward, theoretical investigations using density functional theory find a blue shift from 274 to 268 nm for the S_1 state when switching from the neutral to the zwitterionic form, while the S_2, S_3, and S_4 states are redshifted by 14, 9, and 17 nm, respectively.[51]

Light-Induced Dynamics Simulations. Starting from the 3000 randomly oriented initial conditions for D- and L-Ala, respectively, we ran our FISH molecular dynamics for 1.5 ps in the manifold of four excited states and the ground-state, including the explicit interaction with polarized light. The details of the simulations and the parameters of the laser fields are given in the Methods Section. Two different field polarizations corresponding to R-CPL and L-CPL were employed.

After ~200 fs the S_3 excited state gets populated due to the excitation with the resonant laser pulse. In the course of the dynamics the population is rapidly transferred to lower excited states due to nonradiative relaxation induced by strong nonadiabatic couplings until the first excited state is reached. In the analysis of the trajectories we observe three photochemical processes: (a) up to 93% of the trajectories fragment in the excited state, (b) Ala is completely retained with the initial stereogenic configuration, and (c) the chiral center isomerizes to the opposite enantiomer after fragmentation in the excited state and recombination in the electronic ground-state, where the latter one is a subset of (a).

A representative trajectory for the photolysis of L-Ala illustrating both mechanisms (isomerization and fragmentation) is presented in Figure 2. L-Ala is photoexcited to the S_3 state at 360 fs by L-CPL, where it quickly relaxes through S_2 to the first excited state. In the S_1 state the fragmentation takes place leading to the loss of the COOH group. Subsequently, the crossing of the S_1 and the S_0 state is reached at 440 fs leading to the nonradiative deactivation to the ground electronic state. Here, the hydrogen at the previously chiral center swings through the molecular plane, and COOH recombines to the parent molecule, but this time forming R-Ala. Since the pulse has not ceased yet, the formed R-Ala is photoexcited again at 590 fs and fragments under the loss of COOH from the first excited state.

To investigate the different excitation capabilities of R- and L-CPL for both enantiomers, we computed the electronic-state populations P_L for L-CPL and P_R for R-CPL, respectively, and defined the TDCD as $\mathrm{CD}(t) = 2\frac{P_L - P_R}{P_L + P_R}$.[24] Since the population is rapidly transferred between the excited states, we show the TDCD values for the ground state, reflecting the population difference of all excited states with respect to the ground state. The results are presented in Figure 3 for L-Ala (red curve) and D-Ala (blue curve) as well as for racemic Ala (*rac*-Ala, green curve), which is obtained from the sum of the populations of L- and D-Ala. The CD values can be understood such that if CD is positive R-CPL excites the corresponding enantiomer *more* than L-CPL and vice versa. As expected from the ECD spectra (Figure 1b) the TDCD for L- and D-Ala obtained from MD simulations are opposite in their sign. While the CD values are

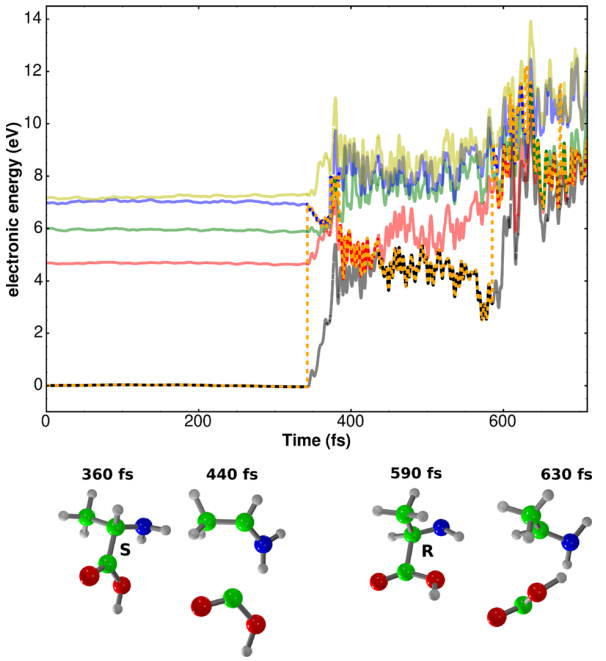

Figure 2. Electronic state energies and snapshots of a representative trajectory of L-Ala irradiated with L-CPL illustrating the fragmentation as well as the recombination to R-Ala. The black, red, green, blue, and yellow lines indicate the energy of the S_0, S_1, S_2, S_3, and S_4 electronic states, respectively. The orange dotted line represents the electronic state in which the trajectory resides at a given time.

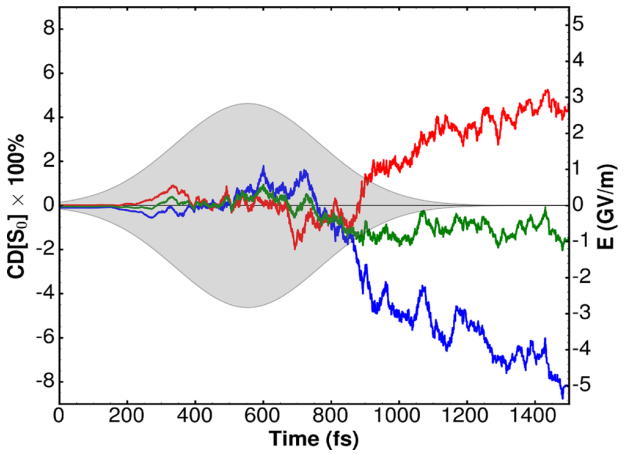

Figure 3. TDCD for the electronic ground state for L-Ala (red curve), D-Ala (blue curve), and *rac*-Ala (green curve). The Gaussian-shaped field envelope $|\mathbf{E}(t)|$ is indicated as gray-shaded area.

close to zero at the beginning and the center of the laser pulse (shown as gray area in Figure 3), they steadily decrease for D-Ala or increase for L-Ala as the pulse intensity decreases until the final population difference is reached with CD = 4.5% for L-Ala and CD = −8.2% for D-Ala, respectively. The observed behavior is not surprising, since at the beginning of the pulse the electronic state population rapidly oscillates between the excited states and the ground ground-state, while at the end of the pulse a steady-state population is reached. As expected, for *rac*-Ala the TDCD always remains close to zero and finally ends with a value of ca. −1.5%. This nonvanishing CD for *rac*-Ala and the not completely stable CD for L/D-Ala at the end of the

DOI: 10.1021/acs.jpca.6b07611
J. Phys. Chem. A 2016, 120, 8976−8982

dynamics might be artificial due to convergence failures upon fragmentation, making the evaluation of the CD values numerically unstable. Nevertheless, the simulation clearly shows the different excitation capabilities of L- and R-CPL to alanine.

Enantiomeric Enrichment. The direct comparison of TDCD to the experiment is not straightforward, since measuring time-dependent electronic state populations is a challenging task, especially for differences no larger than a few percent, and to our knowledge, no such data are available for Ala. Instead, most experiments analyzing the ee values in amino acids use gas chromatography combined with time-of-flight mass spectrometry or chiral photoelectron spectroscopy (PES), where, for example, Ala is ionized with polarized laser pulses.[35,36] Since Ala is a fragile molecule in gas phase and undergoes photolysis reactions, we simulated mass spectra for *rac*-Ala (Figure 4) by approximating the ionization as an instantaneous process. This enables us to directly compare the outcome of our photodynamics simulations to experiments on Ala.

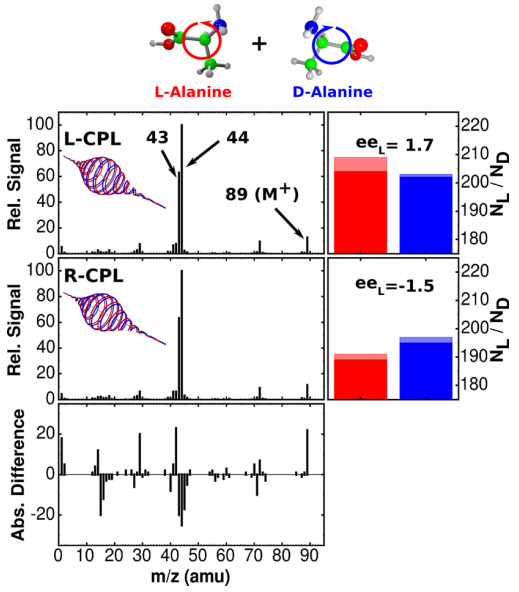

Figure 4. (left) Mass-spectra of *rac*-Ala obtained from MD simulations after irradiation with L-CPL (upper panel) and R-CPL (middle panel), respectively. (right) Number of trajectories having an *S* (red) or R (blue) chiral carbon at the end of the dynamics. The lighter areas indicate the number of trajectories where an inversion due to isomerization of the chiral center has taken place. (lowest) The difference of both mass spectra in absolute units.

For this purpose, we calculated the charge distribution at t = 1.5 ps in the cationic ground state and determined the fragments with a proximity criterion. The obtained Mulliken partial charges were summed over atoms in each fragment, and the fragment with a total charge close to +1 was used to simulate the mass spectra shown in Figure 4. Apart from the parent ion M^+ (m/z = 89) the abundant masses are the m/z = 44 and m/z = 43 fragments. While the 44 fragment results from the loss of COOH by the reaction of $[CH_3CH(NH_2)(COOH)]^+ \rightarrow [CH_3CHNH_2]^+ + COOH$ and is well-described in the literature,[36,52] we also see a significant amount of the 43 fragment, which comes either from the loss of formic acid or from the loss of CO and H_2O, where the charge resides on the remaining $[CH_2CHNH_2]^+$ fragment. However, the simulations show that formic acid or H_2O + CO are always formed after the loss of COOH by transfer of a second hydrogen from $[CH_3CHNH_2]^+$ to COOH, and thus this fragmentation path is a result of the long relaxation time in the excited state. However, in the experiment the charged fragment is rapidly accelerated by the external electric field, and the second hydrogen abstraction is unlikely to happen.

While the fragmentation pattern looks quite similar for L- and R-CPL, the enantiomeric composition of the remaining Ala molecules as well as of fragments containing intact stereogenic centers is different (cf. the difference of the mass spectra in the lower panel of Figure 4). As stated above Ala can either undergo complete fragmentation with the loss of the chiral center or other processes in which an asymmetric carbon atom is retained. The chirality of the fragments was determined and is presented in right panels of Figure 4, giving rise to the ee values induced by the polarized laser pulses, and is calculated according to

$$ee_L = \frac{N_L - N_D}{N_L + N_D} \quad (5)$$

where N_L and N_D are the number of preserved stereogenic centers of L- and D-Ala, respectively. On the one hand, in the case of L-CPL 209 S-type and 202 R-type centers are preserved or formed, giving rise to an ee_L of 1.7%. On the other hand for R-CPL 191 S-type and 197 R-type centers are present at the end of the dynamics simulations inducing an ee_L of −1.5%. These values are lower than the experimentally determined ees, which range up to (4.49 ± 0.14)% for L-CPL and (−4.22 ± 0.21)% for R-CPL, depending on the excitation energy, irradiation time, and the environmental conditions.[11,38] However, the enantioselectivity of the photolysis reaction strongly depends on the reaction rate, and the higher ee values obtained in experiments rely on photolytic yields of 99.97%, achieved with radiation times of several hours,[11] while we can only account for photolysis of up to 93% due to a much shorter pulse duration. Using the empirically found formula for the lower limit for the inducible ee[11,37] with an extent of reaction of ξ = 93% we obtain a lower bound for the inducible ee_L of ∼1.6% for the calculated anisotropy at 190 nm (Figure 1c) and 1.1% for the measured anisotropy spectrum (Figure 1f). Note that due to the high extent of the reaction and the small number of trajectories contributing to the presented ee_L values, there is still an error of ∼0.1%, presuming a Gaussian distribution. As a proof that the effect is mainly due to the interaction with CPL we also present the mass spectrum for the simulations with linear polarized light (LPL) in the Supporting Information, where the fragmentation is still the dominant mechanism, although the fragmentation rate is ∼12% lower than for CPL. Counting the number of trajectories where the stereogenic center is still present, we find an ee of 0.0%, as it is expected.

Finally, we also want to point out that, in several trajectories, the stereogenic center is inverted in the electronically excited state. This is indicated by the light shaded areas in Figure 4. In total seven R→S isomerizations (five with L-CPL and two with R-CPL) and three S→R isomerizations (one with L-CPL and two with R-CPL) have taken place. After photolysis in the excited state, Ala relaxes to the electronic ground state, where the recombination to either the same or opposite enantiomer is possible. This opens also a possibility for the hypothesis that

DOI: 10.1021/acs.jpca.6b07611
J. Phys. Chem. A 2016, 120, 8976−8982

chiral amino acids can be formed under the influence of CPL. However, because of the small amount of trajectories undergoing this inversion, no final conclusion can be made.

The analysis of the influence of the pulse parameters (e.g., pulse length, ellipticity, and intensity) on the enantiomeric enrichment is still an open, but challenging, topic and will be investigated in future work.

CONCLUSIONS

In summary, we have implemented the extension to our FISH method including magnetic field coupling and polarized laser pulses. We have tested and successfully demonstrated our method on the photolysis dynamics of alanine and have shown that circularly polarized light is able to distinguish dynamically on the molecular level between left- and right-handed enantiomers. The photolysis induced by excitation with circularly polarized light leads to nonvanishing enantiomeric enrichment up to ±1.7% of either of the enantiomers, depending on the helicity of the included laser field. Additionally, we have shown that inversion of the chiral center in the excited state induced by circularly polarized light is, in principle, possible. This opens a perspective to enantiomeric enrichment due to photochemistry induced by circularly polarized light and has to be investigated further. Altogether, our findings support the hypothesis that homochirality can be induced by circularly polarized light, which may be responsible for enantiomeric enrichment of chiral molecules on extraterrestrial objects prior to their arrival on Earth.

ASSOCIATED CONTENT

Supporting Information

The Supporting Information is available free of charge on the ACS Publications website at DOI: 10.1021/acs.jpca.6b07611.

Mass spectrum and stereogenic composition of *rac*-Ala irradiated with linear polarized light (PDF)

Movie of a representative trajectory (AVI)

AUTHOR INFORMATION

Corresponding Author

*E-mail: roland.mitric@uni-wuerzburg.de. Phone: +49 (0) 931-31-85135.

Notes

The authors declare no competing financial interest.

ACKNOWLEDGMENTS

Financial support by the European Research Council (ERC) Consolidator Grant "DYNAMO" (Grant No. 646737) is gratefully acknowledged.

REFERENCES

(1) Pasteur, L. Recherches Sur Les Relations Qui Peuvent Exister Entre La Forme Cristalline Et La Composition Chimique, Et Le Sens De La Polarisation Rotatoire. *Ann. Chim. Phys. III* **1848**, *24*, 442−459.

(2) Engel, M.; et al. Distribution and Enantiomeric Composition of Amino Acids in the Murchison Meteorite. *Nature* **1982**, *296*, 837−840.

(3) Gibney, E. Comet Craft Ready to Wake. *Nature* **2014**, *505*, 269−270.

(4) Goesmann, F.; Rosenbauer, H.; Bredehöft, J. H.; Cabane, M.; Ehrenfreund, P.; Gautier, T.; Giri, C.; Krüger, H.; Le Roy, L.; MacDermott, A. J. Organic Compounds on Comet 67P/Churyumov-Gerasimenko Revealed by COSAC Mass Spectrometry. *Science* **2015**, *349*, aab0689.

(5) Fray, N.; Bardyn, A.; Cottin, H.; Altwegg, K.; Baklouti, D.; Briois, C.; Colangeli, L.; Engrand, C.; Fischer, H.; Glasmachers, A. et al. High-Molecular-Weight Organic Matter in the Particles of Comet 67P/Churyumov−Gerasimenko. *Nature* **2016**, DOI: 10.1038/nature19320.

(6) Meinert, C.; de Marcellus, P.; Le Sergeant d'Hendecourt, L.; Nahon, L.; Jones, N. C.; Hoffmann, S. V.; Bredehöft, J. H.; Meierhenrich, U. J. Photochirogenesis: Photochemical Models on the Absolute Asymmetric Formation of Amino Acids in Interstellar Space. *Phys. Life Rev.* **2011**, *8*, 307−330.

(7) Evans, A. C.; Meinert, C.; Giri, C.; Goesmann, F.; Meierhenrich, U. J. Chirality, Photochemistry and the Detection of Amino Acids in Interstellar Ice Analogues and Comets. *Chem. Soc. Rev.* **2012**, *41*, 5447−5458.

(8) Myrgorodska, I.; Meinert, C.; Martins, Z.; Le Sergeant d'Hendecourt, L.; Meierhenrich, U. J. Molecular Chirality in Meteorites and Interstellar Ices, and the Chirality Experiment on Board the ESA Cometary Rosetta Mission. *Angew. Chem., Int. Ed.* **2015**, *54*, 1402−1412.

(9) Bailey, J.; Chrysostomou, A.; Hough, J. H.; Gledhill, T. M.; McCall, A.; Clark, S.; Menard, F.; Tamura, M. Circular Polarization in Starformation Regions: Implications for Biomolecular Homochirality. *Science* **1998**, *281*, 672−674.

(10) Fukue, T.; Tamura, M.; Kandori, R.; Kusakabe, N.; Hough, J. H.; Bailey, J.; Whittet, D. C. B.; Lucas, P. W.; Nakajima, Y.; Hashimoto, J. Extended High Circular Polarization in the Orion Massive Star Forming Region: Implications for the Origin of Homochirality in the Solar System. *Origins Life Evol. Biospheres* **2010**, *40*, 335−346.

(11) Meinert, C.; Cassam-Chenai, P.; Jones, N. C.; Nahon, L.; Hoffmann, S. V.; Meierhenrich, U. J. Anisotropy-Guided Enantiomeric Enhancement in Alanine Using Far-UV Circularly Polarized Light. *Origins Life Evol. Biospheres* **2015**, *45*, 149−161.

(12) Modica, P.; Meinert, C.; de Marcellus, P.; Nahon, L.; Meierhenrich, U. J.; le Sergeant d'Hendecourt, L. Enantiomeric Excesses Induced in Amino Acids by Ultraviolet Circularly Polarized Light Irradiation of Extraterrestrial Ice Analogs: a Possible Source of Asymmetry for Prebiotic Chemistry. *Astrophys. J.* **2014**, *788*, 79.

(13) Dartigalongue, T.; Niezborala, C.; Hache, F. Subpicosecond UV Spectroscopy of Carbonmonoxy-Myoglobin: Absorption and Circular Dichroism Studies. *Phys. Chem. Chem. Phys.* **2007**, *9*, 1611−1615.

(14) Meyer-Ilse, J.; Akimov, D.; Dietzek, B. Ultrafast Circular Dichroism Study of ohe Ring Opening of 7-Dehydrocholesterol. *J. Phys. Chem. Lett.* **2012**, *3*, 182−185.

(15) Rhee, H.; June, Y.-G.; Lee, J.-S.; Lee, K.; Ha, J.-H.; Kim, Z. H.; Jeon, S.-J.; Cho, M. Femtosecond Characterization of Vibrational Optical Activity of Chiral Molecules. *Nature* **2009**, *458*, 310−313.

(16) Boesl von Grafenstein, U.; Bornschlegl, A. Circular Dichroism Laser Mass Spectrometry: Differentiation of 3-Methylcyclopentanone Enantiomers. *ChemPhysChem* **2006**, *7*, 2085−2087.

(17) Li, R.; Sullivan, R.; Al-Basheer, W.; Pagni, R. M.; Compton, R. N. Linear and Nonlinear Circular Dichrosim of R-(+)-3-Methyl-cyclopentanone. *J. Chem. Phys.* **2006**, *125*, 144304.

(18) Bornschlegl, A.; Logé, C.; Boesl, U. Investigation of CD Effects in the Multi Photon Ionisation of R-(+)-3Methylcyclopentanone. *Chem. Phys. Lett.* **2007**, *447*, 187.

(19) Breunig, H. G.; Urbasch, G.; Horsch, P.; Cordes, J.; Koert, U.; Weitzel, K.-M. Circular Dichroism in Ion Yields of Femtosecond-laser Mass Spectrometry. *ChemPhysChem* **2009**, *10*, 1199.

(20) Ma, Y.; Salam, A. On Chiral Selectivity of Enantiomers Using a Circular Polarized Pulsed Laser Under Resonant and Off-resonant Conditions. *Chem. Phys.* **2006**, *324*, 367.

(21) Ma, Y.; Salam, A. Controlling State Population of Enantiomers of Real Chiral Molecules by Using a Circular Polarized Pulsed Laser. *Chem. Phys. Lett.* **2006**, *431*, 247.

(22) Kröner, D. Chiral Distinction by Ultrashort Laser Pulses: Electron Wavepacket Dynamics Incorporating Magnetic Interactions. *J. Phys. Chem. A* **2011**, *115*, 14510−14518.

(23) Kröner, D.; Gaebel, T. Circular Dichroism in Mass Spectrometry: Quantum Chemical Investigations for the Differences

DOI: 10.1021/acs.jpca.6b07611
J. Phys. Chem. A 2016, 120, 8976−8982

Between (R)-3-Methylcyclopentanone and Its Cation. *J. Phys. Chem. A* **2015**, *119*, 9167−9177.
(24) Kröner, D. Laser-driven Electron Dynamics for Circular Dichroism in Mass Spectrometry: From Onephoton Excitations to Multiphoton Ionization. *Phys. Chem. Chem. Phys.* **2015**, *17*, 19643−19655.
(25) Tully, J. C. Molecular Dynamics with Electronic Transitions. *J. Chem. Phys.* **1990**, *93*, 1061.
(26) Hammes-Schiffer, S.; Tully, J. C. Proton Transfer in Solution: Molecular Dynamics with Quantum Transitions. *J. Chem. Phys.* **1994**, *101*, 4657.
(27) Mitrić, R.; Petersen, J.; Bonačić-Koutecký, V. Laser-field-induced Surface-Hopping Method for the Simulation and Control of Ultrafast Photodynamics. *Phys. Rev. A: At., Mol., Opt. Phys.* **2009**, *79*, 053416.
(28) Mitrić, R.; Petersen, J.; Wohlgemuth, M.; Werner, U.; Bonačić-Koutecký, V.; Wöste, L.; Jortner, J. Time-resolved Femtosecond Photoelectron Spectroscopy by Field-induced Surface Hopping. *J. Phys. Chem. A* **2011**, *115*, 3755−3765.
(29) Mitrić, R.; Petersen, J.; Wohlgemuth, M.; Werner, U.; Bonačić-Koutecký, V. Field-induced Surface Hopping Method for Probing Transition State Nonadiabatic Dynamics of Ag(3). *Phys. Chem. Chem. Phys.* **2011**, *13*, 8690−8696.
(30) Stanzel, J.; Neeb, M.; Eberhardt, W.; Lisinetskaya, P. G.; Petersen, J.; Mitrić, R. Switching from Molecular to Bulklike Dynamics in Electronic Relaxation of a Small Gold Cluster. *Phys. Rev. A: At., Mol., Opt. Phys.* **2012**, *85*, 013201.
(31) Lisinetskaya, P. G.; Mitrić, R. Simulation of Laser-induced Coupled Electron-nuclear Dynamics and Time-resolved Harmonic Spectra in Complex Systems. *Phys. Rev. A: At., Mol., Opt. Phys.* **2011**, *83*, 033408.
(32) Petersen, J.; Wohlgemuth, M.; Sellner, B.; Bonačić-Koutecký, V.; Lischka, H.; Mitrić, R. Laser Pulse Trains for Controlling Excited State Dynamics of Adenine in Water. *Phys. Chem. Chem. Phys.* **2012**, *14*, 4687−4694.
(33) Meierhenrich, U. J.; Filippi, J.-J.; Meinert, C.; Bredehoeft, J. H.; Takahashi, J.; Nahon, L.; Jones, N. C.; Hoffmann, S. V. Circular Dichroism of Amino Acids in the Vacuum-Ultraviolet Region. *Angew. Chem., Int. Ed.* **2010**, *49*, 7799−7802.
(34) Powis, I.; Rennie, E.; Hergenhahn, U.; Kugeler, O.; Bussy-Socrate, R. Investigation of the Gas-phase Amino Acid Alanine by Synchrotron Radiation Photoelectron Spectroscopy. *J. Phys. Chem. A* **2003**, *107*, 25−34.
(35) Tia, M.; Cunha de Miranda, B.; Daly, S.; Gaie-Levrel, F.; Garcia, G. A.; Powis, I.; Nahon, L. Chiral Asymmetry in the Photoionization of Gas-Phase Amino-acid Alanine at Lyman-alpha Radiation Wavelength. *J. Phys. Chem. Lett.* **2013**, *4*, 2698−2704.
(36) Tia, M.; Cunha de Miranda, B.; Daly, S.; Gaie-Levrel, F.; Garcia, G. A.; Nahon, L.; Powis, I. VUV Photodynamics and Chiral Asymmetry in the Photoionization of Gas Phase Alanine Enantiomers. *J. Phys. Chem. A* **2014**, *118*, 2765−2779.
(37) Meinert, C.; Bredehoeft, J. H.; Filippi, J.-J.; Baraud, Y.; Nahon, L.; Wien, F.; Jones, N. C.; Hoffmann, S. V.; Meierhenrich, U. J. Anisotropy Spectra of Amino Acids. *Angew. Chem., Int. Ed.* **2012**, *51*, 4484−4487.
(38) Meinert, C.; Hoffmann, S. V.; Cassam-Chenai, P.; Evans, A. C.; Giri, C.; Nahon, L.; Meierhenrich, U. J. Photonenergy-Controlled Symmetry Breaking with Circularly Polarized Light. *Angew. Chem., Int. Ed.* **2014**, *53*, 210−214.
(39) Powis, I. Photoelectron Circular Dichroism of the Randomly Oriented Chiral Molecules Glyceraldehyde and Lactic Acid. *J. Chem. Phys.* **2000**, *112*, 301.
(40) Fukuyama, T.; Matsuo, K.; Gekko, K. Vacuum-Ultraviolet Electronic Circular Dichroism of L-Alanine in Aqueous Solution Investigated by Time-dependent Density Functional Theory. *J. Phys. Chem. A* **2005**, *109*, 6928−6933.
(41) Osted, A.; Kongsted, J.; Mikkelsen, K. V.; Christiansen, O. The Electronic Spectrum of the Micro-Solvated Alanine Zwitterion Calculated Using the Combined Coupled Cluster/Molecular Mechanics Method. *Chem. Phys. Lett.* **2006**, *429*, 430−435.
(42) Jaeger, H. M.; Schaefer, H. F.; Demaison, J.; Csaszar, A. G.; Allen, W. D. Lowest-Lying Conformers of Alanine: Pushing Theory to Ascertain Precise Energetics and Semiexperimental Re Structures. *J. Chem. Theory Comput.* **2010**, *6*, 3066−3078.
(43) Farrokhpour, H.; Fathi, F.; De Brito, A. N. Theoretical and Experimental Study of Valence Photoelectron Spectrum of D,L-Alanine Amino Acid. *J. Phys. Chem. A* **2012**, *116*, 7004−7015.
(44) Jewitt, D. C.; Luu, J. Crystalline Water Ice on the Kuiper Belt Object (50000) Quaoar. *Nature* **2004**, *432*, 731−733.
(45) Swope, W. C.; Andersen, H. C.; Berens, P. H.; Wilson, K. R. A Computer Simulation Method for the Calculation of Equilibrium Constants for the Formation of Physical Clusters of Molecules: Application to Small Water Clusters. *J. Chem. Phys.* **1982**, *76*, 637.
(46) Koslowski, A.; Beck, M. E.; Thiel, W. Implementation of a General Multireference Configuration Interaction Procedure with Analytic Gradients in a Semiempirical Context Using the Graphical Unitary Group Approach. *J. Comput. Chem.* **2003**, *24*, 714−726.
(47) Meath, W. J.; Power, E. A. On the Interaction of Elliptically Polarized Light with Molecules; the Effects of Both Permanent and Transition Multipole Moments on Multiphoton Absorption and Chiroptical Effects. *J. Mod. Opt.* **1989**, *36*, 977−1002.
(48) Abu-Eittah, R.; Obaid, A.; Basahl, S.; Diefallah, E. Molecular Orbital Treatment of Some Amino Acids. *Bull. Chem. Soc. Jpn.* **1988**, *61*, 2609−2613.
(49) Blanco, S.; Lesarri, A.; Lopez, J.; Alonso, J. L. The Gas-phase Structure of Alanine. *J. Am. Chem. Soc.* **2004**, *126*, 11675−11683.
(50) Schellman, J. Circular-dicroism and Optical-Rotation. *Chem. Rev.* **1975**, *75*, 323−331.
(51) Kumar, S.; Kumar Rai, A.; Rai, S. B.; Rai, D. K.; Singh, A.; Singh, V. Infrared, Raman and Electronic Spectra of Alanine: a Comparison with Ab Intio Calculation. *J. Mol. Struct.* **2006**, *791*, 23−29.
(52) Jochims, H.-W.; Schwell, M.; Chotin, J.-L.; Clemino, M.; Dulieu, F.; Baumgärtel, H.; Leach, S. Photoion Mass Spectrometry of Five Amino Acids in the 6−22 eV Photon Energy Range. *Chem. Phys.* **2004**, *298*, 279−297.

DOI: 10.1021/acs.jpca.6b07611
J. Phys. Chem. A 2016, 120, 8976−8982

Photochemical Chiral Symmetry Breaking in Alanine

Matthias Wohlgemuth and Roland Mitrić*

Institute for Physical and Theoretical Chemistry, Julius-Maximilians-University Würzburg, Emil-Fischer-Str. 42, 97074 Würzburg, Germany.

E-mail: roland.mitric@uni-wuerzburg.de

Supplementary Information

1. We attach a movie of a representative trajectory, which is also described in the main text. The movie shows first the fragmentation of *L*-Ala due to the excitation by *L*-CPL in the first excited state, followed by a recombination to *R*-Ala in the electronic ground-state. The laser pulse reexcites R-Ala leading to the loss of COOH.

2. For the proof that the difference in enantiomeric enrichment is due to the helicity of the polarized light, we also show the mass spectrum and stereogenic composition of *rac*-Ala irradiated with linear polarized light (LPL, $\delta = \pi$). As can be seen from Fig. S1 the enantiomeric excess of is exactly zero.

*To whom correspondence should be addressed

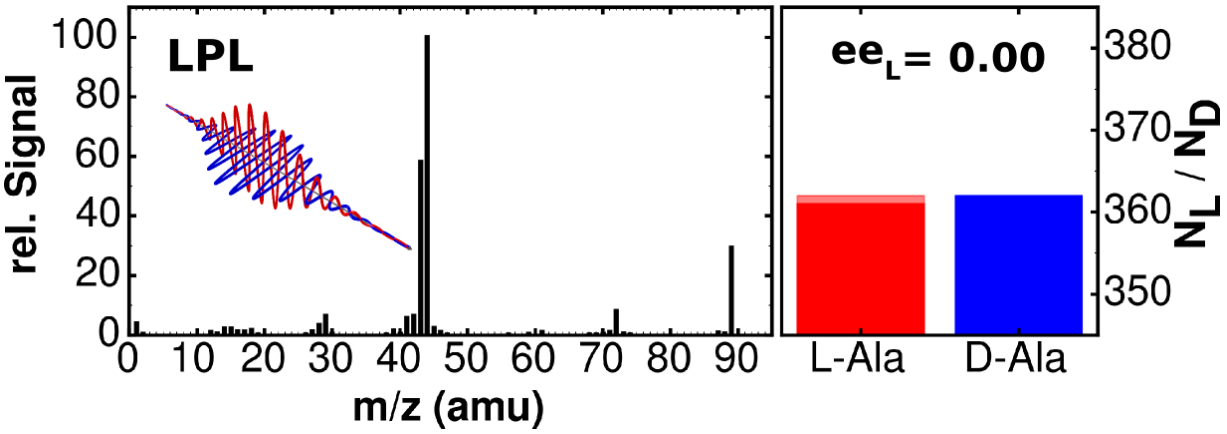

Figure S1: On the left: Mass-spectra of *rac*-Ala obtained from MD simulations after irradiation with LPL at the end of the MD simulations. On the right: Number of trajectories having an S (red) or R (blue) chiral carbon at the end of the dynamics. The lighter areas indicate the number of trajectories where an inversion due to isomerization of the chiral center has taken place.

Chapter 4

EXCITATION ENERGY TRANSPORT IN DNA MODELLED BY MULTI- CHROMOPHORIC FIELD-INDUCED SURFACE-HOPPING

Reproduced with permission from:

M. Wohlgemuth and R. Mitrić:
"Excitation energy transport in DNA modelled by multi-chromophoric field-induced surface hopping,"
Phys. Chem. Chem. Phys., **22**, 16536–16551 (2020).

http://dx.doi.org/10.1039/D0CP02255A

Volume 22
Number 29
7 August 2020
Pages 16435–17012

PCCP

Physical Chemistry Chemical Physics

rsc.li/pccp

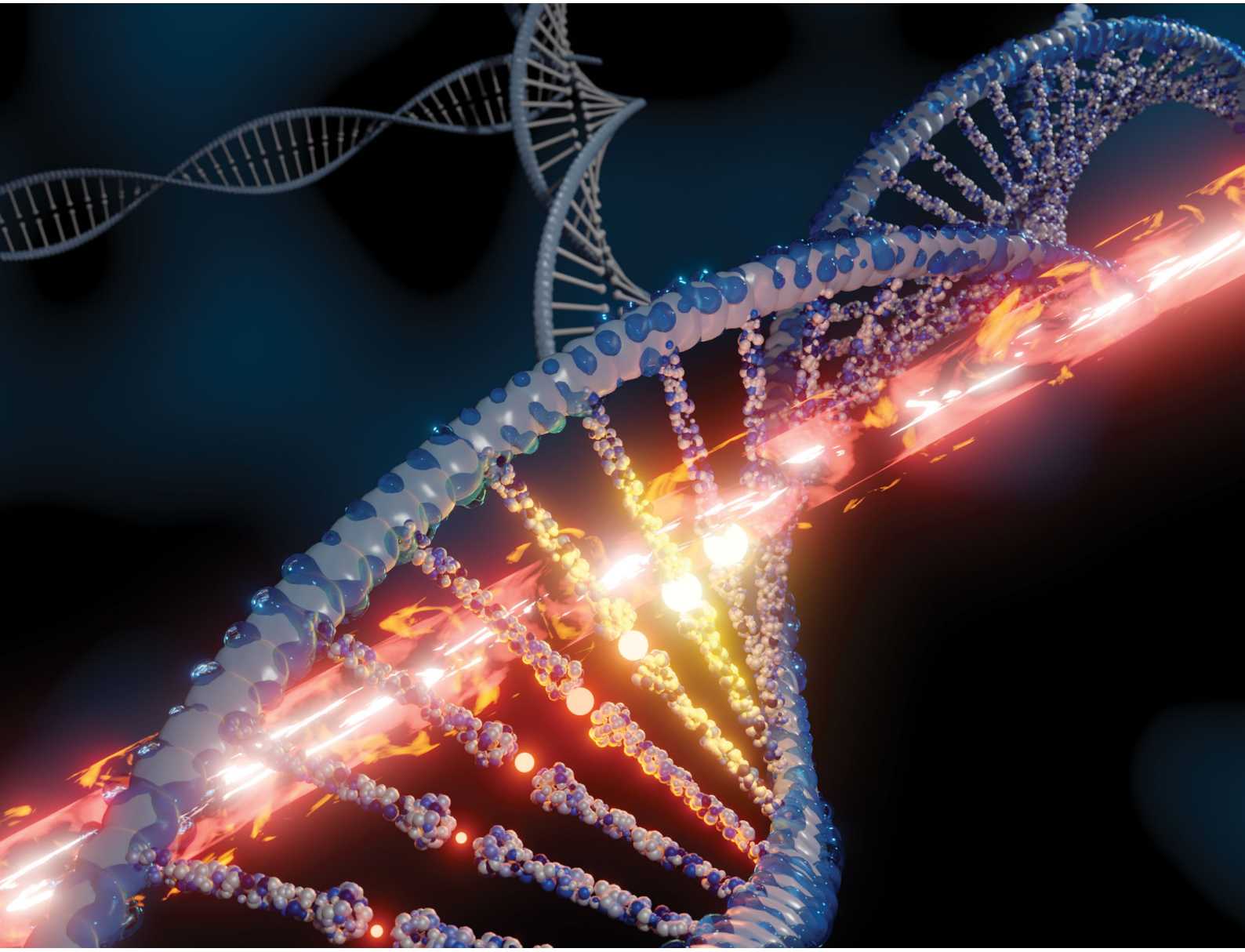

ISSN 1463-9076

ROYAL SOCIETY OF CHEMISTRY

PAPER

Matthias Wohlgemuth and Roland Mitrić
Excitation energy transport in DNA modelled by multi-chromophoric field-induced surface hopping

PCCP

ROYAL SOCIETY OF CHEMISTRY

PAPER

View Article Online
View Journal | View Issue

Cite this: *Phys. Chem. Chem. Phys.*, 2020, **22**, 16536

Excitation energy transport in DNA modelled by multi-chromophoric field-induced surface hopping†

Matthias Wohlgemuth and Roland Mitrić *

Received 27th April 2020,
Accepted 3rd June 2020

DOI: 10.1039/d0cp02255a

rsc.li/pccp

Absorption of ultraviolet light is known as a major source of carcinogenic mutations of DNA. The underlying processes of excitation energy dissipation are yet not fully understood. In this work we provide a new and generally applicable route for studying the excitation energy transport in multi-chromophoric complexes at an atomistic level. The surface-hopping approach in the frame of the extended Frenkel exciton model combined with QM/MM techniques allowed us to simulate the photodynamics of the alternating $(dAdT)_{10}$:$(dAdT)_{10}$ double-stranded DNA. In accordance with recent experiments, we find that the excited state decay is multiexponential, involving a long and a short component which are due to two distinct mechanisms: formation of long-lived delocalized excitonic and charge transfer states *vs.* ultrafast decaying localized states resembling those of the bare nucleobases. Our simulations explain all stages of the ultrafast photodynamics including initial photoexcitation, dynamical evolution out of the Franck–Condon region, excimer formation and nonradiative relaxation to the ground state.

1 Introduction

The fact that UV radiation can trigger carcinogenic mutations in DNA due to the absorption of light has been well established for a long time.[1–3] Understanding DNA excited-state dynamics is thus essential for determining how photolesions are formed. Therefore, the excited states and their relaxation in the monomeric nucleobases as well as in DNA oligo- and polymers have been subject to numerous experimental and theoretical studies in the past decades.[4–7] While the excited state lifetime of the monomeric nucleobases is remarkably short (<1 ps), the deactivation in nucleobase multimers, despite the additional degrees of freedom, takes place on the timescale from 10 to several 100 ps.[8–12] Excitonic[5,8–10,13–18] and delocalized charge transfer (CT)[5,6,10,12,19] states have been made responsible for this difference and the role of these states has been discussed extensively on the basis of experimental and theoretical[14,20–29] work. The processes taking place in the UV excited DNA are until now not fully understood and this topic is at the very frontier of the current research.[15]

Crespo-Hernández *et al.* found that the transient absorption signals, which they associated with intra-strand excimers, decay with time constants of 150 ps for the homopolymeric adenine–thymine (AT) double-stranded DNA (dsDNA) and 51 ps for the alternating AT dsDNA.[12] Transient absorption spectra for similar duplexes were reported and the fingerprint of exciton states was detected.[30] Fluorescence anisotropy data obtained for various dsDNA revealed that ultrafast (<100 fs) energy transfer is made possible in these systems after the population of Franck–Condon exciton states.[8,31,32] Fluorescence from excited states emitting at longer wavelengths than those of the monomeric chromophores has been found for homopolymeric guanine–cytosine (GC) double-stranded DNA[32] and alternating AT duplexes.[9,16] Many of those experiments suggest that fast monomeric deactivation channels as well as long-living exciton states coexist and the observed multiexponential decays are results of this.[16]

From the theoretical point of view, highly correlated *ab initio* methods have been employed to simulate absorption spectra in the Franck–Condon (FC) region *e.g.* by Nogueira *et al.* for alternating AT tetramers[26] and Spata *et al.*[22] for stacked nucleobase trimers of different composition. They used a QM/MM approach where the quantum region was treated with the *ab initio* ADC(2) method for the excited states and included up to four stacked bases in the quantum region. They concluded that delocalization does not occur over more than two bases, while CT states are located at higher energies than the bright states in the FC region. Coupling between locally excited and CT states was also predicted.[23,24] Dinucleotides in the gas phase and in solution were also studied by Plasser *et al.*, and it was found that excitonic states exist with remarkably short intermolecular separation and with CT character.[25] Calculations on adenine tetramers including backbone and solvent suggested that the

Institut für Physikalische und Theoretische Chemie, Julius-Maximilians-Universität Würzburg, Emil-Fischer-Str. 42, 97074 Würzburg, Germany.
E-mail: roland.mitric@uni-wuerzburg.de

† Electronic supplementary information (ESI) available. See DOI: 10.1039/d0cp02255a

excited state dynamics of stacked homopolymeric bases is modulated by the interplay of bright monomeric excited states, $\pi\pi^*$ excitonic, and CT states.[33]

A recent study of the potential energy surface at QM(CASPT2//CASSCF)/MM level, having a stacked thymine dimer in the QM region, suggests that an ultrafast intrabase $\pi\pi^* \rightarrow S_0$ transition reached by three different pathways is responsible for the short component observed in time-resolved experiments.[20] A fourth decay channel was found as well, which is however blocked by a 0.5 eV barrier arising due to a stabilizing inter-base excitonic state. Similarly, Szabia *et al.* recently reported in a QM/MM study a UV-induced repair mechanism for cyclobutane pyrimidine dimers (CpDs) formed by thymine dimerization.[34] There are also several QM/MM studies combined with ground-state molecular dynamics (MD) simulations using accurate *ab initio* and semiempirical methods.[21,24,35]

However, these MD studies focus on the geometries close to the FC region, and thus on the photochemistry in the early stages of the excitation only. An explicit treatment of nonadiabatic dynamics was addressed by Martinez and co-workers by combining an exciton model with Tully's fewest switching algorithm[36] in the frame of time-dependent density functional theory to study the excitation energy transport in the light-harvesting complex II.[37,38] In this model the chromophores are coupled by coulombic dipole–dipole interaction and the electronic wave function is represented in the basis of excitonic eigenstates obtained from the product basis of ground- and singly-excited adiabatic wave functions of the individual chromophores. Recently, this approach was extended by Gonzalez and co-workers by introducing an QM/MM-like electrostatic embedding scheme,[39] which allows for the simulation of chemically bonded chromophores as well. Both methods, however, are lacking the explicit inclusion of the irradiating laser pulse and the excited state dynamics are usually initiated by setting one of the monomers into the excited state close to the absorption band.

In the present work, we combine QM/MM techniques with a state-of-the-art field-induced surface-hopping approach[40,41] in the frame of an extended exciton model, allowing us to investigate the excitation energy transport and non-radiative relaxation including all degrees of freedom. As a model we have chosen the double-stranded B-DNA of 20 alternating Desoxyadenosines (dA) and Desoxythymidines (dT) per strand, where the central 6 base pairs are included in the QM region. This is, to the best of our knowledge, the largest DNA model considered in a QM/MM MD study so far and further the first application to the real-time photodynamics of dsDNA. The chosen model allows us to investigate both intra-strand processes due to π-stacking as well as inter-strand ones like coupled proton/electron transfer. With our simulations we wish to shed more light on the photochemical processes taking place in the first picoseconds after excitation of DNA and present a versatile general tool for simulating excitation energy transport processes in multi-chromophoric complexes.

The presented method is generally and widely applicable and can serve *e.g.* for the investigation of excitation energy transfer processes occurring in light-harvesting complexes,[42–44] biological imaging applications in fluorescent proteins[45–47] or the study and design of photoactivatable drugs as used in photodynamic therapy (PDT).[48–51]

2 Multi-chromophoric field-induced surface hopping (McFISH)

In the following we describe the theoretical formulation of our multi-chromophoric field-induced surface hopping (McFISH) method, which is employed here to simulate the excitation energy transport (EET) and non-radiative relaxation in a DNA double-strand. In the present work, we follow a hybrid multi-quantum classical QM/MM approach, where multiple subsets of nucleobases (*e.g.* a stacked base pair) are described fully quantum mechanically (QM), and the backbone, solvating water molecules, ions as well as the other nucleobases are described by a classical force field (MM). In this way, all electronic states within the stacked pair containing four bases are treated fully quantum-mechanically, which automatically provides the correct description of both local excited as well as charge transfer states. Each of these QM subsystem is individually electrostatically embedded into the environment composed of all other QM subsystems and the MM system by including the atomic point charges into the one-particle Hamiltonian. The exact partitioning of the system is presented in Fig. 1.

In following, we summarize the theoretical approach using the following notation: $\mathbf{R}$ denote spatial positions of the nuclei and $\mathbf{r}$ spatial electron coordinates. Capital indices I and J denote the subsystems, such that $\mathbf{R}_I$ denotes the subset of nuclear coordinates of in subsystem I. Small indices a, $b\ldots$ denote excitations within a single chromophoric subunit.

QM/MM exciton model

As in the conventional hybrid quantum/molecular mechanics (QM/MM) approach[52–54] the total energy of the system is obtained as:

$$E = \langle \Psi_{\mathrm{MC}} | \mathbf{H}_{\mathrm{MC}} | \Psi_{\mathrm{MC}} \rangle + E_{\mathrm{MM}}(\mathbf{R}_{\mathrm{MM}}) + E_{\mathrm{QM/MM}}(\mathbf{R}_1,\ldots,\mathbf{R}_N,\mathbf{R}_{\mathrm{MM}}) \quad (1)$$

where the first term is the QM energy of the multi-chromophoric complex (MC), the second term is the classical force field energy of the MM region and the third term is the interaction between the chromophoric complex and the MM system, respectively. In the electrostatic embedding scheme[53] used here the Coulombic interaction of the QM and MM system is included in $\mathbf{H}_{\mathrm{MC}}$ as a one-electron operator and $E_{\mathrm{QM/MM}}$ reduces to the van der Waals interaction and the classical bonding interaction at the boundary of QM and MM system only.

We consider the MC to be built from N building blocks, which we will further refer as subunits, subsystems or monomers. In the exciton model the electronic Hamiltonian $\mathbf{H}_{\mathrm{MC}}$ of such a chromophoric complex irradiated by an external laser field can be composed from the monomeric Hamiltonian of each subsystem

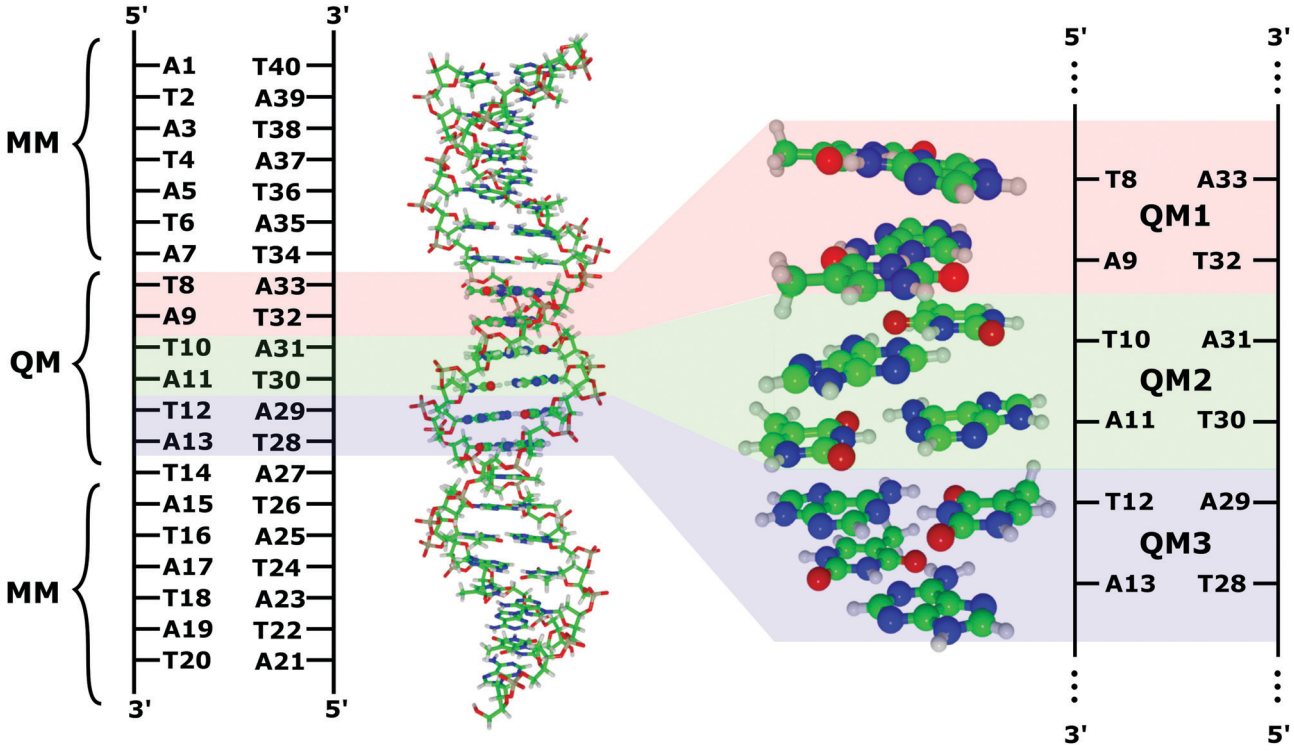

Fig. 1 Partitioning of the $(dAdT)_{10}$:$(dAdT)_{10}$ double-strand DNA-helix (environment of water and ions not shown). Left: Schematic and 3-dimensional structure of the whole system containing the 20 alternating dA:dT base pairs. The system is first divided into a QM part, containing 6 A:T base pairs, which is treated at the semiempirical OM2/MR-CI level and an MM part, consisting of the residual backbone, nucleobases, water and ions, respectively. Right: The 6 base pairs treated quantum mechanically. The red, green and blue areas indicate the partitioning into the 3 subsystems, where each is computed separately and is embedded into the charge field of all surrounding structures.

$\mathbf{H}_I(\equiv \mathbf{H}(\mathbf{r}_I,\mathbf{R}_I))$, the pairwise interaction $\mathbf{V}_{IJ}$[55] and the interaction with the laser field $\mathbf{V}^{\text{ext}}$:

$$\mathbf{H}_{\text{MC}} = \sum_I \mathbf{H}_I \otimes \mathbf{1}_I + \frac{1}{2}\sum_I \sum_{J\neq I} \mathbf{V}_{IJ} \otimes \mathbf{1}_{IJ} + \sum_I \mathbf{V}_I^{\text{ext}}(t) \otimes \mathbf{1}_I, \tag{2}$$

where $\mathbf{1}_I$ and $\mathbf{1}_{IJ}$ are identity operators acting on the electrons of all monomers, except the I-th or the I-th and J-th, respectively.

In eqn (2) the first two terms are time-independent and are completely determined by the structure of the individual monomers. Therefore the natural basis for solving the time-dependent Schrödinger equation (TDSE) with the Hamiltonian (eqn (2)) is the basis spanned by the eigenstates of the time-independent part of eqn (2).

The $\mathbf{V}_{IJ}$ operator in eqn (2) represents the interaction between the chromophores at the sites I and J, respectively:

$$\mathbf{V}_{IJ} = \mathbf{V}_{IJ}^{(\text{nn})} + \mathbf{V}_{IJ}^{(\text{en})} + \mathbf{V}_{IJ}^{(\text{ee})} \tag{3}$$

including the nuclear–nuclear $\mathbf{V}_{IJ}^{(\text{nn})}$ $(\equiv \mathbf{V}(\mathbf{R}_I,\mathbf{R}_J))$, the electron–nuclear $\mathbf{V}_{IJ}^{(\text{en})}$ $(\equiv \mathbf{V}(\mathbf{r}_I,\mathbf{R}_J) + \mathbf{V}(\mathbf{r}_J,\mathbf{R}_I))$ and the electron–electron $\mathbf{V}_{IJ}^{(\text{ee})}$ $(\equiv \mathbf{V}(\mathbf{r}_I,\mathbf{r}_J))$ contributions. Since $\mathbf{V}_{IJ}^{(\text{ee})}$ depends on the electron coordinates of two subsystems, the total wave function of the MC cannot be obtained easily in a self-consistent way.

In order to make such an exciton model practical for calculations in large systems, we introduce the following approximations: (i) the wave functions of the individual monomers are approximated by the wave functions of the isolated monomers embedded in the field of charges of the other monomers and solvent, (ii) no exchange of electrons is allowed between the subunits but does occur between individual chromophores within the subunit, and (iii) the molecular orbitals from different monomers are considered to be orthogonal, which is strictly not exact, since the orbitals are determined independently. Thus we expand the total multi-chromophoric wave function $|\Psi_{\text{MC}}\rangle$ into the direct products basis of the electronic wave functions of the individual QM subsystems:

$$|\phi_{ab\ldots z}\rangle = |\varphi_a^1\rangle \otimes |\varphi_b^2\rangle \otimes \ldots \otimes |\varphi_z^N\rangle = \left|\prod_I \varphi_{k_I}^I\right\rangle, \tag{4}$$

where superscripts 1,2,...,N denote the monomer index number within the MC, the indices a,b,... z are running over all included electronic states for each monomer (*e.g.* $a \in [0,\mathcal{N}_1 - 1]$, $b \in [0,\mathcal{N}_2 - 1]$,...) and k_I is the index of the electronic state of the I-th monomer in the set $ab\ldots z$. Since a QM subsystem itself may contain several chromophores (*e.g.* four in the case of a stacked base pair) such a direct product basis automatically includes both delocalized Frenkel exciton states as well as charge transfer states.

Each eigenstate $|\varphi_i^I\rangle$ in eqn (4) fulfills the general orthogonality relation $\langle\varphi_i^I|\varphi_j^J\rangle = \delta_{ij}\delta_{IJ}$ and satisfies the time-independent Schrödinger equation $\mathbf{H}_I|\varphi_i^I\rangle = \mathscr{E}_i^I|\varphi_i^I\rangle$, with $\mathscr{E}_i^I$ being the i-th electronic state energy of the I-th monomer. In the electrostatic embedding

scheme the monomeric Hamiltonian of the I-th subsystem in the manifold of $\mathcal{N}_I$ electronic states can be written as:

$$\mathbf{H}_I = \sum_i^{\mathcal{N}_I} \left[\mathscr{H}_i^I + V_i^I(\mathbf{R}_{\mathrm{MM}}) + \sum_{J \neq I} V_i^I(\mathbf{R}_J) \right] |\varphi_i^I\rangle\langle\varphi_i^I|, \quad (5)$$

where $\mathscr{H}_i^I$ is the unembedded Hamiltonian matrix element of the i-th electronic state. The terms $V_i^I(\mathbf{R}_{\mathrm{MM}})$ and $V_i^I(\mathbf{R}_J)$ represent the one-electron and nuclear contributions to the wave function of the I-th subsystem due to interaction with the other subsystems (indicated as $\mathbf{R}_J$) and the MM region ($\mathbf{R}_{\mathrm{MM}}$), respectively:

$$V_i^I(\mathbf{R}_K) = \langle\varphi_i^I| \sum_{\nu \in I} \sum_{\alpha \in K} \frac{Q_\alpha}{|\mathbf{r}_\nu^I - \mathbf{R}_\alpha^K|} |\varphi_i^I\rangle + \sum_{\substack{\alpha \in I \\ \beta \in K}} \frac{Q_\alpha Q_\beta}{|\mathbf{R}_\alpha^I - \mathbf{R}_\beta^K|}. \quad (6)$$

Here K stands for either one of the other monomers or the MM system, the index ν runs over electron positions, and the indices α and β over nuclear coordinates of the respective subsystems.

Since the nuclear contributions $\mathbf{V}_{IJ}^{(\mathrm{ne})}$ and $\mathbf{V}_{IJ}^{(\mathrm{nn})}$ in eqn (3) are shifted into the one-electron operator of the monomeric Hamiltonian (eqn (5)), eqn (3) is reduced to classical van der Waals interactions and pure electronic contributions $\mathbf{V}_{IJ}^{(\mathrm{ee})}$. Using the orthogonality of the monomeric electronic states the matrix elements of the $\mathbf{V}_{IJ}^{(\mathrm{ee})}$ operator reduce to pure electronic contributions between 4 electronic states:

$$\mathbf{V}_{IJ}^{(\mathrm{ee})} = \sum_{k,l} \sum_{\substack{k' \neq k \\ l' \neq l}} J_{kl,k'l'}^{IJ} |\varphi_k^I \varphi_l^J\rangle\langle\varphi_{k'}^I \varphi_{l'}^J| \quad (7)$$

where $J_{kl,k'l'}^{IJ}$ are the Coulomb integrals. These can be calculated from the transition densities $\rho_{kk'}^I$ and $\rho_{ll'}^J$ according to:

$$\begin{aligned} J_{kl,k'l'}^{IJ} &= \langle\varphi_k^I| \otimes \langle\varphi_l^J| \sum_{\nu,\lambda} \frac{1}{|\mathbf{r}_\nu^I - \mathbf{r}_\lambda^J|} |\varphi_{k'}^I\rangle \otimes |\varphi_{l'}^J\rangle \\ &= \int \mathrm{d}\mathbf{r}_1^I \int \mathrm{d}\mathbf{r}_1^J \frac{\rho_{kk'}^I(\mathbf{r}_1^I)\rho_{ll'}^J(\mathbf{r}_1^J)}{|\mathbf{r}_1^I - \mathbf{r}_1^J|}. \end{aligned} \quad (8)$$

where the indices λ and ν run over electron positions of the monomer I and J, respectively, and the transition densities are obtained within the basis of the individual monomers by integrating all (N_I) electron coordinates except the first $\mathbf{r}_1^I$:

$$\rho_{kk'}^I(\mathbf{r}_1^I) = N_I \int \mathrm{d}\mathbf{r}_2^I \ldots \int \mathrm{d}\mathbf{r}_{N_I}^I \varphi_k^{I*}(\mathbf{r}^I)\varphi_{k'}^I(\mathbf{r}^I) \quad (9)$$

Since the evaluation of the two-center integral $J_{kl,k'l'}^{IJ}$ is challenging for extended systems, there are several approximations available: (i) replacing the transition density ρ by atomic transition charges obtained from fitting the transition density to the electrostatic potential,[56] (ii) the transition density cube (TDC) method, where ρ is represented on a 3-dimensional grid and the overlap is calculated numerically on that grid[57] and (iii) using the transition dipole approximation (TDA).[58] In this work we employ the TDA, which is the most efficient approximation and can be used if the molecules interacting with each other are sufficiently well separated and short-range contributions can be neglected. However note that any of the available approximations can be used within the presented methodology.

Within the TDA eqn (8) is further represented by a multipole expansion up to the second order and the integral for an uncharged molecule is reduced to

$$J_{kl,k'l'}^{IJ} \approx \frac{\mu_{kk'}^I \cdot \mu_{ll'}^J}{|\mathbf{R}_{IJ}|^3} - 3\frac{(\mu_{kk'}^I \cdot \mathbf{R}_{IJ})(\mu_{ll'}^J \cdot \mathbf{R}_{IJ})}{|\mathbf{R}_{IJ}|^5}, \quad (10)$$

where $\mathbf{R}_{IJ}$ is the vector connecting the center of coordinates of the two monomers and $\mu_{kk'}^I$ is the transition dipole moment for the excitation from electronic state k to k' within the monomer I:

$$\mu_{kk'}^I = \langle\varphi_k^I| \sum_{\nu \in I} \mathbf{r}_\nu^I |\varphi_{k'}^I\rangle. \quad (11)$$

We are aware of the fact that the TDA probably overestimates the excitonic coupling of the chromophores.[59] However, we have chosen this approximation for practical reasons in the simulation of the field-driven dynamics. Fitting the transition charges to the electrostatic potential in the manifold of all excited states is computationally expensive and computing the transition density on the grid needs careful calibration of the chosen grid, especially in the context of the molecular dynamics simulations as performed in this work. In contrast, the computation of transition dipole moments is relatively cheap and is already required to compute the coupling to the external laser field in the McFISH method, as described later in this section. In order to compensate the caveats to this methodological choice, we have chosen a model having two base pairs included in each monomeric unit, such that short-range contributions are partially accounted for.

Exciton state gradients and nuclear dynamics

In order to propagate the nuclear trajectories in the excitonic states as defined by eqn (4) we solve Newton's equations of motion:

$$\mathbf{F} = -\nabla_{\mathbf{R}} E_{ab\ldots z}, \quad (12)$$

where $E_{ab\ldots z}$ is the total energy of the excitonic basis state $|\phi_{ab\ldots z}\rangle$ defined as:

$$\begin{aligned} E_{ab\ldots z} &= \sum_I \langle\varphi_i^I|\mathbf{H}_I|\varphi_i^I\rangle + E_{\mathrm{MM}}(\mathbf{R}_{\mathrm{MM}}) \\ &\quad + E_{\mathrm{QM/MM}}(\mathbf{R}_1, \ldots, \mathbf{R}_N, \mathbf{R}_{\mathrm{MM}}) \\ &= \sum_I \mathscr{E}_i^I(\mathbf{R}_I) + E_{\mathrm{MM}}(\mathbf{R}_{\mathrm{MM}}) \\ &\quad + E_{\mathrm{QM/MM}}(\mathbf{R}_1, \ldots, \mathbf{R}_N, \mathbf{R}_{\mathrm{MM}}) \end{aligned} \quad (13)$$

where $\mathscr{E}_i^I$ is the energy of the I-th monomer being in the i-th electronic state, which is obtained from quantum chemical calculations. By decomposing the total nuclear gradient $\nabla_{\mathbf{R}}$ with respect to all nuclear coordinates of the whole system $\mathbf{R}$ into components of the individual subunits (QM monomers

($\mathbf{R}_1$,...,$\mathbf{R}_N$) as well as the MM part ($\mathbf{R}_{MM}$)), the gradient of eqn (13) can be written as:

$$\nabla_{\mathbf{R}} E_{ab\ldots z} = \begin{pmatrix} \nabla_{\mathbf{R}_1} \mathscr{E}_a^1 \\ \nabla_{\mathbf{R}_2} \mathscr{E}_b^2 \\ \vdots \\ \nabla_{\mathbf{R}_N} \mathscr{E}_z^N \\ \nabla_{\mathbf{R}_{MM}} E_{MM} \end{pmatrix} + \nabla_{\mathbf{R}} E_{QM/MM}, \tag{14}$$

where the first term can be easily obtained from quantum chemical calculations and $\nabla_{\mathbf{R}} E_{QM/MM}$ are the pair-wise gradients obtained from van der Waals potentials.

Note that in the frame of this formulation the gradients $\nabla_{\mathbf{R}} J^{IJ}$ are neglected, since these terms are small due to the slow variation of the intersystem distance $\mathbf{R}_{IJ}$ and the transition dipole moments $\mu_I^{kk'}$.[60,61]

This is in contrast to the previously published approaches of Martinez[37,38] and Gonzalez,[39] which are based on diagonalization of the Hamiltonian $\mathbf{H}_{MC}$ and nuclear as well as electronic propagation on the resultant adiabatic electronic surfaces. While these two approaches are fully equivalent in a purely quantum mechanical treatment, their semiclassical limits differ. In particular, the nuclear gradients of the adiabatic electronic surfaces include contributions from the gradient of the excitonic coupling, which are absent in our method. However, in the course of the dynamics these coupling gradients are usually small since they depend on the only slowly varying interchromophoric distances and (transition) dipole moments. In addition, the inclusion of these effects is associated with the cost of calculating a large number of forces that increases exponentially with the number of monomers and excited states. More precisely, in the extreme case, gradients of potential energy and excitonic coupling in all electronic states of all monomers are needed. For example, already for a system consisting of 2 monomers with 2 electronic states g and e each, an excitonic wave function like |eg⟩ + |ge⟩ requires 4 quantum chemical gradient calculations in total. Instead, as a great advantage for the construction of the total gradient (14) only a single gradient calculation per monomer is needed and therefore scales linear with the number of monomers. Additionally, the decoupling of the quantum chemical calculations allows for the independent treatment of the individual subsystems and is therefore highly parallelizable. In the current implementation of McFISH all quantum chemical calculations can be performed simultaneously and the results are obtained at once. Note that the off-diagonal terms of $\mathbf{H}_{MC}$ are still included in the propagation of the electronic wave function during the surface hopping procedure, allowing the transport of excitation energy between the individual chromophores of the MC.

We also wish to emphasize that the method presented here includes the description of non-adiabatic effects as well as the early stages of the excitation due to the coupling to the external laser field as shown in the next section.

Excitation energy transport

For the simulation of the excitation energy transport (EET) between the chromophoric subunits we employ a surface-hopping approach[36,62] by solving the time-dependent Schrödinger equation (TDSE) for the Hamiltonian as defined in eqn (2). For this purpose, we expand the total (time-dependent) wave function in the excitonic basis as defined in eqn (4):

$$|\Psi_{MC}(t)\rangle = \sum_{ab\ldots z} c_{ab\ldots z}(t) |\phi_{ab\ldots z}(t; \mathbf{R}(t))\rangle, \tag{15}$$

with $c_{ab\ldots z}(t)$ being the time-dependent expansion coefficients and the excitonic states being parametrically dependent on the nuclear trajectory $\mathbf{R}(t)$. Inserting eqn (2) and (15) into the TDSE yields a set of differential equations for the expansion coefficients $\mathbf{C} = [c_{ab\ldots z}, c_{a'b\ldots z}, \ldots, c_{a'b'\ldots z'}]$:

$$\begin{aligned} i\dot{\mathbf{C}}(t) &= \mathbf{H}_{MC}\mathbf{C}(t) - i\mathbf{D}\mathbf{C}(t) \\ &= \left[\sum_I \left(\mathbf{H}_I + \mathbf{V}_I^{ext}(t)\right) \otimes \mathbf{1}_I \right. \\ &\quad \left. + \frac{1}{2} \sum_{J \neq I} \mathbf{V}_{IJ} \otimes \mathbf{1}_{IJ} - i\mathbf{D} \right] \mathbf{C}(t), \end{aligned} \tag{16}$$

where $\mathbf{D}$ is the non-adiabatic coupling matrix, whose elements have the general form:

$$(\mathbf{D})_{ab\ldots z, a'b'\ldots z'} = \left\langle \phi_{ab\ldots z} \middle| \frac{\mathrm{d}}{\mathrm{d}t} \phi_{a'b'\ldots z'} \right\rangle. \tag{17}$$

In the case that the vibrational modes of the individual monomers are uncoupled the non-adiabatic coupling matrix reduces to:

$$\begin{aligned} \mathbf{D} &= \sum_I \mathbf{D}_I \otimes \mathbf{1}_I \\ &= \sum_I \mathbf{1}_I \otimes \sum_{kk'}^{\mathcal{N}_I} \mathbf{d}_{kk'}^I(\mathbf{R}_I(t)) \cdot \dot{\mathbf{R}}_I(t) \left|\varphi_k^I\right\rangle \left\langle \varphi_{k'}^I \right| \end{aligned} \tag{18}$$

where are the non-adiabatic coupling vectors and $\dot{\mathbf{R}}_I$ are the velocities of the nuclei of the I-th monomer. The coupling of the individual monomers to the external laser field is described by the time-dependent $\mathbf{V}^{ext}$ term in eqn (16). Since we are dealing with a system whose individual components are much smaller than the wavelength of the field, the interaction with the electric field $\mathbf{E}(t)$ can be approximated by a dipole term:

$$\mathbf{V}_I^{ext} = -\sum_{kk'} \mu_{kk'}^I(\mathbf{R}_I(t)) \cdot \mathbf{E}(t) \left|\varphi_k^I\right\rangle \left\langle \varphi_{k'}^I \right|, \tag{19}$$

where $\mu_{kk'}^I$ is the transition dipole moment as defined in eqn (11). Within this study we have used a uniformly polarized Gaussian-shaped laser pulse, such that:

$$\mathbf{E}(t) = \frac{\varepsilon_0}{\sqrt{3}} (\hat{\mathbf{e}}_x + \hat{\mathbf{e}}_x + \hat{\mathbf{e}}_z) \exp\left(-\frac{(t - t_0)^2}{2\sigma^2} \right) \sin(\omega_0 t), \tag{20}$$

where ε_0 is the amplitude, t_0 is the center of the pulse, σ is the temporal width and ω_0 is the central frequency of the pulse. The used parameters can be found in the Computational

section. Note that any form of the laser pulse or polarization can be used within this approach[63] and extensions beyond the electric-field coupling are available.[64]

The time-dependent Schrödinger equation (16) is integrated in each nuclear time step Δt and the electronic state in which the trajectory resides is determined by a stochastic surface hopping algorithm, using hopping probabilities calculated from the change of the quantum electronic state populations $\rho = \mathbf{C}\mathbf{C}^{\dagger}$ according to:[65]

$$P_{|\phi_i\rangle\rightarrow|\phi_f\rangle} = \mathbf{\Theta}(-\dot{\rho}_{i,i})\mathbf{\Theta}(\dot{\rho}_{f,f})\frac{-\dot{\rho}_{i,i}}{\rho_{i,i}}\frac{\rho_{f,f}\Delta t}{\sum_k \mathbf{\Theta}(\dot{\rho}_{k,k})\dot{\rho}_{k,k}}, \qquad (21)$$

where the $\mathbf{\Theta}$ functions are defined to be one for positive arguments and zero otherwise. The indices i and f abbreviate the excitonic states (*e.g.* $|\phi_{ab\ldots z}\rangle$ and $|\phi_{a'b'\ldots z'}\rangle$) and the sum runs over all possible excitonic states. If the hopping probability for changing from the excitonic state $|\phi_i\rangle$ to $|\phi_f\rangle$ is greater than a uniformly generated random number a switch to the excitonic state $|\phi_f\rangle$ is made. However, there are several possibilities for state switches: (i) changing from the ground state to an excited state (*e.g.* $|\phi_{00\ldots0}\rangle \rightarrow |\phi_{ab\ldots z}\rangle$), most likely due to excitation by the electric field, (ii) changing from an excited state to the ground state (*e.g.* $|\phi_{ab\ldots z}\rangle \rightarrow |\phi_{00\ldots0}\rangle$), due to non-adiabatic relaxation processes, or (iii) a switch of the excitation site (*e.g.* $|\phi_{a'b\ldots z}\rangle \rightarrow |\phi_{ab'\ldots z}\rangle$). While the first two cases are diabatic events within a single monomer (diabatic hop), the latter one involves state switches in multiple monomers (excitonic hop). Depending on the type of state switch, different energy rescaling mechanism have to be employed.

We assume that all energy originating from the laser pulse is absorbed by the molecule and in the case (i) no velocity rescaling is performed in the occasion of a state switch while the pulse is active. After the pulse has ceased only diabatic hops due to non-adiabatic relaxation processes or excitonic hops due to dipole–dipole coupling can occur. In the case of non-adiabatic relaxation processes we rescale the velocity along the non-adiabatic coupling vector $\mathbf{d}^I_{kk'}$ within the monomer where the state switch occurs. In the case of excitonic hops where a combined deexcitation in monomer I and excitation in monomer J occurs, we transfer the whole deexcitation energy of $\varphi^I_i \rightarrow \varphi^I_{i'}$ to the monomer J, where it is used for the excitation $\varphi^J_j \rightarrow \varphi^J_{j'}$. Residual deexcitation energy from I is equally distributed on both participating monomers. If more energy is required to excite monomer J than available from the deexcitation of monomer I, the required energy is withdrawn from the vibrational kinetic energy of both monomers. The state switch is rejected if the available energy is insufficient. The rescaling factors are obtained such that the total energy is conserved and that the change of kinetic energy is minimized in both monomers.

3 Computational details

An ideal double-stranded B-DNA (dsDNA) duplex containing 20 alternating desoxyadenosines (dA) and desoxythymidines (dT) per strand connected with the phosphate backbone ($(dAdT)_{10}$:$(dAdT)_{10}$) was generated and solvated in a 92 Å cubic water box containing 25 077 water and electrostatically neutralized by adding 19 Mg^{2+} ions. The system was optimized and thermally equilibrated at T = 300 K and p = 1 bar with periodic boundary conditions using the Gromacs 5 program package[66,67] with the Amber99 force-field parameters.[68] For the following dynamics simulations, carried out with our homemade software, we extracted a tube with a length and diameter of 80 × 50 Å containing the DNA, the Mg^{2+} ions and 4768 water molecules and froze the outer shell of water molecules in order to conserve volume and density.

In order to run QM/MM simulations we selected 6 base pairs ($(AT)_3$:$(AT)_3$) lying in the center of the DNA strands as QM part and the rest (28 bases, sugar residue, phosphate backbone, water and ions) as MM part (*cf.* Fig. 1). The boundary bonds from the QM bases to the sugar residues were capped with hydrogens as link-atoms. The semi-empirical multi-reference configuration interaction OM2 method[69,70] as implemented in the MNDO99 software[71,72] is used for the QM region and the Amber99 force-field for the MM region. Note that the formulation of McFISH method (*cf.* Section 2) is independent of the underlying quantum chemical as well as the molecular mechanical methods and can straightforwardly extended to interface with external software providing the necessary quantities.

In the frame of the electrostatic embedding scheme the point-charges of the MM system are included into the QM Hamiltonian as one-particle terms, while charges close to the boundary region are excluded to prevent over-polarization of the QM part. For the QM/MM McFISH simulations the QM system was further split into 3 sub-systems each containing two base pairs (3 (AT):(AT)), where each QM sub-system is electrostatically coupled to the MM system as well as to the other two QM subsystems.

The absorption spectrum and transition densities were obtained from the QM/MM optimized geometry using the OM2/MR-CISD GUGA-CI method,[73] where for the $(AT)_3$:$(AT)_3$ system an active space of 48 occupied and 64 virtual orbitals was used and for each of the (AT):(AT) subsystems an active space including 18 occupied and 24 virtual orbitals has been chosen.

In order to obtain reasonable initial conditions, we have run a 100 ps long QM/MM trajectory in the electronic ground-state at constant temperature (T = 300 K). After thermal equilibration we sampled geometries and velocities in regular time intervals serving as starting points for our semi-classical QM/MM McFISH molecular dynamics. In total 75 trajectories have been propagated for 2 ps starting at t = −40 fs in the electronic ground state with explicit inclusion of the irradiating laser field. For each subsystem we included the ground and 12 excited states. Note that the expansion in eqn (15) in the manifold of 13 monomeric states would require the propagation of the electronic Schrödinger equation in the manifold of 2197 excitonic states. However, since $\mathbf{H}_{MC}$ contains only one- ($\mathbf{H}_I$) and two-monomer ($\mathbf{V}_{IJ}$) terms and due to the orthogonality of the monomeric eigenstates φ^I_i, all matrix elements with three or more different indices in the set $ab\ldots z$ are zero. Therefore we removed matrix elements with three or more different indices by an uniform transformation which reduces the manifold to 469 states.

The Newtonian equations of motion for the nuclei are integrated using the velocity Verlet algorithm[74] with a time

step Δt = 0.1 fs and the electronic Schrödinger equation was numerically integrated using the 4th order Runge–Kutta method with a step size of 10^{-5} fs. We have used an uniformly polarized Gaussian-shaped laser pulse (eqn (20)) centered at t_0 = 0 with amplitude of ε_0 = 0.08 GV m^{-1} corresponding to an intensity of 0.85 GW cm^{-2} and a full width at half maximum (FWHM) of 50 fs ($\sigma \approx 32$ fs), giving rise to a broad spectral width. The central frequency ω_0 of the laser pulse has been chosen as 4.7 eV in order to access the lower energy band of the UV spectrum (see results below). While the pulse is active ($|\mathbf{E}(t)| > 0.01\varepsilon_0$) no velocity rescaling upon electronic state switch is imposed, since we assume that all energy of the laser pulse is absorbed by the molecule. After the pulse has ceased energy rescaling is imposed as described in the previous section.

Analysis of transition density

In order to classify the character of observed excitations we analyze the transition density. In the ESI† a concise explanation of the obtained quantities used to characterize the excitations is provided. Briefly, by partitioning the transition density matrix into fragments (*e.g.* nucleobases or DNA strands) we obtain charge transfer (CT) values showing the percentage amount of CT character to an excited state,[75–77] the delocalization length (DL) indicating the number of fragments participating in an excitation,[59,78] and an average position (POS value)[79] as well as a fractional transition density (FTD)[77,80] both providing the location of an excitation in terms of individual fragments. The CT value ranges from 0, for no CT character, to 1 for a pure CT state. Throughout this work we use a cutoff value of CT $\geq$ 0.3 for an excited state to be considered of having significant CT character. The DL value is 1 if the excitation is localized on one fragment only, and larger if the excitation is delocalized over multiple fragments. Usually this number is fractional, but throughout this work we will skip the decimal place and round the DL value to its closest integer for simplicity. Combining DL and CT values allows us to classify excited states according to (*cf.* Fig. S1 in the ESI†):

1. DL = 1 and CT $<$ 0.3: locally excited (LE) states, where the transitions are solely localized on one fragment,

2. DL $\geq$ 2 and CT $<$ 0.3: Frenkel excitonic excited (EE) states, where multiple local transitions in two or more fragments contribute to an excitation,

3. DL = 1 and CT $\geq$ 0.3: charge transfer (CT) states, where a net charge is transferred between the fragments, and

4. DL $\geq$ 2 and CT $\geq$ 0.3: charge resonance (CR) states, where two electrons are resonantly exchanged between the fragments.

The possible POS value for two fragments range from 1 to 2. If an excitation is solely localized at the first fragment the POS value becomes 1, while it is 2 if the excitation is localized at the second. In both cases the DL value is 1 (local excitation, LE). In all other cases (EE, CT or CR) the POS value is 1.5.

4 Results and discussion

We explore the excitation energy transport and nonradiative relaxation in the DNA duplex with the sequence $(dAdT)_{10}$:$(dAdT)_{10}$ embedded in water (Fig. 1) by employing the previously described QM/MM McFISH method. For this purpose we selected 6 alternating adenine–thymine base pairs ($(AT)_3$:$(AT)_3$) located in the center of the dsDNA as QM system (Fig. 1 right, further denoted as full QM system). We further partitioned the QM system into three subsystems consisting of 2 alternating base pairs (AT):(AT) (further denoted as partitioned QM system, shaded areas in Fig. 1). Each QM subsystem is calculated independently using the semi-empirical multi-reference configuration interaction OM2 (OM2/MRCI) method[69,70] providing an efficient approach to simulate extended systems. Benchmark calculations show that the OM2 approach gives reliable results for the excited states of many organic molecules.[72,81] The OM2 approach was successfully employed in a series of studies on both the static excited state properties and the non-adiabatic dynamics of nucleobases in isolated form,[82,83] in solution,[63,84–86] or embedded in DNA strands.[87] In studies on stacked nucleobase dimers and trimers it was also shown that semiempirical AM1 and PM3 methods provide reasonable energies for charge transfer states.[88] However, note that the presented McFISH method is generally applicable and can be combined with any electronic structure method, such as TDDFT or ADC(2). The residual bases, phosphate backbone, solvent and counter ions form the MM region described by a classical force field.

We have chosen this partition scheme in order to partially include quantum mechanical effects, which would not be present when separating the system between each base pair (*e.g.* short-range effects) or along the helical axis between the strands (*e.g.* intra-strand proton/charge transfer). In order to allow excitation energy transfer between such coupled systems the electronic excited states are coupled *via* their transition dipole moments (transition dipole approximation, TDA). The TDA tends to overestimate excitonic coupling of close-lying chromophores due to short-range contributions stemming from molecular orbital overlap.[59] However, since another side-effect of this partition scheme is that the subsystem distance increases, the overestimation of excitonic coupling is partially compensated. Note that this effect is essentially due to error cancellation, but does not catch the effects due to the overlap of molecular orbitals. Furthermore, we wish to remark that there are certain aspects of the photodynamics that cannot be fully captured within the chosen model. Specifically, this concerns CT processes crossing the boundaries of the subsystems, since the total wave function is constructed from single-subsystem excited state wave functions. This issue of the exciton model has been recently addressed in the literature,[89] but the proposed approach is much too demanding for the system studied here.

UV/vis spectroscopy

In order to justify the partitioning and the TDA, we have calculated UV/vis spectra from the QM/MM optimized geometries, both for the full QM system containing all 6 base pairs as well as for the partitioned QM system with each subsystem being excitonically coupled.

The comparison is presented in Fig. 2A and B, respectively, and a detailed analysis of the lowest 20 electronically excited

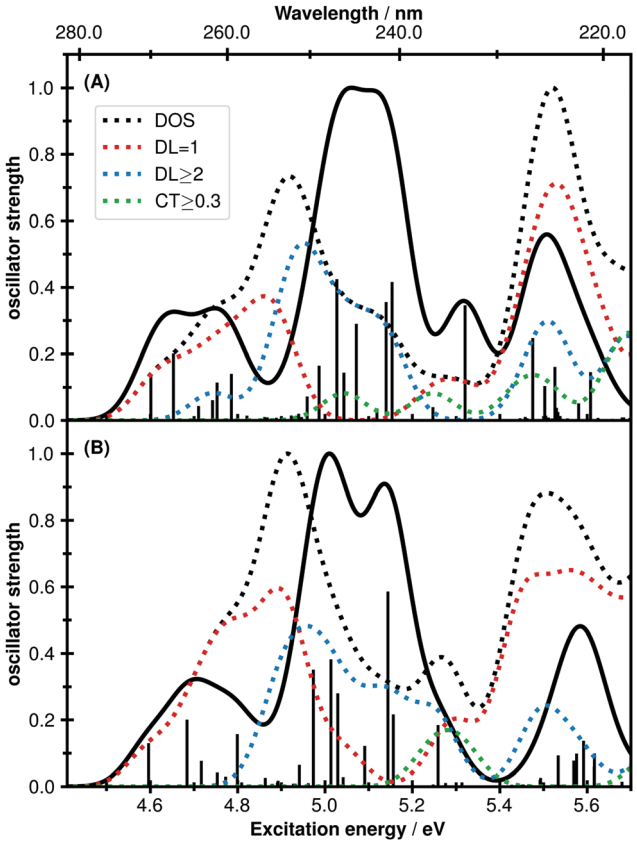

Fig. 2 UV/vis spectra of the QM/MM optimized $(dAdT)_{10}$:$(dAdT)_{10}$ doubled-strand DNA duplex embedded in water and ions. (A) QM system containing all 6 central $(AT)_3$:$(AT)_3$ base pairs. (B) QM region partitioned into 3 subsystems, each consisting of two base pairs, which are then excitonically coupled using the transition dipole approximation. The transitions (sticks) are convolved by a Lorentzian (black line, width 0.05 eV). The dotted lines show the density of states (black) and its decomposition into localized states (red), delocalized states (blue) and states with charge transfer contributions (green).

states is given in Tables S1 and S2 of the ESI.† The obtained spectra for the full QM system (Fig. 2A) and the partitioned QM system using the TDA (Fig. 2B) are of similar shape and nearly every state in the full QM system is also present in partitioned system, although close lying states frequently interchange. Both spectra show two bands in the lower energy region, which are usually experimentally resolved as a single band, with the first being considered the red tail of the spectrum. We have chosen a small width for the convolution to separate these two bands, because they have distinct properties. The first band located between 4.6 eV and 4.8 eV is dominated by localized (red) or slightly delocalized (blue) excitations with ππ* character localized at adenine and the excitations are distributed along the whole dsDNA. The second band, found between 4.8 to 5.2 eV, is dominated by delocalized excitations over two or more nucleobases, and transitions having partly CT character (green) are found in the higher energy region of this band. The contribution of excitations dominantly located in thymine is low in the lower energy region and increases with higher energies (*cf.* Tables S1 and S2 in the ESI†).

The obtained spectra are in satisfactory agreement with experimental spectra of $(dAdT)_{10}$:$(dAdT)_{10}$ oligomers in buffered water solution (*cf.* Fig. S4 in the ESI†), which exhibit a broad band between 4.2–5.2 eV, where the lower end of this band has a small shoulder attributed to the $S_0 \rightarrow S_1$ transition located at adenine.[61,90] Our calculations are also in good agreement with the accurate *ab initio* ADC(2)/MM calculations of the ATAT stacked tetramer embedded in a $(dAdT)_6$:$(dAdT)_6$ duplex and water,[26] where a broad band between 4.5 to 5.5 eV with a maximum at 5.2 eV and an energetically lower-lying shoulder is found. In these calculations also DL and CT values have been analyzed, showing dominantly states of bright ππ* character localized at one or two nucleobases, while the delocalization length is barely above 1.5. Dark nπ* states are blue-shifted compared to spectra computed *in vacuo*. When going to the maximum of this band the DL increases and states involving two or more monomers become more important. The most abundant exciton formed involves two nucleobases, leading to the conclusion that excited states of such stacked DNA bases are mostly localized or delocalized over not more than two stacked bases. Note that in our calculations we do not only have stacked bases but also base pairing. Therefore, we also observe excitonic states delocalized over three up to 4 bases, while the vertical intra-strand delocalization is dominantly limited to 2 bases.

Since the DNA is a flexible molecule and its secondary structure is highly dependent on the environment, the presented spectra represent only one snapshot of the possible spectral compositions. Therefore, we present in Fig. S4 of the ESI† the averaged spectrum of geometries extracted from the ground-state QM/MM trajectory. There, the localized and delocalized states are overlapping much more within the first band and thus excitonic states are accessible by the used laser pulse centered at 4.7 eV. The obtained spectrum is also in good agreement with the experimentally obtained spectrum of Bouvier *et al.*[61] (gray dotted line in Fig. S4, ESI†).

In summary, the good spectral agreement of full QM system and excitonically coupled partitioned QM system together with the good comparison to experimental and high-level *ab initio* results makes us confident that our methodology is sufficiently accurate to simulate the nonradiative relaxation including the excitation energy transfer in dsDNA using our McFISH method, while being computationally efficient as well.

Excited state energy transfer and relaxation

In order to study the nonradiative relaxation of the excited states in dsDNA we perform McFISH simulations including the explicit interaction with the exciting laser field.

As can be seen from Fig. 3 the laser pulse excites up to 67% of the trajectories (gray curve). Approximately 45% of this population is transferred to "excitonic" states (S_E, red curve) and the remaining trajectories are excited to "local" states (S_L, blue curve). Note that the termini "local" and "excitonic" have to be understood here on the basis of excited states of the subsystems, such that "local" excited states are limited to one nucleobase quartet and "excitonic" states are combinations of excited states in different subsystems. Therefore, no assignment of the excitation to

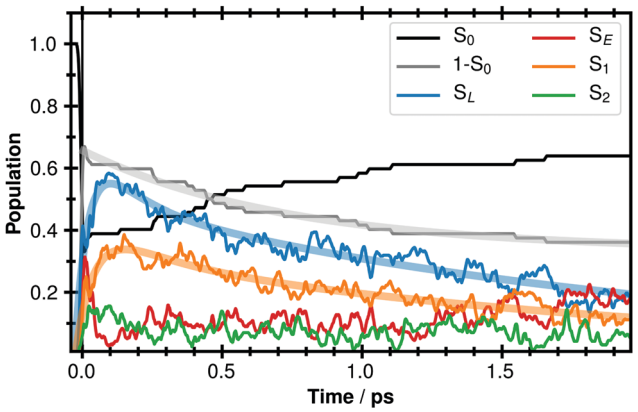

Fig. 3 Combined electronic state populations obtained from McFISH molecular dynamics simulations. The black and gray curves show the ground-state and total excited state population, respectively. The blue and red curves indicate the sum of the population of locally (S_L) and excitonic excited (S_E) states. The orange and green curve are the sum of local (in respect to each subsystem) excited S_1 and S_2 states. The shaded thick curves indicate mono- and biexponential fits to the thin underlying curves.

individual nucleobases can be made. During the first 100 fs most of the population of the S_E states is transiently transferred to S_L states, where the majority (38%) reaches the energetically lowest subsystem state (S_1, orange curve) within 200 fs. In the course of the dynamics the S_L states decay slowly to the ground state approaching 18% after 2 ps. In total half of the initially excited trajectories returned to the ground-state within 2 ps.

In order to determine the lifetimes, we fitted biexponentially decaying model functions to the populations (shaded lines in Fig. 3), and all obtained parameters as well as the analytic form of the model functions are given in the ESI.† For the overall excited state lifetime (gray) we obtained a decay with time constants of τ_2 = 700 fs and $\tau_3 \approx$ 75 ps, giving rise to an average lifetime of $\langle\tau\rangle \approx$ 35 ps. Note that, since the determined lifetime is far beyond the duration of our simulations, it can only serve as a rough estimate to the overall lifetime. For the S_L states (blue) time constants of τ_1 = 48 fs for the population increase of these states, and τ_2 = 130 fs and τ_3 = 2.06 ps ($\langle\tau\rangle$ = 890 fs) for the decaying component were determined. The obtained values are in the same order of magnitude as obtained experimentally on (dAdT)-duplexes.[11,12] For the hetero-polymorphic $(dAdT)_{18}$:$(dAdT)_{18}$ duplexes Kohler *et al.* determined a lifetime of 51 ps, which is 3 times shorter than for the homopolymeric duplexes,[12] and femtosecond fluorescence spectroscopy reveals a wavelength dependent increase of the of the excited state lifetime from 0.5 ps at 330 nm to 3.3 ps at 420 nm.[11] Thus the overall excited state lifetime is found to be much longer than for the isolated nucleobases, which exhibit radiationless decay times of a few 100 fs to 1 ps.[91–96] Interestingly, the fast decaying component of the excited state population with a time constant of 0.7 ps is close to the lifetime of 0.46 ps found for equimolar mixtures of deoxyadenosine monophosphate (dAMP) and thymidine monophosphate (TMP), and the fast decaying component (0.13 ps) of the S_L population is the same as for pure dAMP solutions.[97] These findings suggest and we will later show, that (1) the mechanism leading to the radiationless decay to the ground state in the early stages after photoexcitation involves monomer-like deactivation channels, which are already known from the bare nucleobases, and (2) the formation of and trapping in long-living delocalized excitonic states is responsible for the elongated excited state lifetime as indicated by the second slow decaying component of the excited state population. Therefore, at the end of simulation the excited state dynamics is largely governed by electronic states delocalized over several nucleobases.

While the electronic state population already shows elongation of the excited state lifetime compared to the bare nucleobases, the extent of the delocalization is not clear because multiple chromophores are involved in each subsystem and can participate in the formation of excimers. A nucleobase centered picture is presented in Fig. 4A by calculating the delocalization length (DL) and charge transfer contributions (CT values) along each trajectory. Note that, in contrast to the electronic state populations shown in Fig. 3, all values shown Fig. 4 are now normalized to the number of

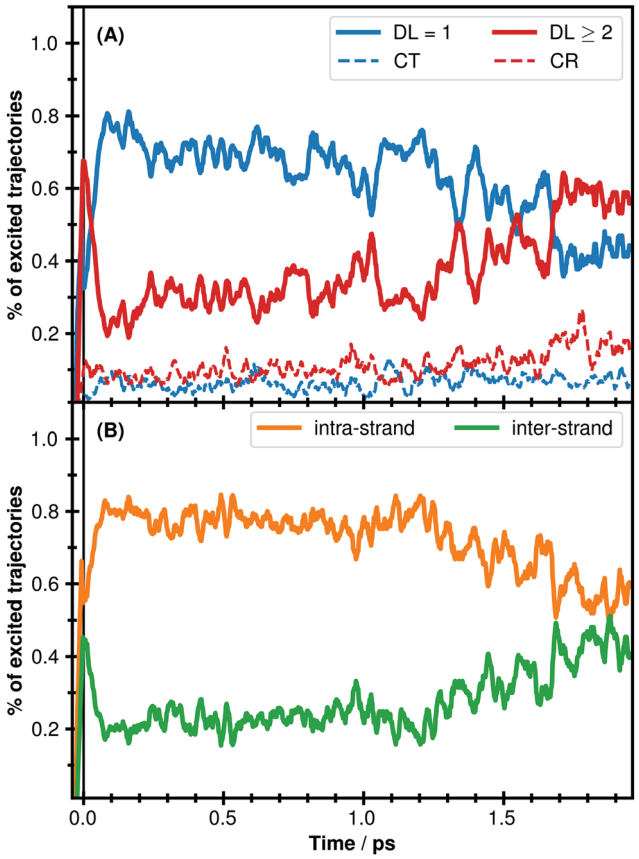

Fig. 4 Analysis of the transition density matrix (TDM) averaged with respect to trajectories being in the excited state. (A) Contribution of local excitations (blue) and delocalized excitations (red). The dotted curves denote charge separated states (CT ≥ 0.3), being either charge transfer states (blue dotted curve, DL = 1) or charge resonance states (red dotted curve, DL ≥ 2). (B) Location of the excitation obtained from POS values using each strand as a fragment. Inter-strand excitations possess 1.25 < POS < 1.75 and are delocalized between the strands and intra-strand excitation have POS ≤ 1.25 or POS ≥ 1.75, respectively, and are thus localized within one of the strands.

trajectories that are in the excited state at a given time. This is reasonable since the transition density is only available for trajectories situated in the excited state and moreover emphasizes the processes taking place in the excited state.

As the used laser field has a central frequency of 4.7 eV, it lies in the center of the first band of the UV/vis spectrum (Fig. 2B) and due to its broad spectral width may populate a variety of excited states: localized states on adenine or thymine as well as ones delocalized over a few bases. Furthermore, delocalized excited states may be Frenkel excitons, charge resonance states or a mixture of them. While for the electronic state populations (Fig. 3) we found an equal distribution of local (S_L) and excitonic (S_E) excitations with respect to the subsystems, Fig. 4A shows that actually dominantly ($\sim$70%) delocalized excited states are initially populated (red curve). A substantial amount of these delocalized states become transiently localized within the first 100 fs (blue curve) leaving about 20% in a delocalized state. As it becomes evident by comparing Fig. 3 and 4A, the increasing localization on a single base is followed by the radiationless decay to the ground state and thus the DL of the remaining trajectories in the excited state increases.

In order to distinguish the Frenkel excitonic states from the charge resonance (CR) states the contribution of states with significant charge transfer character (CT $\geq$ 0.3) is depicted by the dotted curves in Fig. 4A. The contribution of CT states (blue dotted curve, DL = 1), where a net charge is transferred between the nucleobases, is constantly below 10% and therefore these do not play an important role in the excited state dynamics. The contribution of CR states is also low but increases from 10% right after excitation to about $\sim$16% at the end of our simulations. Thus, it follows that after local excited states (LE), excitonic excited (EE) states are the key players in the excited state dynamics. However, since the contribution of CR states slightly increases to the end of our simulations, charge resonances may become more important at later times and are relevant factors in the formation of excimers.[19]

The groundbreaking work of Kohler *et al.* revealed that the base stacking controls the excited state dynamics of DNA and is more important for the homopolymeric $(dA)_n$:$(dT)_n$ than for the alternating $(dAdT)_n$:$(dTdA)_n$ duplexes.[12] In order to investigate this effect we present in Fig. 4B the location where the excitation resides with respect to the strands of the duplex. The excitations that are situated within a single strand (being either localized or delocalized with respect along the strand) are depicted by the orange curve and inter-strand excitations (being either EE or CR) are depicted by the green curve. The laser pulse, as it becomes evident by this graph, excites inter- as well as intra-strand excited states. Since the excited states localize on the bases within the first 100 fs most of the inter-strand population is transferred to the intra-strand population. Considering the time evolution of the DL values from Fig. 4A the intra-strand excited states (Fig. 4B, orange) should decrease in the same way as the LE states (Fig. 4A, blue). However, the intra- and inter-strand population remains constant in the first 1.2 ps. In conclusion this means that during that time delocalized EE states (DL $\geq$ 2) are involving mostly bases situated within in a single strand and are thus delocalized between stacked bases. After 1.2 ps, as the nuclei are rearranging and the inter-strand distance increases, the inter-strand excited state population increases slowly and reaches nearly parity to the intra-strand population after 2 ps. Thus at later times inter-strand EE states become more important. However, this population growth is also paralleled by an increase in the population of CR states (Fig. 4A, red dotted curve).

By correlating the data from Fig. 4A and B the localization or delocalization of the excited states can be visualized, as presented in Fig. 5. Each dot in the left panel of Fig. 5 represents the location (POS) with respect to the strands and delocalization length (DL) of a trajectory at any time of the simulation. The lower (strand A) and upper (strand B) regions corresponds to excitations situated in the respective strand of the duplex, while the central region (A/B) represents inter-strand excited states. The orange dots denote excited states possessing significant CT character (CT $\geq$ 0.3). The inset numbers mark regions either corresponding to (1) LE states, (2) inter-strand CT states, (3) dominantly inter-strand EE states or (4) intra-strand EE states, respectively. The percentage amounts for LE, EE, CT and CR states obtained from these points are summarized in Table 1 where intra-strand depict the points of the upper and lower region and inter-strand depict the points of the central region. The right panels of Fig. 5 show the density of these dots within 4 time intervals (a video showing the complete time-evolution is provided in the ESI†). Since we are dealing with a heteropolymorphic duplex and both strands are therefore built from the same (but complementary) sequence of alternating adenines and thymines the figure shows a symmetric form. As it becomes evident from the first time interval (Fig. 5 right, 0.0–0.1 ps), the laser pulse excites local and intra-strand excitonic excited (EE) states in both strands equally as well as inter-stand EE states, while the EE states are involving mostly two bases (DL = 2). After 1.2 ps the excitations are dominantly localized at one of the strands (*cf.* Fig. 4B). We detect the rise of intra- and inter-stand EE states as well as inter-stand CT states, since the nuclei rearrange and the intra-strand distance increases as the excitation hops between the bases. Excitonic states involving two bases are still dominant, but we also see an increase of CR states and inter-/intra-strand EE states being delocalized over three bases. These processes can be understood as a first stage in the formation of an inter-strand excimer.

In summary (*cf.* Table 1) we observe that – besides LE states (33.1%) – delocalized intra-strand excited states are almost only Frenkel excitonic (EE) states (19.5%), while delocalized inter-strand excited states are EE states (22.4%) as well as CR states (10.3%). As already shown in Fig. 4A CT states play only a minor role but are dominantly involved in inter-strand excited states (5.7%).

To support the hypothesis that the excited state lifetime is extended due to the formation of delocalized excitonic states we statistically analyzed in Fig. 6 the delocalization length (DL), fractional transition density (FTD) and the non-adiabatic coupling to the ground-state by classifying the trajectories by their excited state lifetime (Δt_{S_0}): (i) trajectories decaying within 800 fs to the ground-state, which is in the time scale of the monomeric

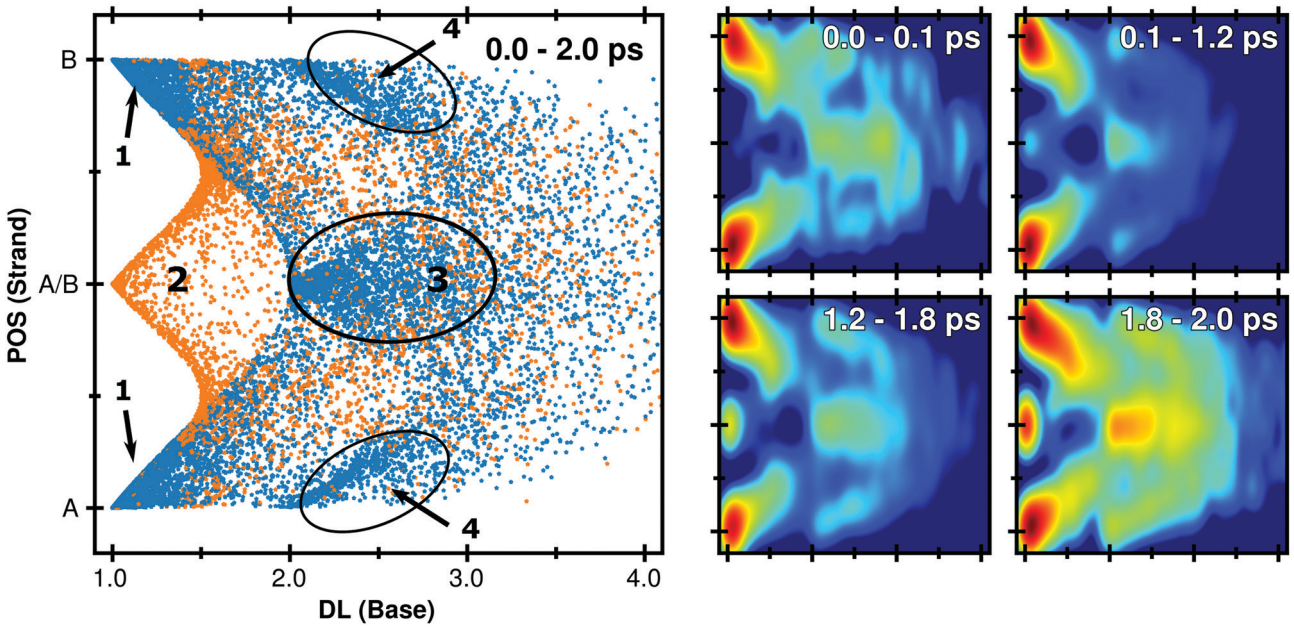

Fig. 5 Distribution of the excitation location (POS) with respect to the two DNA strands as a function of delocalization length (DL) with respect to the individual bases. Left panel: Distribution for the total simulation time. The orange dots denote charge transfer (CT $\geq$ 0.3 and DL = 1) or charge resonance (CT $\geq$ 0.3 and DL $\geq$ 2) states, respectively. The inset numbers and marked regions are: (1) local excited (LE) states, (2) inter-strand charge transfer states, (3) inter-strand excitonic excited (EE) states and (4) intra-strand EE states. Right panels: Density of POS/DL points depicted for 4 time intervals showing the formation of delocalized inter- and intra-strand excitonic states. The density is shown on a logarithmic scale.

Table 1 Distribution of local excited states (LE), Frenkel excitonic excited states (EE), charge transfer states (CT) and charge resonance states (CR) obtained from the points in Fig. 5. All values are given in percent

Location (POS)	LE[a]	EE[b]	CT[c]	CR[d]
Intra-strand[e]	33.1	19.5	1.5	7.5
Inter-strand[f]	0.0	22.4	5.7	10.3

[a] Local excited states (DL = 1, CT $<$ 0.3). [b] Frenkel excitonic excited states (DL $\geq$ 2, CT $<$ 0.3). [c] Charge transfer states (DL = 1, CT $\geq$ 0.3). [d] Charge resonance states (DL $\geq$ 2, CT $\geq$ 0.3). [e] Intra-strand summarizes all points in the lower (POS $\leq$ 1.25) and upper (POS $\geq$ 1.75) of Fig. 5. [f] Inter-strand summarizes all points in the central region (1.25 $<$ POS $<$ 1.75) of Fig. 5.

deactivation (denoted as short trajectories), and (ii) trajectories residing longer than 800 fs in the excited state (denoted as long trajectories).

The diagram in Fig. 6A shows the average non-adiabatic coupling to the ground-state with respect to the delocalization length of the state the trajectories currently reside. For the short (orange) as well as the long (green) living trajectories the coupling to the ground-state vanishes exponentially with the increase of the degree of delocalization, such that excitations that are delocalized over more than 2 bases exhibit no relaxation to the ground-state. In the regime of localized excited states, however, the short trajectories show in average a three times higher non-adiabatic coupling to the ground-state. This indicates that the fast relaxation within the first 800 fs governed by the monomer-like photodynamics of localized excited states.

In order to be able to reach the monomer-like conical intersections with the ground-state the excitation needs to be localized sufficiently long on a single base and thus short trajectories should in average exhibit a longer retention time on a single base. Therefore we determined Fig. 6B the average length of time the fractional transition density (FTD) is constantly localized on a base (max FTD $>$ 0.8). As can be seen, excitations in short trajectories reside in average three times longer (32 fs) localized on a single base than the long ones (11 fs). Additionally, as shown in Fig. S6 in the ESI,† switches of the location are less frequent in short trajectories. An even more pronounced trend is found for the time an excitation is in average situated within one strand (*cf.* Fig. S6 in the ESI†). While excitations in short trajectories are dominantly located in a single strand for 51 fs, excitations in long trajectories are in average only for 16 fs. This indicates in accordance with the previous findings (*cf.* Fig. 4B and 5) that in the early stages of the excited state dynamics the excitation energy is dominantly transported within the strand and that for longer living trajectories inter-strand excitation energy transport is becoming more important.

This finding is substantiated by the overall percentage time (total time in a given state divided by the total time in the excited state) each class of trajectories stays in a localized or delocalized state, respectively, as shown in Fig. 6B. During their time in the excited state, short trajectories (left pie chart) are in average 92% in a localized state (blue) and 8% in a delocalized state, in contrast to long trajectories (right pie chart), which reside only for 74% in a localized and for 26% in a delocalized state. In average short trajectories stay for about 58 fs in a localized state, long trajectories only do so for 29 fs before switching to a delocalized state (not shown). The contribution of delocalized states is therefore two to three times larger in

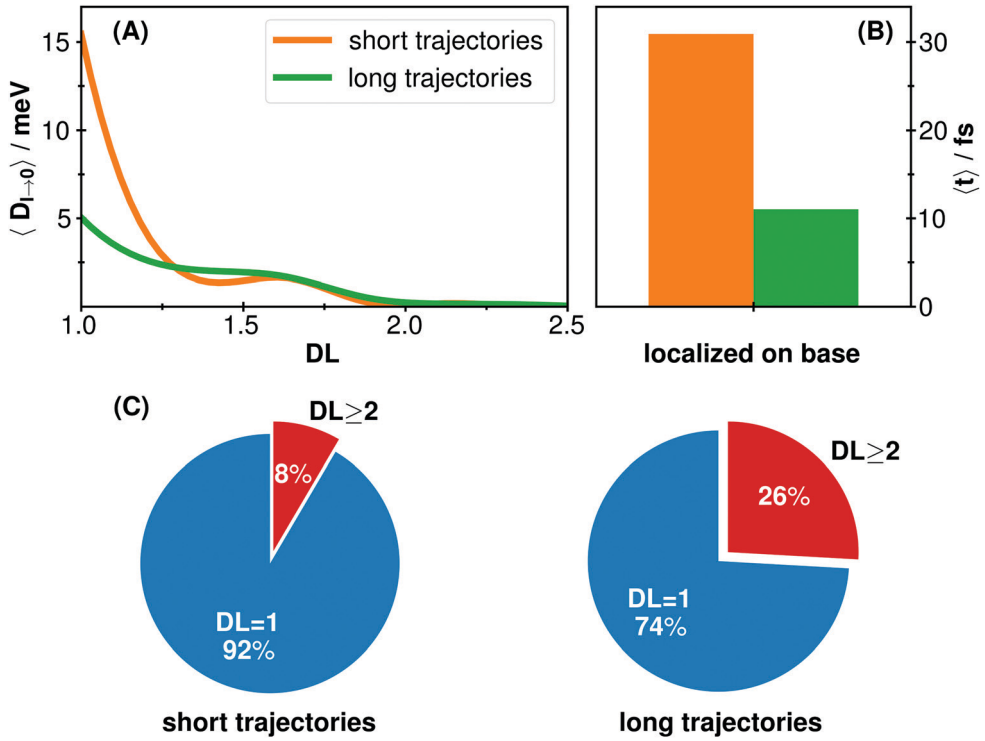

Fig. 6 (A) Average non-adiabatic coupling to the ground state as function of the delocalization length (DL). The plot indicates that short living trajectories (orange line) exhibit a strong coupling to the ground state that arises from states with localized excitations. The long living trajectories (green line) exhibit much lower coupling in the low DL range. The strength of the non-adiabatic coupling decreases in both cases with the delocalization length. (B) Average length of time trajectories reside in a state dominantly localized at a single base (max(FTD) $>$ 0.8) showing that excitations in short (orange) trajectories are 3 times longer localized on a single base than long trajectories. (C) Total percentage of time short (left) and long (right) trajectories reside in localized (blue) and delocalized (red) states.

long living trajectories than in short ones, indicating the influence of the formation of excimers on the elongated excited state lifetime.

In summary, in trajectories which relax quickly to the electronic ground-state, the excitation is longer localized on a single nucleobase, thus providing a longer time to reach the well-known conical intersections of the monomeric nucleobases. This leads to short lifetimes comparable to those of the isolated monomers. In contrast, trajectories which stay for a long time in the excited state frequently switch the location of their excitation, and thus a previously excited monomer can return to its planar equilibrium geometry of the ground-state before reaching the conical intersection. Hence, the average lifetimes of these trajectories are increased.

Deactivation mechanisms

In general the deactivation mechanism observed in the dynamics is basically comparable to the ones already known from the literature for adenine and thymine monomers.[4,98–101] Namely, we observe the out-of-plane movement of the methyl group of thymine associated with the barrierless internal conversion from a ππ* to a nπ* localized excited state[98,100] and the out-of-plane puckering of adenine's amino group.[101,102] In Fig. 7 we present snapshots of an exemplary trajectory (a video showing the complete trajectory is provided in the ESI†). The laser pulse excites dominantly the central region of the QM region (40 fs). In the following 500 fs the excitation is propagated along both strands and all nucleobases until a localized ππ* state is reached, which is converted to an nπ* state in the following 200 fs. Finally, the trajectory relaxes to the electronic ground state at 780 fs *via* a conical intersection involving the out-of-plane movement of the methyl group at thymine.

Radiationless internal conversion from bright localized ππ* state in adenine–thymine base pairs[103–107] and stacked dimers[28] to a CT state followed by proton transfer leading to a conical intersection with the ground state were reported. We also see regularly inter-strand proton transfer reactions as a two step tautomerization mechanism involving the proton transfer from the amino group of adenine to the hydrogen-bonded thymine oxygen and from the thymine NH hydrogen to the corresponding adenine's nitrogen. Although this process is photoinduced, in our simulations, it does not lead to a deactivation to the ground-state. In our case the tautomeric form is not created while the excitation is localized on the given base, but after the excitation has already been transferred to one of the neighboring bases, leaving a residual vibrational kinetic energy on the initially excited base. This energy is large enough to overcome the small barrier separating the canonical form from the tautomeric one, which has been determined to be only 9–11 kcal mol^{-1}.[106–108] This "mutation" due to the inter-strand proton transfer is

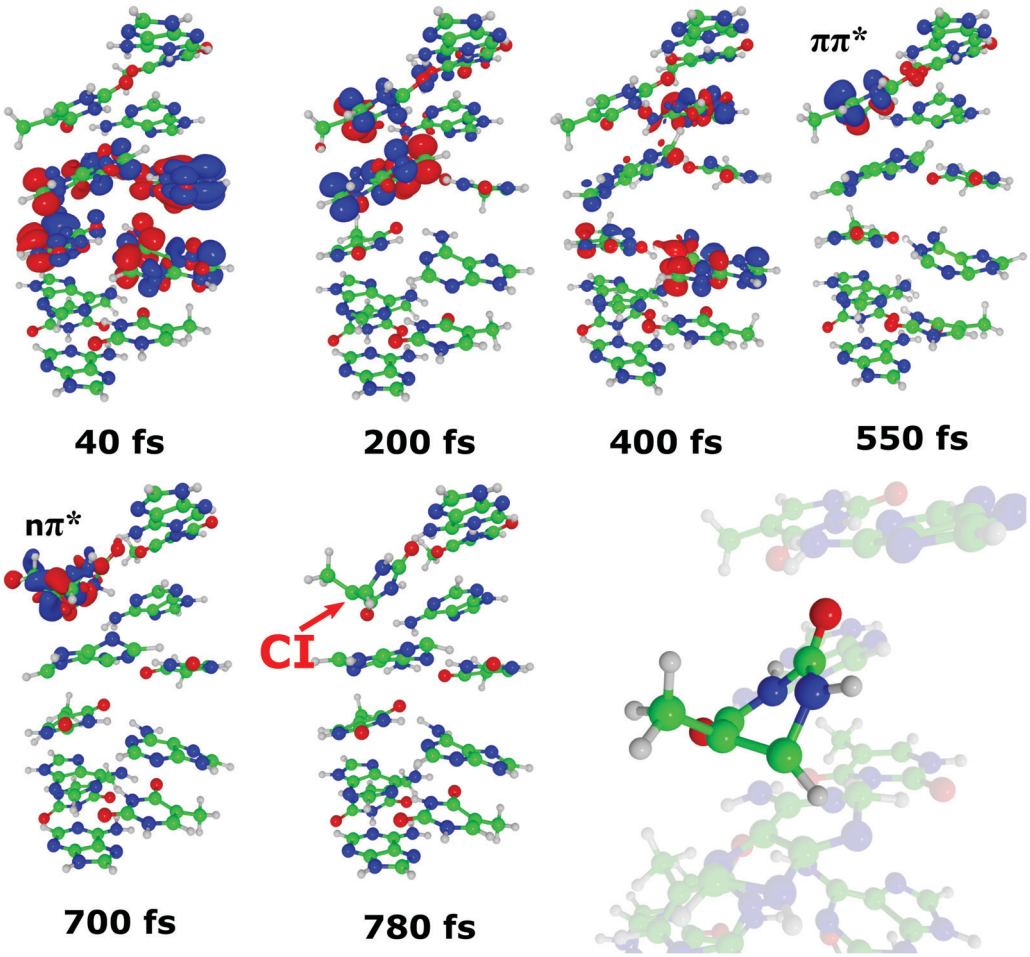

Fig. 7 Snapshots and transition densities of the excited state where the trajectory currently resides, for an exemplary trajectory. The first frame (40 fs) shows the initial excitation of an excitonic state involving 4 nucleobases. The following two snapshots demonstrate the excitation energy transport along the DNA duplex, which is finally trapped in a local ππ* excitation located at thymine (550 fs). The ππ* state internally converts to an nπ* state at 700 fs, followed by the deactivation to the ground-state *via* a methyl group out-of-plane puckering conical intersection at 780 fs.

therefore an outcome of the excess kinetic energy introduced by excitonic hops and thus consequently a thermal effect initially caused by the external laser field. Such a transformation is in contrast to mutations located at a single strand (*e.g.* thymine dimerization), which can not easily repaired by using the second strand as template.[1,109] However, in our case the tautomerized state is not very stable and thus the protons are regularly transferred back, resulting in the canonical form being dominant during the dynamics.

5 Conclusion

With our newly developed McFISH method we introduce a versatile and generally applicable approach to simulate excitation energy transport in complex and extended molecular aggregates including all degrees of freedom by the combination of hybrid quantum/molecular mechanics (QM/MM) techniques and semi-classical surface-hopping dynamics on-the-fly. We have demonstrated our methodology by simulating the laser field-induced dynamics in the solvated double-stranded alternating $(dAdT)_{10}$:$(dAdT)_{10}$ DNA-oligomer. In our model the central 6 base pairs were treated by the semiempirical multi-reference (MR-CI) OM2 method and the remaining DNA as well as the solvating water and ions were described by a molecular mechanical force field. The QM region was further partitioned in 3 subsystems containing 2 base pairs each and afterwards electronically coupled through the transition dipole moments.

We have calculated the UV/vis spectrum of the "full" QM model, considering all 6 base pairs as a single QM system including all quantum-mechanical effects, and compared it with the spectrum obtained for the partitioned system where the 3 subsystems are coupled using the transition dipole approximation. We have extensively analyzed and compared the transition density of the lowest 20 electronically excited states for the two models, finding a good agreement in the energetical position as well as the nature of the excited states. The obtained spectra are also in good agreement with available experimental data and high-level *ab initio* calculations.

In accordance with previous experimental results[12] we find after initial excitation of exciton states that the total excited-state

population of the excited states is multi-exponentially decaying. Two time constants for the overall excited state lifetime have been obtained, the first being 700 fs, which resembles the lifetime of an equimolar mixture of dAMP (130 fs) and TMP,[97] and the second being ~75 ps. From the obtained constants we estimate an average excited state lifetime of ~36 ps which is much longer than the monomeric deactivation lifetimes lying in the sub-ps regime.

A thorough analysis of the simulated trajectories allowed us to identify two groups exhibiting a distinctly different relaxation behavior:

(i) A substantial fraction of the trajectories undergoes an ultrafast internal conversion to the ground state in the early stages of the dynamics following the monomeric decay channels already known from investigations on the bare nucleobases.[94,110] These trajectories stay shorter in delocalized states and thus have more time to reach the conical intersections known for nucleobases.

(ii) The second group of trajectories decay much slower and is linked to the formation of excimers, where the excitation is delocalized either within one strand (intra-strand) or across both of them (inter-strand). We found that trajectories lasting for a long time (>1 ps) in the excited state exhibit also a dominant contribution of delocalized states involving two or more nucleobases. While in the early stages of the excitation the delocalization is dominantly distributed along one strand of the DNA duplex, it becomes increasingly delocalized over both strands and inter-strand charge resonance states become more important.

Our results provide a detailed molecular picture of the excited state relaxation and energy transfer processes in dsDNA. Overall, the simulation results are in good agreement with previously published experimental findings demonstrating that our QM/MM McFISH method is a reliable tool for the investigation of excitation energy transport in complex and large molecular multi-chromophoric aggregates. Therefore, we are planning to simulate and compare a variety of DNA sequences, such as homopolymeric chains, natural DNA as well as unusual DNA structures as found in *e.g.* i-motif DNA.

Conflicts of interest

There are no conflicts to declare.

Acknowledgements

We acknowledge the financial support within the ERC Consolidator Grant "DYNAMO" (Grant No. 646737).

References

1 G. P. Pfeifer, Y.-H. You and A. Besaratinia, *Mutat. Res.*, 2005, **571**, 19–31.
2 J. S. Taylor, *Acc. Chem. Res.*, 1994, **27**, 76–82.
3 A. Lamola and J. Eisinger, *Proc. Natl. Acad. Sci. U. S. A.*, 1968, **59**, 46–51.
4 R. Improta, F. Santoro and L. Blancafort, *Chem. Rev.*, 2016, **116**, 3540–3593.
5 C. T. Middleton, K. de La Harpe, C. Su, Y. K. Law, C. E. Crespo-Hernández and B. Kohler, *Annu. Rev. Phys. Chem.*, 2009, **60**, 217–239.
6 C. E. Crespo-Hernández, B. Cohen, P. M. Hare and B. Kohler, *Chem. Rev.*, 2004, **104**, 1977–2020.
7 J. Eisinger, M. Gueron, R. Shulman and T. Yamane, *Proc. Natl. Acad. Sci. U. S. A.*, 1966, **55**, 1015.
8 I. Vayá, T. Gustavsson, T. Douki, Y. Berlin and D. Markovitsi, *J. Am. Chem. Soc.*, 2012, **134**, 11366–11368.
9 I. Vayá, T. Gustavsson, F.-A. Miannay, T. Douki and D. Markovitsi, *J. Am. Chem. Soc.*, 2010, **132**, 11834–11835.
10 T. Takaya, C. Su, K. de La Harpe, C. E. Crespo-Hernández and B. Kohler, *Proc. Natl. Acad. Sci. U. S. A.*, 2008, **105**, 10285–10290.
11 D. Onidas, T. Gustavsson, E. Lazzarotto and D. Markovitsi, *Phys. Chem. Chem. Phys.*, 2007, **9**, 5143–5148.
12 C. E. Crespo-Hernández, B. Cohen and B. Kohler, *Nature*, 2005, **436**, 1141–1144.
13 D. Markovitsi, *Photochem. Photobiol.*, 2016, **92**, 45–51.
14 A. Banyasz, T. Gustavsson, D. Onidas, P. Changenet-Barret, D. Markovitsi and R. Improta, *Chem. – Eur. J.*, 2013, **19**, 3762–3774.
15 D. Markovitsi, T. Gustavsson and I. Vayá, *J. Phys. Chem. Lett.*, 2010, **1**, 3271–3276.
16 W.-M. Kwok, C. Ma and D. L. Phillips, *J. Phys. Chem. B*, 2009, **113**, 11527–11534.
17 N. K. Schwalb and F. Temps, *Science*, 2008, **322**, 243–245.
18 E. R. Bittner, *J. Photochem. Photobiol., A*, 2007, **190**, 328–334.
19 R. Borrego-Varillas, G. Cerullo and D. Markovitsi, *J. Phys. Chem. Lett.*, 2019, **10**, 1639–1643.
20 I. Conti and M. Garavelli, *J. Phys. Chem. Lett.*, 2018, **9**, 2373–2379.
21 J. J. Nogueira, F. Plasser and L. González, *Chem. Sci.*, 2017, **8**, 5682–5691.
22 V. A. Spata, W. Lee and S. Matsika, *J. Phys. Chem. Lett.*, 2016, **7**, 976–984.
23 L. Blancafort and A. A. Voityuk, *J. Chem. Phys.*, 2014, **140**, 095102.
24 A. A. Voityuk, *Photochem. Photobiol. Sci.*, 2013, **12**, 1303–1309.
25 F. Plasser and H. Lischka, *Photochem. Photobiol. Sci.*, 2013, **12**, 1440–1452.
26 F. Plasser, A. J. Aquino, W. L. Hase and H. Lischka, *J. Phys. Chem. A*, 2012, **116**, 11151–11160.
27 A. W. Lange and J. M. Herbert, *J. Am. Chem. Soc.*, 2009, **131**, 3913–3922.
28 F. Santoro, V. Barone and R. Improta, *J. Am. Chem. Soc.*, 2009, **131**, 15232–15245.
29 S. Tonzani and G. C. Schatz, *J. Am. Chem. Soc.*, 2008, **130**, 7607–7612.
30 I. Buchvarov, Q. Wang, M. Raytchev, A. Trifonov and T. Fiebig, *Proc. Natl. Acad. Sci. U. S. A.*, 2007, **104**, 4794–4797.
31 D. Markovitsi, T. Gustavsson and F. Talbot, *Photochem. Photobiol. Sci.*, 2007, **6**, 717–724.
32 F.-A. Miannay, Á. Bányász, T. Gustavsson and D. Markovitsi, *J. Am. Chem. Soc.*, 2007, **129**, 14574–14575.

33 R. Improta and V. Barone, *Angew. Chem., Int. Ed.*, 2011, **50**, 12016–12019.
34 R. Szabla, H. Kruse, P. Stadlbauer, J. Šponer and A. L. Sobolewski, *Chem. Sci.*, 2018, **9**, 3131–3140.
35 J. Garrec, C. Patel, U. Rothlisberger and E. Dumont, *J. Am. Chem. Soc.*, 2012, **134**, 2111–2119.
36 J. C. Tully, *J. Chem. Phys.*, 1990, **93**, 1061–1071.
37 A. Sisto, D. R. Glowacki and T. J. Martinez, *Acc. Chem. Res.*, 2014, **47**, 2857–2866.
38 A. Sisto, C. Stross, M. W. van der Kamp, M. O'Connor, S. McIntosh-Smith, G. T. Johnson, E. G. Hohenstein, F. R. Manby, D. R. Glowacki and T. J. Martinez, *Phys. Chem. Chem. Phys.*, 2017, **19**, 14924–14936.
39 M. F. Menger, F. Plasser, B. Mennucci and L. González, *J. Chem. Theory Comput.*, 2018, **14**, 6139–6148.
40 R. Mitrić, J. Petersen, M. Wohlgemuth, U. Werner, V. Bonačić-Koutecký, L. Wöste and J. Jortner, *J. Phys. Chem. A*, 2010, **115**, 3755–3765.
41 R. Mitrić, J. Petersen and V. Bonačić-Koutecký, *Phys. Rev. A: At., Mol., Opt. Phys.*, 2009, **79**, 053416.
42 R. van Grondelle and V. I. Novoderezhkin, *Phys. Chem. Chem. Phys.*, 2006, **8**, 793–807.
43 R. Hildner, D. Brinks, J. B. Nieder, R. J. Cogdell and N. F. van Hulst, *Science*, 2013, **340**, 1448–1451.
44 G. S. Schlau-Cohen, Q. Wang, J. Southall, R. J. Cogdell and W. Moerner, *Proc. Natl. Acad. Sci. U. S. A.*, 2013, **110**, 10899–10903.
45 E. A. Jares-Erijman and T. M. Jovin, *Nat. Biotechnol.*, 2003, **21**, 1387–1395.
46 E. Galperin, V. V. Verkhusha and A. Sorkin, *Nat. Methods*, 2004, **1**, 209–217.
47 K. A. Lukyanov, D. M. Chudakov, S. Lukyanov and V. V. Verkhusha, *Nat. Rev. Mol. Cell Biol.*, 2005, **6**, 885–890.
48 D. E. Dolmans, D. Fukumura and R. K. Jain, *Nat. Rev. Cancer*, 2003, **3**, 380–387.
49 T. A. Theodossiou, A. R. Gonçalves, K. Yannakopoulou, E. Skarpen and K. Berg, *Angew. Chem., Int. Ed.*, 2015, **54**, 4885–4889.
50 J. F. Lovell, T. W. Liu, J. Chen and G. Zheng, *Chem. Rev.*, 2010, **110**, 2839–2857.
51 Y. Huang, F. Qiu, R. Chen, D. Yan and X. Zhu, *J. Mater. Chem. B*, 2020, **8**, 3772–3788.
52 E. Brunk and U. Rothlisberger, *Chem. Rev.*, 2015, **115**, 6217–6263.
53 H. M. Senn and W. Thiel, *Angew. Chem., Int. Ed.*, 2009, **48**, 1198–1229.
54 A. Warshel and M. Levitt, *J. Mol. Biol.*, 1976, **103**, 227–249.
55 T. Förster, in *Modern Quantum Chemistry*, ed. O. Sinanoglu, Delocalized Excitation and Excitation Transfer, Academic Press, New York, 1965.
56 M. Madjet, A. Abdurahman and T. Renger, *J. Phys. Chem. B*, 2006, **110**, 17268–17281.
57 B. P. Krueger, G. D. Scholes and G. R. Fleming, *J. Phys. Chem. B*, 1998, **102**, 5378–5386.
58 D. L. Andrews, *Chem. Phys.*, 1989, **135**, 195–201.
59 A. Czader and E. R. Bittner, *J. Chem. Phys.*, 2008, **128**, 035101.
60 B. Bouvier, T. Gustavsson, D. Markovitsi and P. Millié, *Chem. Phys.*, 2002, **275**, 75–92.
61 B. Bouvier, J.-P. Dognon, R. Lavery, D. Markovitsi, P. Millié, D. Onidas and K. Zakrzewska, *J. Phys. Chem. B*, 2003, **107**, 13512–13522.
62 S. Hammes-Schiffer and J. C. Tully, *J. Chem. Phys.*, 1994, **101**, 4657–4667.
63 J. Petersen, M. Wohlgemuth, B. Sellner, V. Bonačić-Koutecký, H. Lischka and R. Mitrić, *Phys. Chem. Chem. Phys.*, 2012, **14**, 4687–4694.
64 M. Wohlgemuth and R. Mitrić, *J. Phys. Chem. A*, 2016, **120**, 8976–8982.
65 P. G. Lisinetskaya and R. Mitric, *Phys. Rev. A: At., Mol., Opt. Phys.*, 2011, **83**, 033408.
66 M. J. Abraham, T. Murtola, R. Schulz, S. Páll, J. C. Smith, B. Hess and E. Lindahl, *SoftwareX*, 2015, **1**, 19–25.
67 H. J. Berendsen, D. van der Spoel and R. van Drunen, *Comput. Phys. Commun.*, 1995, **91**, 43–56.
68 J. Wang, P. Cieplak and P. A. Kollman, *J. Comput. Chem.*, 2000, **21**, 1049–1074.
69 W. Weber and W. Thiel, *Theor. Chem. Acc.*, 2000, **103**, 495–506.
70 W. Weber, PhD thesis, Universität Zürich, Switzerland, 1996.
71 W. Thiel, MNDO Program, Version 06/2010, 2010.
72 M. Korth and W. Thiel, *J. Chem. Theory Comput.*, 2011, **7**, 2929–2936.
73 A. Koslowski, M. E. Beck and W. Thiel, *J. Comput. Chem.*, 2003, **24**, 714–726.
74 W. C. Swope, H. C. Andersen, P. H. Berens and K. R. Wilson, *J. Chem. Phys.*, 1982, **76**, 637–649.
75 A. Luzanov and O. Zhikol, *Int. J. Quantum Chem.*, 2010, **110**, 902–924.
76 A. Luzanov and O. Prezhdo, *Int. J. Quantum Chem.*, 2005, **102**, 582–601.
77 S. Tretiak and S. Mukamel, *Chem. Rev.*, 2002, **102**, 3171–3212.
78 J. Pipek and P. G. Mezey, *Int. J. Quantum Chem.*, 1988, **34**, 1–13.
79 F. Plasser and H. Lischka, *J. Chem. Theory Comput.*, 2012, **8**, 2777–2789.
80 S. Fernandez-Alberti, D. V. Makhov, S. Tretiak and D. V. Shalashilin, *Phys. Chem. Chem. Phys.*, 2016, **18**, 10028–10040.
81 M. R. Silva-Junior and W. Thiel, *J. Chem. Theory Comput.*, 2010, **6**, 1546–1564.
82 Z. Lan, E. Fabiano and W. Thiel, *J. Phys. Chem. B*, 2009, **113**, 3548–3555.
83 E. Fabiano and W. Thiel, *J. Phys. Chem. A*, 2008, **112**, 6859–6863.
84 B. Heggen, Z. Lan and W. Thiel, *Phys. Chem. Chem. Phys.*, 2012, **14**, 8137–8146.
85 Z. Lan, Y. Lu, E. Fabiano and W. Thiel, *ChemPhysChem*, 2011, **12**, 1989–1998.
86 Y. Lu, Z. Lan and W. Thiel, *J. Comput. Chem.*, 2012, **33**, 1225–1235.
87 Y. Lu, Z. Lan and W. Thiel, *Angew. Chem., Int. Ed.*, 2011, **50**, 6864–6867.
88 A. A. Voityuk, *Chem. Phys. Lett.*, 2006, **427**, 177–180.

89 X. Li, R. M. Parrish, F. Liu, S. I. Kokkila Schumacher and T. J. Martinez, *J. Chem. Theory Comput.*, 2017, **13**, 3493–3504.
90 E. Emanuele, D. Markovitsi, P. Millié and K. Zakrzewska, *ChemPhysChem*, 2005, **6**, 1387–1392.
91 S. M. Parker, S. Roy and F. Furche, *Phys. Chem. Chem. Phys.*, 2019, **21**, 18999–19010.
92 M. Barbatti, A. J. Aquino, J. J. Szymczak, D. Nachtigallová, P. Hobza and H. Lischka, *Proc. Natl. Acad. Sci. U. S. A.*, 2010, **107**, 21453–21458.
93 J. J. Szymczak, M. Barbatti, J. T. Soo Hoo, J. A. Adkins, T. L. Windus, D. Nachtigallová and H. Lischka, *J. Phys. Chem. A*, 2009, **113**, 12686–12693.
94 S. Ullrich, T. Schultz, M. Z. Zgierski and A. Stolow, *J. Am. Chem. Soc.*, 2004, **126**, 2262–2263.
95 S. Ullrich, T. Schultz, M. Z. Zgierski and A. Stolow, *Phys. Chem. Chem. Phys.*, 2004, **6**, 2796–2801.
96 H. Kang, K. T. Lee, B. Jung, Y. J. Ko and S. K. Kim, *J. Am. Chem. Soc.*, 2002, **124**, 12958–12959.
97 D. Markovitsi, A. Sharonov, D. Onidas and T. Gustavsson, *ChemPhysChem*, 2003, **4**, 303–305.
98 G. Zechmann and M. Barbatti, *J. Phys. Chem. A*, 2008, **112**, 8273–8279.
99 S. Perun, A. L. Sobolewski and W. Domcke, *J. Phys. Chem. A*, 2006, **110**, 9031–9038.
100 S. Perun, A. L. Sobolewski and W. Domcke, *J. Phys. Chem. A*, 2006, **110**, 13238–13244.
101 A. L. Sobolewski and W. Domcke, *Eur. Phys. J. D*, 2002, **20**, 369–374.
102 S. Perun, A. Sobolewski and W. Domcke, *Chem. Phys.*, 2005, **313**, 107–112.
103 M. Dargiewicz, M. Biczysko, R. Improta and V. Barone, *Phys. Chem. Chem. Phys.*, 2012, **14**, 8981–8989.
104 S. Perun, A. L. Sobolewski and W. Domcke, *J. Phys. Chem. A*, 2006, **110**, 9031–9038.
105 F. L. Gervasio, M. Boero and M. Parrinello, *Angew. Chem., Int. Ed.*, 2006, **45**, 5606–5609.
106 N. Shimizu, S. Kawano and M. Tachikawa, *J. Mol. Struct.*, 2005, **735**, 243–248.
107 L. Gorb, Y. Podolyan, P. Dziekonski, W. A. Sokalski and J. Leszczynski, *J. Am. Chem. Soc.*, 2004, **126**, 10119–10129.
108 H.-H. Ritze, P. Hobza and D. Nachtigallová, *Phys. Chem. Chem. Phys.*, 2007, **9**, 1672–1675.
109 I. Conti, L. Martnez-Fernández, L. Esposito, S. Hofinger, A. Nenov, M. Garavelli and R. Improta, *Chem. – Eur. J.*, 2017, **23**, 15177–15188.
110 E. Samoylova, H. Lippert, S. Ullrich, I. Hertel, W. Radloff and T. Schultz, *J. Am. Chem. Soc.*, 2005, **127**, 1782–1786.

Excitation Energy Transport in DNA modelled by Multi-Chromophoric Field-Induced Surface Hopping

Matthias Wohlgemuth and Roland Mitric*

Institut für Physikalische und Theoretische Chemie, Julius-Maximilians-Universität Würzburg, Emil-Fischer-Str. 42, 97074 Würzburg, Germany.

E-mail: roland.mitric@uni-wuerzburg.de

Supplementary Information

Analysis of the Transition density matrix

We have analyzed the character of the excitation and calculated the delocalization length (DL) and charge transfer character (CT) using the decomposition scheme of the transition density matrix (TDM) adopted from Plasser et al.[1–3] based on the work of Tretiak and co-workers[4]. A schematic representation of in the following derived quantities is given in Fig. S1. Briefly, the TDM expressed in atomic orbitals is decomposed into logical fragments and the CT number Ω_{AB} for two fragments A and B is calculated according to:

$$\Omega_{AB} = \frac{1}{2} \sum_{a \in A} \sum_{b \in B} (\mathbf{DS})_{ab} (\mathbf{SD})_{ab} + D_{ab} (\mathbf{SDS})_{ab} \tag{1}$$

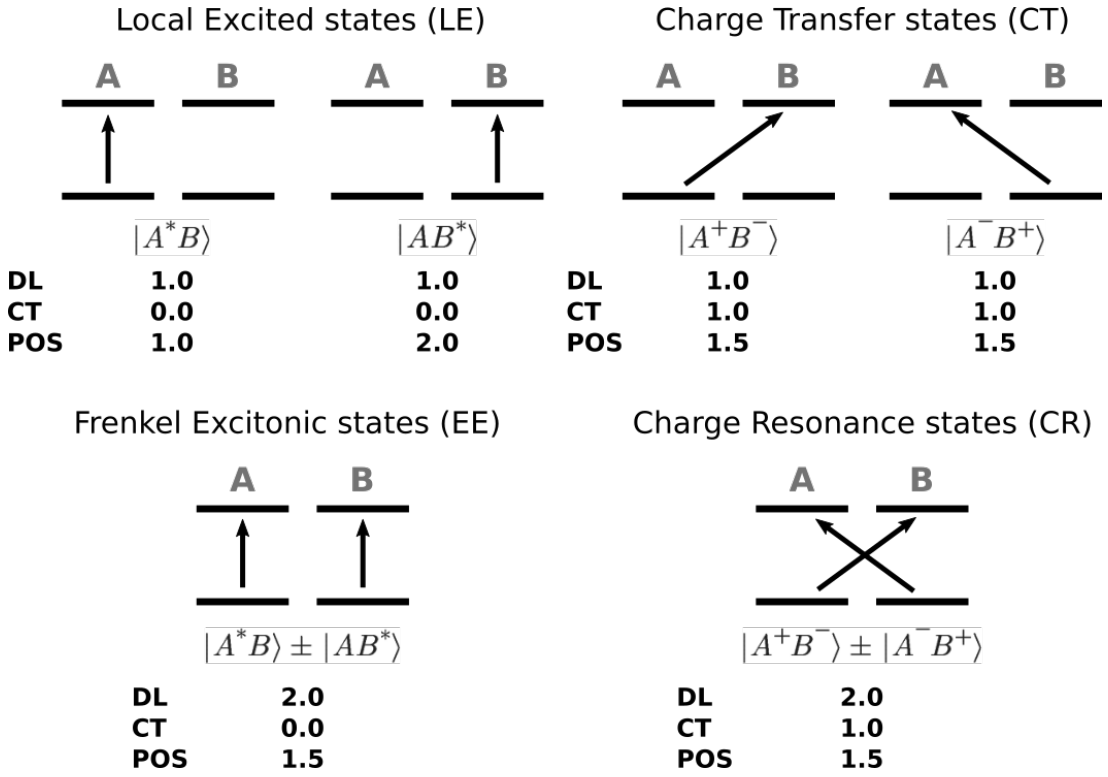

Figure S1: Schematic representation of derived quantities (DL, CT, POS) from transition density matrix analysis for a dimer A and B. The top row represents are localized electronic states being either local excitations (LE) in each monomer or charge transfer excitations (CT). The bottom row shows delocalized excitations being either excitonic excitations (EE) or charge resonance excitations (CR).

where D and S are transition density and overlap matrices (expressed in atomic orbitals), respectively, and the indices a and b are running over the atomic orbitals associated with the fragments. If not stated otherwise we consider the individual nucleobases as fragments. For details how to interpret these charge transfer numbers see Ref.[4–6]. These numbers give rise to an unique decomposition of the excited state into local and charge transfer contributions for the individual fragments. By normalization of the CT numbers by $\Omega = \sum_{AB} \Omega_{AB}$:

$$CT = \Omega^{-1} \sum_{A} \sum_{B \neq A} \Omega_{AB} \tag{2}$$

a the relative contribution of charge transfer character to an excitation is obtained. The CT values are ranging from 0, meaning no charge transfer character, to 1, corresponding to

pure charge transfer character. If not mentioned otherwise, we considered excitations with CT values above 0.3 as excitation with significant CT character. In order to obtain the total TDM for the partitioned QM system, the TDM of each sub-system is contracted with the eigenvectors obtained from diagonalizing the excitonic hamiltonian $\mathbf{H}_{MC}$. Note, that off-diagonal matrix elements representing transitions from one sub-system to another are thus zero and CT excitations between the sub-systems are not included. Therefore, the two charge transfer contributions in the S_4 and S_8 states present in the full QM system (Tab. S1) are absent in the partitioned system since the sub-system boundary is across the T9:A30 and A10:T31 base pairs.

The DL value, defined as the inverse partition ratio[7]:

$$DL = \Omega^2 \left[\sum_A \left(\sum_B \frac{\Omega_{AB} + \Omega_{BA}}{2} \right)^2 \right]^{-1}, \tag{3}$$

measures the distribution of the excitation over multiple fragments and thus ranges from 1 to the number of fragments, where A and B are the indices of the fragments. A DL value close to 1 represents a local transition where the excitation is located (mostly) at one fragment. At larger DL values the excitation is distributed over multiple nucleobases and thus represents either an exciton or a charge resonance state (if CT value is large as well).

Lastly, an average location of the excitation can be computed using[2]:

$$POS = (2\Omega)^{-1} \sum_A A \sum_B (\Omega_{AB}^2 + \Omega_{BA}^2) \tag{4}$$

which ranges from 1 to the number of fragments. The POS value essentially only makes sense if two fragments are considered, thus we only give this value in the main text to obtain a measure for the delocalization between the DNA strands.

Therefore, in order to allow assignment of an excitation to individual nucleobases, we follow the work of Tretiak and co-worker[4,8] defining a fractional transition density (FTD)

for the fragment A according to:

$$FTD = \frac{\sum_{a\in A}\sum_{b\in A} D_{ab}^2}{\sum_A \sum_{a\in A}\sum_{b\in A} D_{ab}^2} \tag{5}$$

where **D** is again the transition density matrix in the atomic basis. The FTD value, ranging from 0 to 1 for each fragment and summing to 1, provides the relative contribution of each fragment to the total transition density and thus allows easily the assignment of the transitions to the monomers. Due to the helical structure of the dsDNA we considered it challenging for the reader to realize the nature and location of excitations from volumetric transition density plots, thus we decided to use the FTD values to create a two dimensional surface plot. In order to visualize also the location of the created hole and the electron due to the excitation we modified the above approach by decomposing the TDM by singular value decomposition (SVD) in order to obtain natural transition orbitals [9] yielding small set of orbitals representing hole and electron, which are transformed in the atomic basis. From these orbitals we calculate the hole (**H**) and electron (**P**) density. Using Eq. (5) by inserting **H** and **P** instead of **D** we obtain two sets of FTD values for the location of hole and the electron, respectively.

The plots presented in the figures S2 and S3, showing the locations of excitations in the UV/Vis spectra discussed in the main text, are then obtained by using a schematic two-dimensional representation, assigning a specific position to each nucleobase. Then each FTD value is convolved with a two-dimensional Gaussian, where the height is determined by the FTD values, centered at the corresponding position of the nucleobase (we put a small offset, such that hole and electron FTD value do not cancel). The figures can be interpreted as follows: (i) if the hole and electron are located at the same nucleobase and only at one, the transition is a localized excitation (LE), (ii) if the hole and electron are on two or more nucleobases an exciplex is formed and (iii) and if electron and hole are on two different nucleobases the transition is of charge transfer character (CT).

Table S1: Summary and analysis of the 20 energetically lowest excited states obtained from the OM2/MM optimized geometry of $(dAdT)_{10} : (dAdT)_{10}$ dsDNA, where the 6 central base pairs ($(AT)_3 : (AT)_3$) are treated as a single QM-System and the remaining DNA, water and ions as MM part. [a]Corresponding assignment in the excitonically coupled 3 (AT) : (AT)-system (cf. Tab. S2). A double assignment indicates a combination of those states.

#	**E (eV)**	**f**	**CT**	**DL**	**contribution (character)**	**eq. exc. state**[a]
1	4.60	0.138	0.05	1.06	97% A29 ($\pi\pi^*$)	S_1
2	4.65	0.203	0.08	1.29	91% A31 ($\pi\pi^*$)	S_2
3	4.71	0.041	0.04	1.31	88% A11 ($\pi\pi^*$)	S_3
4	4.74	0.059	0.30	2.00	52% A09 ($\pi\pi^*$); 27% A09→T10 (CT)	S_5
5	4.75	0.113	0.02	1.08	94% A13 ($\pi\pi^*$)	S_4
6	4.79	0.141	0.04	1.77	90% A33 ($\pi\pi^*$)	S_6
7	4.82	0.010	0.06	1.08	96% A29 ($n\pi^*$)	S_7
8	4.86	0.006	0.19	1.55	72% A09 ($n\pi^*$); 16% A09→T10 (CT)	S_9
9	4.87	0.005	0.04	1.44	83% A29 ($n\pi^*$); 12% A09 ($\pi\pi^*$)	S_8
10	4.89	0.004	0.11	1.97	71% A11 ($\pi\pi^*$); 11% T10 ($n\pi^*$)	S_{10} + S_{11}
11	4.90	0.001	0.02	1.09	96% A31 ($n\pi^*$)	S_{13}
12	4.91	0.004	0.13	1.59	88% A33 ($\pi\pi^*$)	S_{12}
13	4.92	0.011	0.11	2.10	58% A09 ($n\pi^*$); 19% A31 ($\pi\pi^*$)	S_{14} + S_{15}
14	4.93	0.010	0.11	2.75	47% A13 ($\pi\pi^*$); 26% A31 ($\pi\pi^*$)	S_{14} + S_{15}
15	4.94	0.017	0.12	1.91	68% A13 ($n\pi^*$); 16% A31 ($\pi\pi^*$)	S_{14} + S_{15}
16	4.95	0.006	0.09	2.51	72% A13 ($n\pi^*$)	S_{14} + S_{15}
17	4.96	0.070	0.06	3.51	63% A33 ($\pi\pi^*$); 10% T32 ($\pi\pi^*$)	S_{17}
18	4.99	0.166	0.24	3.39	41% T10 ($\pi\pi^*$); 21% T30 ($\pi\pi^*$)	S_{18}
19	5.03	0.435	0.02	1.90	51% T08 ($\pi\pi^*$); 38% T32 ($\pi\pi^*$)	S_{19}
20	5.04	0.144	0.57	2.87	41% A11→T30 (CT); 24% A11→A31 (CT); 17% T12 ($\pi\pi^*$)	-

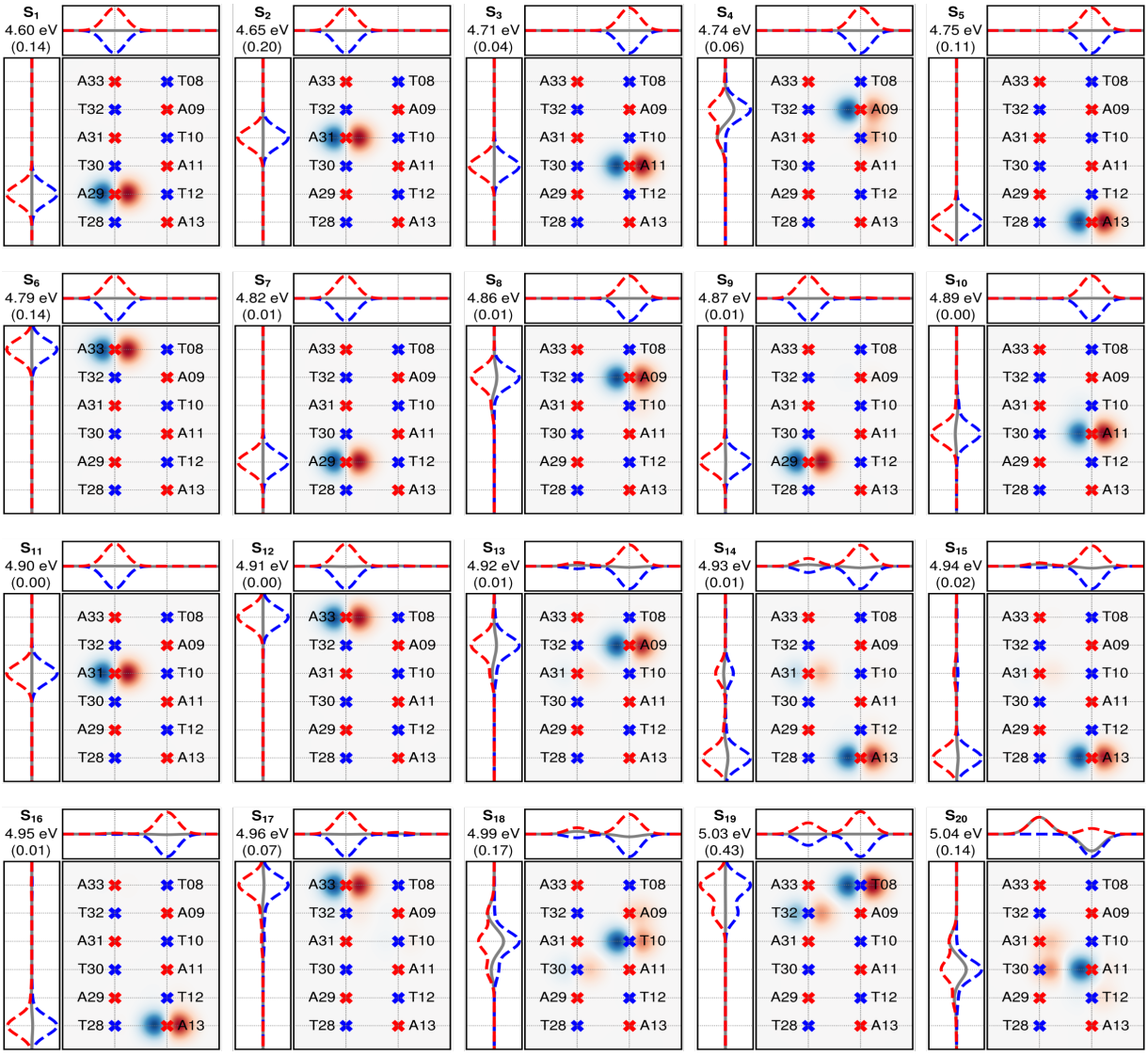

Figure S2: Graphical analysis in terms of the fractional transition density (FTD) of the 20 energetically lowest excited states obtained from the OM2/MM optimized geometry of $(\mathrm{dAdT})_{10} : (\mathrm{dAdT})_{10}$ dsDNA, where the QM region consists of the 6 central base pairs $((\mathrm{AT})_3 : (\mathrm{AT})_3)$. The textured area indicate the location (nucleobase) of the hole (blue) and electron (red) where the excitation is located. The left and top curves are the projection of these densities along the pair- and strand-axis, respectively.

Table S2: Summary and analysis of the 20 energetically lowest excited states obtained from the OM2/MM optimized geometry of $(dAdT)_{10} : (dAdT)_{10}$ dsDNA, where the QM-System consists of 3 sub-systems containing two base pairs each (3 (AT) : (AT)). The sub-systems are then coupled using the transition dipole approximation (TDA). [a] Excitonic wavefunction obtained from diagonalization of the excitonic hamiltonian.

#	**E (eV)**	**f**	**CT**	**DL**	**contribution (character)**	**wavefunction**[a]
1	4.60	0.163	0.03	1.03	98% A29 ($\pi\pi^*$)	$1.0\ \|0\ 0\ 1\rangle$
2	4.68	0.255	0.11	1.31	91% A31 ($\pi\pi^*$)	$1.0\ \|0\ 1\ 0\rangle$
3	4.72	0.095	0.05	1.55	77% A11 ($\pi\pi^*$); 11% A13 ($\pi\pi^*$)	$0.9\ \|0\ 2\ 0\rangle$ $- 0.3\ \|0\ 0\ 2\rangle$
4	4.75	0.049	0.01	1.06	95% A13 ($\pi\pi^*$)	$1.0\ \|0\ 0\ 2\rangle$
5	4.77	0.033	0.02	1.49	72% A09 ($\pi\pi^*$); 14% A33 ($\pi\pi^*$)	$1.0\ \|1\ 0\ 0\rangle$
6	4.80	0.198	0.03	1.53	75% A33 ($\pi\pi^*$); 20% A09 ($\pi\pi^*$)	$1.0\ \|2\ 0\ 0\rangle$
7	4.81	0.011	0.04	1.02	99% A29 ($n\pi^*$)	$1.0\ \|0\ 0\ 3\rangle$
8	4.86	0.028	0.03	1.17	88% A29 ($\pi\pi^*$); 11% T28 ($\pi\pi^*$)	$1.0\ \|0\ 0\ 4\rangle$
9	4.88	0.005	0.07	1.04	99% A09 ($n\pi^*$)	$1.0\ \|3\ 0\ 0\rangle$
10	4.89	0.010	0.05	2.28	44% A11 ($\pi\pi^*$); 40% A13 ($n\pi^*$); 13% T10 ($\pi\pi^*$)	$0.8\ \|0\ 3\ 0\rangle$ $+ 0.6\ \|0\ 0\ 5\rangle$
11	4.89	0.018	0.04	2.03	60% A13 ($n\pi^*$); 30% A11 ($\pi\pi^*$)	$- 0.6\ \|0\ 3\ 0\rangle$ $+ 0.8\ \|0\ 0\ 5\rangle$
12	4.90	0.004	0.14	1.64	87% A33 ($\pi\pi^*$)	$1.0\ \|4\ 0\ 0\rangle$
13	4.91	0.001	0.02	1.02	99% A31 ($n\pi^*$)	$1.0\ \|0\ 4\ 0\rangle$
14	4.93	0.006	0.02	1.20	84% A13 ($n\pi^*$); 16% T12 ($n\pi^*$)	$1.0\ \|0\ 0\ 6\rangle$
15	4.93	0.006	0.06	1.63	61% A09 ($n\pi^*$); 18% A33 ($n\pi^*$)	$1.0\ \|5\ 0\ 0\rangle$
16	4.94	0.079	0.08	1.72	77% A31 ($\pi\pi^*$); 11% A11 ($\pi\pi^*$)	$1.0\ \|0\ 5\ 0\rangle$
17	4.96	0.008	0.06	2.02	67% A33 ($\pi\pi^*$); 18% A09 ($n\pi^*$); 12% T32 ($n\pi^*$)	$1.0\ \|6\ 0\ 0\rangle$
18	4.97	0.450	0.05	2.46	58% T10 ($\pi\pi^*$); 23% T30 ($\pi\pi^*$); 13% A11 ($n\pi^*$)	$1.0\ \|0\ 6\ 0\rangle$
19	5.01	0.490	0.02	1.98	50% T08 ($\pi\pi^*$); 36% T32 ($\pi\pi^*$)	$1.0\ \|7\ 0\ 0\rangle$
20	5.03	0.358	0.04	1.81	61% T28 ($\pi\pi^*$); 28% T12 ($\pi\pi^*$)	$1.0\ \|0\ 0\ 7\rangle$

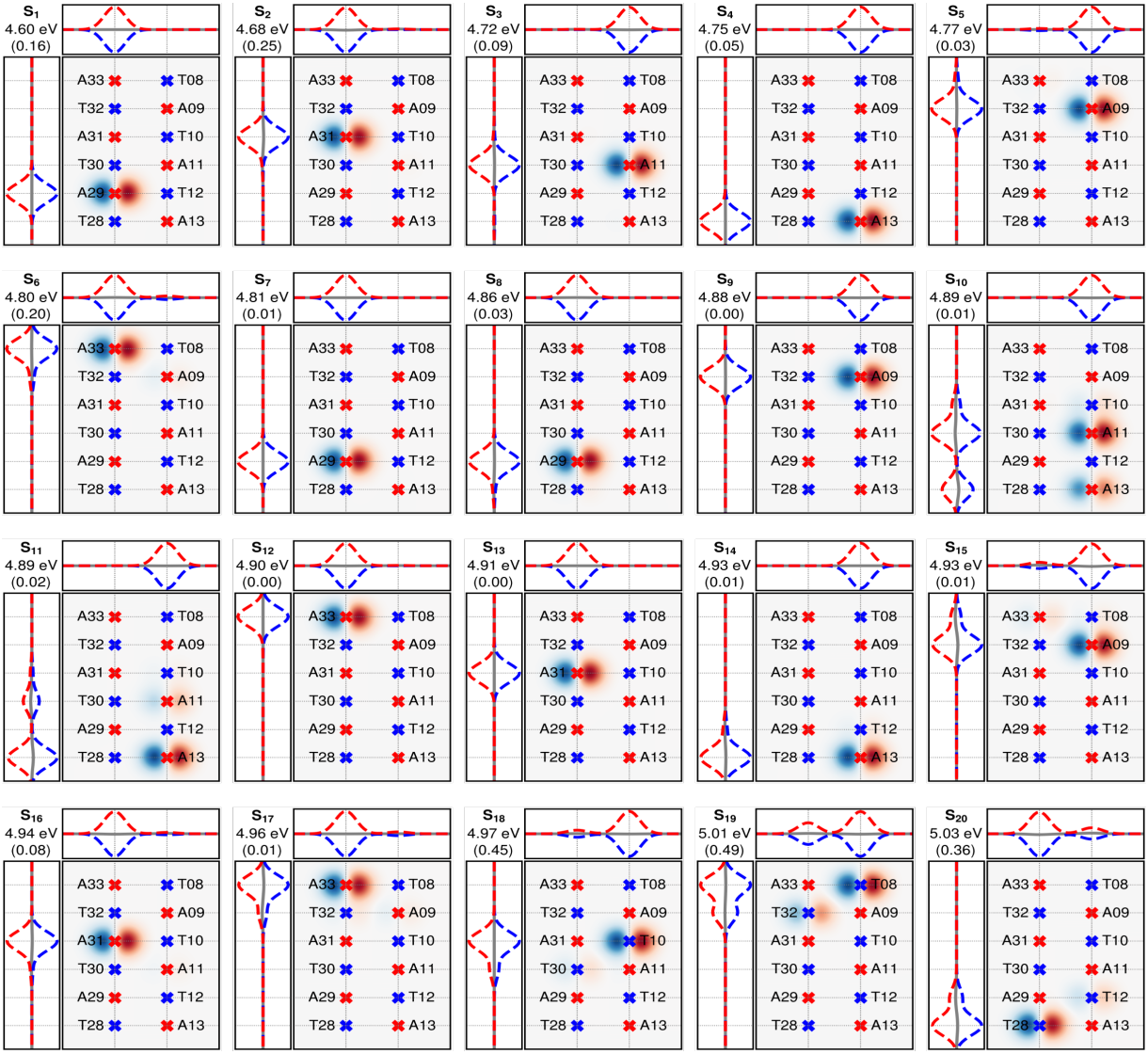

Figure S3: Graphical analysis in terms of the fractional transition density (FTD) of the 20 energetically lowest excited states obtained from the OM2/MM optimized geometry of $(dAdT)_{10} : (dAdT)_{10}$ dsDNA, where the QM region consists of 3 sub-systems containing two base pairs each (3(AT) : (AT)). The sub-systems are coupled using the transition dipole approximation (TDA). The textured area indicates the location (nucleobase) of the hole (blue) and electron (red) where the excitation is located. The left and top curves are the projection of these densities along the pair- and strand-axis, respectively.

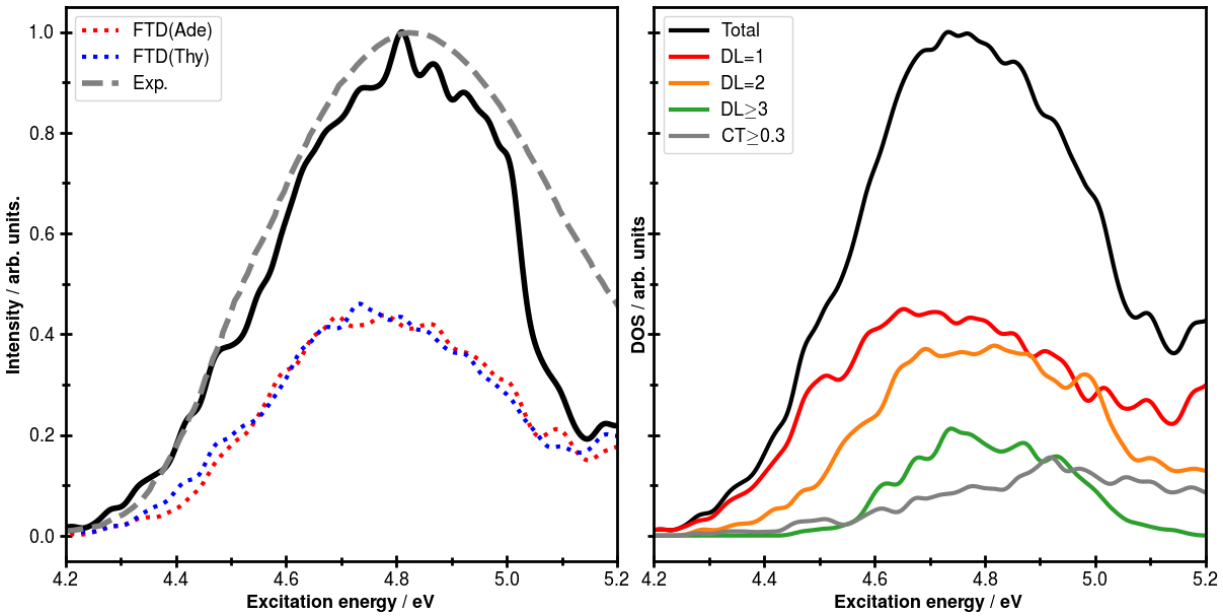

Figure S4: First absorption band of the UV/Vis spectrum averaged over geometries obtained form NVT-MD simulations of the $[(\mathrm{AT}):(\mathrm{AT})]_3$ trimer embedded in $(\mathrm{dAdT})_{10}:(\mathrm{dAdT})_{10}$ dsDNA solvated by water. Left panel: Oscillator strengths convoluted by a Lorentzian (black line, width 0.015 eV) and the contributions of excitations in Adenine (red) and Thymine (blue) to the transition density. The gray dotted lines indicate the absorption spectrum of $(\mathrm{dAdT})_{10}:(\mathrm{dAdT})_{10}$ in aqueous buffered solutions reproduced from Fig. 12 of Ref.[10]. Right panel: Total density of states (black) and decomposition into localized states (blue, DL = 1), delocalized states where the excitation is delocalized over two (DL = 2) or more (DL $\geq$ 3) bases, and states with charge transfer contributions (CT $\geq$ 0.3).

Fitting Parameters

The parameters of Tab. S3 are obtained from by fitting the following model functions to the populations of Fig. 3 of the main text:

$$P_1(t) = B\exp\left(-\frac{t}{\tau_2}\right) + Y_0 \tag{6}$$

$$P_2(t) = B\left[C\exp\left(-\frac{t}{\tau_2}\right) + (1-C)\exp\left(-\frac{t}{\tau_3}\right)\right] + Y_0 \tag{7}$$

$$P_{1+2}(t) = A\exp\left(-\frac{t}{\tau_1}\right) + B\left[(1-C)\exp\left(-\frac{t}{\tau_2}\right) + C\exp\left(-\frac{t}{\tau_3}\right)\right] + Y_0 \tag{8}$$

Table S3: Parameters obtained from fitting the graphs in Fig. 3 of the main text. Parameters marked as "-" have not been fitted. [a]Model functions used to fit the curves are given by Eqs. (6), (7) and (8).[b]Average life time obtained from the weighted sum of the individual components.

Curve	**Model**	**A**	**B**	**C**	$\mathbf{Y}_0$	τ_1 / **fs**	τ_2 / **ps**	τ_3 / **ps**	$\langle\tau\rangle$ / **ps**[b]	$\mathbf{R}^2$
1-S_0	2	-	0.66	0.53	-	-	0.70	74.75	35.5	0.98
S_L	1+2	-0.85	0.31	0.43	-	48	0.13	2.06	0.89	0.92
S_E	1	-	0.31	-	0.11	-	0.02	-	0.02	0.15
S_1	1+2	-0.84	0.21	0.33	-	68	0.18	1.95	0.88	0.88

Fractional transition density analysis

In order to analyze the location of the excited states in time-dependent terms we calculated average FTD values along the trajectories, which is shown in Fig. S5 (again normalized to the number of trajectories in the excited state at a given time). We have used two different patterns for selecting the fragments: (i) using the nucleobases adenine (red curve) and thymine (blue curve) and (ii) using the two strands of the dsDNA (green and orange curve). Since we are dealing with a heteropolymorphic duplex and both strands are therefore built from the same (but complementary) sequence of alternating adenines and thymines, both strands are excited equally by the laser pulse. This symmetry is not broken along the simulations and both strands keep on average equally excited, while on the single trajectory level the location of the excitation is frequently oscillating from one strand to the other. This is also consistent with the results from Fig. 4B of the main text, since either the excitation is localized at one strand, or at later times delocalized over both strands. Both of these cases result in a FTD of 0.5 for each of the strands, since in the localized case about half of the trajectories exhibit excitation on strand A and half on strand B, while in the delocalized case the excitation is equally distributed over strands A and B.

In agreement with experimental findings of Ref.[11] adenine and thymine contribute equally to the excitation at $t = 0$. However, in the following few 200 fs the population is transferred from thymine to adenine until a steady excitation level of thymine at ∼20% and consequently of adenine at ∼80% is reached (cf. Fig. S5 of the main text). This finding is consistent with

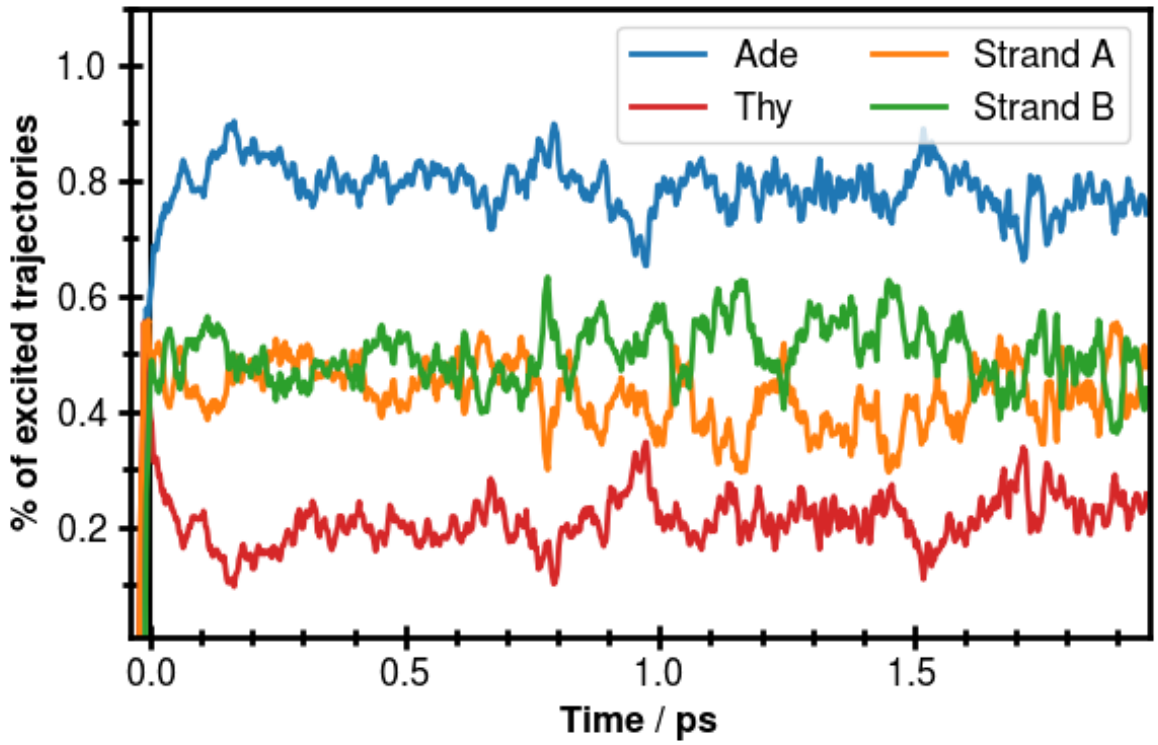

Figure S5: Averaged fractional transition density (FTD) for all adenines (red, Ade) and all thymines (blue, Thy), or strand A (orange) and strand B (green), respectively, showing equal amount of excitation in both strands and a dominant excitation in adenine.

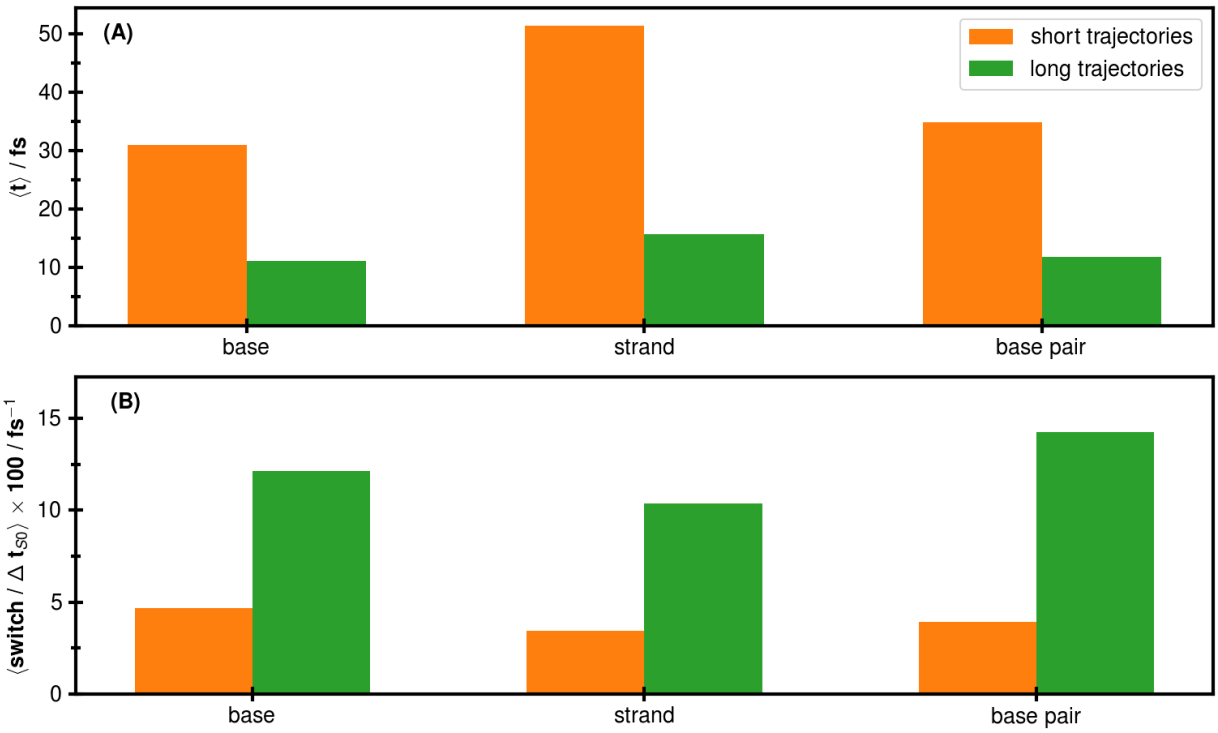

Figure S6: Statistical analysis of FTD, where only the maximum FTD value is considered for averaging. The trajectories are divided into short trajectories (orange), which decay to the ground-state within the first 800 fs, and long trajectories (green) which reside for more than 800 fs in the excited state. **(A)** Average duration an excitation resides at a time dominantly (max FTD > 0.8) on one nucleobase (left), within a base pair (middle) and within one of the strands (right). **(B)** Averaged rate for changing the location of the excitation with respect to a single base (left), horizontally between the strands (middle) and vertically along the stacked base pairs (right).

the short time constant found for the S_L population in Fig. 3 of the main text, which is identical to the experimentally determined lifetime of dAMP[12]. Together with the findings that (i) the DL value (cf. Fig. 4A of the main text) is increasing with time towards the delocalization of the excitation and (ii) from the POS value (cf. Fig. 4B of the main text) it becomes evident that the amount of delocalization between the strands increases, it can be concluded that the energy transport is dominantly conducted through adenine.

In Fig. S6A we show the average time an excitation resides at a single nucleobase (left), within a strand or within a pair of nucleobases. We divided the trajectories in 2 classes, as described in the main text. One group is classified as short and decays within 800 fs to the

ground state. The second group is classified as long and stays more than 800 fs in the excited state. Excitations in short trajectories are in average for 31 fs at a time located on a single nucleobase before switching to another, which is two times as longer than for the long living trajectories (11 fs). The same trend is found for the excitation being located within a base pair (35 fs vs. 11 fs) and a single strand (51 fs vs. 16 fs). The large difference in the latter case indicates that in the early stages of the excited state dynamics the excitation energy is dominantly transported within the strand, while for longer living trajectories inter-strand excitation energy transport is becoming more important (cf. Figs. 4B and 5 of the main text).

The rates of changing the location of an excitation from one base to another are shown in Fig. S6B (left), which support the previous findings. The nucleobase on which the excitation is dominantly localized, is changed in average 12 times per 100 fs in long trajectories, compared to 5 switches per 100 fs for short trajectories (Fig. S6B). The same trend holds for switching from one strand to the other (0.10 fs^{-1} vs. 0.03 fs^{-1}) and transport of the excitation within the stack (0.14 fs^{-1} vs. 0.04 fs^{-1}).

References

(1) Nogueira, J. J.; Plasser, F.; González, L. *Chem. Sci.* **2017**, *8*, 5682–5691.

(2) Plasser, F.; Aquino, A. J.; Hase, W. L.; Lischka, H. *J. Phys. Chem. A* **2012**, *116*, 11151–11160.

(3) Plasser, F.; Lischka, H. *J. Chem. Theory Comput.* **2012**, *8*, 2777–2789.

(4) Tretiak, S.; Mukamel, S. *Chem. Rev.* **2002**, *102*, 3171–3212.

(5) Luzanov, A.; Zhikol, O. *Int. J. Quantum Chem.* **2010**, *110*, 902–924.

(6) Luzanov, A.; Prezhdo, O. *Int. J. Quantum Chem.* **2005**, *102*, 582–601.

(7) Bouvier, B.; Gustavsson, T.; Markovitsi, D.; Millié, P. *Chem. Phys.* **2002**, *275*, 75–92.

(8) Fernandez-Alberti, S.; Makhov, D. V.; Tretiak, S.; Shalashilin, D. V. *Phys. Chem. Chem. Phys.* **2016**, *18*, 10028–10040.

(9) Martin, R. L. *J. Chem. Phys.* **2003**, *118*, 4775–4777.

(10) Bouvier, B.; Dognon, J.-P.; Lavery, R.; Markovitsi, D.; Millié, P.; Onidas, D.; Zakrzewska, K. *J. Phys. Chem. B* **2003**, *107*, 13512–13522.

(11) Kwok, W.-M.; Ma, C.; Phillips, D. L. *J. Phys. Chem. B* **2009**, *113*, 11527–11534.

(12) Markovitsi, D.; Sharonov, A.; Onidas, D.; Gustavsson, T. *ChemPhysChem* **2003**, *4*, 303–305.

Chapter 5

SOLVATION DYNAMICS OF A SINGLE WATER MOLECULE PROBED BY INFRARED SPECTRA – THEORY MEETS EXPERIMENT

Reproduced with permission from:

M. Wohlgemuth, M. Miyazaki, M. Weiler, M. Sakai, O. Dopfer, M. Fujii, and R. Mitrić:
"Solvation dynamics of a single water molecule probed by infrared spectra–theory meets experiment,"
Angew. Chem. Int. Ed., **53**, 14601–14604 (2014).

http://dx.doi.org/10.1002/anie.201409047

Solvation Dynamics

DOI: 10.1002/anie.201409047

Solvation Dynamics of a Single Water Molecule Probed by Infrared Spectra—Theory Meets Experiment**

Matthias Wohlgemuth, Mitsuhiko Miyazaki, Martin Weiler, Makoto Sakai, Otto Dopfer, Masaaki Fujii,* and Roland Mitrić**

Abstract: *The dynamics and energetics of water at interfaces or in biological systems plays a fundamental role in all solvation and biological phenomena in aqueous solution. In particular, the migration of water molecules is the first step that controls the overall process in the time domain. Experimentally, the dynamics of individual water molecules is nearly impossible to follow in solution, because signals from molecules in heterogeneous environments overlap. Although molecular dynamics simulations do not have this restriction, there is a lack of experimental data to validate the calculated dynamics. Here, we demonstrate a new strategy, in which the calculated dynamics are verified by measured time-resolved infrared spectra. The coexistence of fast and slow migrations of water molecules around a CONH peptide linkage is revealed for a model system representative of a hydrate peptide.*

The fruitful interplay between theory and experiment is a major driving force for significant progress in physical chemistry and molecular physics. For example, molecular clusters, in which molecules interact by weak intermolecular forces such as hydrogen bonding and van der Waals forces, have been studied as models for solvation structures since the late 1970s.[1] However, their structures were mostly investigated independently by quantum chemical calculations and spectroscopy, and the conclusions were sometimes unrealistic from today's point of view.[2] Such structural studies experienced "a quantum leap" in the 1990s, when spectroscopists and theoreticians started collaborations. Spectroscopists recorded infrared (IR) spectra with novel high-power IR lasers, and theoreticians in turn suggested various possible cluster structures. Comparison between the spectral signatures in the measured and computed IR spectra then provided definite evidence as to which structure was observed.[3] Nowadays, this combined approach is the de facto standard in the cluster field and has revealed macroscopic properties associated with molecular parameters, such as the structure of bulk water from hydrogen-bonded networks in water clusters[4] and the photostability of DNA bases in their gas-phase clusters.[5]

What is the current situation for the chemical reaction and solvation *dynamics* in molecular clusters? Ultrafast laser experiments measure the time evolution of reaction products not only by simple pump–probe techniques but also by various sophisticated time-resolved laser methods, such as time-resolved photoelectron spectroscopy.[6] These studies mainly focus on the dissociation or the change in the electronic structure of molecules and clusters, because of the inherently low-energy resolution of femtosecond laser pulses, which is limited by the Heisenberg uncertainty principle. Thus, the experimental interest has focused on the assignment of reaction fragments and the evolution of molecular electronic states during the reaction. These are

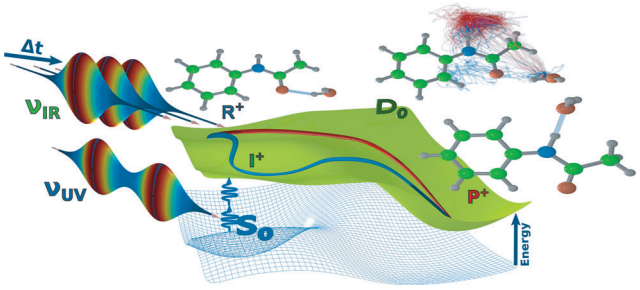

Figure 1. Scheme illustrating the experimental pump–probe procedure and dynamic time evolution after the ionization of the *trans*-acetanilide–water (AA–W) cluster. The CO-bound isomer is ionized by size- and isomer-selective two-photon ionization ($2\nu_{UV}$, pump process) from the neutral ground state (S_0, blue surface) to the cationic ground state (D_0, green surface). There, the W molecule migrates from the hydrogen-bonded CO site (AA^+–W^{CO}, left structure, R^+) to the NH-bound isomer (AA^+–W^{NH}, right structure, P^+) by two different pathways. This motion is monitored by TRIR spectra (ν_{IR}) measured at variable delay Δt (probe process). The red trace indicates the fast migration channel with a direct steep descent pathway, and the blue curve illustrates a slow migration channel through a local minimum (I^+). The middle structure illustrates the migration pathways derived from the MD simulations, whereby the red and blue lines indicate the movement of W for the fast and slow channel trajectories, respectively.

[*] M. Wohlgemuth, Prof. R. Mitrić
Institut für theoretische und physikalische Chemie
Julius-Maximilians-Universität Würzburg
97074 Würzburg (Germany)
E-mail: roland.mitric@uni-wuerzburg.de

Dr. M. Miyazaki, Dr. M. Weiler, Prof. M. Sakai, Prof. M. Fujii
Chemical Resources Laboratory, Tokyo Institute of Technology
Yokohama 226-8503 (Japan)
E-mail: mfujii@res.titech.ac.jp

Prof. O. Dopfer
Institut für Optik und Atomare Physik
Technische Universität Berlin
10623 Berlin (Germany)
E-mail: dopfer@physik.tu-berlin.de

[**] This study was supported by MEXT (innovative area 2503 Japan), the Core-to-Core Program of JSPS, and the DFG (DO 729/4, ENP-MI-1236).

Supporting information for this article (theory for TRIR spectra based on the MD "on the fly"; computational details; reaction pathways for isomerization; Figures S1 and S2; movies of water motions in representative trajectories of the fast, the slow, and all channels) is available on the WWW under http://dx.doi.org/10.1002/anie.201409047.

important parameters of chemical reactions, but the *structural* time evolution is not probed directly. On the other hand, theoretical approaches to the reaction dynamics treat not only the electronic states but also provide the molecular geometry along the reaction pathway. Thus, molecular dynamics (MD) can give indeed a detailed microscopic picture of the reaction pathways and mechanisms.

The experimental limitations related to probing structural dynamics discussed above may not be a serious problem if only chemical reactions of small molecules such as diatomics are studied, because then the reaction coordinate is simple and straightforward. However, in larger and biologically important molecules and clusters, the reaction and solvation coordinate usually stretches across multidimensional space and is not immediately obvious. To overcome this limit, we present here the fruitful interplay between theoretical simulation and advanced laser spectroscopy, which has the potential to expand the reaction dynamics question indeed from simply "how fast?" to "which way?".[7] Such a step would be analogous to the above-mentioned qualitative advances in the static structural characterization of molecular clusters.

Recently, picosecond pump–probe time-resolved IR (ps TRIR) spectra were reported for probing the migration dynamics of a single water molecule (W) around the CONH peptide linkage in the H-bonded *trans*-acetanilide–water (AA–W) cluster.[8] The TRIR spectra were obtained by combining a two-color tunable ps laser system ($\nu_{UV} + \nu_{IR}$) with appropriate time and spectral resolution (3 ps, 12 cm^{-1}) with a molecular beam time-of-flight mass spectrometer (Figure 1). The solvent molecule W in $AA–W^{CO}$ is initially H-bonded as a proton donor at the CO site in the neutral ground state (S_0). When $AA–W^{CO}$ is resonantly ionized via the first excited state (S_1) to the cationic ground state (D_0) using size- and isomer-selective two-photon ionization ($2\nu_{UV}$, pump process), the interaction potential changes drastically. As

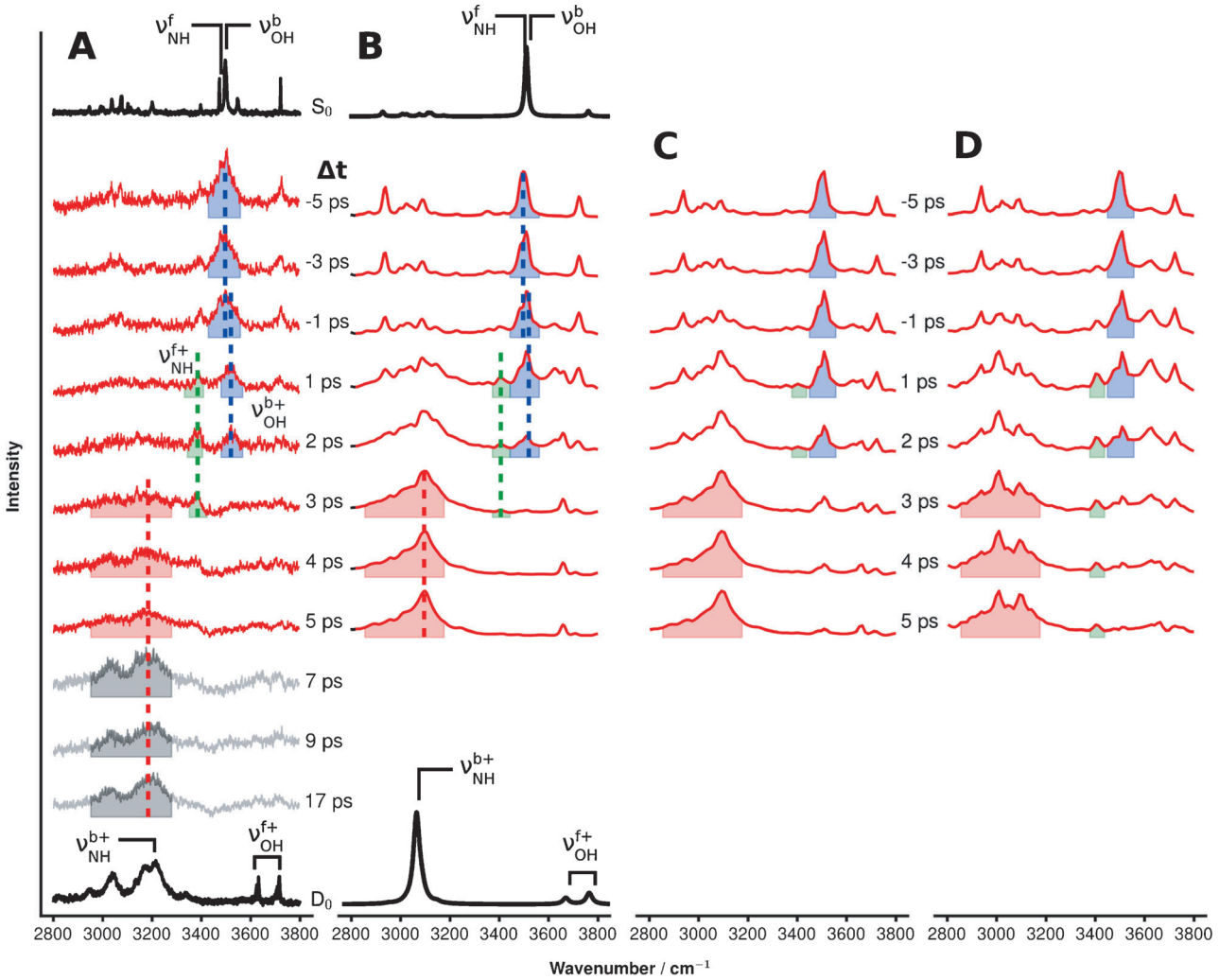

Figure 2. TRIR spectra of $AA^+–W$ from the A) ps experiment[8] and B) MD simulations. The S_0 and D_0 spectra are stationary IR spectra of the CO-bound and NH-bound isomers in the neutral and cationic states determined by ns lasers (A) and DFT harmonic frequency calculations for the optimized structures (B). The weak bands at around ν^f_{NH} and ν^b_{OH} in (A) are combination bands promoted by anharmonic vibrational coupling and thus do not appear in the theoretical spectrum in (B) with harmonic approximations. The highlighted areas indicate the signals uniquely attributed to the NH-bonded isomer (red, P^+), the intermediate structure (green, I^+) and the CO-bound geometry (blue, R^+). The TRIR spectra calculated for trajectories of the fast (C) and slow (D) migration channels are shown separately.

a consequence, W is released from the now repulsive CO site and migrates in an exothermic reaction toward the most attractive NH site. Tunable IR laser radiation (ν_{IR}) introduced at a variable delay Δt after the ionization event probes the isomerization dynamics. Resonant vibrational excitation with ν_{IR} induces the dissociation of the cluster. Thus, the transient IR spectrum can be measured as depletion of the parent cluster ion intensity. The recorded TRIR spectra monitor the W migration in AA^+–W in real time by means of the H-bonded OH stretching mode (ν_{OH}^{b+}) of W in the initially formed AA^+–W^{CO} cation (reactant R^+, blue), the free NH stretching mode (ν_{NH}^{f+}) of the intermediate (I^+, green), in which W binds neither to the CO nor the NH site, and the H-bonded NH stretching mode (ν_{NH}^{b+}) of the AA^+–W^{NH} reaction product (P^+, red). The blue band (R^+) disappears within 3 ps, the time needed to release W from the CO site. At the same time, the green band (I^+) rises and disappears again at about 5 ps. In parallel, the red band (P^+) appears and grows in intensity. These events directly prove that W is released within 3 ps after the ionization and migrates to the NH site via a yet unknown intermediate. Thus, based on these experimental data, the water migration was interpreted as a simple two-step reaction $R^+ \rightarrow I^+ \rightarrow P^+$, with an overall migration time of 5 ps at an ionization excess energy of $E_{exc} = 9000\ cm^{-1}$.[8] The time evolution of the three spectral signatures of R^+, I^+, and P^+ are summarized in Figure 3A. Any $P^+ \rightarrow I^+/R^+$ back reaction is quenched by efficient intracluster vibrational energy redistribution (IVR), which quickly removes the energy from the reaction coordinate.[8] We note that previous simple MD simulations on the analogous formanilide–W cluster fail to properly reproduce essential features of this reaction, including the time constant, the existence of I^+, and the absence of the back reaction.[9]

Although the experimental ps TRIR spectra yield new valuable insight into general reaction parameters (overall time constants, existence of an intermediate), important details of the reaction path (geometry, energetics, barriers) and the competition between multiple possible reaction paths remained unclear.[8] To this end, a sophisticated ab initio MD approach has now been developed to reveal the many more details of the reaction encoded in the highly informative TRIR spectra. To simulate the TRIR spectra, we have carried out "on the fly" MD simulations in the framework of density functional theory and have combined them with the Wigner phase space approach for simulation of the pump–probe spectra.[10] Briefly, the time evolution of the phase space density in the classical limit is described by the Liouville equation $\dot{\rho} = \{H, \rho\}$, where the Hamiltonian function $H = H_0(q,p) - \boldsymbol{\mu}(q)\boldsymbol{\varepsilon}(t)$ is composed of the field-free Hamiltonian H_0 and the interaction with the laser field $\boldsymbol{\varepsilon}(t)$.[11] From the rate of energy absorption $d\langle E\rangle/dt$, the total absorption of energy for a given frequency ω and time delay Δt, corresponding to the measured transient TRIR spectrum, has been calculated [Eq. (1)].

$$\begin{aligned}\langle S_{probe}(\omega,\Delta t)\rangle &= \int_{-\infty}^{\infty} dt \frac{d\langle E\rangle}{dt} = \int_{-\infty}^{\infty} dt \iint d\mathbf{q}d\mathbf{p} H_0\{H,\rho\} \\ &= \sum_{i=1}^{N_{traj}} \int_{-\infty}^{\infty} dt \frac{d\boldsymbol{\mu}(\mathbf{q}_i(t))}{dt} \varepsilon_0 \exp\left(-\frac{(t-\Delta t)^2}{2\sigma^2}\right) \cos\omega t \end{aligned} \quad (1)$$

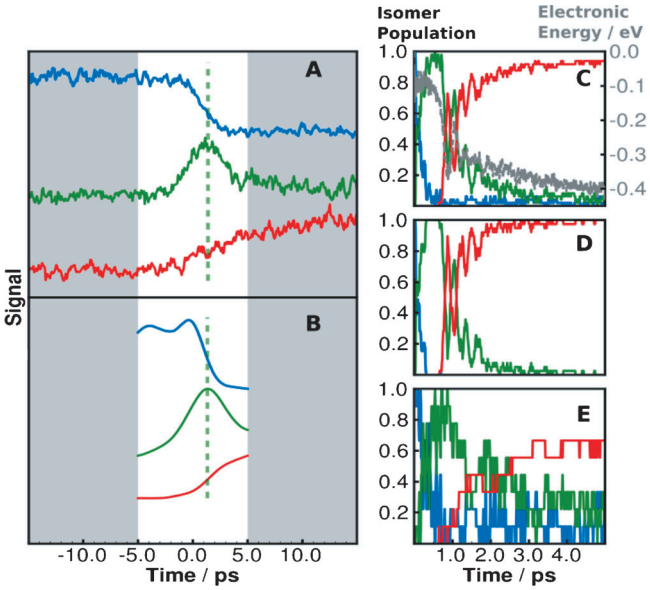

Figure 3. Left: Time evolution of the three vibrational resonances of AA^+–W (ν_{OH}^{b+}, ν_{NH}^{f+}, ν_{NH}^{b+}, indicated by blue, green, and red lines in Figure 2 A,B) determined from A) the experimental TRIR spectra[8] and B) the TRIR spectra from the MD simulations. The white area in (A) and (B) indicates the time interval of the MD simulations [−5 ps, +5 ps], and the dashed green lines show the maxima of the I^+ signal attributed to the free NH stretch mode in the cationic state (ν_{NH}^{f+}). Right: C) Averaged populations of the total ensemble and the trajectories attributed to D) the fast and E) the slow channels, with the CO-bound isomer (blue, R^+), the intermediate structure (green, I^+), and the NH-bound isomer (red, P^+). The gray dashed line in (C) shows the averaged electronic energy from the MD simulations.

The phase space density has been represented by a discrete set of classical trajectories, which have been propagated in the neutral (S_0) and the cationic (D_0) states (Figure 4). The electric field of the probe laser pulse is assumed to have a Gaussian shape with the width σ. To take also the pump pulse width into account, the transient TRIR spectra are convoluted by the change in the population of the cationic state $dP(t)/dt$, which is derived from the experiment, leading to the expression for the TRIR signal given in Equation (2).

$$\langle S_{pump-probe}(\omega,\Delta t)\rangle = \int_{-\infty}^{\infty} dt \langle S_{probe}(\omega,\Delta t - t)\rangle \frac{dP(t)}{dt} \quad (2)$$

As illustrated in Figure 1, we identified two competing mechanisms for the experimentally probed water migration from the initial CO site to the final NH site triggered by photoionization. While in the first channel W migrates along an almost barrierless path across the methyl group (Figure 1, red lines), in the second path W is trapped in a local minimum above the phenyl ring (Figure 1, blue lines). Movies of water motion in representative trajectories of the first and second channels are available in the Supporting Information. The branching ratio for the two paths is 70:30 in favor of the first channel. Figure 3 shows the isomer populations of the first (Figure 3D) and second process (Figure 3E) obtained from the MD simulations. The intermediate state, where the CO–W hydrogen bond is already broken, but the NH–W

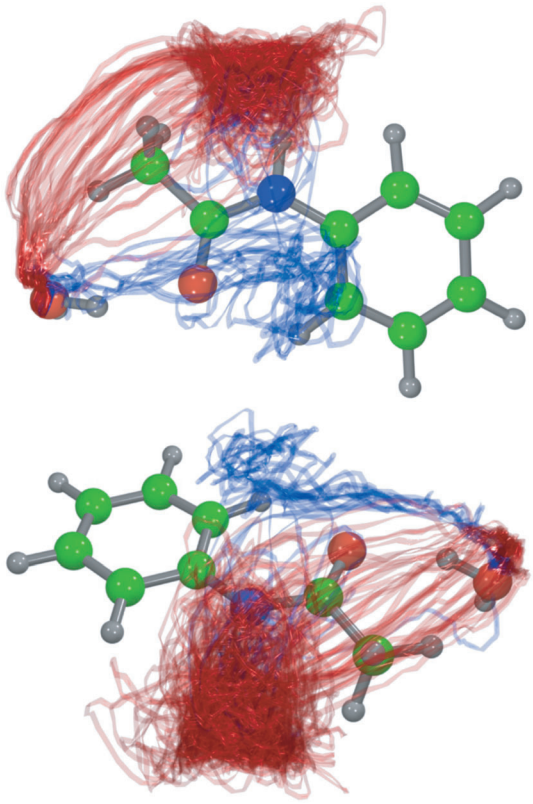

Figure 4. Trajectories obtained from MD simulations in the cationic state shown from two different perspectives. The red and blue curves illustrate the path of the water molecule on migrating from the CO site to the NH site. The blue and red curves are attributed to the slow and fast migration channels, respectively.

hydrogen bond is not yet formed, is reached in both cases within 1 ps. Subsequently, the first path relaxes quickly within further 0.5 ps to the final NH-bound state ("fast channel", Figure 3D), while in the second case complete W transfer is not reached even after 5 ps ("slow channel", Figure 3E). This new two-channel dynamics substantially extends and revises our previous simple one-channel two-step $R^+ \rightarrow I^+ \rightarrow P^+$ mechanism, which was solely derived from the experimental data.[8]

The reliability of the diversity of the reaction pathways predicted by the MD simulations can be tested with high sensitivity by direct comparison between the simulated and measured TRIR spectra (Figure 2). Although the fast channel does not match the initial simple two-step interpretation of the experiment,[8] the simulated TRIR spectra including all trajectories (Figure 2B) well reproduce the observed TRIR spectra (Figure 2A). The TRIR spectra corresponding to the slow channel (Figure 2D), which includes the trapping of W, has a significant intensity for I^+ (green) even at $\Delta t = 5$ ps, whereas the observed TRIR spectra (Figure 2A) do not. This difference clearly indicates that the observed TRIR spectra cannot be reproduced by the slow channel alone, and thus the initial simple two-step model[8] must be revised and extended. Further theoretical and experimental investigations on controlling and directing the reaction by adjusting the excess energy are now in progress.

In conclusion, water migration in AA^+–W includes both slow and fast reaction pathways, and the major channel observed in the ionization experiments is the fast one. It is stressed that this conclusion could only be derived from the direct comparison between the observed and simulated TRIR spectra. In the future, this novel strategy will be used to probe reliably the solvation and reaction dynamics in larger molecular systems such as highly solvated peptides. This approach will thus provide reliable insight into the fundamental mechanisms of various dynamic processes related to solvation at the single-molecule level, and opens the way to controlling the dynamics.

Received: September 15, 2014
Published online: November 27, 2014

Keywords: molecular dynamics · protein hydration · solvation dynamics · time-resolved spectroscopy

[1] a) D. H. Levy, *Adv. Chem. Phys.* **1981**, *47*, 323; b) A. W. Castleman, R. G. Keesee, *Acc. Chem. Res.* **1986**, *19*, 413; c) A. W. Castleman, K. H. Bowen, *J. Phys. Chem.* **1996**, *100*, 12911.
[2] S. K. Kim, E. R. Bernstein, *J. Phys. Chem.* **1990**, *94*, 3531.
[3] a) B. Brutschy, *Chem. Rev.* **2000**, *100*, 3891; b) T. Ebata, A. Fujii, N. Mikami, *Int. Rev. Phys. Chem.* **1998**, *17*, 331.
[4] a) A. Fujii, K. Mizuse, *Int. Rev. Phys. Chem.* **2013**, *32*, 266; b) J. A. Fournier, C. J. Johnson, C. T. Wolke, G. H. Weddle, A. B. Wolk, M. A. Johnson, *Science* **2014**, *344*, 1009; c) V. Buch, S. Bauerecker, J. P. Devlin, U. Buck, J. K. Kazimirski, *Int. Rev. Phys. Chem.* **2004**, *23*, 375.
[5] A. Abo-Riziq, L. Grace, E. Nir, M. Kabelac, P. Hobza, M. S. de Vries, *Proc. Natl. Acad. Sci. USA* **2005**, *102*, 20.
[6] a) A. Stolow, J. G. Underwood, *Adv. Chem. Phys.* **2008**, *139*, 497; b) A. Stolow, A. E. Bragg, D. M. Neumark, *Chem. Rev.* **2004**, *104*, 1719; c) D. M. Neumark, *Annu. Rev. Phys. Chem.* **2001**, *52*, 255; d) T. Suzuki, *Annu. Rev. Phys. Chem.* **2006**, *57*, 555.
[7] a) S. Takeuchi, S. Ruhman, T. Tsuneda, M. Chiba, T. Taketsugu, T. Tahara, *Science* **2008**, *322*, 1073; b) D. A. Blank, *Science* **2008**, *322*, 1056.
[8] K. Tanabe, M. Miyazaki, M. Schmies, A. Patzer, M. Schütz, H. Sekiya, M. Sakai, O. Dopfer, M. Fujii, *Angew. Chem. Int. Ed.* **2012**, *51*, 6604; *Angew. Chem.* **2012**, *124*, 6708.
[9] a) H. Tachikawa, M. Igarashi, T. Ishibashi, *J. Phys. Chem. A* **2003**, *107*, 7505; b) T. Ikeda, K. Sakota, Y. Kawashima, S. Yuiga, H. Sekiya, *J. Phys. Chem. A* **2012**, *116*, 3816.
[10] V. Bonačić-Koutecký, R. Mitrić, *Chem. Rev.* **2005**, *105*, 11.
[11] R. Mitrić, V. Bonačić-Koutecký, *Phys. Rev. A* **2007**, *76*, 031405.
[12] J. P. Perdew, K. Burke, M. Ernzerhof, *Phys. Rev. Lett.* **1996**, *77*, 3865.
[13] R. Krishnan, J. S. Binkley, R. Seeger, J. A. Pople, *J. Chem. Phys.* **1980**, *72*, 650.
[14] S. Grimme, *J. Comput. Chem.* **2004**, *25*, 1463.
[15] W. C. Swope, H. C. Andersen, P. H. Berens, K. R. Wilson, *J. Chem. Phys.* **1982**, *76*, 637.
[16] a) H. Jónsson, G. Mills, K. W. Jacobsen in *Classical and Quantum Dynamics in Condensed Phase Simulations* (Eds.: B. J. Berne, G. Ciccotti, D. F. Coker), World Scientific, Singapore, **1998**, p. 385; b) G. Henkelman, H. Jónsson, *J. Chem. Phys.* **1999**, *111*, 7010; c) G. Henkelman, G. Jóhannesson, H. Jónsson in *Progress on Theoretical Chemistry and Physics* (Ed.: S. D. Schwartz), Kluwer, Dordrecht, **2000**, p. 269; d) D. Sheppard, R. Terrell, G. Henkelman, *J. Chem. Phys.* **2008**, *128*, 134106.

Angewandte Chemie
Eine Zeitschrift der Gesellschaft Deutscher Chemiker

Supporting Information

69451 Weinheim, Germany

Solvation Dynamics of a Single Water Molecule Probed by Infrared Spectra—Theory Meets Experiment**

Matthias Wohlgemuth, Mitsuhiko Miyazaki, Martin Weiler, Makoto Sakai, Otto Dopfer, Masaaki Fujii,* and Roland Mitrić**

anie_201409047_sm_miscellaneous_information.pdf
anie_201409047_sm_all_movie.avi
anie_201409047_sm_fast_movie.avi
anie_201409047_sm_slow_movie.avi

Supporting Information

Theory for time-resolved pump-probe IR (TRIR) spectra based on the MD "on the fly"

In this section, we present a detailed description of the theoretical methodology for the simulation of the TRIR spectra, which is based the molecular dynamics (MD) "on-the-fly" carried out in the frame of density functional theory (DFT). For this purpose, we employ the Wigner representation in which the density operator of the system is represented by a phase space function $\rho(\boldsymbol{q},\boldsymbol{p})$ of the nuclear coordinates and momenta **q** and **p**. As in our previous work $\rho(\boldsymbol{q},\boldsymbol{p})$ is represented by an ensemble of independently propagated classical trajectories according to

$$\rho(\boldsymbol{q},\boldsymbol{p}) = \sum_{i=1}^{N_{traj}} \delta\big(\boldsymbol{q}-\boldsymbol{q}_{i,0}\big)\delta(\boldsymbol{p}-\boldsymbol{p}_{i,0}) \quad (1)$$

where N_{traj} represents the total number of trajectories and $\boldsymbol{q}_{i,0}$ and $\boldsymbol{p}_{i,0}$ are the initial positions and momenta of the i[th] trajectory. The Hamilton function for the system driven by a laser field $\boldsymbol{\epsilon}(t)$ is given by

$$H(\boldsymbol{p},\boldsymbol{q}) = H_0(\boldsymbol{q},\boldsymbol{p}) - \boldsymbol{\epsilon}(t)\cdot\boldsymbol{\mu}(q) \quad (2)$$

where H_0 is the field-free Hamiltonian and $\boldsymbol{\mu}(\boldsymbol{q}) = \boldsymbol{\mu_e}(\boldsymbol{q}) + \boldsymbol{\mu_N}(\boldsymbol{q})$ is the total dipole moment composed of the nuclear and electronic contributions. The time evolution of the phase space density is in the classical limit described by the Liouville equation

$$\dot{\rho} = \{H,\rho\}, \quad (3)$$

where $\{H,\rho\}$ represents the classical Poisson bracket. The solution of this equation is equivalent to the solution of the Hamilton equation of motion for the functions $\dot{\boldsymbol{q}}_i(t)$ and $\dot{\boldsymbol{p}}_i(t)$

$$\dot{\boldsymbol{q}}_i(t) = \frac{\partial H}{\partial \boldsymbol{p}_i} \quad (4)$$

$$\dot{\boldsymbol{p}}_i(t) = -\frac{\partial H}{\partial \boldsymbol{q}_i} = -\frac{\partial V(\boldsymbol{q}(t))}{\partial \boldsymbol{q}_i} + \frac{\partial \boldsymbol{\mu}(\boldsymbol{q}(t))}{\partial \boldsymbol{q}_i}\cdot\boldsymbol{\epsilon}(t), \quad (5)$$

where $-{}^{\partial V}/_{\partial \boldsymbol{q}_i} = \boldsymbol{F_i}$ are the forces acting on the nuclei obtained as gradients of the electronic potential energy surface $V(\boldsymbol{q}(t))$. For weak laser fields, which are employed in this work, the last term of Eq. (5) can be neglected and therefore the phase space ensemble can be propagated freely using quantum chemical MD "on the fly". For this purpose, we utilize the analytic energy gradients, which can be efficiently calculated within the density function theory and employed for the numerical solution of equations of motions Eq. (4) and Eq. (5) using the velocity Verlet algorithm.

In order to simulate the time-resolved pump-probe IR spectrum, we have to consider two interactions with the laser field, separated by the time delay Δt: (1) the first interaction with

the UV pump laser pulse centered at t = 0 ionizes the neutral system (S_0) and leads to the population of the cationic state (D_0), (2) the dynamics in the cationic state is probed by the second IR laser pulse centered at the time delay Δt with the form

$$\epsilon_{probe}(t) = \epsilon_0 \exp\left(-\frac{(t-\Delta t)^2}{2\sigma^2}\right)\cos\omega t \tag{6}$$

where ϵ_0 is the amplitude and σ is the width of the laser pulse. The rate of the energy absorption induced by the interaction with the probe field can be calculated in the phase space representation as

$$\frac{\mathrm{d}\langle E\rangle}{\mathrm{d}t} = \iint \mathrm{d}\boldsymbol{q}\mathrm{d}\boldsymbol{p}\, H_0(\boldsymbol{q},\boldsymbol{p},t)\dot{\rho}(\boldsymbol{p},\boldsymbol{q},t) = \iint \mathrm{d}\boldsymbol{q}\mathrm{d}\boldsymbol{p}\, H_0\{H(\boldsymbol{q},\boldsymbol{p},t),\rho(\boldsymbol{q},\boldsymbol{p},t)\} \tag{7}$$

By expanding the Poisson bracket and using partial integration, this can be reduced to

$$\frac{\mathrm{d}\langle E\rangle}{\mathrm{d}t} = \iint \mathrm{d}\boldsymbol{q}\mathrm{d}\boldsymbol{p}\, \rho(\boldsymbol{q},\boldsymbol{p},t)\frac{\mathrm{d}\boldsymbol{\mu}(\boldsymbol{q})}{\mathrm{d}t}\epsilon_0 \exp\left(-\frac{(t-\Delta t)^2}{2\sigma^2}\right)\cos\omega t \tag{8}$$

The total absorption of energy for a given frequency ω and time delay Δt, which corresponds to the experimental measured transient TRIR spectrum, can be calculated as

$$\langle S_{probe}(\omega,\Delta t)\rangle = \int_{-\infty}^{\infty}\mathrm{d}t\,\frac{\mathrm{d}\langle E\rangle}{\mathrm{d}t} = \int_{-\infty}^{\infty}\mathrm{d}t\,\iint \mathrm{d}\boldsymbol{q}\mathrm{d}\boldsymbol{p}\,\rho(\boldsymbol{q},\boldsymbol{p},t)\frac{\mathrm{d}\boldsymbol{\mu}(\boldsymbol{q})}{\mathrm{d}t}\epsilon_0 \exp\left(-\frac{(t-\Delta t)^2}{2\sigma^2}\right)\cos\omega t \tag{9}$$

By utilizing the representation of the phase space density by classical trajectories given in Eq. (1), this reduces to the following expression for the transient TRIR spectrum for the time delay Δt

$$\langle S_{probe}(\omega,\Delta t)\rangle = \sum_{i=1}^{N_{traj}}\int_{-\infty}^{\infty}\mathrm{d}t\,\frac{\mathrm{d}\boldsymbol{\mu}(\boldsymbol{q_i}(t))}{\mathrm{d}t}\epsilon_0 \exp\left(-\frac{(t-\Delta t)^2}{2\sigma^2}\right)\cos\omega t. \tag{10}$$

Note that this expression can be interpreted as a trajectory average of the windowed Fourier transform of the dipole derivative function of each trajectory, where the probe pulse envelope serves as a window. In order to take also the pump pulse width into account, the transient IR spectra are convoluted by the change in the population of the cationic state, which is obtained directly from the experiment. This leads to the following final expression for the simulation of time-resolved IR spectra

$$\langle S_{pump-probe}(\omega,\Delta t)\rangle = \int_{-\infty}^{\infty}\mathrm{d}t\,\langle S_{probe}(\omega,\Delta t - t)\rangle\frac{\mathrm{d}P(t)}{\mathrm{d}t} \tag{11}$$

where $\frac{dP(t)}{dt}$ is the rate of change of the cationic state population.

Computational Details

Throughout this work, all single-point calculations were carried out in the frame of density functional theory implemented in the Turbomole program package. We employ the gradient corrected Perdew-Burke-Ernzerhof (PBE) functional [12] and the valence triple zeta plus polarization (6-311G**) basis set [13], combined with the resolution of identity (RI) approximation in order to speed up the MD simulations. Note that also Grimme's dispersion correction (D3) [14] has been used throughout the simulations.

The initial conditions for the MD simulations were sampled from a 100 ps classical trajectory in the neutral ground state, which has been run at constant temperature of T = 100 K. This temperature has been chosen in order to reproduce the experimental excess energy after photoionization (Figure S1). After initial equilibration, we have sampled structures and velocities in regular time intervals, thus generating an ensemble of 50 trajectories, which were employed to investigate the isomerization and to simulate the TRIR spectra.

The MD simulations, starting from these initial conditions, were propagated forward for 5 ps in the D_0 cationic state and backward for 5 ps in the neutral S_0 ground state. The integration of the classical equations of motions has been performed using the velocity Verlet algorithm [15] with a time step of 0.1 fs, which is sufficiently small to obtain adequate conservation of energy. At each step of the trajectories, electronic and nuclear dipole moments were calculated in order to serve as basis for simulating the TRIR spectra according to Eq. (10). As probe pulse, we used a Gaussian-shaped laser pulse envelope with a full-width-at-half-maximum (FWHM) of 3 ps. The rise of the population of the cationic state $\frac{dP(t)}{dt}$ in Eq. (11) has been modeled by a Gaussian-shaped function with a FWHM of 2.88 ps, which both correspond to the experimentally determined values. The transient TRIR spectra were calculated in delay intervals from −5 to +5 ps according to Eq. (11).

Reaction pathways for isomerization

In addition to the direct MD simulations, which give direct inside into the isomerization pathways and their branching ratios, we have also carried out an extensive minimum energy path search. For this purpose, we have combined the nudged elasting band (NEB) method with density functional theory calculations. [16] In the NEB method, a string of molecular configurations (images) is spanned between the two states, e.g. two local

minima on the potential energy surface. The initial pathway connecting the initial and final states can be obtained, for example, by interpolation. Starting from this initial guess, the images along the path are relaxed through a force projection scheme. The total force on each image in the NEB method is

$$\boldsymbol{F}^{NEB}(\boldsymbol{q}_i) = \boldsymbol{F}_i^{\perp} + \boldsymbol{F}_i^{\parallel}$$

where $\mathbf{q}_i$ is the configuration (molecular geometry) of one image. The force $\boldsymbol{F}_i^{\perp}$ is the force on the i^{th} image due to the potential, acting perpendicular to the string,

$$\boldsymbol{F}_i^{\perp} = -\nabla V(\boldsymbol{q}_i) + \nabla V(\boldsymbol{q}_i)\boldsymbol{\tau}_i \cdot \boldsymbol{\tau}_i$$

and $\boldsymbol{F}_i^{\parallel}$ is a force stemming from virtual springs connecting the images with each other, acting parallel to the string, in order to ensure

$$\boldsymbol{F}_i^{\parallel} = k(\|\boldsymbol{q}_{i+1} - \boldsymbol{q}_i\| - \|\boldsymbol{q}_i - \boldsymbol{q}_{i-1}\|) \cdot \boldsymbol{\tau}_i$$

where *k* is the force constant of the spring and τ_i is the tangent vector of the string. The artificial spring forces ensure, that the images don't fall in one of the local minima. After minimization of the total energy, the NEB method gives rise to the minimum energy path (MEP), as well as saddle points. In the frame of the NEB methodology, two reaction pathways were found and are illustrated in Figure. S2, showing the fast and the slow migration channels.

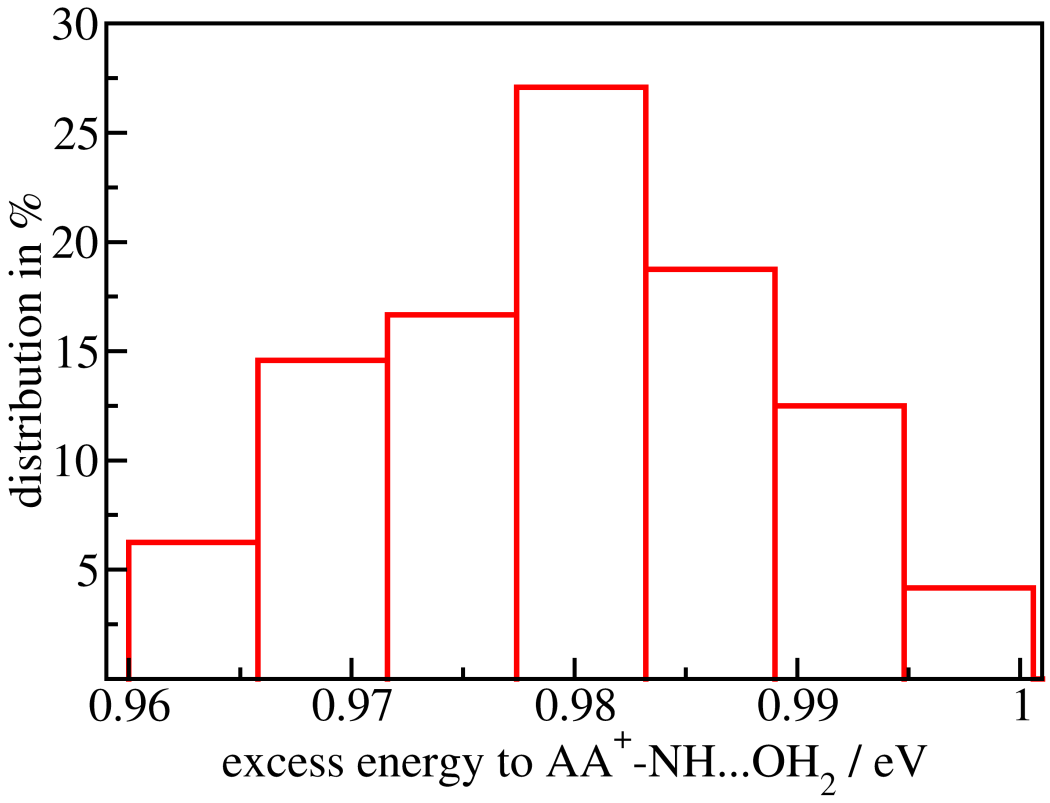

Figure S1. Excess energy distribution of the initial ensemble of trajectories with respect to the cationic NH-bound minimum.

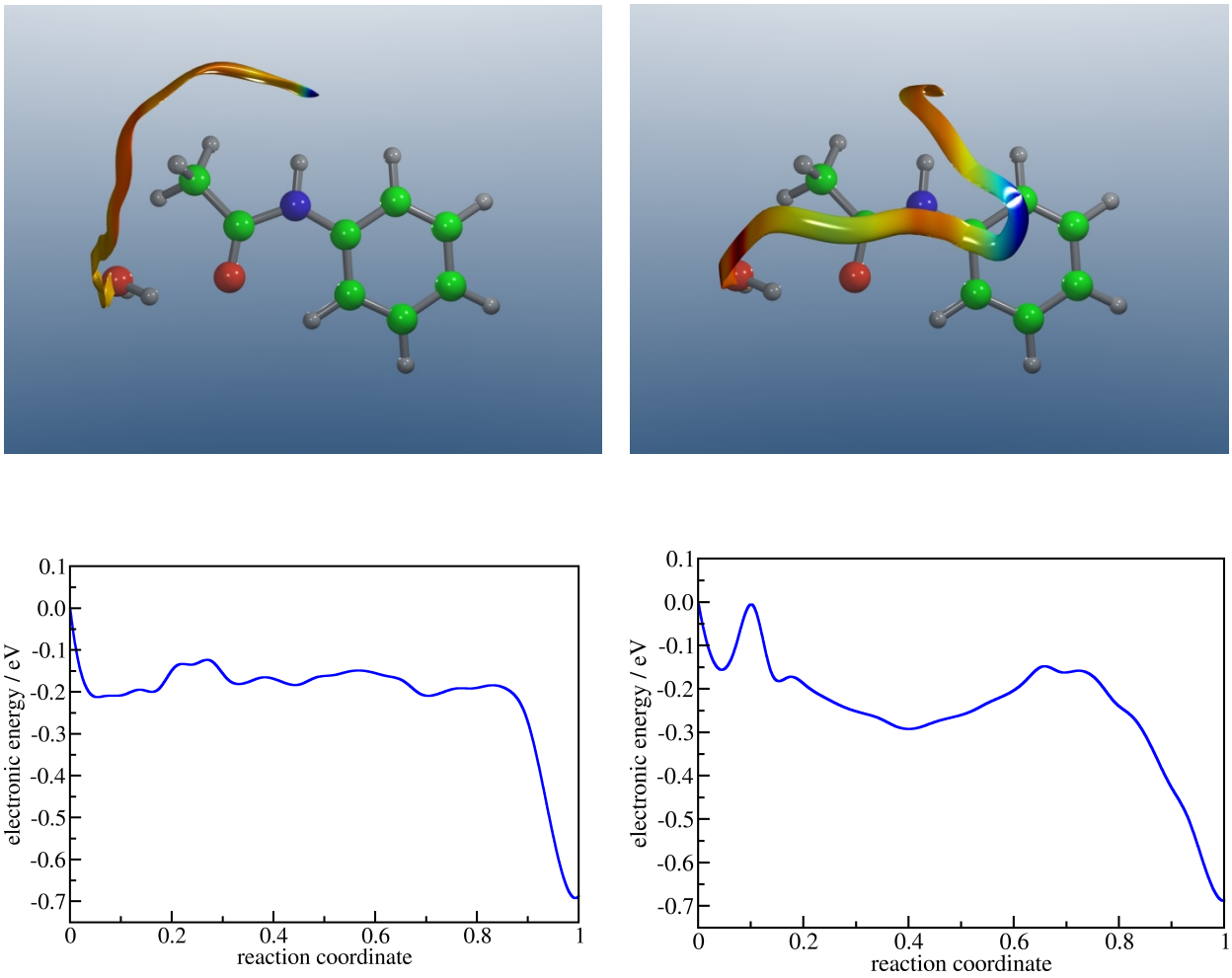

Figure S2. Minumum energy paths (MEPs) of the fast (left) and slow (right) migration channels optimized using the nudged elastic band (NEB) method.

Chapter 6

DECIPHERING ENVIRONMENT EFFECTS IN PEPTIDE BOND SOLVATION DYNAMICS BY EXPERIMENT AND THEORY

Reproduced with permission from:

M. Wohlgemuth, M. Miyazaki, K. Tsukada, M. Weiler, O. Dopfer, M. Fujii, and R. Mitrić:
"Deciphering environment effects in peptide bond solvation dynamics by experiment and theory,"
Phys. Chem. Chem. Phys., **19**, 22564–22572 (2017).

http://dx.doi.org/10.1039/C7CP03992A

PCCP

PAPER

View Article Online
View Journal | View Issue

Cite this: *Phys. Chem. Chem. Phys.*, 2017, **19**, 22564

Deciphering environment effects in peptide bond solvation dynamics by experiment and theory†

Matthias Wohlgemuth, [a] Mitsuhiko Miyazaki, [bc] Kohei Tsukada,[b] Martin Weiler,[b] Otto Dopfer, *[c] Masaaki Fujii*[b] and Roland Mitrić*[a]

Received 14th June 2017,
Accepted 4th August 2017

DOI: 10.1039/c7cp03992a

rsc.li/pccp

Most proteins work in aqueous solution and the interaction with water strongly affects their structure and function. However, experimentally the motion of a specific single water molecule is difficult to trace by conventional methods, because they average over the heterogeneous solvation structure of bulk water surrounding the protein. Here, we provide a detailed atomistic picture of the water rearrangement dynamics around the –CONH– peptide linkage in the two model systems formanilide and acetanilide, which simply differ by the presence of a methyl group at the peptide linkage. The combination of picosecond pump–probe time-resolved infrared spectroscopy and molecular dynamics simulations demonstrates that the solvation dynamics at the molecular level is strongly influenced by this small structural difference. The effective timescales for solvent migration triggered by ionization are mainly controlled by the efficiency of the kinetic energy redistribution rather than the shape of the potential energy surface. This approach provides a fundamental understanding of protein hydration and may help to design functional molecules in solution with tailored properties.

1 Introduction

The interaction of water with solutes and the formation of complex hydrogen-bonded (H-bonded) networks are important driving forces in biochemical reactions and structural rearrangements.[1–7] In particular, the structure and function of proteins is intimately connected with the dynamics of the water network. For example, protein folding and enzyme activity involve hydrogen-bond dynamics that spans multiple timescales.[8–22] With their –CONH– linkages along the peptide chain, proteins offer attractive hydrogen bonding sites, where water can bind either as proton donor at the CO site or as proton acceptor at the NH site, respectively.[23]

The solvation dynamics around proteins has been probed by various experimental methods. However, the results are often inconsistent and contradictory.[9,12,14,15,19,22,24] This difficulty arises from the inherent complexity of protein solvation, such as the existence of multiple solvation layers. In such a situation, individual methods may measure water molecules in different layers. Therefore, most experiments yield only indirect dynamical information averaged over various water molecules in different local environments, giving rise to only a limited picture of the dynamics of individual water molecules.[15] Apparantly, measuring the motion of a specific single water molecule in real biological environments is a challenging experimental task.[25] One possibility to overcome these limitations is the generation of size- and isomer-selected (micro-)hydrated peptides in the gas phase and study the dynamics of a single or several selected solvent molecules with time-resolved pump–probe techniques, such as time-resolved photoelectron spectroscopy[26–29] or the recently developed picosecond time-resolved infrared (ps-TRIR) spectroscopy.[25,30] The latter one has successfully been applied to monitor in real time the ionization-induced $\pi \rightarrow H$ site-switching dynamics of rare gas ligands attached to the phenol molecule[30–34] and the water migration dynamics in the 4-aminobenzonitrile–water[35] and *trans*-acetanilide–water (AA^+–W)[36] cluster cations. Combined with theoretical simulations, such experiments provide a detailed atomistic picture of the dynamics of individual solvent molecules. Conceptually, such experiments involve the preparation of neutral clusters in a cold molecular beam in their ground electronic state (S_0), which are subsequently resonantly ionized *via* the first excited state (S_1) into the cation ground state (D_0) using size- and isomer-selective two-photon ionization. Ionization triggers a response of the solvent to the charge redistribution, because the interaction potential in the ionized D_0 state changes drastically. As a consequence, the ligand is released from its initial binding site in the neutral

[a] *Institut für Physikalische und Theoretische Chemie, Julius-Maximilians-Universität Würzburg, Emil-Fischer-Str. 42, 97074 Würzburg, Germany. E-mail: roland.mitric@uni-wuerzburg.de*
[b] *Laboratory for Chemistry and Life Science, Institute of Innovative Research, Tokyo Institute of Technology, Yokohama 226-8503, Japan. E-mail: mfujii@res.titech.ac.jp*
[c] *Institut für Optik und Atomare Physik, Technische Universität Berlin, 10623 Berlin, Germany. E-mail: dopfer@physik.tu-berlin.de*

† Electronic supplementary information (ESI) available: Movies of the water migration dynamics, REMPI spectra of FA–W. See DOI: 10.1039/c7cp03992a

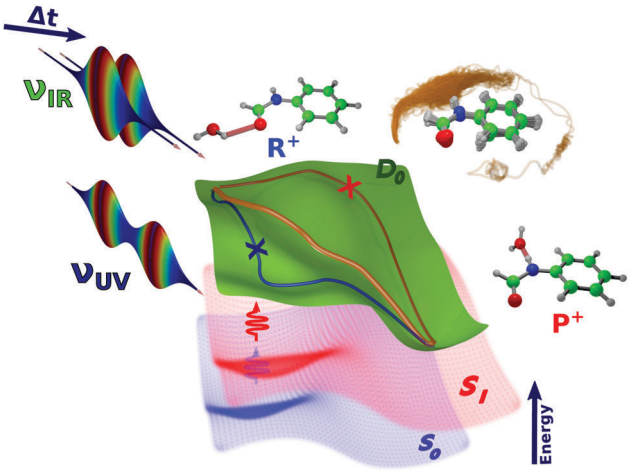

Fig. 1 Scheme illustrating the experimental pump–probe procedure and dynamical time evolution after the ionization of the *trans*-formanilide–water (FA–W) cluster. The CO-bound isomer is ionized by size- and isomer-selective two-color two-photon ionization, (pump process) from the neutral ground state (S_0, blue surface) *via* the first excited state (S_1, red surface) to the cationic ground state (D_0, green surface). There, the water molecule migrates from the hydrogen-bonded CO-site ($FA^+–W^{CO}$, R^+) to the NH-bound isomer ($FA^+–W^{NH}$, P^+). This motion is monitored by ps-TRIR spectra (ν_{IR}) measured at variable delay Δt (probe process). The two crossed pathways indicate the migration channels of AA^+–W, which are not observed in the FA^+–W MD simulations, while a new third channel (yellow trace) opens in plane (*cf.* middle inset structure with traces).

cluster and undergoes an exothermic large-amplitude migration reaction toward the most attractive binding site in the cation cluster on the picosecond timescale. Tunable IR laser radiation (ν_{IR}) introduced at a variable delay (Δt) after the ionization event probes the isomerization dynamics (Fig. 1), because resonant vibrational excitation induces the dissociation of the cluster. In this way the transient time-dependent IR spectrum can be measured, and the vibrational fingerprints of the corresponding transient structures are experimentally obtained. However, to extract full information from the observed time-resolved IR spectra, high-level dynamical theoretical simulations are required.[37] To this end, we have recently introduced a new and generally applicable theoretical approach for the simulation of solvation dynamics and pump–probe ps-TRIR spectra based on *ab initio* molecular dynamics (MD) "on the fly", and successfully applied it to the water migration dynamics of the AA^+–W cluster, which serves as a model for solvating the peptide linkage.[37] With our approach, we were able to identify competing water rearrangement channels and to determine the timescales of the involved relaxation processes. This theoretical approach is verified by simulating the ps-TRIR spectra, which agree well with the experimental ones.[36]

Here, we investigate the influence of the local environment on the solvation dynamics of a single water molecule bound to two aromatic amides, namely *trans*-formanilide–water (FA–W) and *trans*-acetanilide–water (AA–W) clusters. Notice, that although there are certainly more chemically suitable systems for modelling the solvation dynamics of a peptide bond, our choice of an aromatic model peptide is motivated by our experimental technique, which relies on the resonant ionization. The two molecules differ only by the presence of a methyl group directly bound to the peptide linkage in AA. We show that even a small perturbation in the local structure, in this case substitution of H by CH_3, can completely change both the mechanism and the timescale of the water rearrangement around the peptide linkage. Although *N*-methylation of peptides does not play a substantial role in proteins, it is an important matter of interest in drug design and synthesis of new nanomaterials.[38–40] In the electronic ground state of neutral FA–W, water binds with similar binding energies either as a proton acceptor to the NH site ($FA–W^{NH}$) or as a proton donor to the CO site ($FA–W^{CO}$).[41,42] The barriers for isomerization have been determined as 892 ± 92 cm^{-1} (CO → NH) and 869 ± 119 cm^{-1} (NH → CO).[43] However, in the cationic ground state (D_0), the CO site becomes repulsive and thus, as shown by recent high-resolution photoelectron (ZEKE) and IR experiments, water exclusively binds to the NH site.[42,44–46] Therefore, ionization of the $FA–W^{CO}$ cluster triggers water migration from the CO site to the now more stable NH binding site,[42] as has been shown by Sekiya and co-workers by IR spectroscopy. Previous MD simulations at the Hartree–Fock (HF) and density functional theory (DFT) levels suggest water migration in $FA^+–W^{NH}$ after vertical ionization of the $FA–W^{CO}$ isomer within a sub-picosecond timescale.[42,47] However, the role of a possible back reaction, the occurrence of reaction intermediates, and the origin of the predicted shorter lifetime compared to the related AA^+–W cluster remained unclear. Concerning higher degrees of solvation, the formation of H-bonded networks and π-bounded clusters of FA^+ with polar and nonpolar ligands have been studied by infrared photodissociation spectra and quantum chemical calculations of size-selected $FA^+–L_n$ clusters with L = W (n = 1–5), L = Ar (n = 1–8), and L = N_2,[46,48] yielding detailed information about the microsolvation shell structure of this fundamental ion in hydrophilic and hydrophobic environments.

This paper is structured as follows. First, we present the theoretical background to simulate ps-TRIR spectroscopy (Section 2), which is followed by the description of the employed experimental and theoretical methodology (Section 3). In Section 4, we show the results and discuss the obtained ps-TRIR spectra. Finally, we summarize the salient results (Section 5).

2 Simulation of picosecond time-resolved infrared spectroscopy

We present a detailed description of the theoretical methodology for the simulation of the ps-TRIR spectra, which is based on MD "on-the-fly" carried out in the frame of DFT. For this purpose, we employ the Wigner representation in which the density operator of the system is represented by a phase space function $\rho(\mathbf{q},\mathbf{p},t)$ of the nuclear coordinates and momenta. As in our previous work,[49,50] ρ is represented by an ensemble of independently propagated discrete classical trajectories according to

$$\rho(\mathbf{q},\mathbf{p},t) = \sum_{i=1}^{N_{\mathrm{traj}}} \delta(\mathbf{q} - \mathbf{q}_i(t;\mathbf{q}_0,\mathbf{p}_0))\delta(\mathbf{p} - \mathbf{p}_i(t;\mathbf{q}_0,\mathbf{p}_0)), \qquad (1)$$

where N_{traj} is the total number of trajectories and $\mathbf{q}_0$ and $\mathbf{p}_0$ are the initial positions and momenta of the nuclei of the i-th trajectory. The Hamilton function for the system driven by a laser field is

$$H(\mathbf{q},\mathbf{p},t) = H_0(\mathbf{q},\mathbf{p}) - \boldsymbol{\mu}(\mathbf{q})\cdot\mathbf{E}(t), \tag{2}$$

with the field-free Hamiltonian H_0 and the coupling to the external laser field $\mathbf{E}(t)$ through the total dipole moment $\boldsymbol{\mu}(\mathbf{q}) = \boldsymbol{\mu}_N(\mathbf{q}) + \boldsymbol{\mu}_e(\mathbf{q})$, which is composed of the nuclear and electronic contributions, respectively. We treat the interaction with the field as a weak perturbation. The time evolution of the phase space density in the classical limit of the Wigner representation is described by the Liouville equation

$$\dot{\rho} = \{H,\rho\} = \sum_{i=1}^{3N} \frac{\partial H}{\partial q_i}\frac{\partial \rho}{\partial p_i} - \frac{\partial H}{\partial p_i}\frac{\partial \rho}{\partial q_i}, \tag{3}$$

where $\{H,\rho\}$ is the classical Poisson bracket of the Hamilton function (eqn (2)) and the phase space density (eqn (1)). The solution of this equation is equivalent to the solution Hamiltons equations of motion for the functions $q_i(t)$ and $p_i(t)$:

$$\dot{q}_i = \frac{\mathrm{d}H}{\mathrm{d}p_i} \tag{4}$$

$$\dot{p}_i = -\frac{\mathrm{d}H}{\mathrm{d}q_i} = -\frac{\partial V}{\partial q_i} + \frac{\partial \boldsymbol{\mu}}{\partial q_i}\cdot\mathbf{E}(t). \tag{5}$$

The forces acting on the nuclei are $-\frac{\partial V}{\partial q_i} = F_i$ and are obtained as gradients of the electronic potential energy surface $V(\mathbf{q})$. In the 0-th order of perturbation, which can be employed for weak laser fields, the last term of eqn (5) can be neglected, and therefore the phase space ensemble can be propagated freely using quantum chemical MD "on the fly". For this purpose, we utilize analytic energy gradients, which can be efficiently calculated with DFT and are employed for the numerical integration of the equations of motions (4) and (5). In order to simulate time-resolved pump–probe IR spectra, we have to consider two interactions with the laser field, separated by the time delay Δt: (1) the interaction with the UV pump laser pulse centered at $t = 0$ ionizes the neutral cluster and populates the cationic state, and (2) the dynamics in the cationic state is probed by an IR laser pulse centered at the time delay Δt with the Gaussian shape:

$$\mathbf{E}(t) = \mathbf{E}_0 \exp\left(-\frac{(t-\Delta t)^2}{2\sigma^2}\right)\cos\omega t, \tag{6}$$

with the amplitude $\mathbf{E}_0$ and σ the width of the laser pulse. The rate of the energy absorption induced by the interaction with the probe laser is calculated in the phase space representation from the statistical average of the internal energy $\langle E\rangle$:

$$\begin{aligned}\frac{\mathrm{d}\langle E\rangle}{\mathrm{d}t} &= \frac{\mathrm{d}}{\mathrm{d}t}\iint \mathrm{d}\mathbf{p}\mathrm{d}\mathbf{q} H_0(\mathbf{q},\mathbf{p})\rho(\mathbf{q},\mathbf{p},t) \\ &= \iint \mathrm{d}\mathbf{p}\mathrm{d}\mathbf{q} H_0(\mathbf{q},\mathbf{p})\{H,\rho\},\end{aligned} \tag{7}$$

where we use the Liouville equation of motion for the phase space density (eqn (3)). By expanding the Poisson bracket and using partial integration, eqn (7) can be reduced to

$$\frac{\mathrm{d}\langle E\rangle}{\mathrm{d}t} = \iint \mathrm{d}\mathbf{p}\mathrm{d}\mathbf{q}\left[\rho(\mathbf{q},\mathbf{p},t)\frac{\mathrm{d}\boldsymbol{\mu}(\mathbf{q}(t))}{\mathrm{d}t}\cdot\mathbf{E}_0\exp\left(-\frac{(t-\Delta t)^2}{2\sigma^2}\right)\cos\omega t\right]. \tag{8}$$

The total absorption of energy for a given frequency ω and time delay Δt, which corresponds to the experimental measured transient ps-TRIR spectrum, can be calculated by integrating the rate of energy absorption (eqn (8)) over time

$$\left\langle S_{probe}(\omega,\Delta t)\right\rangle = \int_{-\infty}^{\infty}\mathrm{d}t\frac{\mathrm{d}\langle E\rangle}{\mathrm{d}t}. \tag{9}$$

By utilizing the representation of the phase space density by classical trajectories given in eqn (1), this reduces to the following expression for the transient ps-TRIR spectrum for the time delay Δt:

$$\begin{aligned}\left\langle S_{probe}(\omega,\Delta t)\right\rangle = \sum_{i=1}^{N_{traj}}\int_{-\infty}^{\infty}\mathrm{d}t\Bigg[&\frac{\mathrm{d}\boldsymbol{\mu}(\mathbf{q}_i(t,\mathbf{q}_0,\mathbf{p}_0))}{\mathrm{d}t} \\ &\times\mathbf{E}_0\exp\left(-\frac{(t-\Delta t)^2}{2\sigma^2}\right)\cos\omega t\Bigg].\end{aligned} \tag{10}$$

Note that this expression can be interpreted as a trajectory average of the windowed Fourier transform of the dipole derivative function of each trajectory, where the probe pulse envelope serves as a window.

In order to take also the pump pulse width into account, the transient IR spectra are convoluted by the change in the population of the cationic state, which is obtained directly from the experiment. This leads to the following final expression for the simulation of the ps-TRIR spectra

$$\left\langle S_{pump-probe}(\omega,\Delta t)\right\rangle = \int_{-\infty}^{\infty}\mathrm{d}t\left\langle S_{probe}(\omega,\Delta t - t)\right\rangle\frac{\mathrm{d}P(t)}{\mathrm{d}t} \tag{11}$$

where $\frac{\mathrm{d}P(t)}{\mathrm{d}t}$ is the rate of change of the cationic state population, which for the case of a Gaussian-shaped pump pulse is an error function.

3 Methods

3.1 Experimental setup

The principle and apparatus of ps-TRIR spectroscopy have been described elsewhere.[25,30,31,51,52] Briefly, FA–W is ionized *via* the S_1–S_0 origin band[41,43,53–55] by picosecond ultraviolet pulses, ν_{exc} and ν_{ion}. The population of FA^+–W is monitored using a quadrupole mass spectrometer.[56] A picosecond tunable IR pulse, ν_{IR}, is introduced at a certain delay time (Δt) after ν_{ion} and scanned over the 3 μm range. Vibrational transitions are measured as a decrease of the monitored ion current due to vibrational predissociation of FA^+–W. The time evolution of an IR transition is measured by scanning Δt while fixing ν_{IR} to this particular transition. A femtosecond mode-locked Ti:sapphire laser is regeneratively amplified and stretched to a picosecond pulse. The amplified 800 nm output is separated into three pulses. One of these pulses is frequency doubled to pump two

independent optical parametric generator/amplifiers. Signal pulses from these amplifiers are frequency doubled and used as ν_{exc} and ν_{ion}. The second 800 nm pulse is used to pump another parametric generator/amplifier. Then, ν_{IR} is produced by difference frequency generation between the second harmonic of the idler output and the remaining fundamental 800 nm pulse in a KTA crystal. The typical pulse width is $\sim$3 ps, while the energy resolution is $\sim$15 cm^{-1}. These pulses are combined coaxially by beam combiners and focused on the ionization region by a lens. The frequency of ν_{ion} is set to 32 250 cm^{-1} (310 nm). Vapor of FA and water is seeded in He gas, and the mixture is expanded into the vacuum chamber through a pulsed valve at a typical stagnation pressure of 1–2 bar. FA is located just behind the valve and heated to $\sim$343 K, while the water vapor is supplied from a vessel cooled down to $\sim$243 K. The clusters in the jet expansion interact with the laser pulses at $\sim$1 cm downstream from the valve, and the resultant ions are deflected toward the quadrupole mass filter by an electric field. The ion current is amplified and integrated by a digital boxcar to store the signal in a personal computer. The system is operated at 10 Hz. The conditions of the jet expansion and cluster formation are checked by resonance enhanced multiphoton ionization (REMPI) spectroscopy of FA–W measured by picosecond and nanosecond pulses. The latter are obtained by frequency doubling of a Nd:YAG pumped dye laser. Typical REMPI spectra are provided in Fig. S1 in the ESI.†

3.2 Computational methodology

Throughout this work, all single-point calculations are carried out in the frame of DFT. We employ the gradient-corrected Perdew–Burke–Ernzerhof (PBE) functional[57,58] as implemented in the Turbomole program package,[59] as well as the long-range corrected TD-CAM-B3LYP functional[60] as implemented in the Gaussian09 program package,[61] combined with the resolution-of-identity (RI) approximation in order to speed up the MD simulations. As basis set we use the valence triple zeta plus polarization (6-311G**) basis set.[62] Grimme's dispersion correction (D3) is used throughout the simulations.[63]

In order to generate the initial conditions for the MD simulations of FA–W in the D_0 state, we have run a 50 ps long trajectory in the S_1 state at a constant temperature of T = 100 K employing the TD-CAM-B3LYP functional.[60] This temperature is chosen to reproduce the experimental excess energy after photoionization and is the same as the one used for the AA–W simulations.[37] After initial equilibration, we have sampled structures and velocities in regular time intervals, thus generating an ensemble of 40 trajectories, which are employed to investigate the isomerization and to simulate the ps-TRIR spectra.

The MD simulations starting from these initial conditions are propagated for 10 ps forward in the D_0 cationic state and for 5 ps backward in the S_1 excited state. The integration of the classical equations of motions (eqn (4) and (5)) is performed using the velocity Verlet algorithm[64] with a time step of 0.2 fs, which is sufficiently small to obtain adequate conservation of energy. At each step of the trajectories, electronic and nuclear dipole moments are calculated in order to serve as basis for simulating the ps-TRIR spectra according to eqn (10). As probe pulse, we use a Gaussian-shaped laser pulse envelope with a full-width-at-half-maximum (FWHM) of 3 ps. The rise of the population of the cationic state in eqn (11) is modeled by a Gaussian-shaped function with a FWHM of 2.88 ps. The pump and probe pulse widths both correspond to the experimentally determined values. The transient ps-TRIR spectra are calculated in delay intervals from −5 to +10 ps according to eqn (11).

The details for the corresponding AA–W simulations are presented elsewhere,[37] and are mostly the same as for the FA–W simulations, except for the shorter propagation in the cationic state.

4 Results and discussion

In Fig. 2, we compare the experimental and simulated pump–probe ps-TRIR spectra monitoring the migration process of water after photoionization of FA–W^{CO} (Fig. 1) with the migration process in AA$^+$–W.[36,37] The coarse structure of the experimental nanosecond (stationary) and ps-TRIR spectra of FA$^+$–W and AA$^+$–W are similar. The vibrational and isomer assignments of the stationary IR spectra of both clusters are presented in detail elsewhere.[42,46,65] Similarly, the ps-TRIR spectra and their interpretation based on the MD simulations in AA$^+$–W are detailed in ref. 36 and 37. In AA$^+$–W, the water molecule is released from the CO site upon ionization, and migrates to the NH site over the molecular plane. The coexistence of two channels, namely a fast one over the amide group ($\sim$1 ps, 70%) and a slow one over the phenyl ring ($\sim$5 ps, 30%), are identified when the observed ps-TRIR spectra are compared to the MD simulations.

In Fig. 2A the experimental ps-TRIR spectra monitoring the migration process in FA$^+$–W are shown. The vibrational assignments are analogous to those of AA$^+$–W.[36] The intensity of the H-bonded OH stretching band (ν_{OH}^{b+}) of the initially formed FA$^+$–W^{CO} isomer (R$^+$, blue) gradually decreases, followed by the formation and subsequent decrease of the free NH stretching transition (ν_{NH}^{f+}, T$^+$, green). At the same time, the H-bonded NH stretching band (ν_{NH}^{b+}) of the FA$^+$–W^{NH} reaction product (P$^+$, red) rises. Compared to the ps-TRIR spectra of AA$^+$–W (Fig. 2C[36]), the water migration process seems to be slowed down somewhat in the case of FA$^+$–W, which is counterintuitive since FA$^+$–W is a smaller system with less steric hindrance. While in the AA$^+$–W spectra the ν_{OH}^{b+} band (blue) has completely disappeared within 2 ps, it is still observable until 3 ps in the FA$^+$–W spectra. At $\sim$4 ps the ν_{NH}^{f+} band (green) characteristic for a locally trapped intermediate has almost disappeared for AA$^+$–W. In the case of FA$^+$–W, the ν_{NH}^{f+} band (green, T$^+$) still coexists with the ν_{NH}^{b+} band (red, P$^+$) of the FA$^+$–W^{NH} product and disappears only after $\sim$5 ps. The simulated ps-TRIR spectra of FA$^+$–W shown in Fig. 2B are in good agreement with the experimental ones (Fig. 2A). Compared to the spectra simulated for AA$^+$–W (Fig. 2D), one can notice a more pronounced signal of the ν_{NH}^{f+} band (green). The combined experimental and theoretical approach applied to AA$^+$–W has shown that this band

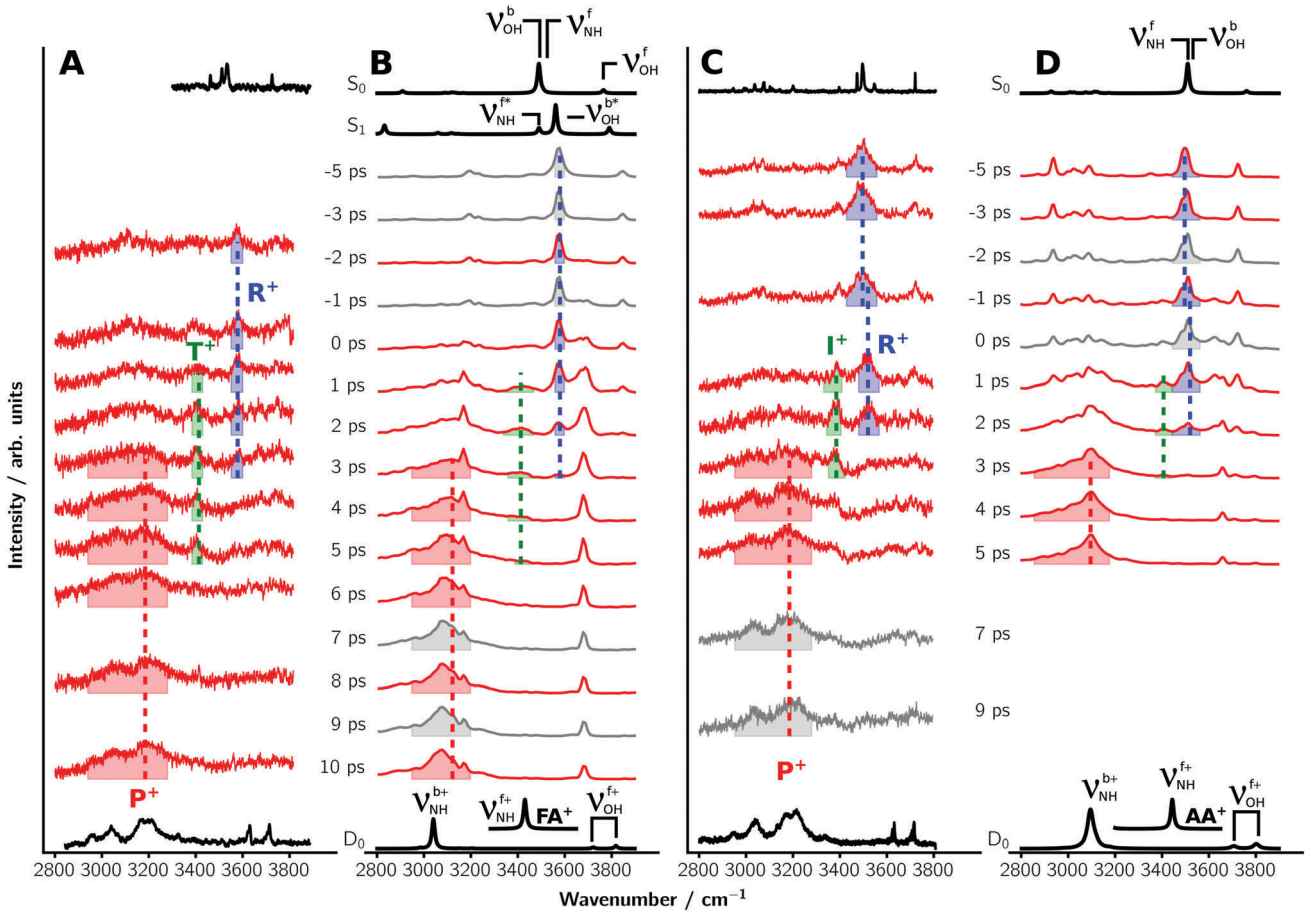

Fig. 2 ps-TRIR spectra of FA^+–W from experiment (A) and MD simulations (B) compared to ps-TRIR spectra (C,[36]) and MD simulations (D,[37]) of AA^+–W. The S_0, S_1 and D_0 spectra are stationary IR spectra of the CO-bound (S_0, S_1) and NH-bound (D_0) isomers in the neutral and cationic states determined by nanosecond lasers (A[42] and C) and DFT harmonic frequency calculations for the optimized structures (B and D). The inset in the D_0 spectra shows the NH stretch mode for bare FA^+ and AA^+. The highlighted areas indicate the signals uniquely attributed to the CO-bonded isomer (blue, R^+), the intermediate or transient structure (green, I^+/T^+), where water is bound neither to the NH nor the CO site, and the NH-bound geometry (red, P^+). The gray shaded spectra denote signals which are not recorded within the experiment or are out of scope of the simulation time, respectively.

can be uniquely attributed to the existence of a slow migration channel, in which water is trapped in a local minimum above the phenyl ring and thus forms a π-bound intermediate state (I^+) responsible for the appearance of the ν_{NH}^{f+} band. As we discuss below, this pathway is completely absent in the case of FA^+–W, and the band assigned to the free NH stretch vibration (ν_{NH}^{f+}) has its origin in an in-plane large-amplitude motion of water around its final equilibrium position at the NH site. Thus, we assign this band not to an intermediate but to a transient band (T^+) of FA^+–W.

To explain these findings, we have first optimized the minimum energy paths along three different reaction coordinates from the CO-bound to the NH-bound isomer of FA^+–W and AA^+–W (Fig. 3). The two out-of-plane paths (across the peptide linkage and above the phenyl ring), which were found by the MD simulations of AA^+–W, are similar for both clusters (Fig. 3 second and third row). Additionally, we have optimized the in-plane pathway for both clusters, which was not observed in the AA^+–W simulations. Significantly, in the case of FA^+–W this path along the H atom of the amide bond is steeply descending. In contrast, in the case of AA^+–W this channel along the methyl group is blocked by a high and broad potential barrier. ZEKE photoelectron experiments assigned with CASSCF calculations find the intermolecular in-plane bending mode at 73 and 49 cm^{-1} for AA^+–W^{NH} and FA^+–W^{NH}, respectively, confirming our findings that the methyl group makes the potential energy surface stiffer along the in-plane bending coordinate and thus enhances steric repulsion.[44,66] Due to the existence of a new favorable reaction coordinate, which is even steeper and shorter than the other two found for AA^+–W, faster water migration is expected for FA^+–W.

Indeed, by monitoring the isomer population of FA^+–W (Fig. 4A), all water molecules reach the NH site for the first time within the first 500 fs after photoionization, while in the case of AA^+–W (Fig. 4B) about 70% of the water molecules first appear at 1 ps at the NH site. This difference is a consequence of the presence of a new migration channel opened by $CH_3 \rightarrow H$ substitution. The out-of-plane pathways, especially the slow migration channel with the locally trapped intermediate, as observed in the AA^+–W MD simulations (Fig. 5, right), are completely absent in the FA^+–W dynamics. Instead, all water

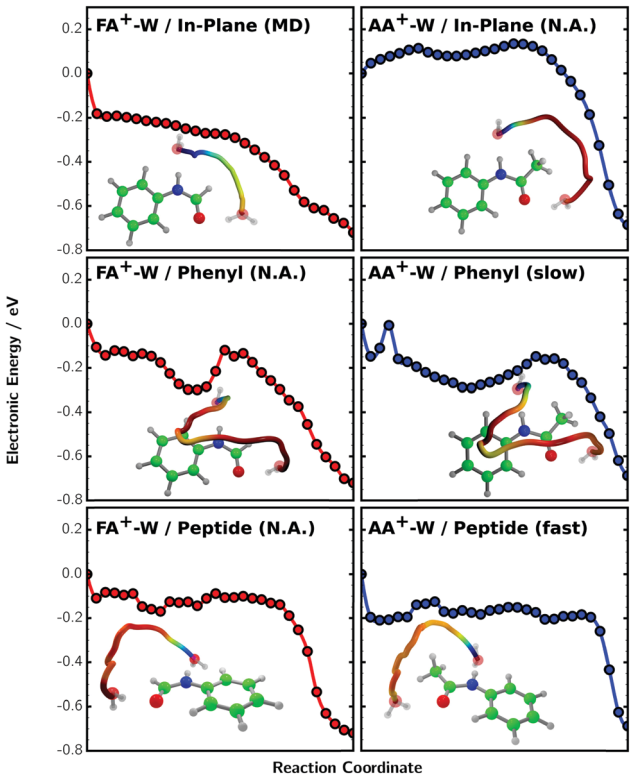

Fig. 3 Minimum energy paths derived from the nudged elastic band method of FA–W^+ (left) and AA–W^+ (right) for the migration of water from the CO to the NH site along the in-plane path (top row), above the phenyl ring (middle row), and above the peptide bond (bottom row). The insets illustrate the path of water, whereby the color encodes the energy at the point of the path. N.A. indicates the pathways not detected by the experiment and the simulations.

molecules follow the steeply descending in-plane pathway (Fig. 5 left and Fig. 3 left).

But why is this migration dynamics not reflected in the ps-TRIR spectra? Instead of a fast migration and a clear appearance of the product band after 500 fs, we observe a strong absorption by the free NH stretching mode accompanied by a slow formation of the H-bonded product band. After the first arrival at the NH site, the water molecules overshoot to the phenyl ring and start to oscillate within a large-amplitude in-plane motion forward and backward around their final equilibrium position (Fig. 5 left), also returning close to their initial position for a short time. This damped oscillation is the reason for the longer persistence of the reactant signal (R^+, blue) and the simultaneous formation of the product (P^+, red) and transient bands (T^+, green) in the ps-TRIR spectra (Fig. 2). Only the theoretical simulations reveal and illustrate the profound influence of the local environment on the dynamical pathways.

In order to analyze the relaxation process that stabilizes the water migration at the product, we present in Fig. 4 three quantities as a function of simulation time for FA^+–W (blue) and AA^+–W (red): (i) the distance of water to the NH-bound equilibrium geometry (Fig. 4C), (ii) the angle spanned by the N–H bond and the oxygen atom of water (O_W, Fig. 4D), and (iii) the kinetic energy of water (Fig. 4E). Immediately after photoionization, the internal energy is quickly transferred into translational energy of water. As can be seen from Fig. 4E, this process is about twice as fast in FA^+–W^{CO} ($\sim$500 fs) than in AA^+–W^{CO} ($\sim$1 ps), due to the steep potential directed into the in-plane motion of water (*cf.* top left of Fig. 3). At the moment when water approaches the NH site for the first time, the translational and vibrational energy of water is more quickly redistributed and transferred to AA^+ than to FA^+ *via* intracluster vibrational energy redistribution (IVR). The additional methyl group in AA^+ substantially increases the density of states by internal rotation and thus enhances the IVR rate, which can also evidently be seen from the final structures of the MD simulations (Fig. 5 bottom row). Notice, that in FA^+–W the phenyl ring provides bath modes, much in the same way as a polypeptide system with a longer backbone. In this sense it affects the IVR dynamics but not the mechanism. In AA^+–W one minor pathway (the slow one) goes over the phenyl ring and affects the overall dynamics of this pathway. However, it will not affect the H $\rightarrow$ CH_3 substitution effect at the amide bond.

To quantify the difference in the effective IVR rate, the maxima of the curves in Fig. 4C and E are fitted to exponentially decaying functions $f(t) = f_0 \exp(-t/\tau)$. The obtained damping constants are $\tau_{C,FA}$ = 2.34 ps and $\tau_{E,FA}$ = 1.71 ps for FA^+–W (blue dashed line) and $\tau_{C,AA}$ = 1.10 ps and $\tau_{E,AA}$ = 1.11 ps for AA^+–W (red dashed line). The curves in Fig. 4D are fitted by a damped harmonic oscillator model $f(t) = f_0 \exp(-t/\tau)\cos(\omega t - \phi) + f_{off}$, where f_0, f_{off}, ω and ϕ are free parameters, giving rise to damping constants $\tau_{D,FA}$ = 1.36 ps for FA^+–W (blue dashed line) and $\tau_{D,AA}$ = 0.46 ps for AA^+–W (red dashed line). Thus, by averaging over all derived time constants, we determine an approximate increase in the overall IVR rate of about a factor of 2.2 for AA^+–W (with respect to FA^+–W), which is also in good agreement with the timescales determined from the experimental and theoretical ps-TRIR spectra. As it is evident from Fig. 5 the translational kinetic energy of water is rapidly transferred to FA^+ and AA^+, respectively, as soon as it reaches the NH-bound site. However, due to the different migration pathways distinct modes are excited in both molecules. In the case of AA^+–W, the out-of-plane migration leads to an excitation of the dihedral degrees of freedom of the peptide linkage and the methyl rotation. In contrast, in FA^+–W the in-plane pathway of water weakly couples to the vibrational modes of FA^+ due to the rigid in-plane bend mode of the peptide linkage and the lack of a methyl rotor, leading to a less efficient energy redistribution.

In Fig. 6 we show the peak width of the product band (P^+, red) of the simulated ps-TRIR spectra (Fig. 2B and D) located between 3000 and 3300 cm^{-1}, which serves as an indicator for cooling by IVR. The broadness of the band sharpens twice as fast for AA^+–W as compared to FA^+–W. These results clearly show that, due to the stronger coupling of the isomerization coordinate to the dihedral degrees of freedom of the peptide linkage (*i.e.*, the angle between the phenyl and amide planes) and the additional density of states of the AA^+–W cluster introduced by CH_3 substitution, IVR is more efficient for

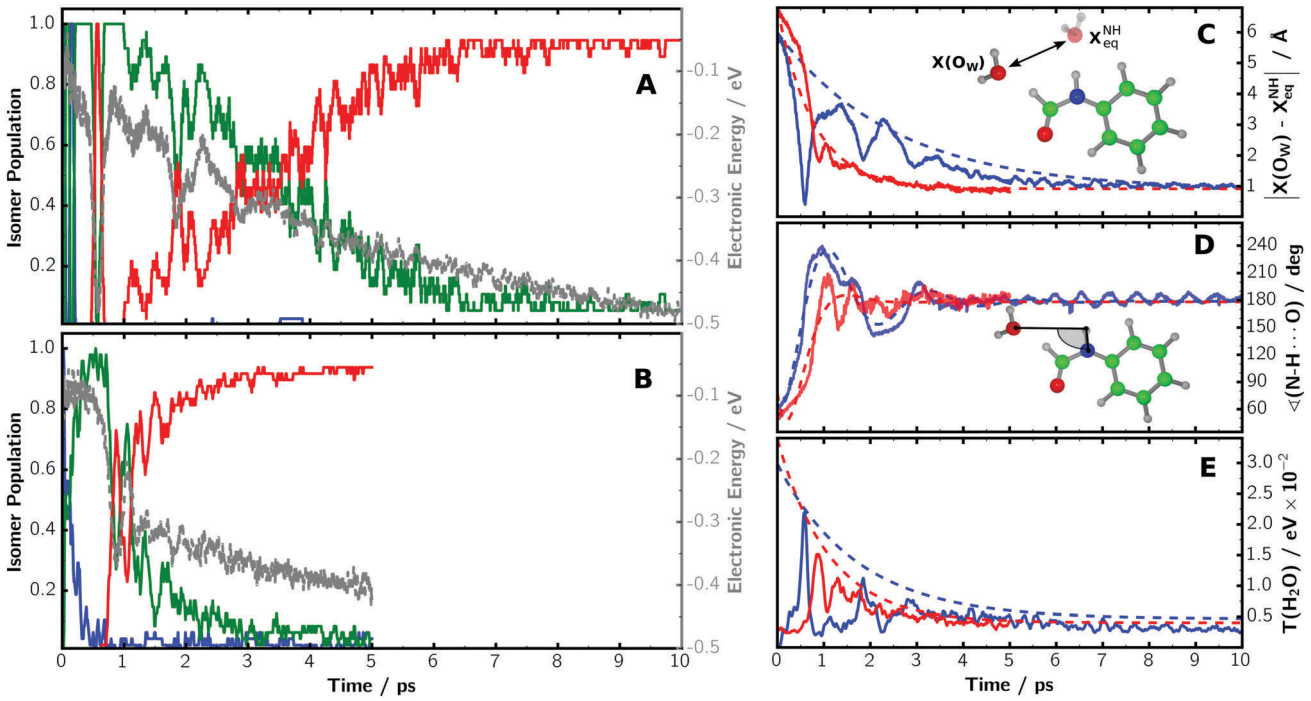

Fig. 4 Left panels: Averaged populations of the FA$^+$–W (A) and AA$^+$–W (B) ensembles, with the CO-bound isomer (blue), the transient or intermediate structure (green), and the NH-bound isomer (red) as a function of simulation time. The gray dashed line shows averaged electronic energy from the MD simulations. Right panels: (C) Averaged distance of the water oxygen (O_W) from its NH-bound equilibrium geometry, (D) averaged angle between the N–H bond of the peptide and OW, and (E) averaged kinetic energy of water along the trajectories of FA$^+$–W (blue) and AA$^+$–W (red). The dashed lines in (C and E) are exponential fits with respect to the maxima of the curves. For (D) a damped harmonic oscillator was fitted to the curve.

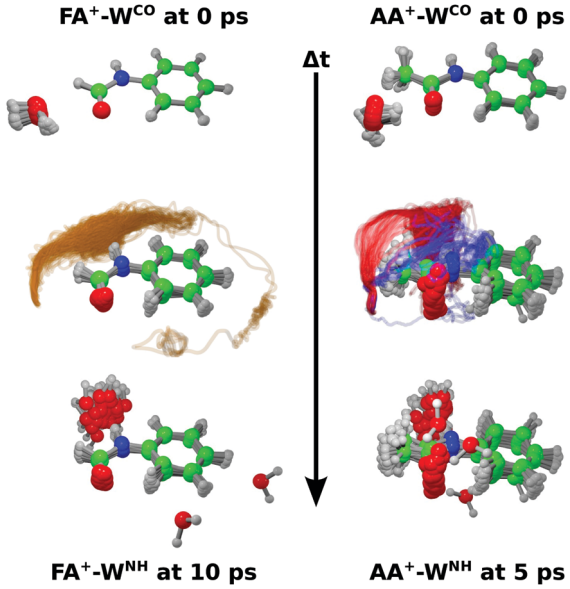

Fig. 5 Trajectories of the ionization-induced water migration derived from the FA$^+$–W (left, 40 trajectories) and AA$^+$–W (right, 50 trajectories) MD simulations, starting from the CO-bound isomer (top row) and ending at the NH-bound isomer (bottom row) at 10 ps and 5 ps after ionization, respectively. The yellow curve for FA$^+$–W indicates the in-plane migration path of water. The out-of-plane pathways for AA$^+$–W correspond to the slow (blue) and fast (red) migration channels, respectively.[37]

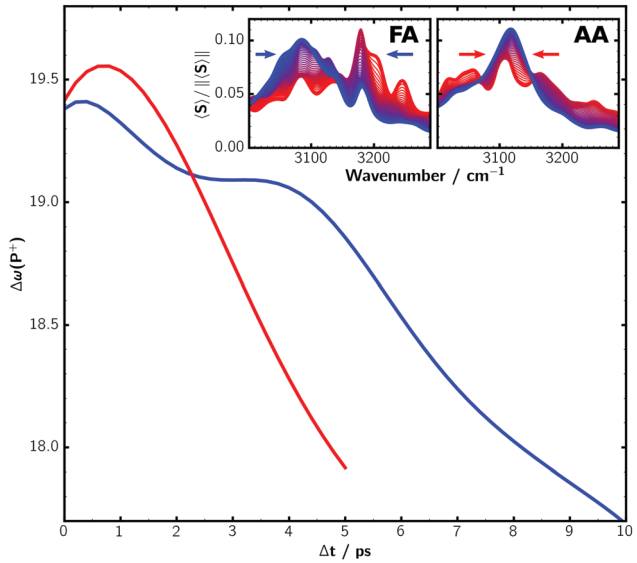

Fig. 6 Average peak width $\Delta\omega$ of the product band (ν^{b+}_{NH}, P$^+$) calculated for FA$^+$–W (blue) and AA$^+$–W (red) from the simulated ps-TRIR spectra (Fig. 2B and D). The peak width has been calculated as $\Delta\omega = (\omega_2-\omega_1)^{-1}\int_{\omega_1}^{\omega_2} d\omega\left[\langle\omega^2\rangle-\langle\omega\rangle^2\right]^{\frac{1}{2}}\frac{\langle S(\omega,\Delta t)\rangle}{\|\langle S(\omega,\Delta t)\rangle\|}$, with ω_1 = 3000 cm^{-1} and ω_2 = 3300 cm^{-1}. The insets show the normalized band of FA$^+$–W and AA$^+$–W, respectively.

the out-of-plane pathways in the AA^+–W migration dynamics than the in-plane pathway in FA^+–W. These factors give rise to a twice longer relaxation time in FA^+–W, although the simple migration process up to the first arrival at the NH site is twice as fast compared to the AA^+–W migration dynamics.

5 Conclusions and outlook

In conclusion, we have provided a detailed atomistic picture of the strongly different water rearrangement dynamics around the peptide linkage in two model systems, which differ by the local environment around the amide moiety (by simple H → CH_3 substitution). In contrast to AA^+–W with two competing out-of-plane pathways (fast and slow), the water migration dynamics in FA^+–W has only a single in-plane reaction pathway, which involves a damped large-amplitude vibrational motion around the single H atom of the amide. The two out-of-plane pathways observed in AA^+–W are completely absent in the FA^+–W dynamics. The initial formation of the NH-bound isomer is twice faster in FA^+–W and completed within 500 fs, whereas in the AA^+–W trajectories only about 70% of the water molecules reach the NH site within ~1 ps *via* the fast channel. However, our calculations have shown that in AA^+–W the kinetic energy of water along the reaction coordinate is redistributed much faster to AA^+ than in FA^+–W, which leads to faster product stabilization in the cluster with larger steric hindrance (AA^+–W). The residual energy of water in FA^+–W leads to an overshooting from the equilibrium position and a long-lasting large-amplitude oscillation in the molecular plane before settling at the final NH binding site, as a result of weak coupling of in-plane intermolecular bend (with very low frequency of 49 cm^{-1}) to other vibrational modes. The consequence is a long persistence of the free NH (ν_{NH}^{f+}) stretching band in the ps-TRIR spectra of FA^+–W. Our results demonstrate that the solvation dynamics at the molecular level can be strongly influenced even by small structural perturbations and that the effective timescales extracted from the time-resolved experiments are determined by the IVR rate and do not necessarily reflect the intrinsic rate of the product formation, which is mainly determined by the shape of the potential energy surface.

Since our method is generally applicable and provides an accurate and efficient way to simulate time-resolved infrared spectroscopy, which is directly comparable to the experimental outcome, a wide variety of applications are conceivable and planned for future work. For example, it will be interesting to study migration and rearrangement dynamics of the presented biomolecules with more than one water molecule, as has been studied experimentally before by stationary spectroscopic experiments.[46] The work on such simulations is currently in progress.

Acknowledgements

This work was supported in part by KAKENHI (JP205104008) on innovative area (2503), KAKENHI (JP15H02157, 384 JP15K13620, JP16H06028) and the Cooperative Research Program of the ''Network Joint Research Center for Materials and Devices'' from the Ministry of Education, Culture, Sports, Science and Technology (MEXT), Japan, the Core-to-Core Program (22003) from the Japan Society for the Promotion of Science (JSPS), and the Deutsche Forschungsgemeinschaft (DFG DO 729/4, ENPMI-1236). Financial support by the European Research Council (ERC) Consolidator Grant ''DYNAMO'' (Grant No. 646737) is gratefully acknowledged. M. M. is grateful for a fellowship from the Alexander von Humboldt foundation (research fellowship for experienced scientists). O. D. is grateful for travel support from the World Research Hub Initiative (WRHI) of Tokyo Institute of Technology.

References

1 G. A. Jeffrey and W. Saenger, *Hydrogen Bonding in Biological Structures*, Sprinter-Verlag, 1991.
2 T. S. Zwier, *Annu. Rev. Phys. Chem.*, 1996, **47**, 205–241.
3 K. Müller-Dethlefs and P. Hobza, *Chem. Rev.*, 2000, **100**, 143–168.
4 C. E. H. Dessent and K. Müller-Dethlefs, *Chem. Rev.*, 2000, **100**, 3999–4022.
5 J. Schermann, *Spectroscopy and Modelling of Biomolecular Building Blocks*, Elsevier, 2008.
6 P. Hobza and K. Müller-Dethlefs, *Non-Covalent Interactions*, The Royal Society of Chemistry, 2009, pp. P001–P226.
7 A. Fujii and K. Mizuse, *Int. Rev. Phys. Chem.*, 2013, **32**, 266–307.
8 G. Otting, E. Liepinsh and K. Wüthrich, *Science*, 1991, **254**, 974–980.
9 V. Denisov, B.-H. Jonsson and B. Halle, *Nat. Struct. Mol. Biol.*, 1999, **6**, 253–260.
10 *Mechanisms of Protein Folding*, ed. R. H. Pain, Oxford University Press, 2000.
11 A. Mitsutake, Y. Sugita and Y. Okamoto, *Pept. Sci.*, 2001, **60**, 96–123.
12 N. Nucci, M. Pometun and A. Wand, *Nat. Struct. Mol. Biol.*, 2011, **18**, 245–249.
13 S. K. Pal and A. H. Zewail, *Chem. Rev.*, 2004, **104**, 2099–2124.
14 B. Halle, *Philos. Trans. R. Soc. London, Ser. B*, 2004, **359**, 1207–1224.
15 B. Bagchi, *Chem. Rev.*, 2005, **105**, 3197–3219.
16 D. Chandler, *Nature*, 2005, **437**, 640–647.
17 M. Chaplin, *Nat. Rev. Mol. Cell Biol.*, 2006, **7**, 861–866.
18 P. Ball, *Chem. Rev.*, 2008, **108**, 74–108.
19 D. Zhong, *Adv. Chem. Phys.*, 2009, **143**, 83–149.
20 D. E. Shaw, P. Maragakis, K. Lindorff-Larsen, S. Piana, R. O. Dror, M. P. Eastwood, J. A. Bank, J. M. Jumper, J. K. Salmon, Y. Shan and W. Wriggers, *Science*, 2010, **330**, 341–346.
21 T. Yoda, Y. Sugita and Y. Okamoto, *Biophys. J.*, 2010, **99**, 1637–1644.
22 M. Grossman, B. Born, M. Heyden, D. Tworowski, G. Fields, I. Sagi and M. Havenith, *Nat. Struct. Mol. Biol.*, 2011, **18**, 1102–1108.
23 S. G. Kalko, E. Guàrdia and J. A. Padró, *J. Phys. Chem. B*, 1999, **103**, 3935–3941.
24 A. C. Fogarty, E. Duboué-Dijon, F. Sterpone, J. T. Hynes and D. Laage, *Chem. Soc. Rev.*, 2013, **42**, 5672–5683.

25 O. Dopfer and M. Fujii, *Chem. Rev.*, 2016, **116**, 5432–5463.
26 D. M. Neumark, *Annu. Rev. Phys. Chem.*, 2001, **52**, 255–277.
27 A. Stolow, A. E. Bragg and D. M. Neumark, *Chem. Rev.*, 2004, **104**, 1719–1758.
28 T. Suzuki, *Annu. Rev. Phys. Chem.*, 2006, **57**, 555–592.
29 A. Stolow and J. G. Underwood, in *Time-Resolved Photoelectron Spectroscopy of Nonadiabatic Dynamics in Polyatomic Molecules*, ed. S. A. Rice, John Wiley & Sons, Inc., 2008, pp. 497–584.
30 M. Fujii and O. Dopfer, *Int. Rev. Phys. Chem.*, 2012, **31**, 131–173.
31 S. Ishiuchi, M. Sakai, Y. Tsuchida, A. Takeda, Y. Kawashima, M. Fujii, O. Dopfer and K. Müller-Dethlefs, *Angew. Chem., Int. Ed.*, 2005, **44**, 6149–6151.
32 M. Miyazaki, A. Takeda, S. Ishiuchi, M. Sakai, O. Dopfer and M. Fujii, *Phys. Chem. Chem. Phys.*, 2011, **13**, 2744–2747.
33 S. Ishiuchi, M. Miyazaki, M. Sakai, M. Fujii, M. Schmies and O. Dopfer, *Phys. Chem. Chem. Phys.*, 2011, **13**, 2409–2416.
34 M. Miyazaki, Y. Sakata, M. Schütz, O. Dopfer and M. Fujii, *Phys. Chem. Chem. Phys.*, 2016, **18**, 24746–24754.
35 M. Miyazaki, T. Nakamura, M. Wohlgemuth, R. Mitrić, O. Dopfer and M. Fujii, *Phys. Chem. Chem. Phys.*, 2015, **17**, 29969–29977.
36 K. Tanabe, M. Miyazaki, M. Schmies, A. Patzer, M. Schütz, H. Sekiya, M. Sakai, O. Dopfer and M. Fujii, *Angew. Chem., Int. Ed.*, 2012, **51**, 6604–6607.
37 M. Wohlgemuth, M. Miyazaki, M. Weiler, M. Sakai, O. Dopfer, M. Fujii and R. Mitrić, *Angew. Chem., Int. Ed.*, 2014, **53**, 14601–14604.
38 C. A. Lipinski, F. Lombardo, B. W. Dominy and P. J. Feeney, *Adv. Drug Delivery Rev.*, 1997, **23**, 3–25.
39 J. Chatterjee, C. Gilon, A. Hoffman and H. Kessler, *Acc. Chem. Res.*, 2008, **41**, 1331–1342.
40 N. Qvit, S. J. Rubin, T. J. Urban, D. Mochly-Rosen and E. R. Gross, *Drug Discovery Today*, 2017, **22**, 454–462.
41 E. G. Robertson, *Chem. Phys. Lett.*, 2000, **325**, 299–307.
42 T. Ikeda, K. Sakota, Y. Kawashima, Y. Shimazaki and H. Sekiya, *J. Phys. Chem. A*, 2012, **116**, 3816–3823.
43 J. R. Clarkson, E. Baquero, V. A. Shubert, E. M. Myshakin, K. D. Jordan and T. S. Zwier, *Science*, 2005, **307**, 1443–1446.
44 S. Ullrich, X. Tong, G. Tarczay, C. E. H. Dessent and K. Müller-Detlefs, *Phys. Chem. Chem. Phys.*, 2002, **4**, 2897–2903.
45 K. Sakota, Y. Shimazaki and H. Sekiya, *Phys. Chem. Chem. Phys.*, 2011, **13**, 6411–6415.
46 J. Klyne, M. Schmies, M. Fujii and O. Dopfer, *J. Phys. Chem. B*, 2015, **119**, 1388–1406.
47 H. Tachikawa, M. Igarashi and T. Ishibashi, *J. Phys. Chem. A*, 2003, **107**, 7505–7513.
48 J. Klyne, M. Schmies and O. Dopfer, *J. Phys. Chem. B*, 2014, **118**, 3005–3017.
49 V. Bonačić-Koutecký and R. Mitrić, *Chem. Rev.*, 2005, **105**, 11–66.
50 R. Mitrić and V. Bonačić-Koutecký, *Phys. Rev. A*, 2007, **76**, 031405.
51 S. Ishiuchi, M. Sakai, Y. Tsuchida, A. Takeda, Y. Kawashima, O. Dopfer, K. Müller-Dethlefs and M. Fujii, *J. Chem. Phys.*, 2007, **127**, 114307.
52 S. Ishiuchi, M. Sakai, K. Daigoku, K. Hashimoto and M. Fujii, *J. Chem. Phys.*, 2007, **127**, 234304.
53 J. A. Dickinson, M. R. Hockridge, E. G. Robertson and J. P. Simons, *J. Phys. Chem. A*, 1999, **103**, 6938–6949.
54 A. Fedorov and J. R. Cable, *J. Phys. Chem. A*, 2000, **104**, 4943–4952.
55 M. Mons, I. Dimicoli, B. Tardivel, F. Piuzzi, E. G. Robertson and J. P. Simons, *J. Phys. Chem. A*, 2001, **105**, 969–973.
56 T. Omi, H. Shitomi, N. Sekiya, K. Takazawa and M. Fujii, *Chem. Phys. Lett.*, 1996, **252**, 287–293.
57 J. Perdew and Y. Wang, *Phys. Rev. B*, 1992, **45**, 13244–13249.
58 J. Perdew, K. Burke and M. Ernzerhof, *Phys. Rev. Lett.*, 1996, **77**, 3865–3868.
59 TURBOMOLE V6.2 2010, a development of University of Karlsruhe and Forschungszentrum Karlsruhe GmbH, 1989–2007, TURBOMOLE GmbH, since 2007; available from http://www.turbomole.com.
60 T. Yanai, D. Tew and N. Handy, *Chem. Phys. Lett.*, 2004, **393**, 51–57.
61 M. J. Frisch, G. W. Trucks, H. B. Schlegel, G. E. Scuseria, M. A. Robb, J. R. Cheeseman, G. Scalmani, V. Barone, B. Mennucci, G. A. Petersson, H. Nakatsuji, M. Caricato, X. Li, H. P. Hratchian, A. F. Izmaylov, J. Bloino, G. Zheng, J. L. Sonnenberg, M. Hada, M. Ehara, K. Toyota, R. Fukuda, J. Hasegawa, M. Ishida, T. Nakajima, Y. Honda, O. Kitao, H. Nakai, T. Vreven, J. J. A. Montgomery, J. E. Peralta, F. Ogliaro, M. Bearpark, J. J. Heyd, E. Brothers, K. N. Kudin, V. N. Staroverov, R. Kobayashi, J. Normand, K. Raghavachari, A. Rendell, J. C. Burant, S. S. Iyengar, J. Tomasi, M. Cossi, N. Rega, J. M. Millam, M. Klene, J. E. Knox, J. B. Cross, V. Bakken, C. Adamo, J. Jaramillo, R. Gomperts, R. E. Stratmann, O. Yazyev, A. J. Austin, R. Cammi, C. Pomelli, J. W. Ochterski, R. L. Martin, K. Morokuma, V. G. Zakrzewski, G. A. Voth, P. Salvador, J. J. Dannenberg, S. Dapprich, A. D. Daniels, Ö. Farkas, J. B. Foresman, J. V. Ortiz, J. Cioslowski and D. J. Fox, *Gaussian 09 Revision E.01*, Gaussian Inc., Wallingford CT, 2009.
62 R. Krishnan, J. Binkley, R. Seeger and J. Pople, *J. Chem. Phys.*, 1980, **72**, 650–654.
63 S. Grimme, *J. Comput. Chem.*, 2004, **25**, 1463–1473.
64 W. C. Swope, H. C. Andersen, P. H. Berens and K. R. Wilson, *J. Chem. Phys.*, 1982, **76**, 637–649.
65 K. Sakota, S. Harada, Y. Shimazaki and H. Sekiya, *J. Phys. Chem. A*, 2011, **115**, 626–630.
66 S. Ullrich and K. Müller-Dethlefs, *J. Phys. Chem. A*, 2002, **106**, 9188–9195.

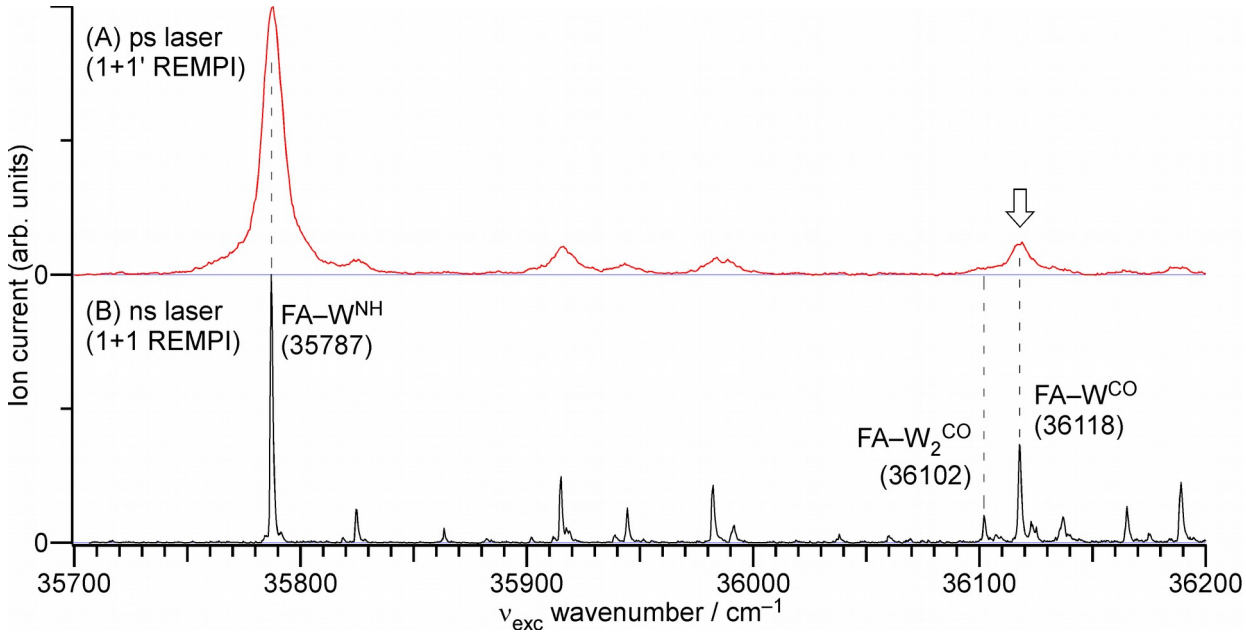

Figure S1. Resonance enhanced multiphoton ionization (REMPI) spectra of the FA–W cluster obtained by using (A) picosecond and (B) nanosecond laser pulses. The frequency of the ionization pulse is 32249 cm^{-1} (310 nm) for (A) (1+1' REMPI) and ν_{exc} for (B) (1+1 REMPI). S_1-S_0 origin transitions of related clusters are labeled. The time-resolved IR spectra are measured by monitoring the origin band of the FA–W^{CO} cluster marked by an arrow. Although the widths of the bands in the picosecond spectrum are broader due to the lower spectral resolution of the picosecond pulse, the transition of the FA–W^{CO} cluster is clearly separated from that of the FA–W_2^{CO} cluster. This observation ensures a selective probe of dynamics of FA–W^{CO}.

Appendix A

PHOTODYNAMICS OF FREE AND SOLVATED TYROSINE

Reproduced with permission from:

G. Tomasello, M. Wohlgemuth, J. Petersen, and R. Mitrić:
"Photodynamics of free and solvated tyrosine,"
J. Phys. Chem. B, **116**, 8762–8770 (2012).

http://dx.doi.org/10.1021/jp302179m

THE JOURNAL OF PHYSICAL CHEMISTRY B

Article

pubs.acs.org/JPCB

Photodynamics of Free and Solvated Tyrosine

Gaia Tomasello, Matthias Wohlgemuth, Jens Petersen, and Roland Mitrić*

Fachbereich Physik, Freie Universität Berlin, Arnimallee 14, D-14195 Berlin, Germany

Supporting Information

ABSTRACT: We present a theoretical simulation of the ultrafast nonadiabatic photodynamics of tyrosine in the gas phase and in water. For this purpose, we combine our TDDFT/MM nonadiabatic dynamics (Wohlgemuth et al. *J. Chem. Phys.* **2011**, *135*, 054105) with the field-induced surface hopping method (Mitrić et al. *Phys. Rev. A* **2009**, *79*, 053416) allowing us to explicitly include the nonadiabatic effects as well as femtosecond laser excitation into the simulation. Our results reveal an ultrafast deactivation of the initially excited bright $\pi\pi^*$ state by internal conversion to a dark $n\pi^*$ state. We observe deactivation channels along the O−H stretching coordinate as well as involving the N−H bond cleavage of the amino group followed by proton transfer to the phenol ring, which is in agreement with previous static energy path calculations. However, since in the gas phase the canonical form of tyrosine is the most stable one, the proton transfer proceeds in two steps, starting from the carboxyl group that first passes its proton to the amino group, from where it finally moves to the phenol ring. Furthermore, we also investigate the influence of water on the relaxation processes. For the system of tyrosine with three explicit water molecules solvating the amino group, embedded in a classical water sphere, we also observe a relaxation channel involving proton transfer to the phenol ring. However, in aqueous environment, a water molecule near the protonated amino group of tyrosine acts as a mediator for the proton transfer, underlining the importance of the solvent in nonradiative relaxation processes of amino acids.

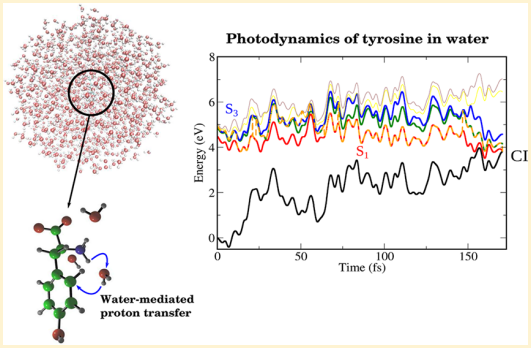

1. INTRODUCTION

Among the vast variety and complexity of biochemical processes, the investigation of the photostability of the building blocks of life such as amino acids and nucleobases is a subject of great importance and intense research. Photostability is governed by the nonradiative relaxation and deactivation occurring upon light irradiation on a femtosecond time scale.[1] The biological molecules found in nature are characterized by the presence of various relaxation pathways that efficiently dissipate the energy gained after UV irradiation to the surrounding environment before any harmful, i.e., irreversible, photoreactions can take place. Of the naturally occurring amino acids, those possessing fluorescent aromatic chromophores, such as tryptophan, tyrosine, and phenylalanine, are mainly responsible for the absorption and fluorescence spectra of proteins,[2] and therefore they are intensively investigated both in gas phase[3] and in solution.[4,5] In particular, tyrosine residues play an important role in enzyme catalysis and have been the focus of extensive investigations. Additionally, since tyrosine is a precursor to dopamine, epinephrine (adrenaline), and other neurotransmitters, it also plays a central role in neurochemistry.

Moreover, due to the fact that the absorption and fluorescence properties of tyrosine are largely influenced by the solvent and neighboring ligands,[6] tyrosine residues can serve as molecular probes for protein solvation and functional electrostatic changes inside proteins. The fluorescence quantum yield of tyrosine, as well as of its chromophore phenol, strongly depends on the excitation wavelength, the temperature, and the pH of the solution. In particular, the fluorescence quantum yield strongly decreases at low pH[7,8] as well as at excitation wavelengths below 245 nm,[9,10] indicating efficient nonradiative processes that must be very fast in order to compete with the fluorescence pathway. Two main fluorescence quenching mechanisms, referred to as external and internal, have been proposed, which both involve a population transfer to the ground state via a conical intersection (CI). The external deactivation channel is the O−H elimination, which has been first revealed by Sobolewski and Domcke on the example of phenol[11,12] and has been attributed to the ubiquitous nature of $\pi\sigma^*$ states that are repulsive along the O−H stretching coordinate.[11] These states exhibit a CI with the lowest bright state of $\pi\pi^*$ character and also with the ground state, leading to ultrafast electronic deactivation. This results in a highly vibrationally excited ground state or, alternatively, in the direct elimination of neutral H atoms as recently observed by time-resolved spectroscopic experiments.[13] In addition, deactivation in amino acids can in general also proceed through decarboxylation and deamination of the side chain.[10,14−17]

However, the experimentally found decrease of the fluorescence lifetimes at low pH, when the amino acids are fully protonated, hints at a different relaxation process, termed

Received: March 6, 2012
Revised: May 25, 2012
Published: June 24, 2012

internal quenching, which might be predominantly governed by proton transfer from the protonated amino group. This assumption is supported by minimum energy path calculations of Sobolewski et al. that have revealed the presence of only a small energy barrier (0.1 eV) for the proton transfer from the amino group to the phenol ring.[18] Further indications for such a mechanism can be obtained by comparison with findings on the fluorescence quenching in tryptophan. Recently, Leonard et al.[19] have investigated excited state quenching and photoproduct formation of tryptophan in aqueous solution by performing femtosecond transient absorption experiments. By varying the pH and comparing with the transient spectra of tryptophan incorporated in a peptide, where electron transfer is the dominant quenching mechanism, they could identify a zwitterionic photoproduct with the indole moiety protonated. Formation of this product occurred via excited state proton transfer from the side chain amino group. This has confirmed earlier theoretical predictions obtained by excited state reaction path calculations.[18,20]

From these extensive studies, it can be inferred that electron and proton transfer processes play a key role in the excited state properties of tyrosine. Therefore, a comprehensive investigation of tyrosine photodynamics should not be restricted to the chromophore part of the system (phenol) only, but the side chain as well as all nuclear degress of freedom should be accounted for. Moreover, it can be expected that for tyrosine in solution or in protein environment also neighboring solvent molecules or amino acid residues should affect the photodynamics.

In the present contribution we report for the first time the theoretical investigation of the laser-induced nonadiabatic dynamics of isolated tyrosine including all nuclear degrees of freedom. We confirm the O−H detachment as a deactivation channel in tyrosine. Moreover, we reveal that in the gas phase, the previously predicted proton transfer from the amino group to the phenol ring is preceded by an additional proton transfer step from the carboxyl group to the amino group. Thus, a two-step proton transfer mechanism is identified. Beyond the gas phase study, we have also investigated the nonadiabatic dynamics of tyrosine in water environment in order to shed light on the influence of the solvent. We reveal the presence of a deactivation channel involving proton transfer from the side chain to the chromophore, similar to the finding in the gas phase. In solution, however, the reaction proceeds involving a nearby water molecule which acts as a bridge for the proton transfer.

Our paper is structured in the following way: First, the theoretical approach is outlined in section 2, involving a brief description of the field-induced surface hopping (FISH) method as well as the calculation of the necessary couplings in the framework of time-dependent density functional theory (TDDFT) and the combination of FISH with the quantum mechanical/molecular mechanical (QM/MM) approach. In section 3 the computational details are presented. Subsequently in section 4, the results of our nonadiabatic dynamics simulations on tyrosine are presented and discussed, finally followed by conclusions and outlook in section 5.

2. THEORETICAL FORMULATION

Field-Induced Surface Hopping (FISH). The FISH method is based on the propagation of independent classical trajectories in a manifold of several electronic states under the influence of laser fields with arbitrary shapes. In order to describe the population transfer between these states, which arises both due to the coupling with the laser field and through the intrinsic nonadiabatic coupling, the trajectories are allowed to switch between the states according to quantum mechanically determined probabilities. This is similar to Tully's surface hopping method[21] which is however only suited to describe field-free nonadiabatic transitions in molecular systems.[22−28]

The detailed description of FISH simulations has been already presented in refs 29 and 30. Briefly, the following steps are needed: First, initial conditions for an ensemble of trajectories are generated. Second, along each trajectory which is propagated in the framework of molecular dynamics "on the fly" the electronic degrees of freedom are propagated by solving the time-dependent Schrödinger equation in the manifold of adiabatic electronic states coupled by the laser field $\vec{E}(t)$ and by the nonadiabatic coupling terms $D_{ij}(\mathbf{R}(t)) = \langle \mathbf{\Psi}_i(\mathbf{R}(t)) | (\mathrm{d}\mathbf{\Psi}_j(\mathbf{R}(t))/\mathrm{d}t \rangle$

$$i\hbar \dot{c}_i(t) = E_i(\mathbf{R}(t))c_i(t) - \sum_j [i\hbar D_{ij}(\mathbf{R}(t)) + \vec{\mu}_{ij}(\mathbf{R}(t))\cdot\vec{E}(t)]c_j(t) \quad (1)$$

where $c_i(t)$ are the expansion coefficients of the electronic wave function from which density matrix elements can be calculated as $\rho_{ij} = c_i^* c_j$. Finally, the hopping probabilities are determined in each nuclear time step from the change of the diagonal density matrix elements ρ_{ii}, which correspond to the electronic state populations, according to

$$P_{i\to j} = \Theta(-\dot{\rho}_{ii})\Theta(\dot{\rho}_{jj})\frac{-\dot{\rho}_{ii}}{\rho_{ii}}\frac{\dot{\rho}_{jj}}{\sum_k \Theta(\dot{\rho}_{kk})\dot{\rho}_{kk}}\Delta t \quad (2)$$

where the Θ functions are defined to be one for positive arguments and zero otherwise.[31,32] The hopping probabilities are used in a stochastic process to decide if a state switch occurs. In the absence of a laser field, the total energy of the system during a state switch is conserved by rescaling the nuclear velocities uniformly. If a laser field is present, energy exchange with the molecular system can occur and thus no velocity rescaling is applied. The electronic state population as a function of time is finally obtained by averaging over the ensemble of trajectories.

The above presented FISH method is suitable for the simulation and control of laser-induced processes[29,33] as well as for the simulation of spectroscopic observables such as time-resolved photoelectron spectra[30,34,35] or harmonic emission.[31]

Nonadiabatic Couplings and Transition Dipole Moments in the Framework of TDDFT. The nonadiabatic couplings D_{ij} as well as the transition dipole moments μ_{ij} are obtained from the linear response TDDFT method according to Mitrić et al. by defining an auxiliary wave function for each excited electronic state, consisting of all single excitations in the manifold of the Kohn−Sham (KS) orbitals.[36,37] It has the form

$$|\Psi_i\rangle = \sum_m^{\mathrm{virt}} \sum_n^{\mathrm{occ}} c_{mn}^i(t)\hat{a}_m^\dagger \hat{a}_n |\Phi_{\mathrm{KS}}\rangle \quad (3)$$

where the operator $\hat{a}_m^\dagger$ creates an electron in the virtual orbital m and $\hat{a}_n$ annihilates one in the occupied orbital n, $|\Phi_{\mathrm{KS}}\rangle$ is the ground state KS determinant, and the coefficients c_{mn}^i are determined from the TDDFT eigenvectors.[36] Employing this wave function, the coupling elements are obtained as

dx.doi.org/10.1021/jp302179m | J. Phys. Chem. B 2012, 116, 8762−8770

$$D_{ij} = \langle \Psi_i(t) | \frac{d\Psi_j(t)}{dt} \rangle \approx \frac{1}{2\Delta t}(\langle \Psi_i(t) | \Psi_j(t + \Delta t) \rangle - \langle \Psi_i(t + \Delta t) | \Psi_j(t) \rangle) \quad (4)$$

$$\mu_{ij} = \langle \Psi_i(t) | \hat{\mu} | \Psi_j(t) \rangle \quad (5)$$

Combination of the FISH Nonadiabatic Dynamics with the TDDFT/MM Approach. The extension of nonadiabatic dynamics to the description of systems interacting with their environment in the framework of the quantum mechanical/molecular mechanical (QM/MM) approach has already been presented previously.[38,39] Briefly, the idea of QM/MM is to separate the system into a quantum mechanical part (QM), for which the excited state energies, gradients, and nonadiabatic couplings are calculated quantum mechanically, and a classical part (MM), which is treated using common force field methods. In the most straightforward mechanical embedding approach, which has been employed in the present work, the interaction of the QM and MM regions is restricted to the steric repulsion between solvent and solute, and the Hamiltonian of the QM system is not directly affected by the MM environment. Therefore, polarization effects from the solvent environment on the QM wave function are not included in this model. However, in our case we treat the most important solvent molecules explicitly as parts of the QM system, hence taking into account their interaction with the solute molecule without further approximations. This allows us to realistically model the solute−solvent interaction in the region of interest for the photodynamical processes under study while retaining a simplified description of the remaining solvent molecules.

In the case that both the QM part (X) and the MM part (Y) are sufficiently well described by the classical force fields, the effect of sterical repulsion between them can be calculated as the difference between the MM energy of the combined system (X + Y) and the QM system alone. The total energy of the combined system in the frame of QM/MM approach can then be written as:

$$E_{QM+MM} = E_{QM}(X) + [E_{MM}(X + Y) - E_{MM}(X)] \quad (6)$$

The forces needed to carry out dynamics "on the fly" are obtained as the gradient of eq 6 and the nonadiabatic couplings are calculated only for the QM part.

3. COMPUTATIONAL METHODS

The structure of isolated tyrosine has been optimized using density functional theory (DFT) employing the PBE0 functional[40] and the TZVP basis set[41] as implemented in TURBOMOLE.[42] For the dynamics simulations, the electronic structure was described in the framework of time-dependent density functional theory (TDDFT) using the PBE0 functional and the smaller SV(P) basis set.[43,44] This allows for a more efficient computation of the needed energies and gradients while giving only minor deviations to the results obtained with the TZVP basis set, as has been examined by comparing the absorption spectra and a limited number of nonadiabatic reference trajectories. Furthermore, the position and character of the lowest-lying excited states are also reproduced at higher levels of theory (CAM-B3LYP[45]/SVP, CAM-B3LYP/TZVP, and CC2[46]/TZVP) as discussed in the Supporting Information, Table S1.

The 60 initial coordinates and momenta have been generated by propagating a trajectory in the electronic ground state at constant temperature (298 K) for 10 ps and then sampling the structures each 100 fs.

For the propagation of the nuclei, the Newtonian equations of motion have been integrated using the velocity Verlet[47] algorithm with a time step of 0.1 fs. Along each trajectory, the electronic Schrödinger equation (1) has been integrated using the fourth order Runge−Kutta method with a time step of 10^{-5} fs.

In order to simulate the excitation by a laser field, the system has been excited resonantly to the most intensive electronic transition by a Gaussian pump laser pulse of the form

$$E(t) = E_0 \exp\left(-\frac{(t - t_0)^2}{2\sigma^2}\right) \sin \omega(t - t_0) \quad (7)$$

The ensemble of trajectories was propagated in the manifold of the ground state and the six lowest excited singlet states including both the interaction with the laser field as well as nonadiabatic effects. The explicit inclusion of the pump pulse allows us to more realistically model the experimental excitation process leading to a population of several excited electronic states. As discussed in section 2 no velocity rescaling is applied after a hopping event during the action of the pulse, since the interaction between molecule and laser field implies the nonconservation of the molecular energy. For times larger than the 2 σ width of the Gaussian pulse ($t_0 \pm 2\sigma$), when the field strength is negligible, the velocity rescaling is enabled and field-free nonadiabatic dynamics with conserved total energy is carried out. In this way the electronic relaxation dynamics after initial excitation is described analogously to the purely field-free nonadiabatic dynamics. The difference of both approaches lies in the initial excitation, which is in the field-free case simplified by starting all trajectories directly in the desired excited state which exhibits the highest oscillator strength.

In order to explore the photodynamics of solvated tyrosine we have considered also the molecule surrounded by water. Under these conditions, tyrosine is most stable in the zwitterionic form. The model for the solvated tyrosine has been obtained by embedding it in a 49 Å cubic water box followed by equilibration using force field molecular dynamics under periodic boundary conditions over 100 ps at a pressure of 1.0 bar and a temperature of 300 K employing the TINKER program.[48] For tyrosine, the OPLS-AA[49−51] and for water the TIP-3P[52] force field were used. After equilibration, a sphere of 21 Å radius, including tyrosine and 1268 water molecules, was cut from the box and further relaxed using the QM/MM approach for 3 ps at 300 K. The QM part consisted of the tyrosine molecule only, which was described by DFT employing the PBE0 functional and the SV(P) basis set. From this QM/MM trajectory, the initial conditions for the nonadiabatic dynamics simulations were generated by sampling at regular time intervals. In order to obtain an almost spherical water droplet, the water spheres of each initial condition have been further truncated to 20 Å. For taking into account the interaction between the solvent and the polar amino group of tyrosine explicitly, the QM part of the system was extended to include also the three water molecules situated most closely to the amino group. This allowed us to investigate also the influence of hydrogen bonding at the amino group on the relaxation dynamics. Since for the zwitterionic tyrosine in water the presence of charge-transfer excitations can be expected, the

dx.doi.org/10.1021/jp302179m | J. Phys. Chem. B 2012, 116, 8762−8770

electronic structure was described using the Coulomb-attenuated B3-LYP functional (CAM-B3LYP)[45] together with the SVP basis set,[43,44] as implemented in the Gaussian 09 program suite.[53] This functional has been developed in order to improve the description of long-range charge transfer transitions. The position and character of the lowest-lying excited states have been validated against higher level calculations (CAM-B3LYP/SVP, CAM-B3LYP/TZVP, and CC2/TZVP) as discussed in the Supporting Information, Table S2. Due to the much higher computational cost employing the CAM-B3LYP functional, only a limited number of trajectories has been propagated.

4. RESULTS AND DISCUSSION

Ultrafast Relaxation of Isolated Tyrosine: Nonadiabatic and Laser-Induced Dynamics. Since in the gas phase the canonical form of tyrosine is more stable than the zwitterionic one, the former has been considered for the gas phase simulation of the present contribution. Among the several low-lying conformers,[54] we have selected the one shown in Figure 1. The electronic absorption spectra for the optimized ground state structure of tyrosine in the gas phase as well as for the whole initial thermal 300 K ensemble of 60 structures obtained with TDDFT [PBE0/SV(P)] are shown in Figure 1. In agreement with experimental data,[3] the spectrum is characterized by two bands at wavelengths above 200 nm corresponding to two $\pi\pi^*$ transitions usually labeled as L_a and L_b according to the Platt notation. The lower-lying state is located at 244 nm (5.07 eV) and the second one at 210 nm (5.89 eV), corresponding to a slight blue shift compared to the experiment, where the first absorption band is situated between 260 and 280 nm (4.77−4.43 eV) and the second, more intense one at 220 nm (5.64 eV), respectively.[3] At the equilibrium geometry (cf. Figure 1b), the two lowest-lying bright states are S_1 and S_3 which both have $\pi\pi^*$ character. The S_1 state can be identified with the less intensive L_b state which is more stable in the gas phase, while S_3 corresponds to L_a, the more intensive state with higher permanent dipole moment. Between these bright states, an additional dark state is found (S_2), which is characterized by orbital excitations within the amino and carboxyl groups. These findings are reproduced at higher levels of theory using the larger TZVP basis set, the range-separated CAM-B3LYP functional as well as the coupled cluster approach CC2 as pointed out in the Supporting Information, Table S1. Moreover, also the results of Sobolewski et al. on tyrosine +2 H_2O at the CC2 level show a similar character of the first three excited states (ref 17, cf. also the Supporting Information). The higher-lying states S_6 and S_{10} are repulsive and are mainly important for the deactivation channels observed during the nonadiabatic dynamics. Specifically, S_6 has $\pi\sigma^*$ character and is repulsive along the O−H stretching coordinate, while S_{10} is the repulsive $\pi\sigma^*$ state located on the N−H stretching coordinate.

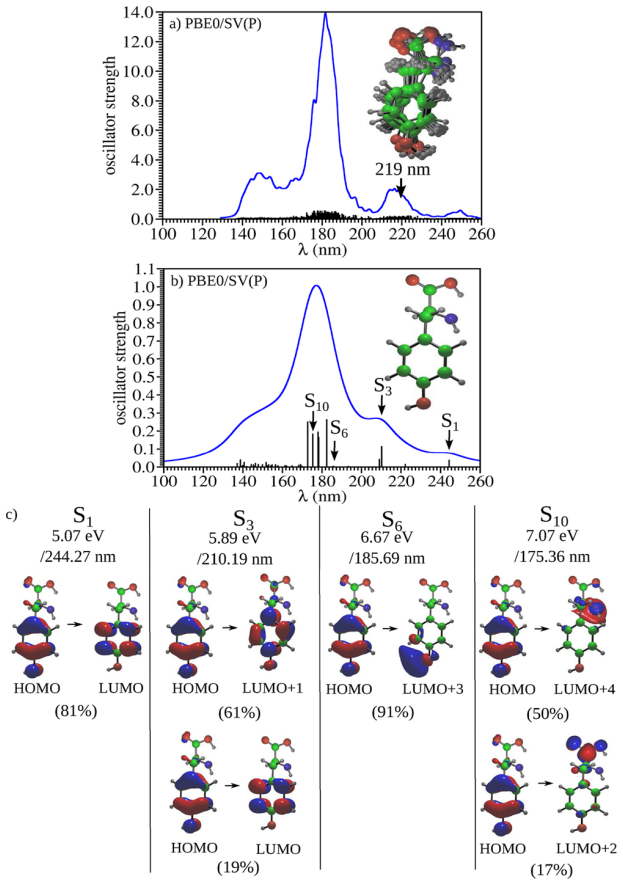

Figure 1. Electronic absorption spectra of isolated tyrosine including the lowest 40 excited singlet states obtained by TDDFT [PBE0/SV(P)] for the thermal ensemble of 60 structures at 300 K (a) and for the equilibrium geometry (b). The individual transitions (black sticks) have been convoluted by a Lorentzian width of 2 nm (blue lines) for the spectrum of the ensemble and by a Lorentzian width of 20 nm for the spectrum of the equilibrium structure. Panel c shows the character of the most relevant singlet states in terms of the leading orbital excitations.

For comparison, we show in Figure 2 the absorption spectrum obtained using the more accurate CAM-B3LYP functional. Overall, the spectrum is quite similar to the one shown in Figure 1, in particular regarding the character and the position of the two $\pi\pi^*$ states S_1 and S_3. However, there is less splitting between the higher states, such that the lowest-lying repulsive state of $\pi\sigma^*$ character corresponds already to S_4 at CAM-B3LYP/SVP level.

In order to study the photodynamics of tyrosine we have performed nonadiabatic molecular dynamics simulations in the manifold of the ground state and the lowest six excited singlet states. We have first propagated the ensemble of trajectories starting directly from the bright state S_3 without including the excitation field. Subsequently, also FISH simulations directly accounting for the field-induced excitation have been carried out.

The nonadiabatic dynamics started in the S_3 state is characterized by ultrafast population transfer via the S_2 to the S_1 state with an S_3 lifetime of 11.8 fs, as shown in Figure 3. The maximal S_1 population of ~60% is reached after 30 fs, followed by slow decay to the ground state. After the total propagation time of 200 fs, about 10% of the trajectories have returned to the ground state. This occurs via an efficient reactive channel characterized by a double proton transfer process (see Figure 4) which drives the system toward a low-lying conical intersection between the S_1 and S_0 states. The degeneracy is induced by an out-of-plane bending of an aromatic carbon in the phenyl ring at the C1 or C2 position, respectively. The major part of the trajectories, however, remains trapped in the S_1 state until the end of the simulation.

During the internal conversion from S_3 to S_2 and S_1, in most cases the electronic state character changes from $\pi\pi^*$ to $n\pi^*$,

dx.doi.org/10.1021/jp302179m | J. Phys. Chem. B 2012, 116, 8762−8770

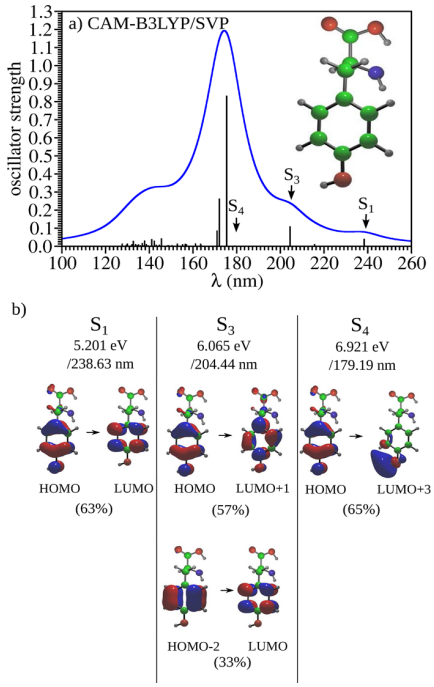

Figure 2. Electronic absorption spectrum of isolated tyrosine including the lowest 40 excited singlet states obtained by TDDFT (CAM-B3LYP/SVP) for the equilibrium geometry optimized at the same level (a). The individual transitions (black sticks) have been convoluted by a Lorentzian width of 20 nm (blue line). Panel b shows the character of the most relevant singlet states in terms of the leading orbital excitations.

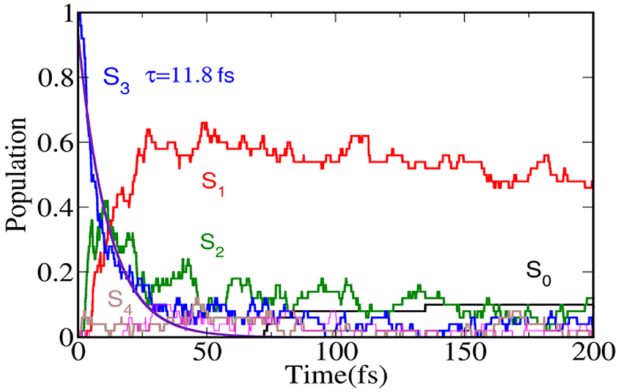

Figure 3. Time-dependent electronic state populations of isolated tyrosine during the field-free nonadiabatic dynamics employing TDDFT [PBE0/SV(P)]. The violet line represents an exponential fit to the population of the state S_3 with a lifetime τ of 11.8 fs.

which is accompanied by a structural rearrangement from the neutral to the zwitterionic form of tyrosine. At this stage the molecule is prearranged for the proton transfer to the phenol ring, where charge density may be accumulated in agreement with the previously proposed H-acceptor model.[20] In previous theoretical investigations using the coupled cluster method CC2, the proton transfer pathway to the phenol ring was found to exhibit a small barrier of 0.1 eV,[18] whereas in our TDDFT calculations this path is even barrierless. Concerning the distribution of charges during the process, it is still an open question if the H transfer is nucleophilic or electrophilic.

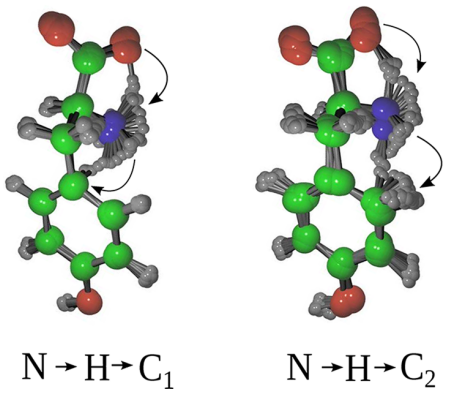

Figure 4. Illustration of the proton transfer from the carboxyl and amino groups to the carbon atoms C1 (left) and C2 (right). For both processes, snapshots of a representative trajectory are superimposed for every 0.5 fs of the relevant part of the dynamics.

Therefore, we have performed a Mulliken population analysis which has revealed a positive charge accumulation at the migrating H and a negative one at the accepting phenol carbon, confirming the electrophilic nature of the process.

Among all of the reactive trajectories, the proton transfer pathways from the amino group to C1 and to C2 have been observed with equal incidence (see Figure 4). Although the C2 position is sterically favored, the C1 position is also an efficient reaction site due to the electron-donating effect induced by the OH group in para position.

Remarkably, for one reactive trajectory a decarboxylation process has been observed after the decay to S_0, giving rise to a bicyclic photoproduct (cf. Figure 5). From the experimental side, there is no data available for photoinduced decarboxylation in tyrosine. However, in the case of tryptophan the deacarboxylation quantum yield has been determined to 0.8%,[55] indicating that such a process is present as a minor reaction channel.

In order to study the role the laser-induced electronic excitation plays in the nonadiabatic dynamics of tyrosine, also simulations using the FISH method have been performed, using the same set of 60 initial conditions as in the field-free case. For the excitation a Gaussian pump pulse has been employed (see eq 7), with the amplitude $E_0 = 0.01E_h/(ea_0)$ corresponding to an intensity of 3.5×10^{12} W/cm^2, a frequency $\omega_{pump} = 5.66$ eV (219 nm) resonant to the bright state S_3, a temporal width of 23.5 fs ($\sigma = 10$ fs) and $t_0 = 20$ fs. As shown in Figure 6, this pulse leads to photoexcitation of about 90% of the trajectories, mainly to the S_3 state, but also to S_2 and S_4. The initial excitation is rapidly followed by internal conversion to the S_1 state after the pulse has ceased. Within 100 fs, almost the total excited state population is transferred to S_1. Subsequently, a slow decay to the ground state is present, which is reached by 17% of the initially excited trajectories after 200 fs.

Compared to the field-free dynamics, the FISH simulation gives rise to a larger number of possible reaction channels for the nonadiabatic deactivation to the ground state. The main pathway is the pure H abstraction from the protonated amino group, which is occasionally followed by proton transfer to the phenol ring.

A more detailed insight into this process responsible for the internal fluorescence quenching can be gained by analyzing the selected nonadiabatic trajectory shown in Figure 7. In this case, at ~14 fs the pump pulse transfers the trajectory to the bright

dx.doi.org/10.1021/jp302179m | J. Phys. Chem. B 2012, 116, 8762–8770

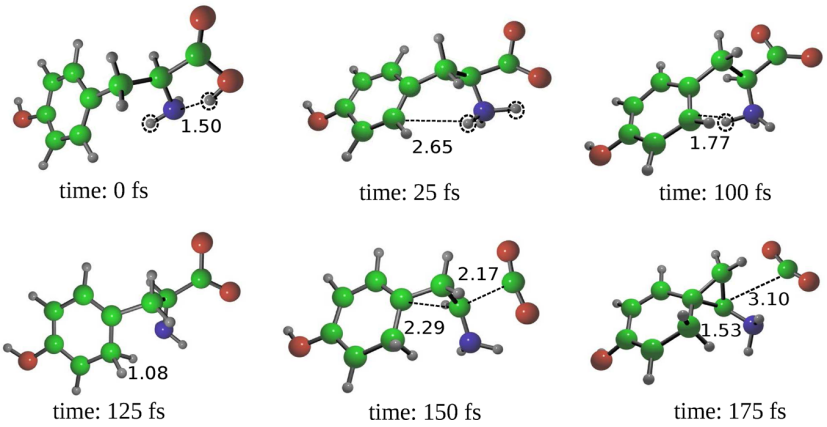

Figure 5. Snapshots of a nonadiabatic trajectory showing decarboxylation of tyrosine. At 25 fs the proton transfer from the carboxyl to the amino group occurs. Subsequently, after 125 fs the phenol C2 atom has been protonated, and the decay to the ground state through a CI is observed. This is finally followed by decarboxylation (CO_2 formation) and the formation of a bicyclic photoproduct after 175 fs. The atom distances and bond lengths are given in Å.

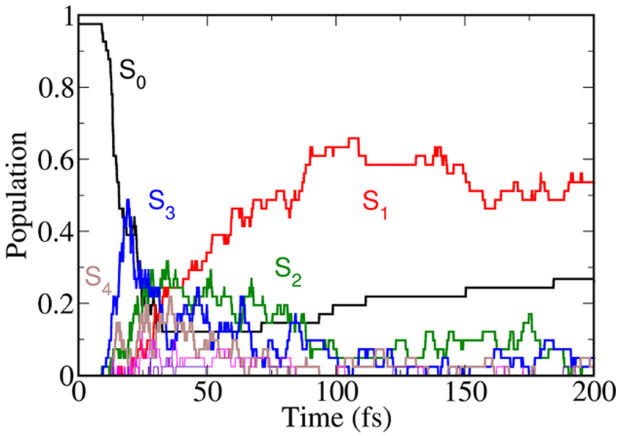

Figure 6. Time-dependent electronic state populations in isolated tyrosine employing FISH nonadiabatic dynamics combined with TDDFT [PBE0/SV(P)]. The excitation is due to a resonant 219 nm pulse with a width of 23.5 fs.

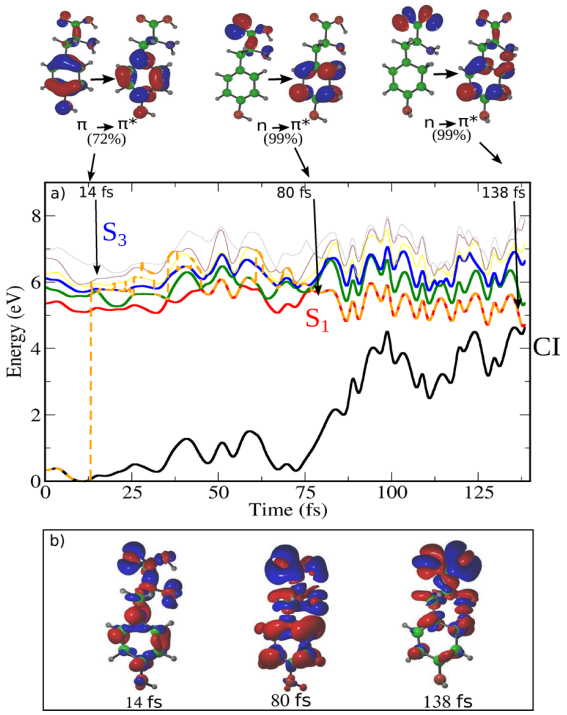

Figure 7. (a) Relative energies of the lowest 6 electronic states obtained by TDDFT [PBE0/SV(P)] along a selected nonadiabatic trajectory where the protonation of the chromophore has been observed as deactivation channel. The actual state in which the trajectory resides is labeled by the orange dashed line. For selected time steps, the character of this state is illustrated on the top of panel a by the main orbital excitations and in panel b by the electron density difference to the ground state.

state S_3, which is of mixed $\pi\pi^*/n\pi^*$ character (with the n orbital localized on the carboxyl group and the π^* orbital on the phenol ring). Within 75 fs the relaxation proceeds to the S_1 state with $n\pi^*$ character. In this state, the proton transfer from the carboxyl group to the amino group takes place, followed by the stretching of one N−H bond. As the dynamics proceeds toward a conical intersection with the ground state, the proton transfer to the phenol ring occurs, and the ground state is reached after ∼140 fs.

Interestingly, within the FISH simulations an additional deactivation channel has been observed, as illustrated for a selected trajectory in Figure 8. Here, the dynamics proceeds mostly in the higher excited states S_2 to S_5, and the final return to the S_1 state does not take place before ∼140 fs. At this time, the S_1 state is of $\pi\sigma^*$ character. The subsequent dynamics is straightforwardly directed toward a conical intersection with the ground state which is reached at 150 fs. This is accompanied by a strong excitation of the O−H stretching vibration, ultimately leading to the breaking of the O−H bond as can be recognized from the time-dependent bond distances shown in Figure 8b. These findings are in agreement with the model by Sobolewski and Domcke, who have identified the O−H detachment as a feasible relaxation mechanism induced by $\pi\pi^*/\pi\sigma^*$ internal conversion and therefore population of a $\pi\sigma^*$ state which is repulsive along the O−H stretching coordinate.[11−13] Experimental evidence for this process has been recently provided by Stavros et al.[13] who have observed H atom elimination through $\pi\sigma^*$ states after excitation at 200 nm. The occurrence of this deactivation channel only within the FISH dynamics

dx.doi.org/10.1021/jp302179m | J. Phys. Chem. B 2012, 116, 8762−8770

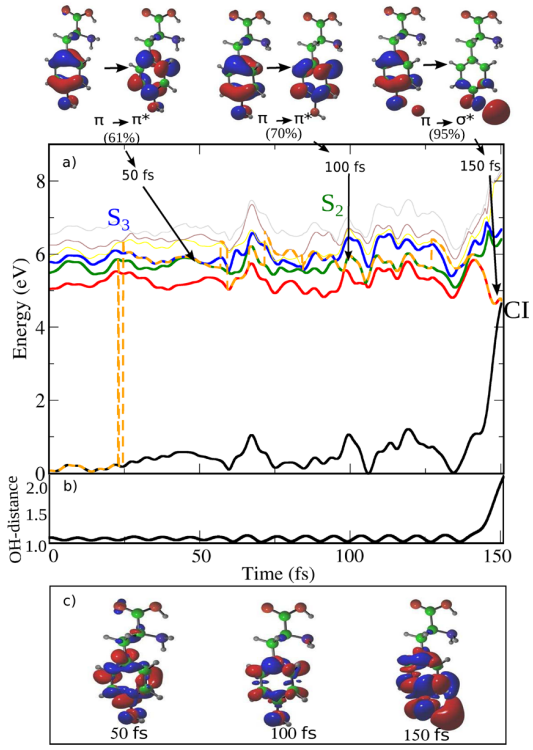

Figure 8. Relative energies of the lowest 6 electronic states obtained by TDDFT [PBE0/SV(P)] along a selected nonadiabatic trajectory where the O−H detachment has been observed as deactivation channel. The actual state in which the trajectory resides is labeled by the orange dashed line. For selected time steps, the character of this state is illustrated on the top of panel a by the main orbital excitations and in panel c by the electron density difference to the ground state. The inset (panel b) shows the temporal evolution of the O−H bond distance in Å along the trajectory.

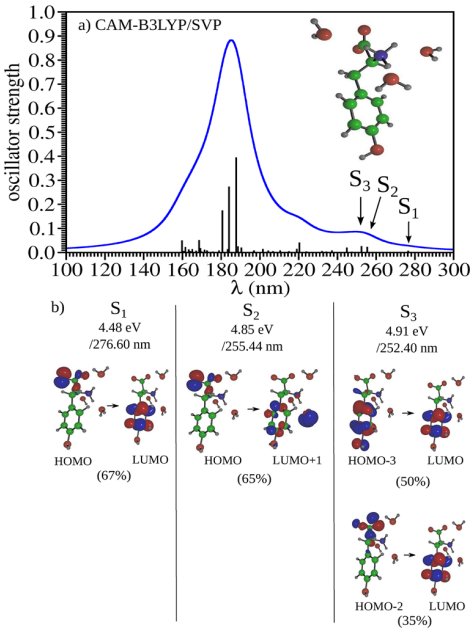

Figure 9. Electronic absorption spectrum of tyrosine with three explicit water molecules embedded in a classical water sphere, calculated with TDDFT [CAM-B3LYP/SVP]. The individual transitions (black sticks) have been convoluted by a Lorentzian width of 20 nm (blue line). Panel b shows the character of the first three excited states S_1, S_2, and S_3 in terms of the leading orbital excitations.

simulations but not within the field-free nonadiabatic dynamics underlines the need for a correct description of the electronic excitation in order to realistically simulate the photodynamical processes.

The character of the near-degeneracies between the S_1 and S_0 states involved in both relaxation channels has been carefully examined, due to the known deficiency of linear response TDDFT in properly describing conical intersections. Employing the complete active space self-consistent field method (CASSCF),[56,57] the presence of small energy gaps has been confirmed as shown in the Supporting Information, Table S3, indicating that the respective TDDFT geometries lie indeed close to a conical intersection.

Ultrafast Dynamics of Microsolvated Tyrosine. In order to investigate the influence of water environment on the dynamical properties and the relaxation channels, we have carried out nonadiabatic dynamics simulations in the framework of QM/MM, where the QM system consisted of tyrosine in the zwitterionic form and three water molecules solvating the protonated amino group. The remaining water environment was described by a classical force field interacting with the QM part using the mechanical embedding scheme. For the electronic structure of the QM system the CAM-B3LYP functional was employed in order to achieve a realistic description of the charge transfer excitations present in polar solvents. The experimental absorption spectrum of tyrosine in water is characterized by two intense peaks at 225 (5.51 eV) and 282 nm (4.39 eV)[5] which have been identified with the L_a and L_b bands. The theoretical spectrum of tyrosine + $3H_2O$ obtained with TDDFT (CAM-B3LYP/SVP) is shown for a selected geometry in Figure 9. This geometry has not been optimized but corresponds to the initial conditions of the nonadiabatic trajectory which will be discussed below. The spectrum exhibits the first transition of $\pi\pi^*$ character at 252 nm, which corresponds to the S_3 state. The lower-lying states have less intensity and are of $n\pi^*$ (S_1) and charge transfer to solvent (CTTS) character (S_2). It should be noticed, that the character and position of the excited states depends strongly on the chosen geometry of tyrosine as well as on the position of the explicit water molecules. In order to validate the chosen computational approach, we have calculated the absorption spectrum for the given structure also at higher computational level employing TDDFT with larger basis sets as well as the coupled cluster method CC2. These calculations are presented in the Supporting Information, Table S2, and show only minor differences to the spectrum shown in Figure 9. According to the electronic state character, the S_3 state was subsequently chosen as initial state for the nonadiabatic dynamics simulations.

Due to the considerable computational cost of calculations using the CAM-B3LYP functional, only a limited number of trajectories has been employed in the nonadiabatic dynamics simulations involving the ground and the 5 lowest excited singlet states. Among a total of 5 trajectories, in one case the nonadiabatic decay involving a proton transfer process is observed. In contrast to the gas phase, in solution a water molecule acts as a bridge for the proton migration, leading to a two-step mechanism which is analyzed in terms of energies and

dx.doi.org/10.1021/jp302179m | J. Phys. Chem. B 2012, 116, 8762−8770

electronic state character in Figure 10, whereas the structural rearrangement is illustrated by the snapshots shown in Figure 11.

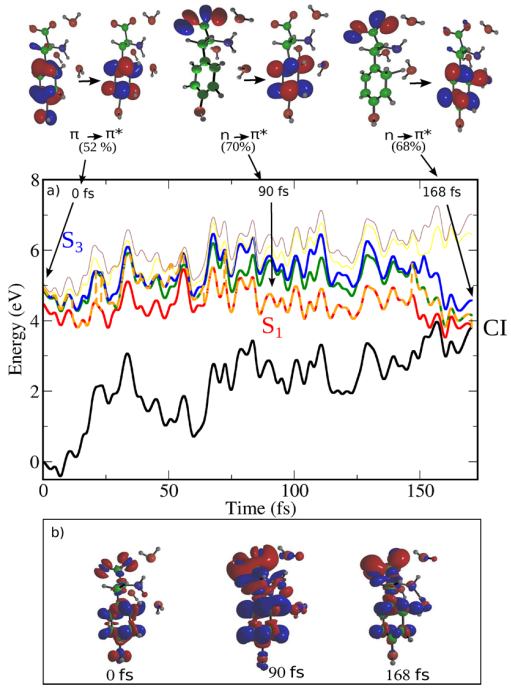

Figure 10. Relative energies of the lowest five electronic states obtained by TDDFT [CAM-B3LYP/SVP] along a selected nonadiabatic trajectory of tyrosine +3 H_2O in a classical water sphere. The actual state in which the trajectory resides is labeled by the orange dashed line. For selected time steps, the character of this state is illustrated on the top of panel a by the main orbital excitations and in panel b by the electron density difference to the ground state.

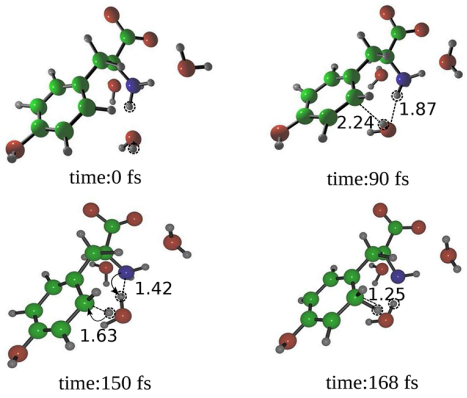

Figure 11. Snapshots of a selected nonadiabatic trajectory of tyrosine in water, showing the double proton transfer mechanism for nonadiabatic decay. At 150 fs the zwitterionic isomer of tyrosine transfers a proton from the amino group to a neighboring water molecule. From there, the proton is further passed to the C2 atom of the phenol ring, and the decay to the ground state occurs after 168 fs. The atom distances and bond lengths are given in Å.

Starting in the $\pi\pi^*$ S_3 state, the trajectory reaches the first excited state, which has then $n\pi^*$ character, after 60 fs. Within the following ~90 fs, the water molecules near the amino group are prearranged as to enable the proton transfer (cf. Figure 11). The latter takes place within the next 20 fs, in which almost simultaneously one proton is donated from the amino group to the nearest water molecule, and another one from the water molecule to the C2 carbon of the phenol ring. Subsequently the decay to the ground state occurs after ~170 fs through to the same "benzene-kink" conical intersection as in the gas phase.

These findings confirm the presence of an "internal" deactivation channel for tyrosine photoreactivity also in a polar solvent. In contrast to the gas phase, neighboring solvent molecules play a decisive role by mediating the proton transfer from the side chain to the phenol ring. This emphasizes the need to introduce explicit water molecules for a correct description of the electrophilic proton addition to the chromophore and therefore of the ultrafast nonradiative decay of tyrosine in water.

5. CONCLUSIONS

We have presented the investigation of nonadiabatic photodynamics of tyrosine in the gas phase and in water. The gas phase dynamics has been explored by a combination of nonadiabatic molecular dynamics "on the fly" with time-dependent density functional theory. Both the field-free nonadiabatic relaxation as well as the laser field-induced dynamics in the framework of the FISH method have been simulated. We have shown that after initial excitation to the bright $\pi\pi^*$ states ultrafast internal conversion occurs to the lowest excited singlet state, which has mainly $n\pi^*$ character at this stage of the dynamics. Subsequently, nonradiative relaxation to the ground state can occur through conical intersections. Beyond the well-known deactivation channel via O−H bond breaking in repulsive $\pi\sigma^*$ states, also the transfer of a proton from the side chain to the phenol ring represents an efficient deactivation path. In the gas phase, where the canonical form of tyrosine is the most stable one, this involves a two-step mechanism: The carboxyl group of the side chain first passes its proton to the amino group, from which it further migrates to the phenol ring. This is accompanied by efficient fluorescence quenching, as radiationless decay from S_1 to S_0 occurs through a conical intersection. The degeneracy in this case is induced by an out-of-plane bending of the aromatic carbon atom (C1 or C2) which is being protonated.

Beyond the gas phase study, we have also investigated the influence of solvent environment on the photodynamics of tyrosine by utilizing the combination of our TDDFT-nonadiabatic dynamics approach with the QM/MM technique. Specifically, the zwitterionic conformer of tyrosine together with three explicit water molecules has been embedded in a classical water sphere of 20 Å radius, and the nonadiabatic relaxation has been simulated. The relaxation mechanism found in this way is analogous to the one observed in the gas phase as it also involves transfer of a proton from the side chain to the phenol ring. However, in this case in the first step a proton is donated from the protonated amino group to a nearby water molecule, which acts as a mediator and subsequently passes the proton to the phenol ring. This emphasizes the decisive role of water in the photodynamics of tyrosine.

■ ASSOCIATED CONTENT

Supporting Information

For validation of the results presented above, the energies and oscillator strengths of the first six excited electronic states are provided for isolated tyrosine in Table S1 as well as for tyrosine + 3H_2O in Table S2, employing TDDFT with larger basis sets

dx.doi.org/10.1021/jp302179m | J. Phys. Chem. B 2012, 116, 8762−8770

as well as the linear response coupled cluster method CC2. Furthermore, the near-degeneracies at the last points of the trajectories analyzed in Figures 7 and 8 are validated by comparing them with the energy gaps at the CASSCF level as shown in Table S3. This material is available free of charge via the Internet at http://pubs.acs.org.

AUTHOR INFORMATION

Corresponding Author

*E-mail: mitric@zedat.fu-berlin.de.

Notes

The authors declare no competing financial interest.

ACKNOWLEDGMENTS

We acknowledge financial support from the Deutsche Forschungsgemeinschaft, FOR 1282 (J.P. and R.M.), SPP 1391 (R.M.), and Emmy Noether Program (MI-1236) (R.M. and M.W.). In addition, G.T. thanks the Alexander von Humboldt Foundation (Grant Card. No. 7000260646) for financial support.

REFERENCES

(1) Zewail, A. H. *J. Phys. Chem. A* **2000**, *104*, 5660−5694.
(2) Konev, S. V. *Fluorescence and Phosphorescence of Proteins and Nucleic Acids*; Plenum: New York, 1967.
(3) Zhang, J. Y.; Nagra, S.; Li, L. *Anal. Chem.* **1991**, *63*, 2995−2999.
(4) Wetlaufer, D.; Edsall, J.; Hollingworth, B. *J. Biol. Chem.* **1958**, *233*, 1421−1428.
(5) Truong, T.; Petit, A. *J. Phys. Chem.* **1979**, *83*, 1300−1305.
(6) Ross, T.; Lee, J. *J. Phys. Chem. B* **1998**, *102*, 4612−4618.
(7) Audrey, W. *Biochem. J.* **1971**, *71*, 217−220.
(8) Guzow, K.; Szabelski, M.; Rzeska, A.; Karolczak, J.; Sulowska, H.; Wiczk, W. *Chem. Phys. Lett.* **2002**, *362*, 519−526.
(9) Köhler, G.; Getoff, N. *Chem. Phys. Lett.* **1974**, *26*, 525−528.
(10) Creed, D. *Photochem. Photobiol.* **1984**, *39*, 563−575.
(11) Sobolewski, A. L.; Domcke, W.; Dedonder-Lardeaux, C.; Jouvet, C. *Phys. Chem. Chem. Phys.* **2002**, *4*, 1093−1100.
(12) Lan, Z. G.; Domcke, W.; Vallet, V.; Sobolewski, A.; Mahapatra, S. *J. Chem. Phys.* **2005**, *122* (Article 224315), 1−13.
(13) Iqbal, A.; Stavros, V. G. *J. Phys. Chem. Lett.* **2010**, *1*, 2274−2278.
(14) Holt, L. A.; Milligan, B.; Rivett, D. E.; Stewart, F. H. *Biochim. Biophys. Acta* **1977**, *499*, 131−138.
(15) Dillon, J. *Photochem. Photobiol.* **1980**, *32*, 37−39.
(16) Beechem, J. M.; Brand, L. *Annu. Rev. Biochem.* **1985**, *54*, 43−71.
(17) Sobolewski, A.; Shemesh, D.; Domcke, W. *J. Phys. Chem. A* **2009**, *113*, 542−550.
(18) Gregoire, G.; Jouvet, C.; Dedonder, C.; Sobolewski, A. *J. Am. Chem. Soc.* **2006**, *129*, 6223−6231.
(19) Leonard, J.; Sharma, D.; Szafarowicz, B.; Torgasin, K.; Haacke, S. *Phys. Chem. Chem. Phys.* **2010**, *12*, 15744−15750.
(20) Blancafort, L.; Gonzalez, D.; Olivucci, M.; Robb, M. A. *J. Am. Chem. Soc.* **2002**, *124*, 6398−6406.
(21) Tully, J. C. *J. Chem. Phys.* **1990**, *93*, 1061−1071.
(22) Mitrić, R.; Bonačić-Koutecký, V.; Pittner, J.; Lischka, H. *J. Chem. Phys.* **2006**, *125* (Article 024303), 1−7.
(23) Tapavicza, E.; Tavernelli, I.; Rothlisberger, U. *Phys. Rev. Lett.* **2007**, *98* (Article 023001), 1−4.
(24) Barbatti, M.; Granucci, G.; Persico, M.; Ruckenbauer, M.; Vazdar, M.; Eckert-Maksić, M.; Lischka, H. *J. Photochem. Photobiol. A.: Chem.* **2007**, *190*, 228−240.
(25) Fabiano, E.; Thiel, W. *J. Phys. Chem. A* **2008**, *112*, 6859−6863.
(26) Barbatti, M.; Lischka, H. *J. Am. Chem. Soc.* **2008**, *130*, 6831−6839.
(27) Lan, Z.; Fabiano, E.; Thiel, W. *J. Phys. Chem. B* **2009**, *113*, 3548−3555.
(28) Vazdar, M.; Eckert-Maksić, M.; Barbatti, M.; Lischka, H. *Mol. Phys.* **2009**, *107*, 845−854.
(29) Mitrić, R.; Petersen, J.; Bonačić-Koutecký, V. *Phys. Rev. A* **2009**, *79* (Article 053416), 1−6.
(30) Mitrić, R.; Petersen, J.; Wohlgemuth, M.; Werner, U.; Bonačić-Koutecký, V.; Wöste, L.; Jortner, J. *J. Phys. Chem. A* **2011**, *115*, 3755−3765.
(31) Lisinetskaya, P. G.; Mitrić, R. *Phys. Rev. A* **2011**, *83* (Article 033408), 1−13.
(32) Mitrić, R.; Petersen, J.; Bonačić-Koutecký, V.Multistate Nonadiabatic Dynamics 'on the fly"in Complex Systems and Its Control by Laser Fields. In *Conical Intersections - Theory, Computation and Experiment*; Domcke, W., Yarkony, D. R., Köppel, H., Eds.; Advanced Series in Physical Chemistry Vol. 17; World Scientific: Singapore, 2011.
(33) Petersen, J.; Mitrić, R.; Wolf, J. P.; Roslund, J.; Bonačić-Koutecký, V.; Rabitz, H. *Phys. Rev. Lett.* **2010**, *105* (Article 073003), 1−4.
(34) Mitrić, R.; Petersen, J.; Wohlgemuth, M.; Werner, U.; Bonačić-Koutecký, V. *Phys. Chem. Chem. Phys.* **2011**, *13*, 8690−8696.
(35) Stanzel, J.; Neeb, M.; Eberhardt, W.; Lisinetskaya, P. G.; Petersen, J.; Mitrić, R. *Phys. Rev. A* **2012**, *85* (Article 013201), 1−6.
(36) Mitrić, R.; Werner, U.; Bonačić-Koutecký, V. *J. Chem. Phys.* **2008**, *129* (Article 164118), 1−9.
(37) Werner, U.; Mitrić, R.; Bonačić-Koutecký, V. *J. Chem. Phys.* **2010**, *132* (Article 174301), 1−8.
(38) Wohlgemuth, M.; Mitrić, R.; Bonačić-Koutecký, V. *J. Chem. Phys.* **2011**, *135* (Article 054105), 1−10.
(39) Petersen, J.; Wohlgemuth, M.; Sellner, B.; Bonačić-Koutecký, V.; Lischka, H.; Mitrić, R. *Phys. Chem. Chem. Phys.* **2012**, *14*, 4687−4694.
(40) Adamo, C.; Barone, V. *J. Chem. Phys.* **1999**, *110*, 6158−6171.
(41) Schäfer, A.; Huber, C.; Ahlrichs, R. *J. Chem. Phys.* **1994**, *100*, 5829−5836.
(42) Ahlrichs, R.; Bär, M.; Haser, M.; Horn, H.; Kolmel, C. *Chem. Phys. Lett.* **1989**, *162*, 165−169.
(43) Schäfer, A.; Horn, H.; Ahlrichs, R. *J. Chem. Phys.* **1992**, *97*, 2571−2578.
(44) Weigend, F.; Ahlrichs, R. *Phys. Chem. Chem. Phys.* **2005**, *7*, 3297−3305.
(45) Yanai, T.; Tew, D.; Handy, N. *Chem. Phys. Lett.* **2004**, *393*, 51−57.
(46) Christiansen, O.; Koch, H.; Jorgensen, P. *Chem. Phys. Lett.* **1995**, *243*, 409−418.
(47) Verlet, L. *Phys. Rev.* **1967**, *159*, 98−103.
(48) Ponder, J. W.; Richards, F. M. *J. Comput. Chem.* **1987**, *8*, 1061.
(49) Jorgensen, W. L.; Maxwell, D. S.; Tirado-Rives, J. *J. Am. Chem. Soc.* **1996**, *118*, 11225−11236.
(50) Jorgensen, W. L.; McDonald, N. A. *J. Mol. Struct. Theochem* **1998**, *424*, 145−155.
(51) Jorgensen, W. L.; Ulmschneider, J. P.; Tirado-Rives, J. *J. Phys. Chem. B* **2004**, *108*, 16264−16270.
(52) Jorgensen, W. L.; Chandrasekhar, J.; Madura, J. D.; Impey, R. W.; Klein, M. L. *J. Chem. Phys.* **1983**, *79*, 926−935.
(53) Frisch, M. J.; ; et al. *Gaussian 09*, revision A.1; Gaussian, Inc.: Wallingford, CT, 2009.
(54) Inokuchi, Y.; Kobayashi, Y.; Ito, T.; Ebata, T. *J. Phys. Chem. A* **2007**, *111*, 3209−3215.
(55) Roshchupkin, D. I.; Talitsky, V. V.; Pelenitsyn, A. B. *Photochem. Photobiol.* **1979**, *30*, 635−643.
(56) Roos, B. O.; Taylor, P. R.; Siegbahn, P. E. M. *Chem. Phys.* **1980**, *48*, 157−173.
(57) Frisch, M. J.; Ragazos, I. N.; Robb, M. A.; Schlegel, H. B. *Chem. Phys. Lett.* **1992**, *189*, 524−528.

Supporting Information: Photodynamics of Free and Solvated Tyrosine

Gaia Tomasello, Matthias Wohlgemuth, Jens Petersen, and Roland Mitrić*

Freie Universität Berlin, Fachbereich Physik, Arnimallee 14, D-14195 Berlin, Germany

E-mail: mitric@zedat.fu-berlin.de

Transition energies of tyrosine in the gas phase.

In order to confirm the validity of our computational approach, we report here the vertical excitation energies and oscillator strengths obtained employing larger basis sets and more accurate methods. In Table S1 these quantities are given for the gas phase equilibrium structure of tyrosine. We compare the values obtained at the PBE0/SV(P)[1–3] level used for the dynamics simulations with those obtained with the larger TZVP basis set[4] as well as using the long-range corrected hybrid functional CAM-B3LYP and the linear response second order coupled cluster (CC2) method.[5]

Table 1: Table S1: Vertical excitation energies of the neutral isomer of tyrosine. [a]The excitation energies have been calculated for the optimized lowest-energy structure obtained at PBE0/TZVP level. [b]The energy values are given in eV. [c]Oscillator strength. The states of $\pi\pi^*$ character are set in boldface. [d]The SVP basis set differs from SV(P) by the presence of a p function for hydrogen.

Method/basis set[a]	$(S_0-S_1)^b/f^c$	$(S_0-S_2)/f$	$(S_0-S_3)/f$	$(S_0-S_4)/f$	$(S_0-S_5)/f$	$(S_0-S_6)/f$
PBE0/SV(P)[d]	**5.07/0.036**	5.58/0.014	**5.89/0.113**	5.93/0.004	6.41/0.002	6.67/0.003
PBE0/TZVP	**4.98/0.035**	5.57/0.029	**5.79/0.107**	5.98/0.029	6.23/0.000	6.45/0.002
CAM-B3LYP/SVP[d]	**5.20/0.038**	5.75/0.009	**6.06/0.106**	6.92/0.000	7.07/0.803	7.20/0.260
CAM-B3LYP/TZVP	**5.13/0.035**	5.73/0.012	**5.95/0.094**	6.46/0.000	6.91/0.842	7.01/0.276
CC2/TZVP	**4.88/0.028**	5.88/0.018	**6.13/0.173**	6.45/0.001	6.98/0.026	7.02/0.291

From the Table S1 it is evident that the energetic position and character of the low-lying excited states are only weakly dependent on the employed computational method. The first excited state S_1 is in all cases a bright state of $\pi\pi^*$ character and can be identified with the experimentally observed L_b state. The second excited state S_2 has a low oscillator strength and is dominated by excitations between molecular orbitals localized on the amino and carboxyl groups. The S_3 state is a bright $\pi\pi^*$state with higher oscillator strength than S_1, hence it can be identified with the L_a state. This state has been used as the starting point for our nonadiabatic dynamics simulations. Notice, that the vertical excitation energies obtained at CC2/TZVP level are also in good agreement with those reported by Sobolewski et al.[6] of tyrosine + 2 H_2O calculated at CC2/aug(N)-cc-pVDZ level on a MP2/cc-pVDZ optimized geometry. In this case, the two bright states S_1 and S_3 are located at 4.93 eV and 6.21 eV while the dark state S_2 lies at 5.85 eV.

Concerning the position of the lowest-lying state of $\pi\sigma^*$ character along the O-H stretching coordinate, a certain dependence on the employed method is found. At the PBE0/SV(P) level this state is the S_6 state, whereas it is S_5 for PBE0/TZVP and S_4 for all approaches using CAM-B3LYP or CC2.

Transition energies of tyrosine in water.

Since in solvated systems charge transfer excitations can play a crucial role in the photochemical processes, density functionals with improved long-range behavior such as CAM-B3LYP have to be employed. In the following we compare the electronic excitation energies obtained with CAM-B3LYP and SVP[2,3] or TZVP basis sets with the respective values at the more accutate CC2 level for the system consisting of tyrosine and three explicit water molecules surrounded by a classically described water sphere using the mechanical embedding scheme. The structure of the system considered here is the initial structure of the trajectory discussed in the main text (cf. Fig. 10). It can be clearly deduced from Table S2 that increasing the basis set size from SVP to TZVP has only a minor effect. In both cases, the excitation energies are also comparable to the respective values obtained using CC2. This has given us confidence to use the computationally efficient CAM-B3LYP/SVP approach to perform the nonadiabatic dynamics simulations.

Table 2: Table S2: Vertical excitation energies of the zwitterionic isomer of tyrosine + 3 H_2O surrounded by a classical water sphere in the frame of the mechanical embedding approach. [a]The excitation energies have been calculated for the initial structure of the QM/MM trajectory analyzed in the main text, Figs. 10 and 11. [b]The energy values are given in eV. [c]Oscillator strength. The states of $\pi\pi^*$ character are set in boldface. [d] Also the S_2 and S_4 states have some $\pi\pi^*$ character, but mixed with $n\pi^*$ and charge-transfer to solvent contributions.

Method/basis set[a]	$(S_0-S_1)^b/f^c$	$(S_0-S_2)/f$	$(S_0-S_3)/f$	$(S_0-S_4)/f$	$(S_0-S_5)/f$	$(S_0-S_6)/f$
CAM-B3LYP/SVP	4.48/0.005	4.85/0.020	**4.91/0.024**	5.01/0.000	5.06/0.017	5.22/0.006
CAM-B3LYP/TZVP	4.70/0.010	4.70/0.011	**4.94/0.014**	5.09/0.003	5.11/0.001	5.25/0.037
CC2/TZVP	4.33/0.022	4.41/0.008	**4.68/0.013**[d]	4.88/0.028	4.94/0.008	5.14/0.003

Conical Intersections.

In order to confirm the presence of a near-degeneracy at the last point of the reactive TDDFT trajectories shown in the main text in Figs. 7 (proton transfer pathway) and 8 (O-H detachment pathway), we provide in Table S3 the energy gaps between S_1/S_0 both at the original TDDFT (PBE0/SV(P)) level as well as employing the complete active space self-consistent field procedure (CASSCF)[7,8] with an active space of 12 electrons in 12 orbitals. The CASSCF values confirm that also at this more accurate level of theory the energy gap is very small, indicating that the respective geometries lie close to a conical intersection.

Table 3: Table S3. $S_1 - S_0$ energy gap calculated for the two near-degeneracies at the end of the trajectories shown in Fig. 7 and 8. [a]The labels CI-1 and CI-2 refer to the near degeneracies of the trajectories showing the proton-transfer reaction, and O-H detachment, respectively. The energy values are given in eV. [b]CASSCF(12,12)/TZVP energies are calculated at State Average level within 2 roots (SA-2r).

Method/basis set	CI-1[a] $(S_0 - S_1)/f$	CI-2[a] $(S_0 - S_1)/f$
PBE0/SV(P)	0.16	0.15
SA-2r CASSCF(12-12)/TZVP[b]	0.42	0.26

References

(1) Adamo, C.; Barone, V. *J. Chem. Phys.* **1999**, *110*, 6158–6170.

(2) Schäfer, A.; Horn, H.; R. Ahlrichs, R. *J. Chem. Phys.* **1992**, *97*, 2571–2578.

(3) Weigend, F.; ; Ahlrichs, R. *Phys. Chem. Chem. Phys.* **2005**, *7*, 3297–3305.

(4) Schäfer, A.; Huber, C.; R. Ahlrichs, R. *J. Chem. Phys.* **1994**, *100*, 5829–5836.

(5) Christiansen, O.; Koch, H.; Jorgensen, P. *Chem. Phys. Lett.* **1995**, *243*, 409–418.

(6) Sobolewski, A.; Shemesh, D.; Domcke, W. *J. Phys. Chem. A* **2009**, *113*, 542–550.

(7) Roos, B. O.; Taylor, P. R.; Siegbahn, P. E. M. *Chem. Phys.* **1980**, *48*, 157–173.

(8) Frisch, M.; Ragazos, I.; Robb, M.; Schlegel, H. *Chem. Phys. Lett.* **1992**, *189*, 524–528.

Appendix B

SINGLE WATER SOLVATION DYNAMICS IN THE 4-AMINOBENZONITRILE–WATER CLUSTER CATION REVEALED BY PICOSECOND TIME-RESOLVEDINFRARED SPECTROSCOPY

Reproduced with permission from:

M. Miyazaki, T. Nakamura, M. Wohlgemuth, R. Mitrić, O. Dopfer, and M. Fujii:
"Single water solvation dynamics in the 4-aminobenzonitrile–water cluster cation revealed by picosecond time-resolved infrared spectroscopy,"
Phys. Chem. Chem. Phys., **17**, 29969–29977 (2015).

http://dx.doi.org/10.1039/C5CP05400A

PCCP

PAPER

View Article Online
View Journal | View Issue

Cite this: *Phys. Chem. Chem. Phys.*, 2015, **17**, 29969

Single water solvation dynamics in the 4-aminobenzonitrile–water cluster cation revealed by picosecond time-resolved infrared spectroscopy

Mitsuhiko Miyazaki,[a] Takashi Nakamura,[a] Matthias Wohlgemuth,[b] Roland Mitrić,*[b] Otto Dopfer*[c] and Masaaki Fujii*[a]

Received 10th September 2015,
Accepted 7th October 2015

DOI: 10.1039/c5cp05400a

www.rsc.org/pccp

The dynamics of a solvent is important for many chemical and biological processes. Here, the migration dynamics of a single water molecule is triggered by the photoionization of the 4-aminobenzonitrile–water (4ABN–W) cluster and monitored in real time by picosecond time-resolved IR (ps TRIR) spectroscopy. In the neutral cluster, water is hydrogen-bonded to the CN group. When this CN-bound cluster is selectively ionized with an excess energy of 1238 cm^{-1}, water migrates with a lifetime of τ = 17 ps from the CN to the NH_2 group, forming a more stable $4ABN^+$–W(NH) isomer with a yield of unity. By decreasing the ionization excess energy, the yield of the CN → NH_2 reaction is reduced. The relatively slow migration in comparison to the ionization-induced solvent dynamics in the related acetanilide–water cluster cation (τ = 5 ps) is discussed in terms of the internal excess energy after photoionization and the shape of the potential energy surface.

1. Introduction

Solvent–solute interactions are some of the most important key factors in solution chemistry.[1–7] They significantly affect the energetics and dynamics of chemical reactions and structural rearrangements, for example protein folding[8–10] and the self-assembly of supramolecules and nanostructures.[11–15] Particularly, the rearrangement of the solvent network, the solvation dynamics, is the initial process in solution-phase chemistry. One of the typical methods to observe the solvation dynamics has been the dynamic Stokes shift, *i.e.* the time-dependent spectral shift of fluorescence.[3,5] Here, the photoexcitation of a solute molecule causes a sudden change in the solute–solvent interaction, which is the driving force for the rearrangement. The triggered gradual reorientation of the solvent induces a spectral shift in the fluorescence of the solute molecule. This method has been applied in time-resolved studies to a wide variety of systems, ranging from dyes[6,16] to biological molecules, such as aromatic amino acid residues and proteins.[1,17,18] Although the dynamic Stokes shift provides a comprehensive view of the solvent rearrangement, it is difficult to probe the dynamics of individual solvent molecules. On the other hand, recent progress of theoretical chemistry and rapid development of computer technology have provided realistic simulations of the dynamics of individual solvent molecules. Therefore, the experimental observation of solvation dynamics at a single molecular level is an essential demand to calibrate the up-to-date theoretical approach for the subsequent reliable prediction to problems in solution chemistry and biology.

Single molecular solvation dynamics can experimentally be studied in solvated clusters of solute and solvent molecules generated in molecular beams and stabilized by hydrogen bonds (H-bonds) and van der Waals interactions (π stacking).[19–22] The solvated clusters are often considered as a nanodroplet or a local structure in solution. The first advantage of solvated clusters is that the number of solute and solvent molecules and their relative orientation can precisely be specified and controlled by combining mass spectrometry with resonant enhanced multiphoton ionization (REMPI). The second advantage is that the relative orientation of the molecules in the cluster is frozen because of efficient cooling in a supersonic expansion down to a few K. The specific orientation can be controlled and precisely be determined by measuring, for example, their IR spectra and analysing them with quantum chemical calculations. This combined strategy of structural determination by comparison of observed and calculated IR spectra is well established for molecular clusters.[23–26]

To observe the solvation dynamics of aromatic clusters generated in molecular beams, we have developed the technique

[a] *Chemical Resources Laboratory, Tokyo Institute of Technology, Yokohama 226-8503, Japan. E-mail: mfujii@res.titech.ac.jp*
[b] *Institut für Theoretische und Physikalische Chemie, Julius-Maximilians-Universität Würzburg, 97070 Würzburg, Germany. E-mail: roland.mitric@uni-wuerzburg.de*
[c] *Institut für Optik und Atomare Physik, Technische Universität Berlin, 10623 Berlin, Germany. E-mail: dopfer@physik.tu-berlin.de*

of mass-selective three-color tuneable UV-UV'-IR picosecond time-resolved infrared (ps TRIR) pump-probe laser spectroscopy.[21,27–33] The different isomers of the solvated aromatic cluster can easily be distinguished by their unique S_1–S_0 UV transition energy. Then, a solvated cluster with a specific conformation can selectively be ionized by the REMPI process *via* S_1 using two-color two-photon (UV-UV') ionization with adjustable ionization excess energy. In most cases, the sudden charge formation by photoionization causes a significant structural reorientation in the cluster, because the most stable structure of the charged cluster is usually different from that of the neutral reactant. The evolving structural dynamics can be traced in real time by measuring the IR spectra by a depletion technique at a variable delay time after the ionization event. In contrast to static spectroscopy, which only can detect the initial and final state of the reaction, such a dynamical approach yields additional essential information about the reaction (*e.g.* rate constant, reaction pathways, intermediates), which completely escapes static nanosecond spectroscopy.

Initially, this ps TRIR spectroscopic technique has been used to characterize the ionization-induced π → H site-switching dynamics of a variety of rare gas ligands attached to the phenol molecule.[21,28–30,32] Subsequently, this approach has been applied to the CO → NH site switching reaction in the *trans*-acetanilide–water cluster (AA–W),[27] which is one of the simplest models of a hydrated peptide linkage (–CONH–). The ps TRIR spectra clearly contain many important details of this fundamental water migration process from the CO to the NH site of this linkage, including the two competing reaction pathways and their rate constants, the occurrence of transient intermediates, the reaction yield and its relation to intracluster vibrational energy redistribution (IVR).[27,34] This migration reaction and the resulting TRIR spectra were subsequently analysed and visualized by "on-the-fly" molecular dynamics (MD) simulations.[34] The important aspect of this combined experimental and computational approach is that the MD simulations could precisely be calibrated by the accurate reproduction of the measured TRIR spectra. The experimentally calibrated simulations revealed that the water migration reaction with 5 ps duration has two pathways, namely a fast and a slow channel, and only the slow channel has an intermediate. This detailed visualization is the first example of combined experimental and theoretical characterization of single molecular solvation dynamics in clusters and in general. The combination of ps TRIR spectroscopy and MD simulations calibrated by experiment can now be applied to various other solvated clusters and therefore we have chosen the 4-aminobenzonitrile–water (4ABN–W) cluster as the second example to be explored by this combination.[35–44] Here, we present the first step of this combined strategy, namely the measurement of the ps TRIR spectra of $4ABN^+$–W and their preliminary analysis by a classical rate equation model.

Ionization-induced water migration has been suggested in several solvated clusters by static nanosecond IR laser spectroscopy of the neutral reactant and the final cation product, including monohydrated clusters of benzene,[22,45–47] aminophenol,[48] formanilide,[49–51] acetanilide,[27,52,53] tryptamine,[54,55] phenylglycine,[56] and 4ABN.[43,44] From these candidates, we have selected 4ABN–W for the following reasons. 4ABN is a benzene derivative substituted with an electron-donating NH_2 group and an electron-withdrawing CN group. It provides several competing binding sites for water, and three different isomers of 4ABN–W coexist in the S_0 state, namely the NH-bound 4ABN–W(NH) isomer in which water is H-bonded to the NH_2 group and two CN-bound 4ABN–W(CN) clusters, in which water is H-bonded in either a bent or linear configuration to the CN group.[39] The latter can be detected only by fluorescence spectroscopy and thus can be neglected in this work. 4ABN–W(CN) holds its binding motif by excitation into S_1, but shows the water migration from the CN to the NH_2 site upon ionization.[43] The large change in the charge distribution of the aromatic chromophore substantially destabilises the CN structure with respect to the NH isomer in $4ABN^+$–W. This CN → NH_2 site switching with 100% yield was inferred from the drastic change in the IR spectra before and after ionization but the dynamics of this water migration and other parameters of the reaction have not been characterized yet. To this end, we apply UV-UV'-IR ps TRIR spectroscopy to 4ABN–W(CN) to monitor the water migration dynamics in real time by the time evolution of the IR spectra measured at a variable delay time Δt after the ionization. Details of the CN → NH_2 water migration reaction triggered by ionization of the 4ABN–W(CN) isomer have been revealed. We also investigate the effect of the ionization excess energy on the reaction yield and discuss its relation to the shape of the potential energy surface and the reaction path in the cation ground state of $4ABN^+$–W.

2. Experimental

The principle for the measurement of the ps time-resolved UV-UV'-IR ion dip (TRIR) spectra are shown in Fig. 1 and are described in detail elsewhere.[21,32,33] Briefly, 4ABN–W clusters are produced in a supersonic jet by expanding 4ABN vapour (70 °C) and a trace amount of residual water seeded in He gas (3 bar) through a pulsed valve into a vacuum chamber. Neutral 4ABN–W dimers are ionized from the neutral ground state (S_0) employing resonant two-color two-photon (1 + 1′) REMPI through the first excited singlet state (S_1) using two ps UV laser beams, ν_{exc} (UV) and ν_{ion} (UV'). ν_{ion} is irradiated at a delay time of 106 ps after ν_{exc} (corresponding to Δt = 0). ν_{exc} and ν_{ion} are tuned to 33 678 ($S_1 0^0$) and 32 780 cm^{-1} for resonant ionization of the 4ABN–W(CN) isomer, respectively.[36,37,39–41,57–59] Thus, according to the reported photoionization efficiency curve, the maximum internal energy of generated $4ABN^+$–W(CN) cation is 1238 cm^{-1} with respect to its ionization energy of 65 220 cm^{-1}. The ions generated in the cation ground state (D_0) are extracted into a quadrupole mass spectrometer. While monitoring the mass-selected $4ABN^+$–W signal, a tuneable ps IR laser, ν_{IR}, is fired at a delay time of 106 ps (Δt = 0) after ν_{exc} and scanned through the 2800–3800 cm^{-1} vibrational range at an adjustable delay (Δt) with respect to ν_{ion}. The ion signal is amplified, integrated, and monitored as a function of ν_{IR} and/or Δt. When ν_{IR} is resonant with a vibrational transition of $4ABN^+$–W, the cluster dissociates upon vibrational excitation, causing a depletion (dip) in the parent ion current. Thus, the IR spectrum of

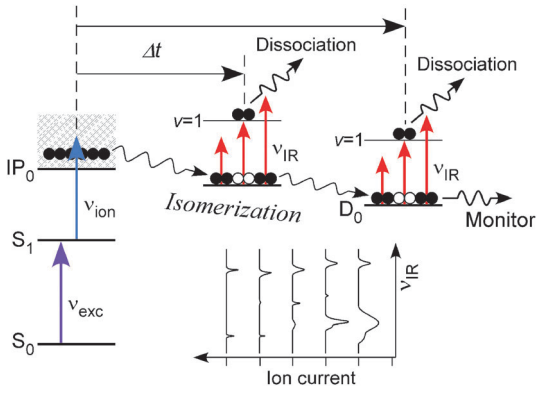

Fig. 1 Strategy of picosecond time-resolved IR ion dip (ps TRIR) spectroscopy. 4ABN–W(CN) is selectively excited (ν_{exc}) and ionized (ν_{ion}) by two ps UV laser beams (1 + 1′ REMPI) to trigger the water migration reaction. The dynamics of this reaction is monitored by a ps IR beam (ν_{IR}) delayed by Δt from ν_{ion}. The IR absorption dissociates the cluster and the resulting depletion of the parent ion signal gives its IR spectrum. If the frequency of the IR laser is fixed to a specific vibrational IR transition and Δt is scanned, the time evolution of this IR transition is obtained. The time profile represents the population change of the species with this characteristic IR transition.

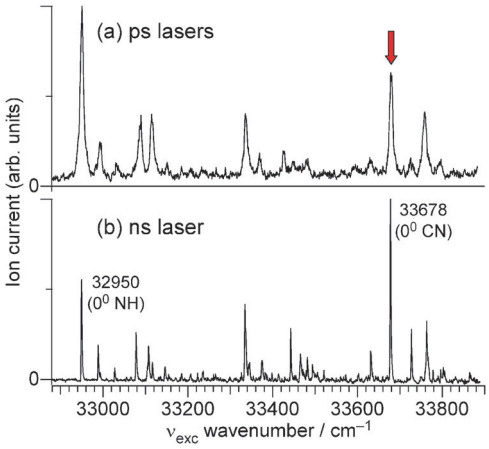

Fig. 2 REMPI spectra of 4ABN–W recorded using ps lasers (a, 1 + 1′ REMPI) and a ns laser (b, 1 + 1 REMPI). In the ps time-resolved experiments, ν_{exc} is fixed to the $S_1 0^0$ band of the ABN–W(CN) isomer indicated by the arrow.

$4ABN^+$–W is obtained by monitoring the depletion of the ion current as a function of ν_{IR}. To monitor the population change of $4ABN^+$–W associated with a particular vibrational transition, ν_{IR} is fixed to this resonance and Δt is varied by scanning the delay stage for ν_{ion} to shorter time with respect to ν_{exc}. The time evolution of the signal depletion is converted to the population change by taking the logarithm of the depletion. The generation of the ps UV/UV' and IR laser pulses is described elsewhere.[21,32,33] The key parameters are a 10 Hz repetition rate, 3 ps pulse widths, 12 cm^{-1} spectral resolution, and pulse energies of 1 μJ, 10 μJ, and 50–70 μJ for ν_{exc}, ν_{ion}, and ν_{IR}, respectively. The UV/UV' and IR laser beams are combined coaxially and focused by a CaF_2 lens with 300 mm focal length into the supersonic expansion. Similar REMPI and IR depletion experiments have also been performed using standard IR/UV nanosecond lasers, as described in detail previously.[60]

3. Results and discussion

3.1. REMPI spectrum

Fig. 2(a) and (b) show the 1 + 1′ REMPI and 1 + 1 REMPI spectra of 4ABN–W measured using picosecond and nanosecond lasers, respectively. The nanosecond spectrum well reproduces previous reports.[36,37,39–41,57–59] Bands at 32 950 and 33 678 cm^{-1} have been assigned to $S_1 0^0$ bands of the NH and CN isomers, respectively. The other peaks are ascribed to vibronic transitions originating from zero-point vibrational levels in the S_0 state of these isomers,[39,43] and no hot band transition is observed. This result confirms that the internal (vibrational) degrees of freedom of the clusters are efficiently cooled down in the jet. The 1 + 1′ REMPI spectrum obtained by picosecond lasers reproduces well that recorded by nanosecond lasers, although the widths of the bands are broadened due to the inferior spectral resolution of the picosecond laser pulses (12 cm^{-1}). The $S_1 0^0$ band of each cluster is still well resolved from the other transitions, ensuring selective excitation of the CN isomer to its $S_1 0^0$ origin under these conditions, as also confirmed by the previously reported hole-burning spectra.[39,43] Thus, the time-resolved spectroscopy is carried out by fixing ν_{exc} to the $S_1 0^0$ band of the CN isomer.

3.2. Picosecond time-resolved IR spectra

Fig. 3(c) shows the ps TRIR spectra measured by varying Δt from −3 to +59 ps. For comparison, static nanosecond IR spectra of $4ABN^+$–Ar(π), 4ABN–W(CN) (reactant R) in the S_1 state and $4ABN^+$–W(NH) corresponding to the reaction product (P^+, Δt = +50 ns) measured by nanosecond lasers are shown in Fig. 3(a), (b) and (d), respectively.[43,59] In this excitation scheme, the IR absorption of 4ABN–W(CN) in S_1 overlaps with the IR absorption of the nascent $4ABN^+$–W clusters in the ps TRIR spectra of D_0 at small delay because of the temporal overlap of the ν_{ion} and ν_{IR} pulses (~4 ps from a cross-correlation measurement). Specifically, a sharp band B at 3409 cm^{-1} colored in red in the nanosecond spectrum of the S_1 state of 4ABN–W(CN) is assigned to the free NH_2 symmetric stretching vibration ($\nu^s_{NH}(S_1)$). The corresponding picosecond TRIR spectra before photoionization ($\Delta t < 0$) show the same $\nu^s_{NH}(S_1)$ transition. The antisymmetric stretching mode of free NH_2 is also observed at 3526 cm^{-1} in the nanosecond spectrum but not detected in the ps TRIR spectra because of its weak intensity. The bands in the picosecond TRIR spectra are broader because of the lower spectral resolution (12 cm^{-1}) arising from the shorter laser pulse duration. The ps TRIR spectra change immediately after ionization (Δt = 1 and 2 ps). The $\nu^s_{NH}(S_1)$ band B of the reactant R becomes weaker and disappears after around Δt = 2 ps (consistent with the pulse duration of the ps laser system). Instead, the TRIR spectrum at Δt = 0 shows a new band A at 3390 cm^{-1} (green) assigned to the NH_2 free symmetric stretching mode of $4ABN^+$ (ν^s_{NH}), as inferred from the experimental $4ABN^+$–Ar spectrum in Fig. 3(a).[59,61] This band A can be seen in the TRIR

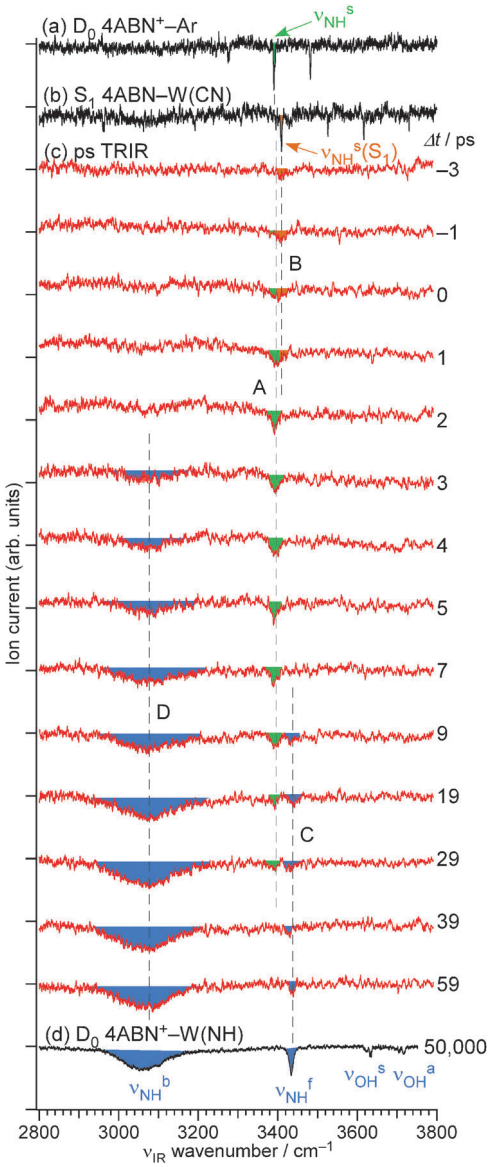

Fig. 3 Picosecond time-resolved IR ion dip (ps TRIR) spectra of 4ABN$^+$–W for selective ionization of the 4ABN–W(CN) isomer *via* 1 + 1′ REMPI as a function of Δt (E_{exc} = 1238 $^{-1}$) (c). Static spectra measured for the S_1 state (b) and the D_0 state (d) using nanosecond lasers are shown for comparison.[43] The IR spectrum of cold 4ABN$^+$–Ar clusters is shown in (a).[59] The positions used to monitor time evolutions (bands A, C and D) are indicated by dashed lines.

spectra at Δt = 0 and 1 ps adjacent to the $\nu^s_{NH}(S_1)$ band B. Its intensity gradually increases, decays again after around Δt = 9 ps, and has completely disappeared before 39 ps. Before Δt = 3 ps, no other intense band is observed, in particular in the range below 3300 cm^{-1}. Thus, the water ligand has to be either located still at the CN site and/or has already been released from the CN site but has not yet arrived at the NH_2 site.

After Δt = 3 ps, a new broad band D (blue) at around 3080 cm^{-1} appears and grows with increasing delay. In addition, a much narrower band C (blue) at 3434 cm^{-1} appears after Δt = 7 ps. Finally, the spectrum at Δt = 39 ps has converged and resembles the static one observed at Δt = 50 ns after ionization recorded by nanosecond lasers. These bands D and C were assigned to the H-bonded and free NH stretching vibrations, ν^b_{NH} and ν^f_{NH}, of the amino group, respectively, arising from H-bonding with water.[43] Those are the spectral signatures characteristic of the final 4ABN$^+$–W(NH) reaction product, P$^+$.[43,44] Therefore, the disappearance of ν^s_{NH} and the subsequent appearance of ν^b_{NH} and ν^f_{NH} unambiguously demonstrate the direct time-resolved observation of the water migration from the CN to the NH_2 site of 4ABN$^+$ triggered by photoionization of 4ABN$^+$–W(CN). The symmetric and antisymmetric OH stretching vibrations of the water ligand (ν^s_{OH} and ν^a_{OH}, respectively) cannot be detected in the ps TRIR spectra although both bands are clearly observed in the nanosecond spectrum at Δt = 50 ns as sharp and weak bands. The energy resolution of the picosecond IR laser is lower, and thus such sharp and weak transitions cannot be detected in the ps TRIR spectra under the current sensitivity conditions.

3.3 Time evolution of IR absorption

The ps TRIR spectra probe the water migration from the CN to the NH_2 binding site triggered by photoionization in real time. In this dynamical process, we should consider the populations of the reactant R (4ABN–W(CN) in S_1), the Franck–Condon state FC$^+$ (4ABN$^+$–W(CN)) prepared by vertical ionization of R, and the product P$^+$ (4ABN$^+$–W(NH)). In the water migration dynamics of the AA$^+$–W cation, the water ligand migrates from the initially CO-bound site to the final NH-bound site *via* an intermediate I$^+$, in which the water ligand does bind neither at the initial nor final binding site. Thus, we may also consider the existence of such an I$^+$ state for the CN → NH_2 migration reaction in 4ABN$^+$–W. However, the ps TRIR spectra of 4ABN$^+$–W do not detect the H-bonded OH stretching vibration of the water ligand, and as a result, ν^s_{NH} is the only spectral signature of FC$^+$. Unfortunately, ν^s_{NH} is also characteristic of any I$^+$ candidate. Hence, we cannot separate FC$^+$ from any intermediate I$^+$ in the measured ps TRIR spectra, even if such an I$^+$ were to exist. Consequently, the time-evolution of ν^s_{NH} corresponds to the sum of the populations of FC$^+$ and possibly I$^+$ in this analysis, denoted AF$^+$ (amino-free species), *i.e.*, the population of ions with a free NH_2 group.

As already deduced from the nanosecond experiments, the ps TRIR spectra in Fig. 3(c) clearly confirm that essentially all ionized CN-bound clusters are converted to NH-bound clusters with 100% yield at the employed ionization excess energy of 1238 cm^{-1}. As the clusters are isolated systems without the possibility of energy release, the NH_2 → CN back reaction may be expected and has indeed been observed for the π ↔ H reaction in the phenol$^+$–Kr dimer.[21,28] In this cluster, the Kr atom migrates from the initial π binding site above the aromatic ring to H-bonded OH site upon ionization. However the H → π back reaction eventually causes a nonvanishing π ↔ H equilibrium. For 4ABN$^+$–W, the lack of any NH_2 → CN back reaction and unity yield for the CN → NH_2 forward reaction indicates that efficient IVR in P$^+$ prevents the back reaction because of fast removal of vibrational energy from the reaction coordinate. The efficient IVR is attributed to the bath modes arising from the intermolecular vibrations not involved in the reaction coordinate

and intramolecular modes below ~3500 cm^{-1}, resulting from the sum of the exothermicity of the CN → NH_2 reaction (2332 cm^{-1}) and the ionization excess energy of 1238 cm^{-1} used in the two-color ps experiments.[44]

The time evolutions describing the CN → NH_2 forward reaction measured at three relevant vibrational bands, namely ν^s_{NH} (band A), ν^f_{NH} (band C), and ν^b_{NH} (band D), probed at dashed lines in Fig. 3 are shown in Fig. 4(a)–(c), respectively. Here, ν^s_{NH} corresponds to AF^+ (FC^+ + I^+) while the latter two bands represent P^+. Although only two bands corresponding to AF^+ and P^+ are observed in the TRIR spectra, FC^+ and I^+ are treated separately from AF^+ because the inclusion of I^+ in the rate equations usually results in a multi-exponential behaviour even for $[AF^+] = [FC^+ + I^+]$. Although various reaction pathways are feasible, we consider the simplest case, namely the one-directional two-step forward reaction, $FC^+ \rightarrow I^+ \rightarrow P^+$ in our initial analysis. The rate equations for this reaction scheme are expressed as follows:

$$\frac{d[FC^+]}{dt} = -k_1[FC^+], \quad (1)$$

$$\frac{d[I^+]}{dt} = k_1[FC^+] - k_2[I^+], \quad (2)$$

$$\frac{d[P^+]}{dt} = k_2[I^+]. \quad (3)$$

Here, $[X]$ are the populations of X, and k_1 and k_2 are rate constants. The rate eqn (1)–(3) are solved under an initial condition of $[FC^+](t = 0) = 1$, $[I^+](t = 0) = [P^+](t = 0) = 0$:

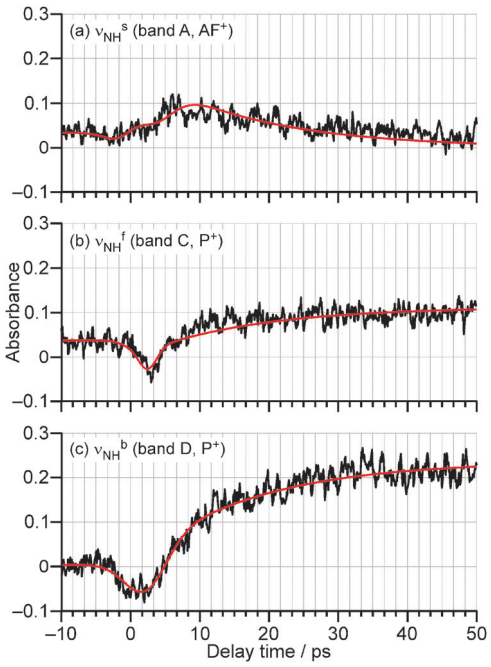

Fig. 4 Experimental time evolution of three vibrational bands (A, C and D) of 4ABN$^+$–W as indicated in Fig. 3: (a) ν^s_{NH} (band A, green, AF^+); (b) ν^f_{NH} (band C, blue, P^+); (c) ν^b_{NH} (band D, blue, P^+). The best fit curves obtained by a two-step reaction model are included in red.

$$[FC^+] = e^{-k_1 t}, \quad (4)$$

$$[I^+] = \frac{k_1}{k_2 - k_1}\left(e^{-k_1 t} - e^{-k_2 t}\right), \quad (5)$$

$$[P^+] = \frac{1}{k_2 - k_1}\left\{k_2\left(1 - e^{-k_1 t}\right) - k_1\left(1 - e^{-k_2 t}\right)\right\}, \quad (6)$$

Thus, the total population change of FC^+ and I^+ corresponding to the time evolution of free ν^s_{NH} is:

$$[FC^+ + I^+] = [AF^+] = \frac{1}{k_2 - k_1}\left(k_2 e^{-k_1 t} - k_1 e^{-k_2 t}\right) = 1 - [P^+]. \quad (7)$$

These results are multiplied by an unit step function at $t = 0$, $u(t)$, to express the sudden production of FC^+ at $t = 0$. In addition, the cross-correlation between ν_{ion} and ν_{IR}, which can be approximated by a Gaussian profile with 4 ps FWHM, is taken into account as a Gaussian convolution on these expressions.

Final fits to the experimental time profiles (red traces in Fig. 4) yield $1/k_1 = \tau_1 \leq 0.1$ ps and $1/k_2 = \tau_2 = 17 \pm 2$ ps. The obtained fits reasonably well reproduce the experimental time evolutions. Nevertheless, due to coherent spikes near $\Delta t = 0$, which are taken empirically into account by Gaussian functions in the fitting, a definite analysis near $\Delta t = 0$ is difficult. Moreover, because expressions (5)–(7) are symmetric with respect to k_1 and k_2, interconversion of k_1 and k_2 gives the same trace. Therefore, from the observed data one cannot determine the rate-determining step, unless the decay rate of $[FC^+]$ is monitored independently. In addition, as mentioned below, the cationic potential energy surface has several local shallow minima with similar depths. Thus, both steps could be the rate-determining one. Moreover, more complicated reaction schemes evolve if these local minima are taken into account. Hence, more experimental data and/or sophisticated MD simulations are required to fully analyse the CN → NH_2 reaction mechanism.

Interestingly, the total reaction time of ~17 ps derived for the CN → NH_2 isomerization in 4ABN$^+$–W from the simple rate equation analysis is much longer than that of the CO → NH water migration in AA^+–W, which takes only 5 ps.[27,34] As both reactions are water migrations around simple benzene derivatives, there is not a substantial difference in the length of the reaction paths. Then, the speed of the water migration in 4ABN$^+$–W should be slower than that in AA^+–W. The difference of the reaction rate may be related to the different internal energies of the cluster cations. As mentioned above, 4ABN$^+$–W(CN) is generated here with an excess energy of 1238 cm^{-1} by two-color REMPI, which corresponds to the maximum internal energy of the cation directly after ionization. On the other hand, in the previous study of AA^+–W, the AA^+–W(CO) isomer was generated by one-color REMPI. The ionization energy of AA–W(CO) has not been determined yet, but it is lower than 64 870 cm^{-1} derived from the two-color REMPI spectrum.[62] Based on this estimation, the excess energy of AA^+–W after ionization is above 7230 cm^{-1}. According to the theoretical calculation at the M06-2X/aug-cc-pVTZ level, the ionization potential of the reactant AA–W(CO) is 2500 cm^{-1} above that of

the product AA–W(NH), and then the excess energy for ionization is about 6000 cm^{-1}.[63] Because of the Franck–Condon principle, this value is the maximum internal (mostly vibrational) energy of the generated cations, and usually not all the excess energy can be converted into internal energy (the remaining energy goes into kinetic energy of the photoelectron). However, although the Franck–Condon factors are not well known for both ionization processes, more than a factor five difference in the ionization excess energy may result in a significant difference in the initial internal energies of AA^+–W(CO) and $4ABN^+$–W(CN). Thus, one of the reasons for the slower CN → NH_2 isomerization of $4ABN^+$–W may be the smaller available internal energy. In addition, possible reaction barriers will also affect the rate constant. Density functional (DFT) calculations at the M06-2X/aug-cc-pVTZ level indeed exhibit a CN-bound local minimum of $4ABN^+$–W and a transition state near the minimum with a barrier of 377 cm^{-1} (Fig. 5) for isomerization toward the NH-bound global minimum along the in-plane path.[44] However, also for AA^+–W a barrier between the CO-bound and NH-bound minima has been predicted.[34] Hence, currently we attribute the faster rate in AA^+–W to the larger excess energy. Future time-resolved experiments at various excess energies are required to explore the dependence of the reaction rate on the excess energy and the barrier heights.

3.4 Reaction rate and excess energy

To explore the effect of the ionization excess energy on the migration reaction, we consider the IR spectra after ionization of 4ABN–W(CN) *via* its S_1 origin with variable excess energy by using nanosecond laser systems. The excitation scheme is essentially the same as that in Fig. 1 but all picosecond lasers are replaced by tuneable nanosecond lasers. The IR spectra measured at Δt = 50 ns are shown in Fig. 6 for excess energies between 2136 and 296 cm^{-1}. The spectra are measured in the vicinity of ν_{NH}^{b} (signature of P^+), ν_{NH}^{s} and $2\delta_{NH_2}$ (FC^+ and I^+), and ν_{NH}^{f} (P^+). At a relatively high ionization excess energy of 2136 cm^{-1} above ionization potential (IP_0) (Fig. 6(a), 1 + 1 REMPI), both ν_{NH}^{b} and ν_{NH}^{f} appear clearly but ν_{NH}^{s} cannot be seen, indicating a CN → NH_2 reaction yield of close to unity. This result is

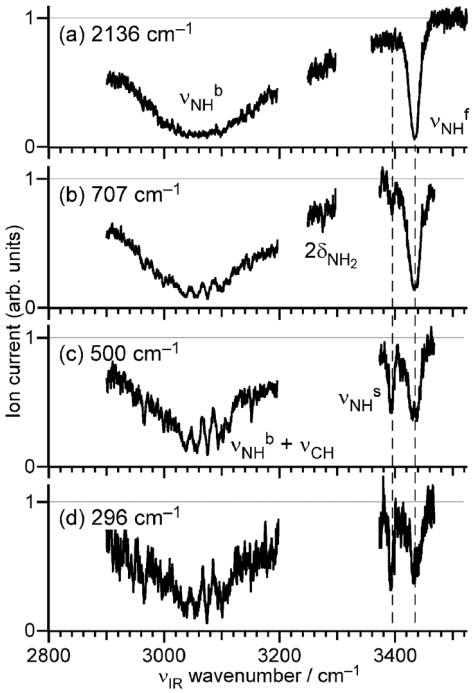

Fig. 6 Excess energy dependence of the IR spectrum of $4ABN^+$–W ionized *via* the $S_1 0^0$ origin band of 4ABN–W(CN). The ionization excess energies are indicated in each panel.

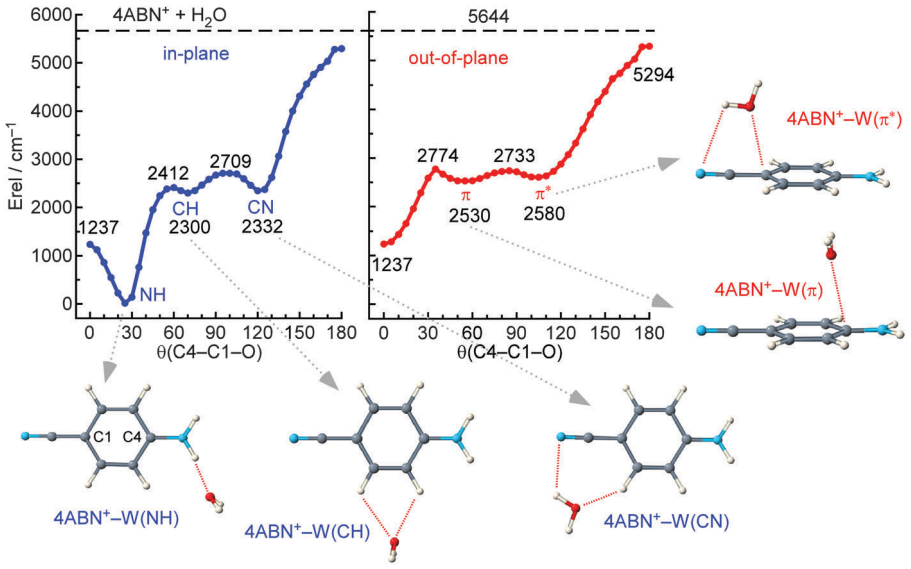

Fig. 5 Potential for $4ABN^+$–H_2O and structures of the minima along the minimum energy paths (M06-2X/aug-cc-pVTZ) for water moving around the $4ABN^+$ cation in the molecular plane (left) and in the plane perpendicular to it (right).[44] All E_{rel} values (cm^{-1}) are given with respect to the energy of the NH-bound global minimum (E_{rel} = 0). E_{rel} = 5644 cm^{-1} corresponds to the dissociation limit into $4ABN^+$ and water (dashed line).

reasonable because the water migration lifetime is ~17 ps, and then the migration reaction must be finished after the 50 ns delay.

Significantly, the spectral features change when the ionization excess energy was reduced to 707 cm^{-1} (Fig. 6(b)). Besides ν_{NH}^{f} and ν_{NH}^{b}, the weak ν_{NH}^{s} band characteristic of a free amino group is clearly observed although the spectrum was measured at 50 ns delay. When the excess energy is suppressed further down to 500 cm^{-1} (Fig. 6(c)) and 296 cm^{-1} (Fig. 6(d)), this spectral signature of the free amino group of $4ABN^{+}$–W increases in relative intensity and becomes almost comparable to the strength of the ν_{NH}^{f} band. This observation means that some of the nascent $4ABN^{+}$–W(CN) population does not reach the NH-bound reaction product P^{+} because their internal energy is not high enough to surmount the reaction barrier. It cannot be decided whether these cations are trapped at the $4ABN^{+}$–W(CN) local minimum or at one of the other local minima along the CN → NH_2 reaction pathway(s) such as CH-bound or $\pi^{(*)}$-bound structures (Fig. 5). The sharp structures between 2900–3200 cm^{-1} appearing on top of the broad ν_{NH}^{b} band in the low excess energy spectra may be explained as follows. These bands are expected to be ν_{CH} fundamentals from their positions, although their IR intensities are calculated to be weak (there may also be contributions from overtone and combination bands coupled to ν_{NH}^{b}). The lower CN → NH_2 reaction yield strongly reduces the intensity of ν_{NH}^{b}, and the buried weak transitions start to appear under small excess energy conditions. The distribution of the internal energy is determined by the Franck–Condon factor between the S_1 origin and the D_0 state of the $4ABN^{+}$–W(CN) structure. For increasing ionization excess energy, more and more vibrational states in the cation become accessible, which increases the population of nascent $4ABN^{+}$–W(CN) states lying above the migration barrier. As a consequence, the intensity of the ν_{NH}^{f} and ν_{NH}^{b} bands of the final P^{+} reaction product increases with respect to the small but nonvanishing ν_{NH}^{s} signal of the AF^{+} population not reaching the P^{+} state. At a relatively high excess energy of 2136 cm^{-1}, the fraction of the AF^{+} product is very small and almost invisible in the IR spectrum. For such high energies, the CN → NH_2 reaction yield approaches unity (as observed in the ps TRIR spectra for an ionization excess energy of 1238 cm^{-1}). Since the signatures of both AF^{+} and P^{+} coexist already at an excess energy of 296 cm^{-1}, the effective barrier for the water migration is lower than 296 cm^{-1} for the nascent $4ABN^{+}$–W(CN) population, which is consistent with the barrier of 377 cm^{-1} estimated for cold $4ABN^{+}$–W(CN) from the M06-2X calculations (Fig. 5). This phenomenon that the reduction of the ionization excess energy may stop an isomerization reaction has been observed earlier for the case of the ionization-induced OH → NH_2 migration in 4-aminophenol–H_2O.[48]

Fig. 5 reproduces the salient parts of the potential energy surface of $4ABN^{+}$–W calculated at the M06-2X/aug-cc-pVTZ level, namely the minimum energy paths for water migration around ABN^{+} in the aromatic plane or in the perpendicular plane.[44] This potential reveals a strongly bound $4ABN^{+}$–W(NH) global minimum with a dissociation energy of D_e = 5644 cm^{-1} and several less stable local minima along the in-plane and out-of-plane paths, including the CN-bound, CH-bound, and $\pi^{(*)}$-bound structures (for details of their structural and vibrational properties, we refer to ref. 44). Most relevant for the current study are the facts that all local minima along the in-plane and out-of-plane pathways have similar relative energies separated by low barriers. Thus, ionization of 4ABN–W(CN) reaches FC^{+} states close to the $4ABN^{+}$–W(CN) minimum and allows for isomerization toward the two equivalent and deep $4ABN^{+}$–W(NH) global minima *via* low reaction barriers both along in-plane and out-of-plane pathways. These competing paths are not considered in the current simple rate constant model. Clearly, sophisticated MD simulations are required to analyse the details of the competing reaction pathways and their rate constants. Once the $4ABN^{+}$–W(CN) isomer has reached the strongly bound $4ABN^{+}$–W(NH) global minimum, fast IVR removes internal energy out of the reaction coordinate and readily traps water in that minimum, thereby preventing any back reaction to the much less stable local minima. The calculated potential predicts an exothermicity of 2300 cm^{-1} for the CN → NH_2 forward reaction and a high and steep barrier of 2400 cm^{-1} for the NH_2 → CN back reaction. Hence, removal of only a small amount of internal energy from the reaction coordinate *via* IVR is required to trap water in the deep double minimum potential of the two equivalent NH sites of the amino group (separated by a barrier of 1237 cm^{-1}).

4. Conclusions

In summary, the time constant for the dynamics of water migration around the aromatic phenyl ring in $4ABN^{+}$–W is measured as about 17 ps using ps TRIR spectroscopy. The migration lifetime of 17 ps for the CN → NH_2 forward reaction is 3–4 times slower than the CO → NH reaction in AA–W,[27] and the slow migration is rationalized by the difference of the internal energy available from the employed photoionization excess energy. The reaction proceeds with essentially 100% yield at an ionization excess energy of 1238 cm^{-1} and the NH_2 → CN back reaction is efficiently quenched by rapid IVR of the deep $4ABN^{+}$–W(NH) global minimum. However, some finite population of nascent $4ABN^{+}$–W(CN) clusters do not reach the final NH-bound reaction product when the ionization excess energy is reduced, and the $4ABN^{+}$–W clusters are trapped in the shallow $4ABN^{+}$–W(CN) local minimum close to the FC^{+} state and/or in one of the shallow CH or $\pi^{(*)}$ local minima along the in-plane or out-of-plane isomerization pathways. Although the present experiment provides an initial view on the dynamics of this solvent rearrangement reaction, its preliminary analysis using simple classical rate equations leaves several important questions to be solved in upcoming MD simulations, such as the competition between the various possible reaction pathways and their branching ratios, the appearance of reaction intermediates along these pathways, and the dependence of these parameters on the internal energy available for the reaction. The experiments will be extended along two lines. First, the expected strong dependence of the properties of the reaction on the ionization excess energy will be characterized, particularly at the lowest

possible excess energy when the reaction is nearly quenched. The second extension is toward larger 4ABN–W_n clusters[44] to probe the dynamics of the H-bonded solvent network around the solute at the molecular level, thereby approaching more realistic solute–solvent systems.

Acknowledgements

This work was supported in part by KAKENHI on innovative area (2503) and the Cooperative Research Program of the "Network Joint Research Center for Materials and Devices" from the Ministry of Education, Culture, Sports, Science and Technology (MEXT), Japan, the Core-to-Core Program 22003 from the Japan Society for the Promotion of Science (JSPS), and the Deutsche Forschungsgemeinschaft (DFG DO 729/4, ENP-MI-1236).

References

1 B. Bagchi, *Annu. Rev. Phys. Chem.*, 1989, **40**, 115–141.
2 W. P. de Boeij, M. S. Pshenichnikov and D. A. Wiersma, *Annu. Rev. Phys. Chem.*, 1998, **49**, 99–123.
3 G. R. Fleming and M. H. Cho, *Annu. Rev. Phys. Chem.*, 1996, **47**, 109–134.
4 H. J. Bakker and J. L. Skinner, *Chem. Rev.*, 2010, **110**, 1498–1517.
5 N. Nandi, K. Bhattacharyya and B. Bagchi, *Chem. Rev.*, 2000, **100**, 2013–2045.
6 R. Jimenez, G. R. Fleming, P. V. Kumar and M. Maroncelli, *Nature*, 1994, **369**, 471–473.
7 E. W. Castner, G. R. Fleming and B. Bagchi, *J. Chem. Phys.*, 1988, **89**, 3519–3534.
8 M. S. Cheung, A. E. Garcia and J. N. Onuchic, *Proc. Natl. Acad. Sci. U. S. A.*, 2002, **99**, 685–690.
9 G. A. Papoian, J. Ulander, M. P. Eastwood, Z. Luthey-Schulten and P. G. Wolynes, *Proc. Natl. Acad. Sci. U. S. A.*, 2004, **101**, 3352–3357.
10 R. H. Zhou, *Proc. Natl. Acad. Sci. U. S. A.*, 2003, **100**, 13280–13285.
11 W. Y. Lu, W. H. Qiu, J. Kim, O. Okobiah, H. X. Hu, G. W. Gokel and D. P. Zhong, *Chem. Phys. Lett.*, 2004, **394**, 415–422.
12 K. Suzuki, M. Kawano and M. Fujita, *Angew. Chem., Int. Ed.*, 2007, **46**, 2819–2822.
13 C. L. Shen and R. M. Murphy, *Biophys. J.*, 1995, **69**, 640–651.
14 A. N. Rissanou, E. Georgilis, E. Kasotaids, A. Mitraki and V. Harmandaris, *J. Phys. Chem. B*, 2013, **117**, 3962–3975.
15 J. He, X. L. Huang, Y. C. Li, Y. J. Liu, T. Babu, M. A. Aronova, S. J. Wang, Z. Y. Lu, X. Y. Chen and Z. H. Nie, *J. Am. Chem. Soc.*, 2013, **135**, 7974–7984.
16 N. Sarkar, K. Das, A. Datta, S. Das and K. Bhattacharyya, *J. Phys. Chem.*, 1996, **100**, 10523–10527.
17 S. M. Bhattacharyya, Z. G. Wang and A. H. Zewail, *J. Phys. Chem. B*, 2003, **107**, 13218–13228.
18 L. Nilsson and B. Halle, *Proc. Natl. Acad. Sci. U. S. A.*, 2005, **102**, 13867–13872.
19 A. Stolow, A. E. Bragg and D. M. Neumark, *Chem. Rev.*, 2004, **104**, 1719–1757.
20 Q. Zhong and J. A. W. Castleman, *Chem. Rev.*, 2000, **100**, 4039–4057.
21 M. Fujii and O. Dopfer, *Int. Rev. Phys. Chem.*, 2012, **31**, 131–173.
22 O. Dopfer, *Z. Phys. Chem.*, 2005, **219**, 125–168.
23 T. S. Zwier, *Annu. Rev. Phys. Chem.*, 1996, **47**, 205–241.
24 B. Brutschy, *Chem. Rev.*, 2000, **100**, 3891–3920.
25 T. Ebata, A. Fujii and N. Mikami, *Int. Rev. Phys. Chem.*, 1998, **17**, 331–361.
26 A. B. Wolk, C. M. Leavitt, E. Garand and M. A. Johnson, *Acc. Chem. Res.*, 2014, **47**, 202–210.
27 K. Tanabe, M. Miyazaki, M. Schmies, A. Patzer, M. Schütz, H. Sekiya, M. Sakai, O. Dopfer and M. Fujii, *Angew. Chem., Int. Ed.*, 2012, **51**, 6604–6607.
28 M. Miyazaki, A. Takeda, S. Ishiuchi, M. Sakai, O. Dopfer and M. Fujii, *Phys. Chem. Chem. Phys.*, 2011, **13**, 2744–2747.
29 S. Ishiuchi, M. Miyazaki, M. Sakai, M. Fujii, M. Schmies and O. Dopfer, *Phys. Chem. Chem. Phys.*, 2011, **13**, 2409–2416.
30 S. Ishiuchi, M. Sakai, Y. Tsuchida, A. Takeda, Y. Kawashima, O. Dopfer, K. Müller-Dethlefs and M. Fujii, *J. Chem. Phys.*, 2007, **127**, 114307.
31 S. Ishiuchi, M. Sakai, K. Daigoku, K. Hashimoto and M. Fujii, *J. Chem. Phys.*, 2007, **127**, 234304.
32 S. Ishiuchi, M. Sakai, Y. Tsuchida, A. Takeda, Y. Kawashima, M. Fujii, O. Dopfer and K. Müller-Dethlefs, *Angew. Chem., Int. Ed.*, 2005, **44**, 6149–6151.
33 S. Ishiuchi, M. Sakai, K. Daigoku, T. Ueda, T. Yamanaka, K. Hashimoto and M. Fujii, *Chem. Phys. Lett.*, 2001, **347**, 87–92.
34 M. Wohlgemuth, M. Miyazaki, M. Weiler, M. Sakai, O. Dopfer, M. Fujii and R. Mitrić, *Angew. Chem., Int. Ed.*, 2014, **53**, 14601–14604.
35 E. M. Gibson, A. C. Jones and D. Phillips, *Chem. Phys. Lett.*, 1988, **146**, 270–274.
36 E. M. Gibson, A. C. Jones, W. G. Bouwman, D. Phillips and J. Sandell, *J. Phys. Chem.*, 1988, **92**, 5449–5455.
37 E. Alejandro, J. A. Fernández and F. Castaño, *Chem. Phys. Lett.*, 2002, **353**, 195–203.
38 E. Alejandro, C. Landajo, A. Longarte, J. A. Fernández and F. Castaño, *J. Chem. Phys.*, 2003, **119**, 9513–9522.
39 K. Sakota, N. Yamamoto, K. Ohashi, M. Saeki, S. Ishiuchi, M. Sakai, M. Fujii and H. Sekiya, *Chem. Phys.*, 2002, **283**, 209–219.
40 K. Sakota, N. Yamamoto, K. Ohashi, H. Sekiya, M. Saeki, S. Ishiuchi, M. Sakai and M. Fujii, *Chem. Phys. Lett.*, 2001, **341**, 70–76.
41 K. Sakota, N. Yamamoto, K. Ohashi, M. Saeki, S. Ishiuchi, M. Sakai, M. Fujii and H. Sekiya, *Phys. Chem. Chem. Phys.*, 2003, **5**, 1775–1779.
42 M. A. Lee, S. H. Nam, H. S. Park, N. R. Cheong, S. Ryu, J. K. Song and S. M. Park, *Bull. Korean Chem. Soc.*, 2008, **29**, 2109–2113.
43 T. Nakamura, M. Schmies, A. Patzer, M. Miyazaki, S. Ishiuchi, M. Weiler, O. Dopfer and M. Fujii, *Chem. – Eur. J.*, 2014, **20**, 2031–2039.

44 M. Schmies, M. Miyazaki, M. Fujii and O. Dopfer, *J. Chem. Phys.*, 2014, **141**, 214301.
45 M. Miyazaki, A. Fujii, T. Ebata and N. Mikami, *Chem. Phys. Lett.*, 2001, **349**, 431–436.
46 N. Solca and O. Dopfer, *Chem. Phys. Lett.*, 2001, **347**, 59–64.
47 H. Tachikawa and M. Igarashi, *J. Phys. Chem. A*, 1998, **102**, 8648–8656.
48 M. Gerhards, A. Jansen, C. Unterberg and A. Gerlach, *J. Chem. Phys.*, 2005, **123**, 074320.
49 T. Ikeda, K. Sakota, Y. Kawashima, Y. Shimazaki and H. Sekiya, *J. Phys. Chem. A*, 2012, **116**, 3816–3823.
50 K. Sakota, Y. Shimazaki and H. Sekiya, *Phys. Chem. Chem. Phys.*, 2011, **13**, 6411–6415.
51 H. Tachikawa, M. Igarashi and T. Ishibashi, *J. Phys. Chem. A*, 2003, **107**, 7505–7513.
52 K. Sakota, S. Harada, Y. Shimazaki and H. Sekiya, *J. Phys. Chem. A*, 2011, **115**, 626–630.
53 M. Weiler, T. Nakamura, H. Sekiya, O. Dopfer, M. Miyazaki and M. Fujii, *ChemPhysChem*, 2012, **13**, 3875–3881.
54 K. Sakota, Y. Kouno, S. Harada, M. Miyazaki, M. Fujii and H. Sekiya, *J. Chem. Phys.*, 2012, **137**, 224311.
55 M. Schütz, K. Sakota, R. Moritz, M. Schmies, T. Ikeda, H. Sekiya and O. Dopfer, *J. Phys. Chem. A*, 2015, **119**, 10035–10051.
56 H. M. Kim, K. Y. Han, J. Park, G. S. Kim and S. K. Kim, *J. Chem. Phys.*, 2008, **128**, 041104.
57 T. Kobayashi and O. Kajimoto, *J. Chem. Phys.*, 1987, **86**, 1118–1124.
58 T. Kobayashi, K. Honma, O. Kajimoto and S. Tsuchiya, *J. Chem. Phys.*, 1987, **86**, 1111–1117.
59 T. Nakamura, M. Miyazaki, S. Ishiuchi, M. Weiler, M. Schmies, O. Dopfer and M. Fujii, *ChemPhysChem*, 2013, **14**, 741–745.
60 T. Omi, H. Shitomi, N. Sekiya, K. Takazawa and M. Fujii, *Chem. Phys. Lett.*, 1996, **252**, 287–293.
61 M. Schmies, A. Patzer, S. Kruppe, M. Miyazaki, S. Ishiuchi, M. Fujii and O. Dopfer, *ChemPhysChem*, 2013, **14**, 728–740.
62 S. Ullrich and K. Müller-Dethlefs, *J. Phys. Chem. A*, 2002, **106**, 9188–9195.
63 M. Schmies, PhD thesis, Technische Universität Berlin, 2015.

LIST OF PUBLICATIONS

[1]M. Wohlgemuth and R. Mitrić, "Excitation energy transport in DNA modelled by multi-chromophoric field-induced surface hopping," Phys. Chem. Chem. Phys. **22**, 16536–16551 (2020).

[2]A. Röder, K. Issler, L. Poisson, A. Humeniuk, M. Wohlgemuth, et al., "Femtosecond dynamics of the 2-methylallyl radical: a computational and experimental study," J. Chem. Phys. **147**, 013902 (2017).

[3]M. Wohlgemuth, M. Miyazaki, K. Tsukada, M. Weiler, O. Dopfer, et al., "Deciphering environment effects in peptide bond solvation dynamics by experiment and theory," Phys. Chem. Chem. Phys. **19**, 22564–22572 (2017).

[4]M. Wohlgemuth and R. Mitrić, "Photochemical chiral symmetry breaking in alanine," J. Chem. Phys. A **120**, 8976–8982 (2016).

[5]M. Miyazaki, T. Nakamura, M. Wohlgemuth, R. Mitrić, O. Dopfer, et al., "Single water solvation dynamics in the 4-aminobenzonitrile–water cluster cation revealed by picosecond time-resolved infrared spectroscopy," Phys. Chem. Chem. Phys. **17**, 29969–29977 (2015).

[6]M. Wohlgemuth, M. Miyazaki, M. Weiler, M. Sakai, O. Dopfer, et al., "Solvation dynamics of a single water molecule probed by infrared spectra–theory meets experiment," Angew. Chem. Int. Ed. **53**, 14601–14604 (2014).

[7]A. Humeniuk, M. Wohlgemuth, T. Suzuki, and R. Mitrić, "Time-resolved photoelectron imaging spectra from non-adiabatic molecular dynamics simulations," J. Chem. Phys. **139**, 134104 (2013).

[8]M. I. Röhr, J. Petersen, M. Wohlgemuth, V. Bonačić-Koutecký, and R. Mitrić, "Nonlinear absorption dynamics using field-induced surface hopping: zinc porphyrin in water," ChemPhysChem **14**, 1377–1386 (2013).

[9]J. Petersen, M. Wohlgemuth, B. Sellner, V. Bonačić-Koutecký, H. Lischka, et al., "Laser pulse trains for controlling excited state dynamics of adenine in water," Phys. Chem. Chem. Phys. **14**, 4687–4694 (2012).

[10]G. Tomasello, M. Wohlgemuth, J. Petersen, and R. Mitrić, "Photodynamics of free and solvated tyrosine," J. Phys. Chem. B **116**, 8762–8770 (2012).

[11]R. Mitrić, J. Petersen, M. Wohlgemuth, U. Werner, and V. Bonačić-Koutecký, "Field-induced surface hopping method for probing transition state nonadiabatic dynamics of Ag_3," Phys. Chem. Chem. Phys. **13**, 8690–8696 (2011).

[12]R. Mitrić, J. Petersen, M. Wohlgemuth, U. Werner, V. Bonačić-Koutecký, et al., "Time-resolved femtosecond photoelectron spectroscopy by field-induced surface hopping," J. Phys. Chem. A **115**, 3755–3765 (2011).

[13]M. Wohlgemuth, V. Bonačić-Koutecký, and R. Mitrić, "Time-dependent density functional theory excited state nonadiabatic dynamics combined with quantum mechanical/molecular mechanical approach: photodynamics of indole in water," J. Chem. Phys. **135**, 054105 (2011).

[14]R. Mitrić, U. Werner, M. Wohlgemuth, G. Seifert, and V. Bonačić-Koutecký, "Nonadiabatic dynamics within time-dependent density functional tight binding method," J. Phys. Chem. A **113**, 12700–12705 (2009).

ACKNOWLEDGMENTS

I would like to thank the many people and institutions that supported me during the research time and preparation of this thesis. First of all, I would like to express my gratitude to my supervisor Prof. Dr. Roland Mitrić for giving me the opportunity to work in his group on such interesting topics. I am grateful for his competent guidance, his patience and for giving me the chance to broaden my knowledge beyond the research.

I want to thank my co-workers at FU Berlin and JMU Würzburg Dr. Jens Petersen, Dr. Merle Röhr, Dr. Polina Lisinetskaya, Dr. Alexander Humeniuk, Dr. Gaia Tomasello, Dr. Evgenii Titov, Joscha Hoche, Kevin Issler, Joachim Lindner, Michael Wenzel and David Fischermeier for the many scientific discussions, the friendly atmosphere in the group and their support. In particular, I wish to thank Dr. Jens Petersen for being a good friend in the past decade, helping me solve complicated problems and finally for carefully proofreading many of my publications and this thesis.

I am grateful to my collaborators Prof. Dr. Masaaki Fujii (Tokyo Institute of Technology), Prof. Dr. Otto Dopfer (TU Berlin), Prof. Dr. Mitsuhiko Miyazaki (Tohoku University) for providing outstanding experiments and fruitful scientific discussions.

Also, I would like to acknowledge the funding by the Deutsche Forschungsgemeinschaft through Emmy-Noether-Program (Grant No. 77534479) and GRK 2112 as well as by the European Research Council through Consolidator Grant (Grant No. 646737), which allowed me to finish my studies without being pressed for time nor money.

Finally, I would like to thank my family and friends for their support and patience through all these years.

SELBSTSTÄNDIGKEITSERKLÄRUNG

Ich erkläre gegenüber der Freien Universität Berlin, dass ich die vorliegende Dissertation selbstständig und ohne Benutzung anderer als der angegebenen Quellen und Hilfsmittel angefertigt habe. Die vorliegende Arbeit ist frei von Plagiaten. Alle Ausführungen, die wörtlich oder inhaltlich aus anderen Schriften entnommen sind, habe ich als solche kenntlich gemacht. Diese Dissertation wurde in gleicher oder ähnlicher Form noch in keinem früheren Promotionsverfahren eingereicht.
Mit einer Prüfung meiner Arbeit durch ein Plagiatsprüfungsprogramm erkläre ich mich einverstanden.

Berlin, 21. April 2021

Matthias Wohlgemuth

DECLARATION OF AUTHORSHIP

I declare to the Freie Universität Berlin that I have completed the submitted dissertation independently and without the use of sources and aids other than those indicated. The present thesis is free of plagiarism. I have marked as such all statements that are taken literally or in content from other writings. This dissertation has not been submitted in the same or similar form in any previous doctoral procedure.
I agree to have my thesis examined by a plagiarism examination software.

Berlin, April 21, 2021

Matthias Wohlgemuth